INTERFACES BETWEEN LIGHT AND MATTER FOR QUANTUM INFORMATION PROCESSING

TECHNISCHE UNIVERSITÄT DARMSTADT

Vom Fachbereich Physik
der Technischen Universität Darmstadt

zur Erlangung des Grades
eines Doktors der Naturwissenschaften (Dr. rer. nat.)

genehmigte Dissertation von
M. Sc. Nils Trautmann
aus Erbach

Referent: Prof. Dr. Gernot Alber
Korreferent: Prof. Dr. Reinhold Walser

Tag der Einreichung: 20.12.2016
Tag der Prüfung: 30.01.2017

Darmstadt 2017
D17

ABSTRACT

Quantum communication and quantum computation are anticipated quantum technologies which enable us to tackle problems which are hard or even impossible to solve by classical means. A major challenge in implementing real life applications for quantum communication and quantum computation is to implement efficient interfaces between different kinds of quantum systems which serve as carriers of quantum information, such as single photons and single material quantum systems (i.e. atoms, ions ...). These different kinds of quantum systems have different advantages and disadvantages if it comes to practical applications. Single photons, which may serve as flying qubits, can be transmitted over larger distances without suffering from too much decoherence while single material quantum systems may be used as matter qubits to store and process quantum information locally. For many applications, the particular advantages of both kinds of systems are needed. Hence, we require interfaces between flying qubits and matter qubits.

In the first part of this thesis, we develop suitable protocols for implementing interfaces between these flying qubits and matter qubits. The key challenge is to design the interactions to allow the efficient coupling of single photons to single material quantum systems, such as atoms and ions. This is not only of interest for possible practical applications of quantum mechanics but also drives fundamental research, as it is directly connected to a precise control and enhancement of matter-field interactions.

The second part of this thesis is concerned with the applications of quantum technologies for simulating complex quantum systems, which cannot be treated by classical means. In many cases, the simulation of complex quantum systems turns out to be a difficult task due to the basic structure of quantum mechanics. The same aspects of quantum mechanics, which allow us to tackle computationally hard problems by using quantum algorithms, create difficulties in understanding the behavior of complex quantum systems. However, the understanding of complex quantum systems is not only of fundamental importance but might also enable us to give answers to problems of practical significance, such as an explanation for high-temperature superconductivity. Here, we develop protocols for implementing such quantum simulations based on ions trapped in state of the art ion traps. The applications of these kinds of quantum simulations are ranging from fundamental research to process design, control, and optimization.

ZUSAMMENFASSUNG

Quantenkommunikation und Quantumcomputing sind zukunftsweisende Quantentechnologien, welche die Lösung von Problemen ermöglichen, die mittels rein klassischer Methoden unlösbar sind. So erlaubt die Quantenkryptographie den informationstheoretisch sicheren Austausch eines geheimen Schlüssels über große Distanzen und Quantenalgorithmen machen es möglich, komplexe Probleme, wie die Primfaktorzerlegung großer Zahlen, in polynomieller Zeit zu lösen. Eine der größten Herausforderungen in der praktischen Anwendung dieser Technologien ist die Implementierung effizienter Schnittstellen zwischen verschiedenen Quantensystemen, die als Träger von Quanteninformation genutzt werden, wie z.B. einzelne Photonen, die als photonische Qubits dienen, oder einzelne materielle Quantensysteme (z.B. Atome, Ionen...), die als materielle Qubits Anwendung finden. Diese Quantensysteme haben im Bezug auf praktische Anwendungen jeweils spezifische Vor- und Nachteile. Einzelne Photonen können über große Distanzen übertragen werden ohne dabei durch Dekohärenz zu stark in Mitleidenschaft gezogen zu werden. Materielle Quantensysteme, wie Atome und Ionen, andererseits können genutzt werden, um Quanteninformation lokal zu speichern und zu verarbeiten. Für viele Anwendungen sind jedoch die spezifischen Vorteile der beiden oben genannten Systeme von Nöten. Folglich sind Schnittstellen zwischen photonischen Qubits und materiellen Qubits erforderlich.

Der erste Teil dieser Arbeit beschäftigt sich mit der Entwicklung geeigneter Protokolle zur Implementierung solcher Schnittstellen. Die Herausforderung liegt hierbei in der präzisen Kontrolle der Wechselwirkung zwischen Licht und Materie, um eine effiziente Kopplung von einzelnen Photonen an einzelne materielle Quantensysteme, wie Atome oder Ionen, zu gewährleisten. Dies ist nicht nur für praktische Anwendungen von Interesse, sondern treibt auch die Grundlagenforschung weiter voran, da hierzu auch die fundamentale Wechselwirkung von Licht mit Materie auf dem Niveau einzelner Photonen untersucht wird.

Der zweite Teil dieser Arbeit beschäftigt sich mit möglichen Anwendungen von Quantentechnologien für die Simulation von Quantensystemen, die aufgrund ihrer Komplexität nicht mehr mittels klassischer Computer untersucht werden können. Es stellt sich heraus, dass viele der Eigenschaften der Quantenmechanik, die es uns ermöglichen schwere Probleme mittels eines Quantencomputers in polynomieller Zeit zu lösen, die Simulation komplexer Quantensysteme mittels klassischer Computer erschweren oder gar praktisch unmöglich machen. Die Untersuchung derartiger Systeme ist nicht nur von Interesse für die Grundlagenforschung sondern weist auch den Weg zur Beantwortung vieler Fragen von immenser praktischer Bedeutung, wie z.B. die Erklärung des Phänomens der Hochtemperatursupraleitung. In diesem Teil der Arbeit werden Protokolle zur Simulation solcher komplexen Quantensysteme mittels Ionenfallen vorgestellt. Die möglichen Anwendungen dieser Art von Quantensimulationen reichen hierbei von Grundlagenforschung bis hin zur anwendungsorientierten Forschung zur Entwicklung, Optimierung und Kontrolle von Prozessen.

ACKNOWLEDGMENTS

This Ph.D. thesis would not have been possible without a significant number of people. Above all, I want to thank Gernot Alber for his guidance, advice, and his great support. I also like to thank Reinhold Walser for being the second referee of this thesis and investing his time in studying my work. I also like to thank all the members of my work group, especially József Zsolt Bernád and Mauricio Torres for the constant support and the great environment in our group. I always enjoyed the environment in the complete group with many discussions and debates.

Also, I want to thank the large number of inspiring people whom I had the opportunity to collaborate and discuss with over the course of the last years. I am grateful for the stimulating scientific discussions. Apart from the people I already mentioned these are in particular: Girish S. Agarwal, Sarah Croke, Gergely Ferenczi, Philipp Hauke, Luis L. Sánchez-Soto, Markus Sondermann and Matthias Sonnleitner. My special thanks and appreciation goes to Stephen M. Barnett, Dieter Jaksch, Tamás Kiss, Gerd Leuchs, Thomas H. Seligman and Peter Zoller and their work groups for their hospitality and the fascinating discussions.

I am grateful to CASED and CROSSING for supporting me with an excellent infrastructure and for the opportunity to work in an interdisciplinary environment.

Most importantly, I want to express my sincere gratitude to my family and friends, especially my parents and my wife Anika. Your love and support have been a great source of happiness and motivation.

CONTENTS

1

INTRODUCTION AND OUTLINE

The interaction between matter and the electromagnetic radiation field is one of the most fundamental interactions in nature. Thus, the theory of classical electrodynamics developed by Maxwell is one of the main pillars of classical physics. The desire to understand these interactions triggered many of the important discoveries at the beginning of the 20th century, such as the theory of special relativity [1] or the theory of quantum mechanics [2], originally developed to understand the structure of atomic spectra. The success of the newly discovered quantum theory quickly spawned the interest in developing a consistent fully relativistic theory of quantum electrodynamics [3], unifying the concepts of the new quantum theory with the theory of classical electrodynamics. The development of this first quantum field theory is considered to be one of the major breakthroughs in physics during the 20th century and many concepts such as gauge theories and renormalization which are still fundamental to our understanding of nature until today have been developed along this way. Today, the theory of quantum electrodynamics is one of the best tested theories in science history.

Starting with the invention of the laser [4], experimental advances during the last decades such as atom trapping [5], ion trapping [6], and laser cooling [7] have enabled us to control and probe single quantum systems with extremely high accuracy. These advances and the realization of optical and microwave cavities with extremely high quality factors led to beautiful experiments probing the interactions between single material quantum systems, such as atoms or ions, and the electromagnetic radiation field. Thereby, enabling us to confirm the predictions of quantum mechanics and quantum electrodynamics not only for macroscopic ensembles, but also for single quantum systems. These advances have not only led to a deeper understanding of physics but have also paved the way towards new quantum technologies. Applications of these anticipated quantum technologies include

1. quantum metrology [8], enabling high precision measurements only limited by the laws of nature;

2. quantum computing [9], aiming for exponentially enhanced computing power to tackle computationally hard problems;

3. quantum cryptography or quantum communication [10], enabling information theoretically secure communication between remote parties;

4. quantum simulations [11], enabling the deeper understanding of complex many-body problems, which are too complicated to be treated by classical means.

The first part of this thesis is mainly concerned with the development of new protocols and schemes for applications in quantum computing, quantum cryptography, and

quantum communication while the second part is focused on protocols for performing quantum simulations.
In order to exploit the laws of quantum mechanics, for the above mentioned quantum technological applications, one has to deal with single quantum systems instead of macroscopic devices [1]. So, rather than storing a single bit redundantly in thousands or even millions of atoms as done in classical computing architectures, the qubits used for quantum information processing have to be stored in single highly controlled quantum systems, such as single atoms or single ions. These systems, however, are extremely fragile towards interactions with the surrounding environment. Uncontrolled interactions with the environment result in the decay of the coherence properties of these quantum systems over time causing decoherence and dissipation. The coherence properties of these single quantum systems are a significant advantage of the quantum technologies discussed above compared to their classical counterparts. Hence, shielding a quantum system against decoherence and dissipation is one of the main steps required for the implementation and use of these quantum technologies.

Quantum systems which have proven themselves to be incredibly insensitive towards environmental interactions are single photons. They can be transmitted over hundreds of kilometers by preserving their coherence properties. Hence, photons are ideal for transmitting quantum information over macroscopic distances, which is crucial for quantum cryptography and for scaling up architectures for quantum computation [14]. Unfortunately, this insensitivity comes with the price of weak interactions resulting in weak optical nonlinearities. Under normal circumstances, single photons do not interact and nonlinearities induced by optical media are typically small and can only be harnessed if a larger number of photons is present. Interactions between single quantum systems, such as single photons, are of importance if it comes to applications for quantum computing or quantum simulation. However, they are also required for applications in quantum cryptography such as overcoming losses in fibers by implementing a quantum repeater.

Single material quantum systems, such as atoms or ions, on the other hand offer stronger interactions among each other, but as such are also more affected by their environment resulting in decoherence. Hence, a suitable architecture requires interfaces between photons carrying quantum information over larger distances and material systems used to create local interactions.

1.1 INTERFACES BETWEEN LIGHT AND MATTER

The first part of this thesis is concerned with interfaces between single photons and single material quantum systems. These investigations are not only of interest for possible practical applications of quantum mechanics but are also driving fundamental research forward as they are directly connected to a precise control and enhancement of matter-field interactions. This opens the door to many exciting experiments addressing fundamental questions in physics, such as loophole-free violations of Bell inequalities. Our aim is to provide suitable protocols for efficient coupling between photons and single material quantum systems.

A large part of the current theoretical and experimental research is concerned with efficient coupling of single material quantum systems to single photons and

1 A quantum system is not necessarily a microscopic system. It has been shown that well-controlled macroscopic objects, such as superconducting circuits [12] or large molecules [13], can also show the desired properties.

is based on fiber- and cavity-based architectures. Thereby, specific modes of the electromagnetic radiation field are selected by an optical resonator. An attractive feature of this approach is the drastically simplified structure of the matter-field interaction. Consequently, a variety of impressive experiments has already been performed based on this architecture.

A relatively new route towards efficient matter-field coupling focuses on the opposite regime involving extreme multimode scenarios in the absence of optical resonators. Instead of enhancing the coupling of the quantum emitters to one particular mode of the radiation field by using an optical resonator, the coupling of the quantum emitter to a continuum of modes is enhanced by confining the photons to sub-wavelength length scales. This can be achieved in a variety of architectures ranging from one-dimensional waveguides, such as nanowires [15–19], nanofibers [20, 21], or coplanar waveguides (circuit QED) [22, 23] to free-space [24] scenarios by focusing light by a parabolic mirror. These new architectures circumvent the limited accessibility of cavities enclosing the radiation field in three dimensions, thereby enabling enhanced access to the radiation field simplifying measurement and detection. The free-space approach [25] offers interesting perspectives for scaling up quantum communication to larger distances by avoiding losses in optical fibers. Photon losses in optical fibers are currently limiting fiber-based quantum communication architectures to distances of several hundred kilometers [26]. These losses are no fundamental limitation and could, in principle, be overcome by implementing a quantum repeater [27]. However, the implementation of such a repeater is a demanding task and is connected to many unsolved problems in the area of quantum information processing. Free-space quantum communication offers the opportunity to scale up quantum communication to distances of thousands of kilometers or more by establishing a satellite-based quantum communication network. As soon as photons are propagating outside the atmosphere losses are reduced drastically and a free-space channel could outperform fiber-based communication systems. Hence, the direct coupling of single photons to a multimode radiation field in the absence of optical resonators offers interesting perspectives for advancing quantum communication and quantum information processing. Unfortunately, the majority of the protocols developed for fibers and cavities cannot be adapted to these new kinds of architectures because typically they rely on intrinsic single mode effects such as vacuum Rabi oscillations induced by mode selection by an optical resonator. Hence, there are numerous open questions on how efficient interfaces between single material quantum systems and single photons propagating in a multimode radiation field can be realized. In the first part of this work, we address some of the questions connected to efficient coupling between matter and multimode radiation fields on the single-photon level.

CHAPTER 2 provides an introduction to the theory of cavity quantum electrodynamics (cavity QED). This theory serves as the theoretical foundation for all further investigations in the first part of this thesis.

CHAPTER 3 introduces the framework of the photon-path-representation for single-photon states. This method provides suitable tools for handling the vast number of dynamical degrees of freedom which are needed to describe a multimode electromagnetic radiation field coupled to single quantum emitters. We use the relations derived in this chapter for studying the dynamics of these kinds of systems in cases in which only a single initial excitation (either a photonic excitation or an excitation of one of the material quantum systems) is present in

the system. By using this photon-path-representation, we can develop suitable protocols for an efficient coupling of single quantum emitters to single photons propagating in free-space or in one-dimensional waveguides.

CHAPTER 4 presents the first of these protocols. It can be used for generating high-fidelity maximally entangled states between distant matter qubits connected via a free-space link. These maximally entangled states are a valuable resource for many applications ranging from quantum cryptography to fundamental tests of quantum mechanics (such as a test of Bell's inequalities). In our investigation, a new setup of two opposing parabolic mirrors is considered each of them with a single ion trapped at its focal point. We show that by using parabolic mirrors it is possible to overcome low photon collection efficiencies, typically connected to the free-space channel. The results of this investigation have been published in

> *"Generation of entangled matter qubits in two opposing parabolic mirrors"*
> by N. Trautmann, J. Z. Bernád, M. Sondermann, G. Alber, L. L. Sánchez-Soto, and G. Leuchs, Phys. Rev. A **90**, 063814 (2014).

CHAPTER 5 explores the influence of the temporal shape of single-photon wave packets on the coupling efficiency of single photons to single material systems. Any deviation of the temporal shape of a single-photon wave packet from its ideal form, which leads to almost unit coupling efficiency, is one of the factors which limits the efficiency of matter-field coupling on the single-photon level. Techniques to overcome this hurdle have been developed [28] and tested in experiment [29] for fiber- and cavity-based systems. If the waveform of the incoming wave packet is known, the absorption process of the material quantum system can be controlled by applying additional suitably tailored laser pulses and almost complete absorption of the incoming wave packet can be accomplished. However, the corresponding protocol relies on vacuum Rabi oscillations induced by a high finesse cavity. Hence, this protocol is not compatible with a free-space link or architectures relying on the direct coupling of a quantum emitter to a one-dimensional waveguide. We present a new protocol for accomplishing the same task without mode selection by an optical resonator. We show how it can be used to realize highly efficient, high-fidelity quantum state transfer between distant matter qubits. Thereby, we mainly focus on applications for free-space communication. However, as we are dealing with extreme multimode scenarios, our results can also be applied to quantum emitters directly coupled to one-dimensional waveguides. The results of this investigation have been published in

> *"Time-Reversal-Symmetric Single-Photon Wave Packets for Free-Space Quantum Communication"*
> by N. Trautmann, G. Alber, G. S. Agarwal, and G. Leuchs,
> Phys. Rev. Lett. **114**, 173601 (2015).

CHAPTER 6 demonstrates that dissipative processes such as spontaneous decay or cavity loss can be turned into valuable tools for quantum information processing and quantum communication. The protocol discussed in chapter 5 requires a precise knowledge about an incoming photon wave packets to enable its efficient absorption. Unfortunately, in general, detailed information about waveform or the arrival time of an incoming wave packet are not available. In this chapter, we

demonstrate that this is not a fundamental limitation and that single photons of quite an arbitrary shape can trigger a highly efficient state transfer of a single material system. This can be achieved by properly balancing dissipative processes, such as spontaneous decay or cavity loss, with the help of impedance matching. This proposed scheme can be applied to cavity-based architectures and does not require mode selection by an optical resonator. Thus, it can also be used to enhance the direct coupling of single photons to single material quantum systems implanted in one-dimensional waveguides or even in free-space. Our new scheme can serve as a basic building block for various protocols relevant for quantum information processing. We demonstrate its use for building a deterministic single-atom single-photon quantum memory and a deterministic frequency converter between photonic qubits of different wavelengths which could serve as an interface between several quantum information processing architectures. The results of this investigation have been published in

> *"Dissipation-enabled efficient excitation transfer from a single photon to a single quantum emitter"* by N. Trautmann and G. Alber,
> Phys. Rev. A **93**, 053807 (2016).

CHAPTER 7 discusses the influence of the center of mass motion of a trapped atom or ion on the process of photon absorption. In many theoretical investigations concerned with the coupling of trapped atoms or ions to the radiation field, it is assumed that the dynamics of the center of mass motion of the material system can be neglected due to tight trapping of the atom or ion and due to its large mass compared to the small electron mass. We go beyond this assumption and investigate the impact of the center of mass motion on the attempt to absorb a single photon by a single trapped atom or ion in free-space efficiently. As it turns out, the center of mass motion can be a limiting factor of significant importance, especially if no sub-Doppler cooling techniques are applied to the trapped atom or ion. In the experiment described in [30], for example, the coupling efficiency is reduced by roughly 50% just due to the center of mass motion. It is demonstrated that by time-dependent modulation of a harmonic trapping frequency an atomic or ionic center of mass state can be squeezed so strongly that highly efficient single-photon absorption is possible even in cases of weak confinement by a trapping potential. The results of this investigation have been published in

> *"Efficient single-photon absorption by a trapped moving atom"*
> by N. Trautmann, G. Alber, and G. Leuchs,
> Phys. Rev. A **94**, 033832 (2016).

CHAPTER 8 explores optical nonlinearities and multi-photon processes. All previous investigations discussed above deal with situations in which at most a single photon was present in the quantized radiation field. In the case of multiple photons being present in the radiation field, the description of the resonant interaction of photons with single material systems becomes much more complicated because nonlinear saturation effects start to play a role. We investigate the interaction of single material quantum systems with highly non-classical multi-photon states by taking the full multimode aspects of the radiation field into account. We extend the photon-path-representation for single-photon states introduced in chapter 3 in order to describe the dynamics of such systems by a diagrammatic method. Our method can be applied to study the dynamics of quantum emitters

coupled to one-dimensional waveguides or to the radiation field confined in large or half-open cavities or even in free-space. Thus, our method could be used to design suitable protocols for quantum information processing and quantum communication in a variety of architectures ranging from metallic nanowires coupled to quantum dots to possible applications in free-space. The results of this investigation have been published in

"Elementary quantum electrodynamical processes in multimode scenarios - a photon-path-representation for multiphoton states"
by N. Trautmann and G. Alber, to be published in "Lectures on Quantum Information" (Wiley-VCH, edited by D. Bruss and G. Leuchs).

1.2 QUANTUM SIMULATION

In general terms,

> *"Simulation is the process of representing the dynamic behavior of one system by the behavior of another system."*
>
> –Encyclopedia of Computer Science [31]

Due to the rapid development of classical information technology over the last decades, simulations are often carried out using classical computing architectures. However, the notion of simulation is not restricted to the use of classical computers. The second part of this thesis is concerned with applications of quantum technologies for simulating complex systems which can hardly be treated by classical means. Simulations are used to gain knowledge about the behavior of a complex system. They are often performed to access observables which are difficult to measure in experiments or to replace experiments to some extent if they are too expensive or too resource consuming. Applications of simulations are ranging from fundamental research to process design, control, and optimization.

The simulation of complex quantum systems, especially interacting many-body systems, turns out to be a difficult task due to the basic structure of quantum mechanics. The same aspects of quantum mechanics, which allow us to tackle computationally hard problems by using quantum algorithms, create difficulties in understanding the behavior of complex quantum systems. Thus, a current direction of research is to connect the dynamics of one particular quantum system to the dynamics of another well-controlled quantum system. These quantum simulations enable us to understand the behavior of complex quantum many-body systems, which is not only of fundamental importance but might also enable us to give answers to problems of vital practical importance, such as an explanation for high-temperature superconductivity.

CHAPTER 9 shows how to simulate the dynamical Casimir effect, an effect predicted theoretically by cavity QED [32], by using an ion chain confined in a Paul trap. This effect is directly connected to the vacuum fluctuations of the electromagnetic radiation field, a direct manifestation of Heisenberg's uncertainty principle. The dynamical Casimir effect allows for the observation of these vacuum fluctuations by turning them into real observable photons. Unfortunately, the observation of this effect in a cavity QED experiment would require the rapid variation of the length of a cavity with relativistic velocities, a daunting challenge. We show that the dynamics of the multimode radiation field inside a variable-length cavity

can be mapped to the dynamics of transverse phonons of an ion crystal. The proposed quantum simulator allows for probing the photon production caused by the dynamical Casimir effect on the single-photon level by using the sophisticated methods of measuring phonic excitations available for ion chains. The results of this investigation have been published in

> *"Quantum simulation of the dynamical Casimir effect with trapped ions"*
> by N. Trautmann and P. Hauke, New J. Phys. **18**, 043029 (2016).

Part I

INTERFACES BETWEEN LIGHT AND MATTER

2

CAVITY QUANTUM ELECTRODYNAMICS

In this chapter, we formulate the theory of cavity quantum electrodynamics (cavity QED), which provides the basic framework for all further investigations in the first part of this thesis. The theory of cavity QED has been developed to describe the interaction of quantum emitters, such as atoms or ions, with the quantized radiation field inside an optical resonator. The typical experiments are concerned with photon energies around a few electron volts (eV). Thus, processes connected to much higher energy scales, such as pair production, can safely be neglected. The theory formulated in this chapter corresponds to the low energy limit of the full relativistic theory of quantum electrodynamics. In this low energy limit, the formalism of the theory can be simplified considerably which allows us to focus on the effects which can be observed in typical cavity QED experiments.

One of the basic ideas of cavity QED is to treat the macroscopic objects forming the cavities or the mirrors almost classically. Thereby, it is possible to focus on the dynamics of a single or a few quantum emitters interacting with the quantized radiation field. We start our discussion of cavity QED in the absence of these quantum emitters, a situation in the following referred to as the free radiation field. In a second step, we include the description of the interaction of the quantized radiation field with the microscopic quantum emitters mentioned above.

2.1 THE FREE RADIATION FIELD

As starting point of our investigation of the free radiation field, we choose the Maxwell equations and investigate the induced dynamics of the vector potential $\mathbf{A}$ and the scalar potential ϕ. In a first step, we isolate the dynamical degrees of freedom which are required to describe the classical radiation field. For this purpose, we make use of the Coulomb gauge condition which allows us to focus solely on the vector potential $\mathbf{A}$. In a second step, a Lagrangian respectively a Hamiltonian formulation of the theory describing these dynamical degrees of freedom is derived. Finally, we apply the canonical quantization procedure to obtain the theory of quantum electrodynamics for the free radiation field.

We start our considerations with the classical Maxwell equations (in SI units), which describe the dynamics of the electric field $\mathbf{E}$ and the magnetic field $\mathbf{B}$ coupled to a charge distribution ρ and an electric current $\mathbf{j}$

$$\nabla \cdot \mathbf{E} = \frac{\rho}{\epsilon_0} \tag{2.1}$$

$$\nabla \cdot \mathbf{B} = 0 \tag{2.2}$$

$$\nabla \times \mathbf{E} = -\frac{\partial}{\partial t}\mathbf{B} \tag{2.3}$$

$$\nabla \times \mathbf{B} = \mu_0 \mathbf{j} + \mu_0 \epsilon_0 \frac{\partial}{\partial t}\mathbf{E} \tag{2.4}$$

with ϵ_0 and μ_0 being the vacuum permittivity and the vacuum permeability. The electric field and the magnetic field can be expressed in terms of the vector potential $\mathbf{A}$ and the scalar potential ϕ by defining the relations

$$\mathbf{B} = \nabla \times \mathbf{A} \tag{2.5}$$

$$\mathbf{E} = -\nabla\phi - \frac{\partial}{\partial t}\mathbf{A} \,. \tag{2.6}$$

By using the above ansatz, we guarantee that the homogeneous Maxwell equations Eqs. (2.2) and (2.3) are satisfied by the electric and magnetic field. In fact, introducing the vector potential is not only a matter of convenience but it is also the right way to obtain a Lagrangian or Hamiltonian formulation of the theory, which is needed to apply the canonical quantization procedure. However, the connection between the vector potential and the corresponding electric and magnetic fields is not unique. In order to circumvent the ambiguity of the vector potential $\mathbf{A}$ and the scalar potential ϕ, we impose the so called Coulomb gauge condition

$$\nabla\mathbf{A} = 0 \,. \tag{2.7}$$

By imposing this gauge condition, the Gauss law (Eq. (2.1)) takes the following form

$$-\nabla^2\phi = \frac{\rho}{\epsilon_0} \,. \tag{2.8}$$

In a similar fashion, Eq. (2.4) can be written in the form

$$\left[\nabla^2 - \frac{1}{c^2}\frac{\partial^2}{\partial t^2}\right]\mathbf{A} = \nabla\left(\frac{1}{c^2}\frac{\partial}{\partial t}\phi\right) - \mu_0\mathbf{j} \tag{2.9}$$

with $c = \sqrt{\epsilon_0\mu_0}^{-1}$ being the speed of light. It is possible to split the electric field $\mathbf{E}$ in a longitudinal part $\mathbf{E}_\parallel$ with $\nabla \times \mathbf{E}_\parallel = 0$ and a transversal part $\mathbf{E}_\perp$ with $\nabla\mathbf{E}_\perp = 0$. Due to the Coulomb gauge condition, the following relations hold true

$$\mathbf{E}_\parallel = -\nabla\phi \,,$$
$$\mathbf{E}_\perp = -\dot{\mathbf{A}} \,.$$

For quantizing the theory, we have to develop a Lagrangian formulation of the theory. In the case of the free radiation field (in the absence of any matter), i.e. $\rho = 0$, $\mathbf{j} = 0$, Eq. (2.8) reduces to

$$\nabla^2\phi = 0 \,. \tag{2.10}$$

In the following, we impose suitable boundary conditions on the scalar field ϕ. These boundary conditions are motivated by physical considerations. They allow us to model mirrors or other macroscopic objects without the need of taking the dynamical degrees of freedom connected to such a macroscopic object into account, which would result in a complex many-body problem. The free-space scenario is modeled by imposing the boundary condition that $\phi(\mathbf{x})$ vanishes as $||\ \mathbf{x}\ || \to \infty$. For describing the dynamics inside a finite volume V confined by, for example, perfectly conducting walls, we assume that $\phi(\mathbf{x})$ has a constant value over the surface ∂V of the volume V. For properly chosen boundary conditions, the solution of Eq. (2.10) is unique. Due to the uniqueness of the solution, we won't consider ϕ as dynamical degree of freedom because it is completely determined by the boundary conditions. Thus, in

the following, we solely deal with the quantization of the vector potential $\mathbf{A}$ and treat the scalar potential ϕ classically. For the rest of this chapter, we focus on the case of time-independent boundary conditions. This implies $\frac{\partial}{\partial t}\mathbf{E}_{\parallel} = 0$. The formulation of the theory for time-dependent boundary conditions is introduced in chapter 9 for discussing the dynamical Casimir effect. In case of the free radiation field, Eq. (2.9) simplifies considerably and takes the form

$$\left[\nabla^2 - \frac{1}{c^2}\frac{\partial^2}{\partial t^2}\right]\mathbf{A} = 0\,. \tag{2.11}$$

In order to develop a Hamiltonian formulation of this theory and to quantize it later on, we have to determine all independent dynamical degrees of freedom. For isolating these dynamical degrees of freedom, we expand the vector field $\mathbf{A}$ in terms of suitable mode functions $\mathbf{g}_i$. For the sake of simplicity, we consider the dynamics of the radiation field only in a finite volume V with suitably chosen boundary conditions. As discussed previously for the scalar field ϕ, the boundary conditions are motivated by physical considerations. For example, an ideally conducting surface is modeled by the constraint that the electric field is perpendicular to the surface (for all points on the surface). In Coulomb gauge, this directly translates to the vector potential $\mathbf{A}$ and hence to the mode functions $\mathbf{g}_i$. By imposing the boundary conditions, we make sure that we only have to deal with a countably infinite number of modes of the radiation field. A suitable set of real valued orthonormal mode functions $\mathbf{g}_i$ fulfills the following conditions

$$\nabla\mathbf{g}_i(\mathbf{x}) = 0 \tag{2.12}$$

$$\left[\nabla^2 + \frac{1}{c^2}\omega_i^2\right]\mathbf{g}_i = 0 \tag{2.13}$$

$$\int_V \mathbf{g}_i(\mathbf{x})\mathbf{g}_j(\mathbf{x})d^3\mathbf{x} = \delta_{i,j} \tag{2.14}$$

for suitable mode frequencies $\omega_i \geq 0$. Thereby, Eq. (2.12) is a consequence of the gauge fixing condition of Eq. (2.7), Eq. (2.13) is the vectorial Helmholtz equation, and Eq. (2.14) is the orthonormalization condition. Furthermore, we assume that our set of mode functions is complete, i.e.,

$$\sum_i \mathbf{g}_i(\mathbf{x}_1)\mathbf{g}_i(\mathbf{x}_2) = \delta^3_{\perp}(\mathbf{x}_1 - \mathbf{x}_2) \text{ for all } \mathbf{x}_1, \mathbf{x}_2 \in V$$

with $\delta^3_{\perp}$ denoting the transverse delta function in three dimensions (see [33] for a definition of $\delta^3_{\perp}$). If our set of mode functions satisfies all the previous conditions, we can expand the vector potential in terms of these mode functions

$$\mathbf{A}(\mathbf{x}) = \frac{1}{\sqrt{\epsilon_0}}\sum_i q_i\mathbf{g}_i(\mathbf{x})$$

by introducing suitable coefficients $q_i > 0$. These coefficients are the dynamical degrees of freedom which can be used to derive the Hamiltonian formulation of the theory. For our choice of mode functions, the time evolution of the vector potential induced by Eq. (2.11) is given by

$$\mathbf{A}(t, \mathbf{x}) = \frac{1}{\sqrt{\epsilon_0}}\sum_i q_i(t)\mathbf{g}_i(\mathbf{x})$$

with

$$q_i(t) = q_i(t_0)\cos\left(\omega_i\left(t - t_0\right)\right) + \frac{\dot{q}_i(t_0)}{\omega_i}\sin\left(\omega_i\left(t - t_0\right)\right)\,.$$

This time evolution can be described by a Lagrange function which corresponds to a system of harmonic oscillators

$$\begin{aligned} L_{\text{rad}} &= \sum_i \frac{1}{2}\dot{q}_i^2 - \frac{1}{2}\omega_i^2 q_i^2 \\ &= \frac{\epsilon_0}{2}\int_V \mathbf{E}_\perp^2(\mathbf{x}) - c^2\mathbf{B}^2(\mathbf{x})d^3\mathbf{x}\,. \end{aligned}$$

This Lagrange function induces the canonical conjugated momenta

$$p_i = \frac{\partial L_{\text{rad}}}{\partial \dot{q}_i} = \dot{q}_i$$

and leads to the following Hamilton function describing the dynamics

$$\begin{aligned} H_{\text{rad}} &= \sum_i \frac{1}{2}p_i^2 + \frac{1}{2}\omega_i^2 q_i^2 \\ &= \frac{\epsilon_0}{2}\int_V \mathbf{E}_\perp{}^2(\mathbf{x}) + c^2\mathbf{B}^2(\mathbf{x})d^3\mathbf{x}\,. \end{aligned}$$

In order to perform the canonical quantization of the theory, we just replace the coefficients q_i and their corresponding canonical conjugated momenta p_i by suitable operators defined on a suitable Hilbert space $\mathcal{H}_{\text{rad}}$:

$$q_i \rightarrow \hat{q}_i\,, \tag{2.15}$$

$$p_i \rightarrow \hat{p}_i\,. \tag{2.16}$$

These operators fulfil the following canonical commutation relations

$$[\hat{q}_i, \hat{q}_j] = 0\,, \tag{2.17}$$

$$[\hat{p}_i, \hat{p}_j] = 0\,, \tag{2.18}$$

$$[\hat{q}_i, \hat{p}_j] = i\hbar\delta_{i,j}\,. \tag{2.19}$$

For later convenience, we introduce the annihilation and creation operators $\hat{a}_i$ and $\hat{a}_i^\dagger$ which are defined as

$$\begin{aligned} \hat{a}_i &= \frac{1}{\sqrt{2\hbar\omega_i}}\left(\omega_i\hat{q}_i + i\hat{p}_i\right), \\ \hat{a}_i^\dagger &= \frac{1}{\sqrt{2\hbar\omega_i}}\left(\omega_i\hat{q}_i - i\hat{p}_i\right)\,. \end{aligned}$$

These operators fulfill the commutation relations

$$[\hat{a}_i, \hat{a}_j^\dagger] = \delta_{i,j}\,. \tag{2.20}$$

We can express all the field operators and the Hamilton operator in terms of these creation and annihilation operators. We obtain the following expressions for the field operators

$$\hat{\mathbf{A}}(\mathbf{x}) = \sum_i \sqrt{\frac{\hbar}{2\omega_i\epsilon_0}}\mathbf{g}_i(\mathbf{x})\left(\hat{a}_i + \hat{a}_i^\dagger\right) \tag{2.21}$$

$$\hat{\mathbf{E}}_\perp(\mathbf{x}) = i\sum_i \sqrt{\frac{\omega_i\hbar}{2\epsilon_0}}\mathbf{g}_i(\mathbf{x})\left(\hat{a}_i - \hat{a}_i^\dagger\right) \tag{2.22}$$

$$\hat{\mathbf{B}}(\mathbf{x}) = \sum_i \sqrt{\frac{\hbar}{2\omega_i\epsilon_0}}\nabla\times\mathbf{g}_i(\mathbf{x})\left(\hat{a}_i + \hat{a}_i^\dagger\right) \tag{2.23}$$

and the following expression for the Hamilton operator

$$\hat{H}_{\text{rad}} = \hbar \sum_i \omega_i \hat{a}_i^\dagger \hat{a}_i + \frac{\hbar}{2} \sum_i \omega_i \, .$$

The second term $\frac{\hbar}{2} \sum_i \omega_i$, which corresponds to the infinite vacuum energy, is a consequence of the commutation relations (2.20). This term is just a multiple of the identity. In order to obtain a meaningful Hamilton operator, we have to renormalize the ground state energy and neglect this vacuum energy contribution. In the following, we describe the dynamics of the radiation field by using the Hamilton operator

$$\hat{H}_{\text{rad}} = \hbar \sum_i \omega_i \hat{a}_i^\dagger \hat{a}_i \, . \tag{2.24}$$

We are now equipped with a description of the quantized dynamics of the free radiation field confined to a finite volume V. In order to obtain a description of the dynamics in free-space, we just have to consider a limit in which $V \to \mathbb{R}^3$.

Up to now, we just dealt with the description of the dynamics of the radiation field and not with the different quantum states of the radiation field connected to the Hilbert space $\mathcal{H}_{\text{rad}}$. A quantum state of particular importance is the vacuum state $|0\rangle_{\text{rad}} \in \mathcal{H}_{\text{rad}}$ which is the ground state of the Hamilton operator $\hat{H}_{\text{rad}}$ and fulfills the property

$$\hat{a}_i \, |0\rangle_{\text{rad}} = 0 \text{ for all } i \, .$$

Based on this state, it is possible to construct all the other important classes of states of the radiation field like photon number states, coherent states, and coherent squeezed states [34].

2.2 MODELING MATTER-FIELD INTERACTIONS

In this section, we extend the quantum theory of the free radiation field developed in the previous section in order to take the interaction between the radiation field and a single quantum emitter into account. We consider an electrically neutral quantum emitter, such as an atom, composed of N charged non-relativistic point like particles with the charges $Q_1 ... Q_N$, the masses $m_1 ... m_N$ and the positions $\mathbf{R}_1 ... \mathbf{R}_N$ interacting, with the radiation field. As in the previous section, we won't quantize the scalar field ϕ because the scalar field is completely determined by the boundary condition and the distribution of the charges. Thus, we solve the classical equation Eq. (2.8) directly for the charge density

$$\rho(\mathbf{x}) = \sum_{\alpha=1}^{N} Q_\alpha \delta(\mathbf{x} - \mathbf{R}_\alpha) \, .$$

We can construct the solution by using an appropriate Green's function G_{∇^2} which satisfies the equation

$$\nabla^2_{\mathbf{x}_1} G_{\nabla^2}(\mathbf{x}_1, \mathbf{x}_2) = \delta(\mathbf{x}_1 - \mathbf{x}_2)$$

and which fulfills suitable boundary conditions. By applying this Green's function, we obtain

$$\phi(\mathbf{x}) = -\frac{1}{\epsilon_0} \sum_{\alpha=1}^{N} Q_\alpha G_{\nabla^2}(\mathbf{x}, \mathbf{R}_\alpha) \, .$$

The dynamics of the transverse vector potential $\mathbf{A}$ and the point like particles can be described by the minimal coupling Hamiltonian

$$H = \sum_\alpha \frac{1}{2m_\alpha} \left[\mathbf{P}_\alpha - Q_\alpha \mathbf{A}(\mathbf{R}_\alpha)\right]^2 + H_{\text{rad}} - \frac{1}{\epsilon_0} \sum_{\alpha>\beta} Q_\alpha Q_\beta G_{\nabla^2}(\mathbf{R}_\alpha, \mathbf{R}_\beta) - \frac{1}{2\epsilon_0} \sum_\alpha Q_\alpha^2 G_{\nabla^2}(\mathbf{R}_\alpha, \mathbf{R}_\alpha)$$

with

$$\mathbf{P}_\alpha = m_\alpha \dot{\mathbf{R}}_\alpha + Q_\alpha \mathbf{A}(\mathbf{R}_\alpha)$$

being the canonical conjugated momentum to $\mathbf{R}_\alpha$ and H_{rad} being the Hamiltonian of the free radiation field introduced in the previous section. For a detailed discussion of the Hamiltonian formulation of the interacting theory see [33].

In the following, we neglect the energy shift caused by the self interaction term $-\frac{1}{2\epsilon_0} \sum_\alpha Q_\alpha^2 G_{\nabla^2}(\mathbf{R}_\alpha, \mathbf{R}_\alpha)$. In order to quantize this theory, we just have to replace the $\mathbf{R}_\alpha$ and the canonical conjugated momenta $\mathbf{P}_\alpha$ by suitable operators

$$\begin{aligned}
\mathbf{R}_\alpha \quad &\rightarrow \quad \hat{\mathbf{R}}_\alpha \\
\mathbf{P}_\alpha \quad &\rightarrow \quad \hat{\mathbf{P}}_\alpha \\
\text{with} \quad \left[\left(\hat{\mathbf{R}}_\alpha\right)_i, \left(\hat{\mathbf{R}}_\beta\right)_j\right] &= 0 \qquad (2.25) \\
\left[\left(\hat{\mathbf{P}}_\alpha\right)_i, \left(\hat{\mathbf{P}}_\beta\right)_j\right] &= 0 \qquad (2.26) \\
\left[\left(\hat{\mathbf{R}}_\alpha\right)_i, \left(\hat{\mathbf{P}}_\beta\right)_j\right] &= i\hbar\delta_{i,j}\delta_{\alpha,\beta} \, . \qquad (2.27)
\end{aligned}$$

In a similar way, we also replace the corresponding degrees of freedom connected to the radiation field q_i and p_i (as done in the previous section) by suitable operators $\hat{q}_i$ and $\hat{p}_i$. We assume that the operators $\hat{\mathbf{R}}_\alpha$ and $\hat{\mathbf{P}}_\alpha$ referring to the position and momentum of the point like particles commute with the operators $\hat{q}_i$ and $\hat{p}_i$ referring to the degrees of freedom of the radiation field. A suitable choice for representing these operators is the Hilbert space

$$\mathcal{H} = \mathcal{H}_{\text{atom}} \otimes \mathcal{H}_{\text{rad}}$$

with $\mathcal{H}_{\text{rad}}$ being a Hilbert space connected to the dynamical degrees of freedom of the radiation field (i.e., all the operators $\hat{p}_i$ and $\hat{q}_i$ can be considered to be defined on this Hilbert space) and $\mathcal{H}_{\text{atom}}$ being Hilbert space linked to the dynamical degrees of freedom of the atom (i.e., all the operators $\hat{\mathbf{R}}_\alpha$ and $\hat{\mathbf{P}}_\alpha$ can be considered to be defined on this Hilbert space). We obtain the Hamilton operator

$$\hat{H} = \sum_\alpha \frac{1}{2m_\alpha} \left[\hat{\mathbf{P}}_\alpha - Q_\alpha \hat{\mathbf{A}}(\hat{\mathbf{R}}_\alpha)\right]^2 - \frac{1}{\epsilon_0} \sum_{\alpha>\beta} Q_\alpha Q_\beta G_{\nabla^2}(\hat{\mathbf{R}}_\alpha, \hat{\mathbf{R}}_\beta) + \hat{H}_{\text{rad}} \, .$$

For typical atomic systems, the extension of the atom ($\approx 10^{-10}$m) is much smaller than a typical optical wavelength (which is of the order of several hundred nanometers). This fact allows us to apply the dipole approximation. Thereby, we assume that all the charges are centered around $\mathbf{R}$ and replace

$$\sum_\alpha \frac{1}{2m_\alpha} \left[\hat{\mathbf{P}}_\alpha - Q_\alpha \hat{\mathbf{A}}(\hat{\mathbf{R}}_\alpha)\right]^2 \rightarrow \sum_\alpha \frac{1}{2m_\alpha} \left[\hat{\mathbf{P}}_\alpha - Q_\alpha \hat{\mathbf{A}}(\mathbf{R})\right]^2 \, .$$

In the previous step, we replaced the evaluation of the field operators $\hat{\mathbf{A}}(\hat{\mathbf{R}}_\alpha)$ at the position of the charges by the evaluation of the field operator at the center of the atom $\mathbf{R}$. The dipole approximation is often accompanied by the Göppert-Mayer transformation which can be described by the unitary operator

$$\hat{U} = e^{\frac{i}{\hbar} \hat{\mathbf{d}} \cdot \hat{\mathbf{A}}(\mathbf{R})}$$

with

$$\hat{\mathbf{d}} := \sum_{\alpha} Q_{\alpha} \hat{R}_{\alpha}$$

being the dipole operator of the charge distribution. By applying this transformation, we obtain

$$\hat{H} = \hat{H}_{\text{atom}} + \hat{H}_{\text{rad}} + \hat{H}_{\text{int}} \tag{2.28}$$

with

$$\begin{aligned} \hat{H}_{\text{atom}} &= \sum_{\alpha} \frac{1}{2m_{\alpha}} \hat{\mathbf{P}}_{\alpha}^2 - \frac{1}{\epsilon_0} \sum_{\alpha>\beta} Q_{\alpha} Q_{\beta} G_{\nabla^2}(\hat{\mathbf{R}}_{\alpha}, \hat{\mathbf{R}}_{\beta}) \,, \\ \hat{H}_{\text{int}} &= -\hat{\mathbf{d}} \cdot \hat{\mathbf{E}}_{\perp}(\mathbf{R}) \,. \end{aligned}$$

Thereby, we have neglected the term

$$\sum_{i} \frac{1}{2\epsilon_0 \omega_i} \left(\vec{g}_i(\mathbf{R}) \cdot \hat{\mathbf{d}} \right)^2$$

which just leads to a shift of the atomic energy levels. After applying the approximations introduced above, the interaction between the quantum emitter and the radiation field is solely characterized by the dipole moment of the charge distribution and the electric field at the position of the quantum emitter. One of the advantages of the Göppert-Mayer transformation is that, after applying the transformation, the canonical conjugated momenta $\hat{\mathbf{P}}_{\alpha}$ coincide with the kinetic momenta. The Hamilton operator given in Eq. (2.28) serves as the basic model of the quantum optical systems which we consider in the first part of this thesis.

2.3 SUMMARY

In this chapter, we have given an introduction to the theory of cavity QED. We have started with the derivation of the quantum theory of the free electromagnetic radiation field in Sec. 2.1. The modeling of the interactions of the quantized electromagnetic radiation field with microscopic single quantum emitters, such as atoms or ions, has been discussed in Sec. 2.2. Thereby, we have introduced the dipole approximation, which leads to an excellent description of many processes in the optical regime. In our discussion of cavity QED, we have not addressed the propagation of the electromagnetic radiation field inside a dielectric medium and have modeled mirrors or optical resonators by introducing suitable boundary conditions. However, it is possible to generalize the theory introduced above to describe the propagation of photons in linear dielectric media [35]. This can be done by choosing the mode functions to be solutions of a generalized Helmholtz equation, which takes the dielectric constants of the linear medium into account. In this way, it is possible to investigate the propagation of the radiation field and matter-field coupling in the presence of one-dimensional waveguides, such as nanowires, nanofibers, or hollow fibers and many other photonic structures of interest. The theory of cavity QED introduced in this chapter provides us with the theoretical foundation for all further investigations in the first part of this thesis.

3

PHOTON PATH REPRESENTATION FOR SINGLE-PHOTON STATES

The formulation of the theory of cavity QED introduced in the previous section allows us to study the interaction of single quantum emitters with the electromagnetic radiation field on the single-photon level. However, the theoretical discussion of the dynamics of such systems is often complicated by the multitude of dynamical degrees of freedom involved in the description of the multimode electromagnetic radiation field. In this chapter, we introduce a method which allows us to deal with this vast number of dynamical degrees of freedom and to investigate the dynamics of the quantized multimode radiation field interacting with several quantum emitters. We restrict ourselves to scenarios in which only a single initial excitation (either a photonic excitation or an excitation of one of the quantum emitters) is present in the system. In chapter 8, we generalize this method to be able to deal with multiple excitations present in the system. We focus on situations such as free-space, large cavities, or half-open cavities. However, the method discussed here can be adapted to other scenarios of interest in which no mode selection by a high finesse optical resonator takes place, such as surface plasmons coupling to a quantum dot [16] or photons propagating along a nanofiber coupling to atoms trapped in the evanescent field surrounding the fiber [20]. By using this method, we can interpret the dynamics of the system in descriptive way as sequences of spontaneous absorption and emission processes. These emission and absorption processes are connected to the propagation of single photons from one quantum emitter to another. Due to this descriptive interpretation, we refer to our method as single-photon-path-representation.

In Sec. 3.1, we start with the introduction of a suitable model for the quantum emitters interacting with the radiation field. This model is based on the considerations discussed in the previous chapter. In Sec. 3.2, we discuss the spontaneous decay process of a single excited atom in free-space. The description of this process serves as an essential building block of the photon-path-representation, which we develop in Sec. 3.3. Finally, in Sec. 3.4, we connect the photon-path-representation to the framework of geometrical optics by using semiclassical approximations for taking the presence of mirrors or an optical resonator into account.

3.1 SCENARIO AND MODEL

In the scenario which we have in mind, we consider several, well separated quantum emitters located at fixed positions in a large, half-open cavity or even in free-space. An example of such a scenario is depicted in Fig. 3.1. For modeling the system, we use the framework of cavity quantum electrodynamics developed in the previous chapter. We model the interaction between the radiation field and the atoms by using the dipole

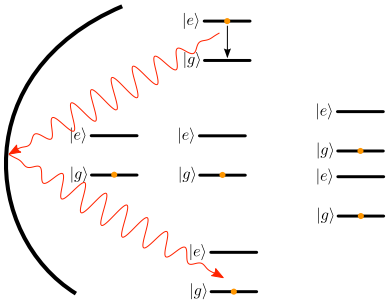

Figure 3.1.: Basic scenario: several two-level atoms placed in a large, half-open cavity or even in free-space. Initially, there is only a single excitation in the system, either a photonic or an atomic one.

approximation introduced previously. Furthermore, we focus on n identical two-level atoms, i.e., we restrict the dynamics of the atoms to two electronic states of the quantum emitters. It is a straightforward task to generalize the following considerations to much more general level schemes and we go beyond this two-level approximations in chapter 4 and 5.

In order to apply the framework of cavity quantum electrodynamics developed in the previous section, we have to go a little bit beyond the considerations of chapter 2 to describe n well-separated quantum emitters in the following referred to as atoms. For modeling the dynamics of this system, we introduce suitable Hilbert spaces $\mathcal{H}^1_{\text{atom}}$... $\mathcal{H}^n_{\text{atom}}$ for each of these atoms 1 ...n and suitable Hamilton operators $\hat{H}^1_{\text{atom}}$...$\hat{H}^n_{\text{atom}}$ (see chapter 2) defined on these Hilbert spaces modeling the free dynamics of each of the atoms. We also introduce a suitable Hilbert space $\mathcal{H}_{\text{rad}}$ (see chapter 2) to represent the radiation field with the Hamilton operator $\hat{H}_{\text{rad}}$ defined on this Hilbert space. The Hilbert space of the whole system is given by

$$\mathcal{H} = \mathcal{H}^1_{\text{atom}} \otimes ... \otimes \mathcal{H}^n_{\text{atom}} \otimes \mathcal{H}_{\text{rad}} \, .$$

We model the interaction between the atoms and the radiation field by the dipole approximation introduced in the previous chapter. For this purpose, we introduce appropriate operators H^i_{int} modeling the interaction between atom i and the radiation field. These operators are given by

$$\hat{H}^i_{\text{int}} = -\hat{\mathbf{d}}_i \cdot \hat{\mathbf{E}}_\perp(\mathbf{R}_i)$$

with $\mathbf{R}_i$ denoting the position of atom i and $\hat{\mathbf{d}}^i$ denoting the dipole operator of atom i defined in the previous chapter and defined on the Hilbert space $\mathcal{H}^{\text{atom}}_i$. The Hamilton operator describing the complete system is now given by

$$\hat{H} = \hat{H}_{\text{rad}} + \sum_i \hat{H}^i_{\text{atom}} + \sum_i \hat{H}^i_{\text{int}} \, .$$

The cavities or mirrors are modeled by imposing boundary conditions on the mode functions $\mathbf{g}_i$ as discussed in Sec. 2.1. Thereby, we have neglected terms which are induced by the scalar potential ϕ and correspond to a dipole-dipole interaction of the neighboring atoms (we assume that the distances between the atoms and the distances between the atoms and the mirrors are sufficiently large).

The two-level approximation mentioned previously corresponds to a restriction of the Hilbert spaces $\mathcal{H}_1^{\text{atom}}$... $\mathcal{H}_n^{\text{atom}}$ to two eigenstates of the Hamilton operators $\hat{H}_{\text{atom}}^1$...$\hat{H}_{\text{atom}}^n$. We denote these eigenstates by $|e\rangle_i \in \mathcal{H}_i^{\text{atom}}$ and $|g\rangle_i \in \mathcal{H}_i^{\text{atom}}$ for the excited state respectively the ground state of atom i. Furthermore, we renormalize the ground state energies of the Hamilton operators $\hat{H}_{\text{atom}}^1$...$\hat{H}_{\text{atom}}^n$. We can represent these operators by

$$\hat{H}_{\text{atom}}^i = \hbar\omega_{eg} |e\rangle_i \langle e|_i$$

with ω_{eg} denoting the transition frequency between the ground state $|g\rangle_i$ and the excited state $|e\rangle_i$. In the two-level approximation, the operators $\hat{H}_{\text{int}}^i$ are given by

$$\hat{H}_{\text{int}}^i = -\left(\mathbf{d}_i |e\rangle_i \langle g|_i + \text{H.c.}\right) \cdot \hat{\mathbf{E}}_\perp(\mathbf{R}_i)$$

with

$$\mathbf{d}_i = \langle e|_i \hat{\mathbf{d}}_i |g\rangle_i$$

being the dipole matrix element which characterizes the transitions $|e\rangle_i \to |g\rangle_i$ of atom i. Thereby, we have assumed that

$$\langle e|_i \hat{\mathbf{d}}_i |e\rangle_i = \langle g|_i \hat{\mathbf{d}}_i |g\rangle_i = 0$$

which can always be achieved by choosing electronic eigenstates with well defined parity.

In the following, we apply the so-called rotating-wave approximation (RWA) which is typically well justified in the optical regime. This approximation is based on a separation of time scales. For typical atomic systems and optical transitions the transition frequencies ω_{eg} which are of the order of 10^{15}s^{-1} are much larger than all other relevant frequencies or decay rates of the system. Typical spontaneous decay rates, for example, are of the order of 10^9s^{-1} for dipole allowed transitions and thus six orders of magnitude smaller than the typical transition frequencies. In order to apply the RWA, we split the electric field operator in a negative and positive frequency part

$$\hat{\mathbf{E}}_\perp(\mathbf{x}) = \hat{\mathbf{E}}_\perp^-(\mathbf{x}) + \hat{\mathbf{E}}_\perp^+(\mathbf{x})$$

whereby

$$\hat{\mathbf{E}}_\perp^+(\mathbf{x}) = \left[\hat{\mathbf{E}}_\perp^-(\mathbf{x})\right]^\dagger = i\sum_i \sqrt{\frac{\omega_i\hbar}{2\epsilon_0}} \mathbf{g}_i(\mathbf{x})\hat{a}_i \,.$$

By doing so, we can rewrite the operator and obtain

$$\begin{aligned} \hat{H}_{\text{int}}^i &= -|e\rangle_i \langle g|_i \mathbf{d}_i \cdot \hat{\mathbf{E}}_\perp^+(\mathbf{R}_i) - |g\rangle_i \langle e|_i \mathbf{d}_i^* \cdot \hat{\mathbf{E}}_\perp^-(\mathbf{R}_i) \\ &- |e\rangle_i \langle g|_i \mathbf{d}_i \cdot \hat{\mathbf{E}}_\perp^-(\mathbf{R}_i) - |g\rangle_i \langle e|_i \mathbf{d}_i^* \cdot \hat{\mathbf{E}}_\perp^+(\mathbf{R}_i) \,. \end{aligned}$$

The RWA can be justified by going to the interaction picture with respect to

$$H_0 = \hat{H}_{\text{rad}} + \sum_i \hat{H}_{\text{atom}}^i \,.$$

In the interaction picture

$$|e\rangle_i \langle g|_i \to |e\rangle_i \langle g|_i \, e^{i\omega_{eg}(t-t_0)}$$

and

$$\hat{\mathbf{E}}_\perp^+(\mathbf{x}) \to i\sum_i \sqrt{\frac{\omega_i\hbar}{2\epsilon_0}} \mathbf{g}_i(\mathbf{x})\hat{a}_i e^{-i\omega_i(t-t_0)} \,.$$

Thus, in the interaction picture the expressions

$$|e\rangle_i \langle g|_i \, \mathbf{d}_i \cdot \hat{\mathbf{E}}_\perp^-(\mathbf{R}_i)$$

and

$$|g\rangle_i \langle e|_i \, \mathbf{d}_i^* \cdot \hat{\mathbf{E}}_\perp^+(\mathbf{R}_i)$$

are oscillating rapidly with frequencies $\pm\left(\omega_{eg}+\omega_i\right)$ and correspond to highly off resonant transitions. By applying the RWA, we neglect these expressions and just keep the terms which are slowly oscillating. By going back to the Schrödinger picture we obtain

$$\hat{H}_{\text{int}}^i = -|e\rangle_i \langle g|_i \, \mathbf{d}_i \cdot \hat{\mathbf{E}}_\perp^+(\mathbf{R}_i) - |g\rangle_i \langle e|_i \, \mathbf{d}_i^* \cdot \hat{\mathbf{E}}_\perp^-(\mathbf{R}_i) \, .$$

3.2 DESCRIPTION OF THE SPONTANEOUS DECAY PROCESS IN FREE-SPACE

One of the basic processes which takes place if a single atom interacts with a multimode radiation field is the spontaneous decay process, i.e., the depopulation of the excited state and the subsequent emission of a single photon. One of its characteristic features is an exponential decay law describing the depopulation of the excited state.

For studying this process, we consider a single two-level atom interacting with the radiation field in free-space. The basic idea of the photon-path-representation is to start from the spontaneous decay process and to treat all deviations caused by the presence of a cavity, a mirror or additional atoms as perturbations described in a proper perturbative expansion. To do so, it is of fundamental importance to understand this spontaneous decay process. In this section, we briefly recapitulate the description of the spontaneous decay process by Weisskopf and Wigner [36] (even more general considerations can be found in [37]) to use it as the core building block for developing the photon-path-representation. We consider a single two-level atom located at a fixed position $\mathbf{R}$ in free-space.

We consider the radiation field to be initially in the vacuum state and the atom to be in the excited state. This corresponds to an initial state of the form

$$|\psi(t_0)\rangle = |e\rangle \otimes |0\rangle_{\text{rad}} \, . \tag{3.1}$$

Due to the RWA, the number of excitations, i.e., the number of atomic excitations plus the number of photons, is a conserved quantity. Thus, we can use the following ansatz for the time evolution of the wave function

$$|\psi(t)\rangle = |\psi_{\text{atomic}}(t)\rangle + |\psi_{\text{photonic}}(t)\rangle$$

with

$$|\psi_{\text{atomic}}(t)\rangle = b(t) \, |e\rangle \otimes |0\rangle_{\text{rad}}$$

representing the part of the Hilbert space corresponding to a single atomic excitation and

$$|\psi_{\text{photonic}}(t)\rangle = |g\rangle \otimes \sum_i f_i(t) a_i^\dagger \, |0\rangle_{\text{rad}}$$

representing the part of the Hilbert space corresponding to a single photonic excitation.

The Schrödinger equation induces the following system of coupled differential equations

$$\begin{aligned} \frac{d}{dt} b(t) &= -i\omega_{eg} b(t) + \frac{i}{\hbar} \langle g| \otimes \langle 0|_{\text{rad}} \, \mathbf{d} \cdot \hat{\mathbf{E}}_\perp^+(\mathbf{R}) \, |\psi_{\text{photonic}}(t)\rangle \, , \qquad (3.2) \\ \frac{d}{dt} |\psi_{\text{photonic}}(t)\rangle &= -\frac{i}{\hbar} \hat{H}_{\text{rad}} \, |\psi_{\text{photonic}}(t)\rangle + \frac{i}{\hbar} |g\rangle \otimes \left[\mathbf{d}^* \cdot \hat{\mathbf{E}}_\perp^-(\mathbf{R}) \, |0\rangle_{\text{rad}}\right] b(t) \, . \end{aligned}$$

We can rewrite the last equation as integral equation

$$|\psi_{\text{photonic}}(t)\rangle \quad = \quad \frac{i}{\hbar}\,|g\rangle \otimes \int_{t_0}^{t} b(t_1) e^{-\frac{i}{\hbar}\hat{H}_{\text{rad}}(t-t_1)} \mathbf{d}^* \cdot \hat{\mathbf{E}}_{\perp}^{-}(\mathbf{R})\,|0\rangle_{\text{rad}}\, dt_1\,. \tag{3.3}$$

By using the previous expression and combining it with Eq. (3.2), we obtain

$$\frac{d}{dt}b(t) = -i\omega_{eg}b(t) - \frac{1}{\hbar^2}\int_{t_0}^{t} b(t_1)\,\langle 0|_{\text{rad}} \left(\mathbf{d}\cdot\hat{\mathbf{E}}_{\perp}^{+}(\mathbf{R},t)\right)\left(\mathbf{d}^*\cdot\hat{\mathbf{E}}_{\perp}^{-}(\mathbf{R},t_1)\right)|0\rangle_{\text{rad}}\, dt_1 \tag{3.4}$$

with

$$\hat{\mathbf{E}}_{\perp}^{\pm}(\mathbf{x},t) = e^{\frac{i}{\hbar}\hat{H}_{\text{rad}}(t-t_0)}\hat{\mathbf{E}}_{\perp}^{\pm}(\mathbf{x},t_0)e^{-\frac{i}{\hbar}\hat{H}_{\text{rad}}(t-t_0)}$$

being the field operator $\hat{\mathbf{E}}_{\perp}^{\pm}(\mathbf{x},t)$ in the interaction picture. In order to solve Eq. (3.4), we have to evaluate the expression

$$\begin{array}{rc} & \frac{1}{\hbar^2}\,\langle 0|_{\text{rad}} \left(\mathbf{d}\cdot\hat{\mathbf{E}}_{\perp}^{+}(\mathbf{R},t_2)\right)\left(\mathbf{d}^*\cdot\hat{\mathbf{E}}_{\perp}^{-}(\mathbf{R},t_1)\right)|0\rangle_{\text{rad}} \\ = & \sum_i \frac{\omega_i}{2\epsilon_0\hbar}\,\mid \mathbf{d}\cdot\mathbf{g}_i(\mathbf{R})\mid^2 e^{-i\omega_i(t_2-t_1)}\,. \end{array}$$

By using arguments similar to the ones used to justify the RWA, we can replace

$$\frac{1}{\hbar^2}\,\langle 0|_{\text{rad}} \left(\mathbf{d}\cdot\hat{\mathbf{E}}_{\perp}^{+}(\mathbf{R},t_2)\right)\left(\hat{\mathbf{E}}_{\perp}^{-}(\mathbf{R},t_1)\cdot\mathbf{d}^*\right)|0\rangle_{\text{rad}} \tag{3.5}$$

in Eq. (3.4) by [1]

$$\frac{1}{\hbar^2}\left[\mathbf{d}\cdot\hat{\mathbf{E}}_{\perp}(\mathbf{R},t_2), \hat{\mathbf{E}}_{\perp}(\mathbf{R},t_1)\cdot\mathbf{d}^*\right]\,. \tag{3.6}$$

The previous approximation is valid because by going from Eq. (3.5) to Eq. (3.6) we introduced additional terms with the time dependence $e^{i\omega_i(t_2-t_1)}$. These terms are highly off resonant with respect to the dynamics of the excited state of the two-level atom with the time dependence $e^{-i\omega_{eg}(t_2-t_1)}$. Thus, we can neglect the contribution of these terms due to their large detuning $(\omega_{eg}+\omega_i)$.

For evaluating Eq. (3.6), we have to choose suitable mode functions. Therefore, we start with a description of the radiation field in a finite volume V discussed in Sec. 2.1 and consider a suitable limit $V \to \mathbb{R}^3$. A common and quite convenient choice is to consider the radiation field inside a cube with periodic boundary conditions [2] and with edge length l centered around the origin

$$V = [-l/2, l/2]^3\,.$$

In order to approach the free-space dynamics, we consider the limit $l \to \infty$. A convenient choice for the mode functions $\mathbf{g}_i$ [3] is given by

$$\mathbf{g}_i^{x,y,z}(\mathbf{x}) = \frac{1}{\sqrt{l}^3} e^{i\mathbf{x}\cdot\mathbf{k}_i}\boldsymbol{\epsilon}_i$$

for

$$\mathbf{k}_i \in \frac{2\pi}{l}\mathbb{Z}^3 \;\; \mid\mid \boldsymbol{\epsilon}_i \mid\mid = 1 \text{ and } \boldsymbol{\epsilon}_i \perp \mathbf{k}_i\,.$$

1 The commutator is actually a multiple of the identity operator, but is treated in the following as a scalar.

2 Periodic boundary conditions for the mode functions: $\mathbf{g}_i(-l/2,y,z) = \mathbf{g}_i(l/2,y,z)$ and similar constrains for the y and z axis.

3 The mode functions used in Sec. 2.1 were chosen to be real valued. Similar considerations also hold true for complex valued mode functions.

The corresponding mode frequencies are given by $\omega_i = ||\mathbf{k}_i||c$. In the limit $l \to \infty$, we can replace the sum over $\mathbf{k}_i \in \frac{2\pi}{l}\mathbb{Z}^3$ by an integral over $\mathbb{R}^3$. We obtain

$$\begin{aligned} & \tfrac{1}{\hbar^2}\left[\mathbf{d}\cdot\hat{\mathbf{E}}_\perp(\mathbf{R},t_2),\hat{\mathbf{E}}_\perp(\mathbf{R},t_1)\cdot\mathbf{d}^*\right] \\ = \; & -i\tfrac{\Gamma}{\omega_{eg}^3}\delta^{(3)}(t_2-t_1) \to \Gamma\delta(t_2-t_1) \end{aligned} \tag{3.7}$$

with $\delta^{(3)}$ being the third derivative of the δ-distribution and

$$\Gamma = \frac{\omega_{eg}^3 \,||\, \mathbf{d} \,||^2}{3\pi\epsilon_0\hbar c^3}$$

being the spontaneous decay rate of the two-level atom in free-space. In the second line of Eq. (3.7), we replaced $\delta^{(3)}(t_2 - t_1)$ by $i\omega_{eg}^3\delta(t_2 - t_1)$ which is justified because the short time behavior of $b(t)$ is dominated by rapid oscillations with the frequency ω_{eg}. By using Eq. (3.7), we can simplify Eq. (3.4) considerably and obtain

$$\frac{d}{dt}b(t) = \left[-i\omega_{eg} - \frac{\Gamma}{2}\right] b(t) \; .$$

The solution of Eq. (3.1) for the initial state chosen in Eq. (3.1) is given by

$$b(t) = e^{\left(-i\omega_{eg}-\Gamma/2\right)(t-t_0)} \; . \tag{3.8}$$

Eq. (3.8) describes the spontaneous decay of the initial atomic excitation due to the coupling of the atom to the radiation field. The corresponding emission of the photon is described by Eq. (3.3).

3.3 DERIVATION OF THE PHOTON-PATH-REPRESENTATION

In this section, we derive the photon-path-representation. As mentioned previously, we start with the description of the spontaneous decay process discussed in the previous section and we treat all deviations caused by the presence of a cavity, a mirror, or additional atoms as perturbations in an appropriately defined perturbation series. The basic idea is that all these deviations are connected with time delays due to the finite speed of light because a photon needs time to propagate to one of the boundaries of the cavity or to another atom. These time delays cause the perturbation series to terminate after taking finitely many terms into account if the time interval under consideration is finite.

We start with an initial state $|\psi(t_0)\rangle$ which corresponds to the number of excitations being equal to one. As in the previous section, we can make the following ansatz for the time evolution of the wave function

$$|\psi(t)\rangle = |\psi_{\text{atomic}}(t)\rangle + |\psi_{\text{photonic}}(t)\rangle$$

with

$$|\psi_{\text{atomic}}(t)\rangle \;=\; \left(\sum_{\alpha=1}^{n} b_\alpha(t)\,|e\rangle_\alpha\,\langle g|_\alpha\right)|g\rangle_1\otimes|g\rangle_2\otimes\ldots\otimes|g\rangle_n\otimes|0\rangle_{\text{rad}} \tag{3.9}$$

representing the part of the Hilbert space corresponding to a single atomic excitation and

$$|\psi_{\text{photonic}}(t)\rangle \;=\; \sum_i f_i(t)a_i^\dagger\,|0\rangle_{\text{rad}}\otimes|g\rangle_1\otimes|g\rangle_2\otimes\ldots\otimes|g\rangle_n$$

representing the part of the Hilbert space corresponding to a single photonic excitation. This simple ansatz for the wave function $|\psi(t)\rangle$ is only valid in case of a single initial excitation. We discuss a generalization of the photon-path-representation for several initial excitations in chapter 8.

The Hamilton operator $\hat{H}$ introduced in Sec. 3.1 induces the following system of coupled differential equations

$$\frac{d}{dt}|\psi_{\text{atomic}}(t)\rangle = -i\omega_{eg}|\psi_{\text{atomic}}(t)\rangle + \frac{i}{\hbar}\sum_{\alpha=1}^{n}|e\rangle_\alpha \langle g|_\alpha \mathbf{d}_\alpha \cdot \hat{\mathbf{E}}_\perp^+(\mathbf{R}_\alpha)|\psi_{\text{photonic}}(t)\rangle , \tag{3.10}$$

$$\frac{d}{dt}|\psi_{\text{photonic}}(t)\rangle = -\frac{i}{\hbar}\hat{H}_{\text{rad}}|\psi_{\text{photonic}}(t)\rangle + \frac{i}{\hbar}\sum_{\alpha=1}^{n}|g\rangle_\alpha \langle e|_\alpha \mathbf{d}^*{}_\alpha \cdot \hat{\mathbf{E}}_\perp^-(\mathbf{R}_\alpha)|\psi_{\text{atomic}}(t)\rangle . \tag{3.11}$$

The solution of Eq. (3.11) is given by the following integral expression

$$\begin{aligned}|\psi_{\text{photonic}}(t)\rangle = {} & e^{-\frac{i}{\hbar}\hat{H}_{\text{rad}}(t-t_0)}|\psi_{\text{photonic}}(t_0)\rangle \\ & +\frac{i}{\hbar}\sum_{\alpha=1}^{n}\int_{t_0}^{t} e^{-\frac{i}{\hbar}\hat{H}_{\text{rad}}(t-t_1)}\mathbf{d}_\alpha^*\cdot\hat{\mathbf{E}}_\perp^-(\mathbf{R}_\alpha)|g\rangle_\alpha\langle e|_\alpha|\psi_{\text{atomic}}(t_1)\rangle\, dt_1 .\end{aligned} \tag{3.12}$$

By inserting this solution into Eq. (3.10), we obtain

$$\begin{aligned}\frac{d}{dt}|\psi_{\text{atomic}}(t)\rangle = {} & -i\omega_{eg}|\psi_{\text{atomic}}(t)\rangle + \frac{i}{\hbar}\sum_{\alpha=1}^{n}|e\rangle_\alpha\langle g|_\alpha \mathbf{d}_\alpha\cdot\hat{\mathbf{E}}_\perp^+(\mathbf{R}_\alpha,t)|\psi_{\text{photonic}}(t_0)\rangle \\ & -\frac{1}{\hbar^2}\int_{t_0}^{t}\sum_{\alpha,\alpha'=1}^{n}|e\rangle_\alpha\langle g|_\alpha\langle 0|_{\text{rad}}\left(\mathbf{d}_\alpha\hat{\mathbf{E}}_\perp^+(\mathbf{R}_\alpha,t)\right)\left(\hat{\mathbf{E}}_\perp^-(\mathbf{R}_{\alpha'},t_1)\mathbf{d}_{\alpha'}^*\right)|0\rangle_{\text{rad}}|g\rangle_{\alpha'} \\ & \langle e|_{\alpha'}|\psi_{\text{atomic}}(t_1)\rangle\, dt_1 .\end{aligned} \tag{3.13}$$

The basic idea is to rewrite the previous expression by using well known quantities from classical electrodynamics. We replace

$$\frac{1}{\hbar^2}\langle 0|_{\text{rad}}\left(\mathbf{d}_{\alpha_2}\hat{\mathbf{E}}_\perp^+(\mathbf{R}_{\alpha_2},t_2)\right)\left(\hat{\mathbf{E}}_\perp^-(\mathbf{R}_{\alpha_1},t_1)\mathbf{d}_{\alpha_1}^*\right)|0\rangle_{\text{rad}}$$

by

$$\frac{1}{\hbar^2}\left[\mathbf{d}_{\alpha_2}\hat{\mathbf{E}}_\perp(\mathbf{R}_{\alpha_2},t_2),\hat{\mathbf{E}}_\perp(\mathbf{R}_{\alpha_1},t_1)\mathbf{d}_{\alpha_1}^*\right] .$$

This expression, however, can be expressed in terms of the retarded dyadic Green's function of the d'Alembert operator ($\Box = \frac{1}{c^2}\frac{\partial^2}{\partial t^2} - \Delta$) $\mathbf{G}_\Box(\mathbf{x},\mathbf{x}',t)$ which is defined by the following equations

$$\begin{aligned}\Box_{\mathbf{x}}\mathbf{G}_\Box(\mathbf{x},\mathbf{x}',t) &= \delta_\perp^3(\mathbf{x}-\mathbf{x}')\delta(t) , \\ \mathbf{G}_\Box(\mathbf{x},\mathbf{x}',t) &= 0\ \forall t<0 .\end{aligned} \tag{3.14}$$

The presence of a cavity is modeled by imposing suitable boundary conditions on the Green's function. It is also possible to model the presence of a linear medium by considering the Green's function connected to a different wave equation, which

describes the propagation of the radiation field in the medium. After some math, we obtain

$$\begin{aligned}&\tfrac{1}{\hbar^2}\left[\mathbf{d}_{\alpha_2}\hat{\mathbf{E}}_\perp(\mathbf{R}_{\alpha_2},t_2),\hat{\mathbf{E}}_\perp(\mathbf{R}_{\alpha_1},t_1)\mathbf{d}^*_{\alpha_1}\right]\\ &=-\tfrac{i}{\epsilon_0\hbar}\mathbf{d}_{\alpha_2}\cdot\left[\nabla\times\nabla\times\mathbf{G}_\square(\mathbf{R}_{\alpha_2},\mathbf{R}_{\alpha_1},t_2-t_1)-\nabla\times\nabla\times\mathbf{G}_\square(\mathbf{R}_{\alpha_2},\mathbf{R}_{\alpha_1},t_1-t_2)\right]\cdot\mathbf{d}^*_{\alpha_1}.\end{aligned} \tag{3.15}$$

A detailed derivation of the previous relation can be found in Appendix A.

The basic idea for deriving the photon-path-representation is to split the Green's function $\mathbf{G}_\square(\mathbf{x},\mathbf{x}',t)$ in two parts

$$\mathbf{G}_\square(\mathbf{x},\mathbf{x}',t)=\mathbf{G}^{\text{free}}_\square(\mathbf{x},\mathbf{x}',t)+\mathbf{G}^{\text{boundary}}_\square(\mathbf{x},\mathbf{x}',t)$$

with

$$\mathbf{G}^{\text{free}}_\square(\mathbf{x},\mathbf{x}',t)=\frac{1}{4\pi\,||\,\mathbf{x}-\mathbf{x}'\,||}\delta\left(t-||\,\mathbf{x}-\mathbf{x}'\,||\,/c\right)$$

being the Green's function in free-space and $\mathbf{G}^{\text{boundary}}_\square(\mathbf{x},\mathbf{x}',t)$ being a homogeneous solution of the equation

$$\square_{\mathbf{x}}\mathbf{G}^{\text{boundary}}_\square(\mathbf{x},\mathbf{x}',t)=0$$

chosen such that the boundary conditions are satisfied. The free-space part $\mathbf{G}^{\text{free}}_\square(\mathbf{x},\mathbf{x}',t)$ leads to the spontaneous decay process described in the previous section and the function $\mathbf{G}^{\text{boundary}}_\square(\mathbf{x},\mathbf{x}',t)$ models the reflection of the photons due to the presence of the mirrors. By using the previous relations, Eq. (3.13) can be written as follows

$$\begin{aligned}\frac{d}{dt}\left|\psi_{\text{atomic}}(t)\right\rangle &= \left[-i\omega_{eg}-\frac{\Gamma}{2}\right]\left|\psi_{\text{atomic}}(t)\right\rangle+\frac{i}{\hbar}\sum_{\alpha=1}^{n}\left|e\right\rangle_\alpha\left\langle g\right|_\alpha\mathbf{d}_\alpha\cdot\hat{\mathbf{E}}^+_\perp(\mathbf{R}_\alpha,t)\left|\psi_{\text{photonic}}(t_0)\right\rangle\\ &\quad+\int_{t_0}^{t}\hat{T}(t-t_1)\left|\psi_{\text{atomic}}(t_1)\right\rangle dt_1\end{aligned} \tag{3.16}$$

with

$$\hat{T}(t)=\frac{i}{\epsilon_0\hbar}\sum_{\alpha,\alpha'=1}^{n}\mathbf{d}_\alpha\left[\begin{cases}\nabla\times\nabla\times\mathbf{G}_\square(\mathbf{R}_\alpha,\mathbf{R}_{\alpha'},t) & \text{for } \alpha\neq\alpha'\\ \nabla\times\nabla\times\mathbf{G}^{\text{boundary}}_\square(\mathbf{R}_\alpha,\mathbf{R}_{\alpha'},t) & \text{for } \alpha=\alpha'\end{cases}\right]\mathbf{d}^*_{\alpha'}\left|e\right\rangle_\alpha\left\langle e\right|_{\alpha'}\ .$$

Thereby, we took the spontaneous decay process induced by $\mathbf{G}^{\text{free}}_\square(\mathbf{x},\mathbf{x}',t)$ directly into account. Finally, Eq. (3.16) takes the form

$$\begin{aligned}\left|\psi_{\text{atomic}}(t)\right\rangle &= e^{(-i\omega_{eg}-\Gamma/2)(t-t_0)}\left|\psi_{\text{atomic}}(t_0)\right\rangle\\ &\quad+\frac{i}{\hbar}\int_{t_0}^{t}e^{(-i\omega_{eg}-\Gamma/2)(t-t_1)}\sum_{\alpha=1}^{n}\left|e\right\rangle_\alpha\left\langle g\right|_\alpha\mathbf{d}_\alpha\cdot\hat{\mathbf{E}}^+_\perp(\mathbf{R}_\alpha,t_1)\left|\psi_{\text{photonic}}(t_0)\right\rangle dt_1\\ &\quad+\int_{t_0}^{t}\int_{t_0}^{t_1}e^{(-i\omega_{eg}-\Gamma/2)(t-t_2)}\hat{T}(t_2-t_1)\left|\psi_{\text{atomic}}(t_1)\right\rangle dt_1dt_2\ .\end{aligned} \tag{3.17}$$

The advantage of this equation is that the wave function $\left|\psi_{\text{atomic}}(t)\right\rangle$ lies in the part of the Hilbert space which corresponds to a single atomic excitation and the photonic field being in the vacuum state. This space is finite-dimensional and the integral equation in Eq. (3.17) induces a system of coupled integral equations for the scalar functions $b_1(t)$,... , $b_n(t)$ introduced in Eq. (3.9). Thus, by using $\mathbf{G}_\square(\mathbf{x},\mathbf{x}',t)$, we were able to

eliminate the infinitely many photonic degrees of freedom and derive a coupled system of finitely many integral equations. This system of equations can now be solved by an iteration procedure starting with

$$|\psi_{\text{atomic}}(t)\rangle = 0 \,.$$

By doing so, we obtain the time evolution of the wave function $|\psi_{\text{atomic}}(t)\rangle$ connected to the atomic excitations. The corresponding time evolution of $|\psi_{\text{photonic}}(t)\rangle$ connected to the photonic excitations can be obtained by using Eq. (3.12).

One of the main advantages of Eq. (3.17) is that each term is linked to a relatively simple physical picture. The term in the first line of Eq. (3.17) corresponds to the spontaneous decay of an initial atomic excitation in free-space as discussed in the previous section. The term in the second line corresponds to the absorption of an initial photonic excitation by atom α and the subsequent spontaneous decay of this atomic excitation due to the spontaneous decay process. The last line corresponds to a jump of the excitation from atom α_1 to atom α_2 mediated by the radiation field and the subsequent decay of the excitation. Thereby, atom α_1 decays by emitting a single photon at time t_1 which propagates to atom α_2. The propagation of the photon can be described by using the appropriate Green's functions. After reaching atom α_2 the photon gets absorbed at time t_2 and atom α_2 is transferred from the ground state to its excited state. Solving Eq. (3.17) by performing an iteration procedure generates sequences of spontaneous emission and absorption processes. Each term generated by the iteration procedure can be interpreted as such a sequence and a hopping of the excitation among the atoms. If only a finite time interval is considered the iteration procedure converges after finitely many steps because each photonic excitation can only propagate with the speed of light (as encoded in the Green's function). Thus, the iteration procedure enables us to solve Eq. (3.17) exactly and allows a descriptive interpretation of the corresponding expressions as sequences of spontaneous emission and absorption processes.

3.4 CONNECTION WITH GEOMETRICAL OPTICS

In the previous section, we introduced suitable Green's functions to describe the propagation of photons. However, it is in general a highly non-trivial task to obtain suitable expressions for these Green's functions if scenarios beyond free-space or mirrors with special geometries are considered. In the following, we introduce semiclassical methods for evaluating these functions. Thereby, we connect the photon-path-representation to the framework of geometrical optics, which provides us with a descriptive interpretation of the corresponding expressions.

Semiclassical methods are linked to the short wavelength limit of a particular partial differential equation. The focus lies on scenarios where the solution of the partial differential equation is dominated by rapid oscillations with wavelengths much shorter than any other length scale present in the system, which is the case for many optical phenomena.

We consider the scalar wave equation

$$\left[\frac{n^2(\mathbf{x})}{c^2}\frac{\partial^2}{\partial t^2} - \nabla^2\right] u(\mathbf{x},t) = 0 \tag{3.18}$$

with $n(\mathbf{x})$ being the spatial dependent diffractive index. We are interested in evaluating the corresponding time evolution for a given $u(\mathbf{x}, t_0)$ and $\dot{u}(\mathbf{x}, t)$. We solve the equation by using the ansatz

$$u(\mathbf{x}, t) = \mathrm{Re}\left[\varphi(\mathbf{x}, t) e^{ikS(\mathbf{x},t)}\right] \tag{3.19}$$

whereby $\varphi(\mathbf{x}, t)$ represents a slowly varying envelope and $e^{ikS(\mathbf{x},t)}$ represents rapid oscillations. In the following, we assume that the variations of $\varphi(\mathbf{x}, t)$ as a function of $\mathbf{x}$ and t are much smaller than the variations of $kS(\mathbf{x}, t)$. To be precise, we require the eikonal $S(\mathbf{x}, t)$ to be independent of k and that for large values of k the following expansion of $\varphi(\mathbf{x}, t)$ is valid

$$\varphi(\mathbf{x}, t) = \varphi_0(\mathbf{x}, t) + \frac{1}{k}\varphi_1(\mathbf{x}, t) + \frac{1}{k^2}\varphi_2(\mathbf{x}, t) + ...$$

The semiclassical approximation corresponds to neglecting all the higher terms $\varphi_1(\mathbf{x}, t)$, $\varphi_2(\mathbf{x}, t)$... in the limit $k \to \infty$. By inserting our semiclassical ansatz of Eq. (3.19) into the wave equation (3.18), we obtain

$$\begin{aligned} 0 \;=\; & \varphi\left[\left(\dot{S}\right)^2 - \frac{c^2}{n^2(\mathbf{x})}\left(\nabla S\right)^2\right] - ik^{-1}\left[2\dot{\varphi}\dot{S} + \varphi\ddot{S} - \frac{c^2}{n^2(\mathbf{x})}\left[2\left(\nabla\varphi\right)\left(\nabla S\right) + \varphi\nabla^2 S\right]\right] \\ & -k^{-2}\left[\ddot{\varphi} - \frac{c^2}{n^2(\mathbf{x})}\nabla^2\varphi\right] \end{aligned} \tag{3.20}$$

which induces a hierarchy of equations for $S(\mathbf{x}, t)$ and $\varphi_1(\mathbf{x}, t), \varphi_2(\mathbf{x}, t)$... . We truncate this hierarchy by neglecting all the terms which are of the order of k^{-n} with $n \geq 2$. We obtain

$O(1)$

$$\left(\dot{S}\right)^2 - \frac{c^2}{n^2(\mathbf{x})}\left(\nabla S\right)^2 = 0 \tag{3.21}$$

$O(k^{-1})$

$$2\dot{\varphi}_0\dot{S} + \varphi_0\ddot{S} - \frac{c^2}{n^2(\mathbf{x})}\left[2\left(\nabla\varphi_0\right)\left(\nabla S\right) + \varphi_0\nabla^2 S\right] = 0\,. \tag{3.22}$$

The eikonal equation (3.21) can be linked to a suitable problem of classical mechanics. This can be done by using the Hamilton–Jacobi equation and by identifying the function S with Hamilton's principal function which satisfies the following equation

$$H(\mathbf{x}, \nabla S) + \frac{\partial}{\partial t}S(\mathbf{x}, t) = 0$$

with $H(\mathbf{x}, \mathbf{p})$ being the corresponding Hamilton function. The principal function fulfills the property

$$\mathbf{p} = \nabla S\,.$$

In order to match the eikonal equation (3.21), we have to choose the Hamiltonian

$$H(\mathbf{x}, \mathbf{p}) = \sqrt{\frac{c^2}{n^2(\mathbf{x})}\mathbf{p}^2}$$

which corresponds to a massless, relativistic, free particle. In the following, we consider trajectories which match the initial condition

$$\mathbf{p}(\mathbf{x}(t_0)) = \nabla S(\mathbf{x}(t_0), t_0)\,.$$

Along such a trajectory, we obtain

$$\frac{d}{dt}S(\mathbf{x}(t),t) = \nabla S(\mathbf{x}(t),t)\dot{\mathbf{x}}(t) + \dot{S}(\mathbf{x}(t),t) = \mathbf{p}(t)\cdot\dot{\mathbf{x}}(t) - H = L(\mathbf{x}(t),\dot{\mathbf{x}}(t))$$

with L being the corresponding Lagrange function. Thus, the solution of S along the trajectory is given by

$$S(\mathbf{x}(t),t) = S(\mathbf{x}(t_0),t_0) + \int_{t_0}^{t} L(\mathbf{x}(t'),\dot{\mathbf{x}}(t'))dt' \ .$$

Eq. (3.22) is usually called transport equation. By using this equation, we can construct a solution for $\varphi_0(\mathbf{x},t)$. This can also be done by considering the derivative of $\log\left(\varphi^2\right)$ along a trajectory. By putting all these things together, we obtain

$$u(\mathbf{x},t) = \mathrm{Re}\left[\sum_j \sqrt{\left|\det\left(\frac{\partial \mathbf{x}^j(t)}{\partial \mathbf{x}^j(t_0)}\right)\right|}^{-1} u(\mathbf{x}^j(t_0),t_0)e^{ik\int_{t_0}^{t} L(\mathbf{x}^j(t'),\dot{\mathbf{x}}^j(t'))dt'}\right] + O(k^{-1})$$

with $\mathbf{x}^j(t)$ being trajectories compatible with the initial conditions such that $\mathbf{x}^j(t) = \mathbf{x}$. In our particular case of wave equation (3.18), this simplifies further to

$$u(\mathbf{x},t) = \mathrm{Re}\left[\sum_j \sqrt{\left|\det\left(\frac{\partial \mathbf{x}^j(t)}{\partial \mathbf{x}^j(t_0)}\right)\right|}^{-1} u(\mathbf{x}^j(t_0),t_0)\right] + O(k^{-1}) \ . \tag{3.23}$$

The trajectories $\mathbf{x}^j(t)$, hereby, correspond to the rays of geometrical optics. The previous construction works well in case that the wavelength is sufficiently short and we are far away from caustics (points in space and time where several rays meet). Close to a caustic the expression in Eq. (3.23) becomes divergent because the Jacobian determinant vanishes. As we see later on, it is, in fact, possible to deal even with this situation and to generalize the considerations above to much broader classes of wave equations [38, 39].

In the following, we are interested in applying the semiclassical expressions derived above also for describing the propagation of the radiation field in the presence of boundary conditions used to model cavities or mirrors. This causes some complications because a boundary condition is something abrupt, i.e., it corresponds to an infinitely short length scale. The previous expressions, however, were derived under the assumption that the wavelength is by far the shortest length scale present in the system. To circumvent this problem, one can study the propagation of a plane wave near such a boundary condition or near an abrupt change of the dielectric constant. Thereby, it is possible to derive appropriate rules for the propagation of the corresponding trajectories $\mathbf{x}(t)$ near such a boundary and to introduce suitable factors into Eq. (3.18) (This can be done as long as the surface connected to the boundary condition varies on a much larger length scale than the typical wavelength we are interested in.). It is also possible to extend the previous investigations in order to apply them to vector fields [38].

We can use the semiclassical relations derived above for evaluating the Green's function $\mathbf{G}_{\square}(\mathbf{x}_2,\mathbf{x}_1,t)$. We focus on the description of the propagation of the electric field in vacuum with the boundary conditions being the only deviations from the free-space scenario. For evaluating the previous expression, we divide the entire volume V in two parts as depicted in Fig. 3.2. The first volume V_1 corresponds to a sphere

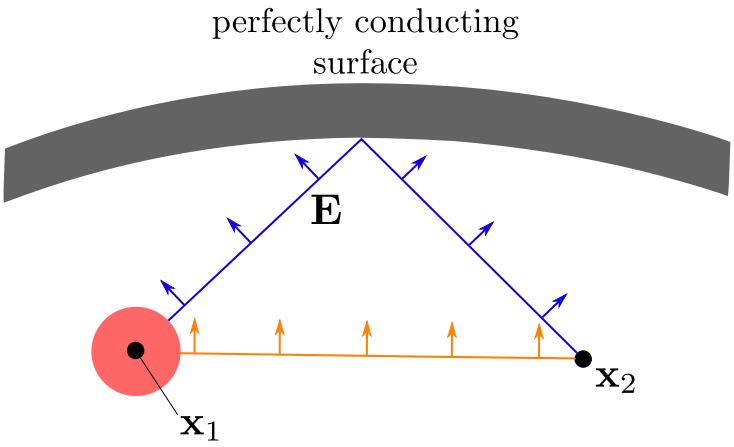

Figure 3.2.: Evaluation of the Green's function $\mathbf{G}_\square$ in the presence of a boundary condition. The red circle corresponds to the sphere centered around $\mathbf{x}_1$ in which we evaluate the field by using $\mathbf{G}_\square^{\text{free}}$. The blue and the orange line correspond to two different trajectories (rays) connecting points in the sphere with $\mathbf{x}_2$. The arrows indicate the direction of the field.

with radius r around $\mathbf{x}_1$. The radius is chosen such that it is much larger than the typical wavelength λ but is chosen sufficiently small that the surface of the sphere is still far away from the nearest boundary. The second volume V_2 is just everything else except the sphere. In volume V_1 we just use $\mathbf{G}_\square^{\text{free}}(\mathbf{x}_2, \mathbf{x}_1, t)$ in order to evaluate the time evolution of the field and in volume V_2 we apply the semiclassical expression (3.23) in order to take the boundary conditions into account. By doing so, we obtain the following semiclassical approximation of the Green's function

$$\begin{aligned}\nabla \times \nabla \times \mathbf{G}_\square(\mathbf{x}_2, \mathbf{x}_1, t - t_1) = -\tfrac{1}{4\pi c^2} \textstyle\sum_j \sqrt{\left|\det\left(\frac{\partial \mathbf{x}^j(t_j)}{\partial \mathbf{x}^j(t_0)}\right)\right|}^{-1} \\ \cdot \delta''\left[t - r/c - (t_j - t_0)\right] \tfrac{1}{||\mathbf{x}^j(t_0) - \mathbf{x}_1||} \mathbf{M}_j \left[\mathbb{1} - \tfrac{(\mathbf{x}^j(t_0) - \mathbf{x}_1) \otimes (\mathbf{x}^j(t_0) - \mathbf{x}_1)}{||\mathbf{x}^j(t_0) - \mathbf{x}_1||^2}\right], \end{aligned} \tag{3.24}$$

whereby the sum is running over all trajectories $\mathbf{x}^j(t)$ with $\mathbf{x}^j(t_j) = \mathbf{x}_2$ and $\mathbf{x}^j(t_0) \in \partial V_1$. The trajectories $\mathbf{x}^j(t)$ are just the straight lines known from geometrical optics which, away from the boundary conditions, fulfill the differential equations

$$\frac{d^2}{dt^2} \mathbf{x}^j(t) = 0$$

and the initial conditions

$$\begin{aligned}\mathbf{x}^j(t_0) &\in \partial V_1 \\ \dot{\mathbf{x}}^j(t_0) &= c \tfrac{\mathbf{x}^j(t_0) - \mathbf{x}_1}{||\mathbf{x}^j(t_0) - \mathbf{x}_1||}. \end{aligned}$$

The matrices $\mathbf{M}_j$ are unitary matrices which take the vectorial nature of the field into account. They describe the change in orientation the field experiences by propagating through volume V_2 and take phase flips caused by the boundary conditions into account. A detailed derivation of the above semiclassical expression can be found in Appendix B.

The above considerations are only valid as long as $\mathbf{x}_2$ does not lie in a caustic, such as a focal point. These caustics, however, are of particular interest because close to a caustic the field strength and consequently matter-field coupling are enhanced. It is possible to extend the above considerations and to apply semiclassical methods to evaluate the Green's function close to a caustic. This can be done by propagating the field inside a sphere centered around the focal point $\mathbf{x}_2$ by using the relation

$$\mathbf{E}(\mathbf{x}_2, t) = \frac{1}{c^2} \int_{V_2} \dot{\mathbf{G}}^{\text{free}}_{\Box}(\mathbf{x}_2, \mathbf{x}, \frac{r}{c}) \mathbf{E}(\mathbf{x}, t - \frac{r}{c}) + \mathbf{G}^{\text{free}}_{\Box}(\mathbf{x}_2, \mathbf{x}, \frac{r}{c}) \dot{\mathbf{E}}(\mathbf{x}, t - \frac{r}{c}) d^3\mathbf{x}$$

which describes the propagation of the field in free-space. For evaluating this expression, we have to use the semiclassical expression (3.24) only on the surface of the sphere (at a sufficient distance from the caustic).

3.5 SUMMARY

In this chapter, we have introduced the photon-path-representation for single-photon states. Thereby, we have recapitulated the description of the spontaneous decay process by Weisskopf and Wigner [36] and have used it as a basic building block for developing a more general method for taking the presence of several quantum emitters and additional macroscopic objects, such as mirrors or cavities, into account. This photon-path-representation is well suited for investigating the time evolution of simple quantum emitters in large, half-open cavities or even in free-space where a full multimode description of the radiation field has to be taken into account. By applying this method, the time evolution of the system can be evaluated in a straightforward and descriptive manner and the different terms generated by this approach can be interpreted as sequences of spontaneous emission and absorption processes. We have also used semiclassical methods to connect the photon-path-representation with the framework of geometrical optics. By using this connection, it is possible to obtain simple and descriptive analytical expressions describing the propagation of single photons in a cavity or in the presence of mirrors without the need to solve complicated partial differential equations.

This framework allows us to investigate matter-field coupling on the single-photon level which is not only of interest for understanding fundamental processes in nature but also of relevance for many practical applications because the precise control of the interaction between matter and the radiation field is a key ingredient to the quantum technologies discussed in chapter 1. Hence, the photon-path-representation serves as a starting point for many of the investigations presented in the following chapters.

4

ENTANGLEMENT GENERATION USING PARABOLIC MIRRORS

A valuable resource in the fields of quantum communication and quantum cryptography are entangled states shared between remote parties. They can be used for many interesting applications, such as the teleportation of quantum states over macroscopic distances [40] or the generation of a shared secret key by using an entanglement-based protocol [41]. The ability to generate remote entangled matter qubits is of particular importance because matter qubits in contrast to photonic qubits can be manipulated and measured with high accuracy and can even be stored locally for a certain amount of time.

The generation of distant entangled matter qubits has been demonstrated by using fiber-based communication channels [29, 42, 43]. However, as already discussed in chapter 1 fiber-based communication is not always feasible. The aim of this chapter is to close a certain gap between fiber-based and free-space communication and to provide a suitable protocol for the generation of entangled states shared between two distant matter qubits using a free-space channel. The main issue with a free-space communication is the low photon collection efficiency. We show that this can be improved by placing the two matter qubits at the focal points of the parabolic mirrors [24, 30, 44]. Our scheme involves an extreme multimode scenario, i.e., the atoms are coupled to a continuum of modes of the radiations field because the parabolic mirror is a half-open cavity. Thereby, we deal with intrinsic multimode effects, such as spontaneous decay processes which are usually considered as sources of unwanted decoherence. Interestingly enough, we can use these effects as tools for entanglement generation rather than avoiding them. To investigate the coupling of the matter qubits to the multimode radiation field connected to such a free-space approach, we based our theoretical investigation on the photon-path-representation developed in the previous chapter.

This chapter is organized as follows. In Sec. 4.1, we start with a detailed description of the setup, which we have in mind, and give an outline of the protocol. We present a suitable theoretical model in Sec. 4.2 and also discuss the basic steps which we perform to evaluate the time evolution of the system. We use the semiclassical methods [38, 45] introduced in Sec. 3.4 to deal with the boundary conditions imposed to model the parabolic mirrors. In Sec. 4.3, we briefly summarize the results of our theoretical analysis. We address the feasibility of the scheme and the main experimental imperfections in Sec. 4.4. Moreover, we compare our protocol with other schemes for free-space quantum communication in Sec. 4.5.

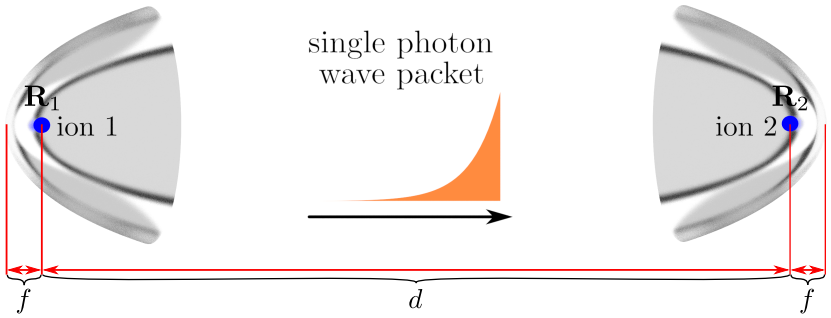

Figure 4.1.: Sketch of the setup: Two $^{171}Yb^+$ ions are trapped at the focal points $\mathbf{R}_1$ and $\mathbf{R}_2$ of two parabolic mirrors. The focal length of the mirrors is denoted f and the distance between the two ions denoted d.

4.1 SETUP AND PROTOCOL

In the following, we consider a setup consisting out of two parabolic mirrors opposing each other and two $^{171}Yb^+$ ions, each of them trapped close to the focal point of one of the parabolic mirrors. The $^{171}Yb^+$ ions provide us with a suitable electronic level structure and serve as matter qubits. The corresponding setup is depicted in Fig. 4.1.

The main advantage of this configuration is that the parabolic mirrors direct any electromagnetic field from one focal point to the other with high efficiency. Thus, if ion 1 emits a photon, this photon is directed towards the second parabolic mirror and refocused onto the position of the second ion. Due to the refocusing onto the second ion, matter-field coupling is enhanced and the probability for absorbing the photon is increased.

We concentrate on the level scheme formed by the levels $6^2S_{1/2}$ and $6^2P_{1/2}$ of the $^{171}Yb^+$ ions. The corresponding level structure is shown in Fig. 4.2. In the following, we choose the levels $|6^2S_{1/2}, F = 1, m = -1\rangle$ and $|6^2S_{1/2}, F = 1, m = 1\rangle$ to represent our qubits. The quantization axis is chosen to be the symmetry axis of our setup, in the following referred to as the z-axis.

The basic idea of our scheme is to initially prepare ion 1 in the state

$$|6^2P_{1/2}, F = 1, m = 0\rangle_1$$

and ion 2 in the state

$$|6^2S_{1/2},\ F = 1, m = 0\rangle_2$$

and to use the time evolution to generate an entangled state. We thereby assume that the radiation field is initially prepared in the vacuum state $|0\rangle_{\text{rad}}$. The time evolution which generates an entangled state of the matter qubits can be divided into four parts.

In the first part of the time evolution, ion 1 undergoes a spontaneous decay process. It can decay to three distinct electronic energy levels: to $|6^2S_{1/2}, F = 1, m = -1\rangle$ by emitting a right-circularly polarized (σ_+) photon , to $|6^2S_{1/2}, F = 1, m = 1\rangle$ by emitting a left-circularly polarized (σ_-) photon, and to $|6^2S_{1/2}, F = 0, m = 0\rangle$ by emitting a linearly polarized (π) photon. Because we do not know which of the three mentioned processes takes place, the complete state of the system is a linear superposition of the three corresponding probability amplitudes. As a consequence, ion 1 and the radiation field get entangled. In the second part of the time evolution, the generated photon,

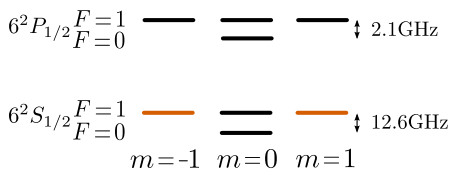

Figure 4.2.: Hyperfine level scheme of a $^{171}Yb^+$ ion: The states of the logical qubit, depicted in orange, are defined by the electronic levels $|6^2S_{1/2}, F = 1, m = -1\rangle$ and $|6^2S_{1/2}, F = 1, m = 1\rangle$.

which is entangled with ion 1, propagates to ion 2 (due to the geometry of the parabolic mirror). In the third part of the time evolution, the photon may excite ion 2. If this absorption process takes place, the state of the photon is mapped onto the state of the second ion: if it absorbs a σ_+ polarized photon, the second ion ends up in the state $|6^2P_{1/2}, F = 1, m = 1\rangle$, if it absorbs a σ_- polarized photon, the second ion ends up in the state $|6^2P_{1/2}, F = 1, m = -1\rangle$. However, the probability for absorbing a π polarized photon is negligible because the dipole allowed transition is detuned from the frequency of the photon by several GHz. After this third part of the time evolution, the ions end up in an entangled state (because the photon was entangled with ion 1). However, after the absorption process ion 2 is in an excited state which is not radiatively stable because it is effected by spontaneous decay processes. So, we have to perform a state transfer from the manifold $6^2P_{1/2}$ to the manifold $6^2S_{1/2}$ that is radiatively stable. We do this by using the fourth part of the time evolution, i.e., the spontaneous decay of ion 2. To that end, we have to take the different decay channels into account. For example, consider that ion 2 is in the state $|6^2P_{1/2}, F = 1, m = 1\rangle$: it can decay into the states $|6^2S_{1/2}, F = 1, m = 0\rangle$, $|6^2S_{1/2}, F = 0, m = 0\rangle$ and $|6^2S_{1/2}, F = 1, m = 1\rangle$. However, only the last process generates entanglement. In a similar way, one can treat the case that ion 2 is in the state $|6^2P_{1/2}, F = 1, m = -1\rangle$.

Finally, to discard the undesired decay processes, we have to perform a post-selection. Since only in case of successful entanglement generation, both ions end up in the qubit state. By probing the occupation of the qubit states, we discard the undesired decay processes. This can be performed with negligible loss of entanglement by using dispersive state detection. It suffices to couple weak off-resonant coherent pulses to the π transitions from $S_{1/2}, F = 1, m = \pm 1$ to $P_{1/2}, F = 1, m = \pm 1$. The population is then detected by the phase shifts imprinted onto the coherent states. This procedure allows us to check the population of the qubit states while preserving the possible linear superpositions and thus does not disturb the entangled state. We discuss this post selection procedure in more detail in Sec. 4.4.

One of the main error sources in a photonic channel is the possibility of photon loss. In order generate highly entangled matter qubits, we have to make sure that we can deal with these loss processes properly. Fortunately, it turns out that our post-selection procedure also detects photon losses so that the scheme is loss tolerant. This is due to the fact that upon photon loss ion 2 remains in $|S_{1/2}, F = 1, m = 0\rangle$ and post-selection is probed on π-transitions, which are for $|S_{1/2}, F = 1, m = 0\rangle$ either forbidden or detuned so strongly that no phase shift of the probe pulse occurs. Of course, losses reduce the success probability but the fidelity after a successful post selection is not affected. The low success probability can be overcome with a high repetition rate.

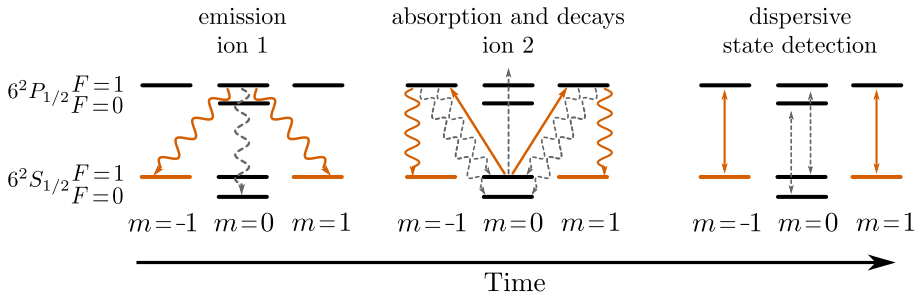

Figure 4.3.: Sequence of the processes which are the building blocks for the remote entanglement preparation: The states of the logical qubit, depicted in orange, are defined by the electronic levels $|6^2S_{1/2}, F = 1, m = -1\rangle$ and $|6^2S_{1/2}, F = 1, m = 1\rangle$. Optical transitions which are necessary for the entanglement generation are indicated by solid arrows whereas the undesired transitions are indicated by dashed arrows. The three columns correspond to three phases. The first column shows the possible decay channels of the first ion's initially prepared state $|6^2P_{1/2}, F = 1, m = 0\rangle$; the second column shows the possible excitation processes of the second ion which was initially prepared in the state $|6^2S_{1/2}, F = 1, m = 0\rangle$ followed by the spontaneous decay used to accomplish the state transfer from the $6^2P_{1/2}$ manifold to the radiatively stable $6^2S_{1/2}$ manifold; the last column shows the optical transitions used to perform the post-selection procedure based on hyperfine splitting and off-resonant matter-field interactions.

All the steps for generating entangled states described above are depicted in Fig. 4.3. This figure also indicates all the dipole allowed transitions between the $6^2S_{1/2}$ and $6^2P_{1/2}$ manifold.

4.2 THEORETICAL ANALYSIS

In this section, we evaluate the time evolution of the system for the initial state described in the previous section. We make use of the photon-path-representation developed in chapter 3. For applying the photon-path-representation, we have to generalize it to describe the multi-level atoms used here.

4.2.1 *System Hamiltonian*

We start our theoretical investigation of the system by modeling the dynamics of the system by introducing a suitable Hamilton operator. As in chapter 3, we apply the dipole approximation and the RWA. The corresponding Hamilton operator is given by

$$\hat{H} = \hat{H}_{\text{rad}} + \sum_{\alpha\in\{1,2\}} \hat{H}^{\alpha}_{\text{atom}} + \sum_{\alpha\in\{1,2\}} \hat{H}^{\alpha}_{\text{int}}$$

where $\hat{H}_{\text{rad}}$ models the free radiation field introduced in Sec. 2.1, $\hat{H}^{\alpha}_{\text{atom}}$ describes the free dynamics of each of the ions and $\hat{H}^{\alpha}_{\text{int}}$ models the interaction between the ions and the radiation field. We indicate the set of states in the manifold $6^2P_{1/2}$ by S_e (excited) and the set of states in the manifold $6^2S_{1/2}$ by S_g (ground). In the following, we neglect

the shifts of the eigenenergies of both of the ions caused by an additional magnetic field. Thus, the eigenenergies of both of the ions coincide. The vectors $|i\rangle_1$, $|j\rangle_2$ for $i, j \in S_e \cup S_g$ represent the eigenstate of ion 1 and ion 2 with energies $\hbar\omega_i$ and $\hbar\omega_j$. We obtain

$$\hat{H}^{\alpha}_{\text{atom}} = \hbar \sum_j \omega_j \, |j\rangle_\alpha \, \langle j|_\alpha \ .$$

And for the interaction Hamiltonian, we get

$$\hat{H}^{\alpha}_{\text{int}} = -\hat{\mathbf{d}}^-_\alpha \hat{\mathbf{E}}^-(\mathbf{R}_\alpha) - \hat{\mathbf{d}}^+_\alpha \hat{\mathbf{E}}^+(\mathbf{R}_\alpha)$$

with $\mathbf{R}_\alpha$ denoting the position of ion α and

$$\hat{\mathbf{d}}^-_\alpha = \sum_{i \in S_e} \sum_{j \in S_g} \mathbf{d}^{ij}_\alpha \ |j\rangle_\alpha \ \langle i|_\alpha$$

being the corresponding dipole operator with $\mathbf{d}^{ij}_\alpha$ denoting the dipole operator of the transition between the electronic states $i \in S_e$ and $j \in S_g$. The initial state of the system is given by

$$|\psi(t_0)\rangle = |6^2P_{1/2}, F = 1, m = 0\rangle_1 \otimes |6^2S_{1/2},\ F = 1, m = 0\rangle_2 \otimes |0\rangle_{\text{rad}}$$

4.2.2 *Photon-path-representation*

For evaluating the time evolution, we use the photon-path-representation developed in chapter 3. To do this, we have to adapt the photon-path-representation in order to be compatible with the level structure of the $^{171}Yb^+$ ions. This, however, is a straight forward task.

As in chapter 3, we split the wave function in two parts

$$|\psi(t)\rangle = |\psi_{\text{atomic}}(t)\rangle + |\psi_{\text{photonic}}(t)\rangle$$

with $|\psi_{\text{atomic}}(t)\rangle$ representing a single atomic excitation and $|\psi_{\text{photonic}}(t)\rangle$ representing a single photonic excitation. The time evolution of the wave function $|\psi_{\text{atomic}}(t)\rangle$ can be evaluated by using the relation

$$\begin{aligned}
|\psi_{\text{atomic}}(t)\rangle \ = \ & e^{\left[-\frac{i}{\hbar}\sum\limits_{\alpha\in\{1,2\}} \hat{H}^{\alpha}_{\text{atom}} - \hat{\Gamma}/2\right](t-t_0)} \, |\psi_{\text{atomic}}(t_0)\rangle \\
& + \frac{i}{\hbar} \int_{t_0}^{t} e^{\left[-\frac{i}{\hbar}\sum\limits_{\alpha\in\{1,2\}} \hat{H}^{\alpha}_{\text{atom}} - \hat{\Gamma}/2\right](t-t_1)} \sum_{\alpha\in\{1,2\}} \sum_{i\in S_g} \sum_{j\in S_e} \\
& |j\rangle_\alpha \, \langle i|_\alpha \, \mathbf{d}^{ij}_\alpha \cdot \hat{\mathbf{E}}^+_\perp(\mathbf{R}_\alpha, t_1) \, |\psi_{\text{photonic}}(t_0)\rangle \, dt_1 \\
& + \int_{t_0}^{t} \int_{t_0}^{t_1} e^{\left[-\frac{i}{\hbar}\sum\limits_{\alpha\in\{1,2\}} \hat{H}^{\alpha}_{\text{atom}} - \hat{\Gamma}/2\right](t-t_2)} \hat{T}(t_2 - t_1) \, |\psi_{\text{atomic}}(t_1)\rangle \, dt_1 dt_2
\end{aligned} \tag{4.1}$$

with

$$\begin{aligned}
\hat{T}(t) \ = \ & \frac{i}{\epsilon_0 \hbar} \sum_{\alpha_1,\alpha_2=1}^{N} \sum_{i_1,j_2\in S_e} \sum_{i_2,j_1\in S_g} \\
& |j_2\rangle_{\alpha_2} \, \langle i_2|_{\alpha_2} \, \mathbf{d}^{i_2 j_2}_{\alpha_2} \left[\begin{cases} \nabla\times\nabla\times\mathbf{G}_\square(\mathbf{R}_{\alpha_2}, \mathbf{R}_{\alpha_1}, t) & \text{for } \alpha_1 \neq \alpha_2 \\ \nabla\times\nabla\times\mathbf{G}^{\text{boundary}}_\square(\mathbf{R}_{\alpha_2}, \mathbf{R}_{\alpha_1}, t) & \text{for } \alpha_1 = \alpha_2 \end{cases} \right] \mathbf{d}^{i_1 j_1}_{\alpha_1} \, |j_1\rangle_{\alpha_1} \, \langle i_1|_{\alpha_1} \ ,
\end{aligned}$$

$$\hat{\Gamma} = \sum_{\alpha\in\{1,2\}} \sum_{i\in S_e} \sum_{j\in S_g} \Gamma_\alpha^{ij} \left|i\right\rangle_\alpha \left\langle i\right|_\alpha$$

and

$$\Gamma_\alpha^{ij} = \frac{|\ \omega_i - \omega_j\ |^3 ||\ \mathbf{d}_\alpha^{ij}\ ||^2}{3\pi\epsilon_0\hbar c^3}$$

being the spontaneous decay rate connected to the atomic transition $|i\rangle \to |j\rangle$. As described in chapter 3, we obtain a solution for $|\psi_{\text{atomic}}(t)\rangle$ by performing an iteration procedure starting with $|\psi_{\text{atomic}}(t)\rangle = 0$.

The time evolution of the wave function $|\psi_{\text{photonic}}(t)\rangle$ can be evaluated by using the relation

$$\begin{aligned} |\psi_{\text{photonic}}(t)\rangle &= e^{-\frac{i}{\hbar}\hat{H}_{\text{rad}}(t-t_0)} |\psi_{\text{photonic}}(t_0)\rangle \\ &\quad + \frac{i}{\hbar} \sum_{\alpha\in\{1,2\}} \int_{t_0}^{t} e^{-\frac{i}{\hbar}\hat{H}_{\text{rad}}(t-t_1)} \sum_{j\in S_g} \sum_{i\in S_e} \mathbf{d}_\alpha^{ij} \cdot \hat{\mathbf{E}}_\perp^-(\mathbf{R}_\alpha) \left|j\right\rangle_\alpha \left\langle i\right|_\alpha |\psi_{\text{atomic}}(t_1)\rangle\, dt_1 \,. \end{aligned} \tag{4.2}$$

It turns out that for all the dipole allowed transitions between the $6^2P_{1/2}$ and the $6^2S_{1/2}$ manifold (which are depicted in Fig. 4.3), the norms of the corresponding dipole matrix elements $\mathbf{d}_\alpha^{ij}$ coincide. Furthermore, transitions between the $6^2P_{1/2}$ and the $6^2S_{1/2}$ manifold are connected with the typical transition frequency ω_{eg} which corresponds to the wavelength of 369.5 nm. All the deviations from this frequency are caused by hyperfine splitting and are of the order of a few GHz, which is small compared to ω_{eg}. Thus, each of the excited states in $6^2P_{1/2}$ can decay to 3 ground states in $6^2S_{1/2}$ via three dipole allowed transitions with almost identical spontaneous decay rates Γ_α^{ij}. Thus, in good approximation, we can replace the operator $\hat{\Gamma}$ in Eq. (4.1) by $3\Gamma\mathbb{1}$ with Γ being the spontaneous decay rate associated to one of the dipole allowed transitions.

4.2.3 *Semiclassical expressions describing photon propagation between the parabolic mirrors*

For evaluating the time evolution, we also have to find suitable expressions for the Green's functions $\mathbf{G}_\square$. We obtain an appropriate expression for $\mathbf{G}_\square$ by applying the semiclassical methods developed in Sec. 3.4. The application of these methods is justified if the typical length scales induced by the parabolic mirrors are much larger than the typical wavelength λ_{eg}, i.e., $d, f \gg \lambda_{eg}$, which is the case for the parabolic mirrors used in [30] ($f = 2.1$mm, $\lambda_{eg} = 369.5$ nm). To apply semiclassical methods, we have to construct the rays of geometrical optics, which can be used to describe the propagation of the photons through the setup. In the following, we construct the corresponding rays starting in the focal point $\mathbf{R}_1$ of the first mirror. For constructing these rays, we can make use of the defining property of a parabolic mirror to map any ray of light starting in the focal point to a ray parallel to the symmetry axis of the setup. We obtain the rays depicted in Fig. 4.4.

We can distinguish between several classes of rays. The first class (red) are the rays which get reflected by the first parabolic mirror, propagate along the symmetry axis to the second parabolic mirror, get reflected by the second mirror, and, finally, end in the second focal point. All the rays, connecting the two focal points, have the same optical

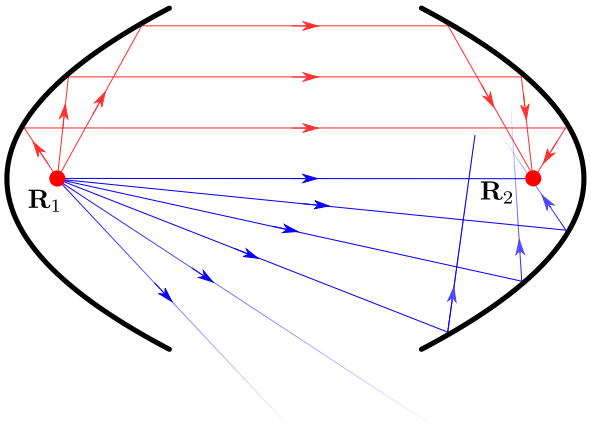

Figure 4.4.: Rays of geometrical optics: The red rays, connecting the focal point $\mathbf{R}_1$ with the focal point $\mathbf{R}_2$, are constructed by using the defining property of the parabolic mirrors. The blue rays also start in the focal point $\mathbf{R}_1$ but do not get reflected by the first parabolic mirror. Many of the blue rays do not reach the focal point $\mathbf{R}_2$.

path length $4f + d$. The corresponding trajectories simultaneously reach the second focal point after

$$\tau = \frac{4f + d}{c} .$$

Hence, the second focal point lies in a caustic with respect to these rays and the field strength at the second focal point is enhanced. Many of these rays return to the first focal point after the time 2τ and proceed going from focal point to focal point. The second class of rays (blue) are the rays which do not get reflected by the first parabolic mirror. Many of these rays do not reach the second focal point and if they do, they will not cause a caustic. It turns out that the contribution of these class of rays to the field at the second focal point is roughly reduced by a factor $\frac{\lambda_{eg}}{d}$ as compared to the contribution of the first class of rays. In the following, we neglect their contribution due to our initial assumption $d \gg \lambda_{eg}$ and we only use the first class of rays for evaluating the expression $\mathbf{d}_2 \nabla \times \nabla \times \mathbf{G}_\square(\mathbf{R}_2, \mathbf{R}_1, t)\mathbf{d}_1$. By applying the results of Sec. 3.4 and assuming perfectly conducting parabolic mirrors, we obtain

$$\frac{1}{\epsilon_0 \hbar} \mathbf{d}_2 \nabla \times \nabla \times \mathbf{G}_\square(\mathbf{R}_2, \mathbf{R}_1, t)\mathbf{d}_1 = \frac{\omega_{eg}^3}{8\pi^2 \hbar \epsilon_0 c^3} \sum_{i=1,3,5..} \delta(t - \tau i) \mathbf{d}_2 \left[\int_{\Omega_i} [\mathbb{1} - \mathbf{n} \otimes \mathbf{n}] \, d\sigma \right] \mathbf{d}_1 \tag{4.3}$$

with Ω_i corresponding to the solid angle connected to the first class of rays. In a similar way, we obtain

$$\begin{aligned} &\tfrac{1}{\epsilon_0 \hbar} \mathbf{d}_2 \nabla \times \nabla \times \mathbf{G}_\square(\mathbf{R}_1, \mathbf{R}_1, t)\mathbf{d}_1 = \\ &\delta(t) \tfrac{\omega_{eg}^3 \mathbf{d}_2 \cdot \mathbf{d}_1}{3\pi \hbar \epsilon_0 c^3} + \tfrac{\omega_{eg}^3}{8\pi^2 \hbar \epsilon_0 c^3} \sum_{i=2,4,6..} \delta(t - \tau i) \mathbf{d}_2 \left[\textstyle\int_{\Omega_i} [\mathbb{1} - \mathbf{n} \otimes \mathbf{n}] \, d\sigma \right] \mathbf{d}_1 . \end{aligned} \tag{4.4}$$

By using the above expressions, we are able to evaluate the time evolution of $|\psi(t)\rangle$. Based on the semiclassical methods developed in the previous chapter, we can also derive suitable expressions if we go beyond our assumption of perfectly conducting mirrors. We consider a more realistic model of the mirrors later on.

4.2.4 *Tracing over the photonic degrees of freedom*

In order to evaluate the fidelity of the entangled state generated by our procedure, we have to trace over the photonic degrees of freedom because they are ignored after finishing the procedure (no postselection of the photonic state). If the radiation field contains information about the state of our matter qubits, the fidelity of the entangled state drops. By tracing over the photonic degrees of freedom, we can take these effects into account. In the following, we are interested in the density operator

$$\hat{\varrho}(t) = \mathrm{Tr}_{\mathrm{rad}} \left[|\psi(t)\rangle \langle \psi(t)| \right]$$

with $\mathrm{Tr}_{\mathrm{rad}}$ denoting the partial trace over the Hilbert space $\mathcal{H}_{\mathrm{rad}}$. We can split this operator in two parts

$$\hat{\varrho}(t) = \hat{\varrho}_e(t) + \hat{\varrho}_g(t)$$

with

$$\hat{\varrho}_e(t) = \langle 0|_{\mathrm{rad}} \, |\psi_{\mathrm{atomic}}(t)\rangle \langle \psi_{\mathrm{atomic}}(t)| \, |0\rangle_{\mathrm{rad}}$$

corresponding to atomic states with a single excitation and

$$\hat{\varrho}_g(t) = \mathrm{Tr}_{\mathrm{rad}} \left[|\psi_{\mathrm{photonic}}(t)\rangle \langle \psi_{\mathrm{photonic}}(t)| \right]$$

denoting the states with both atoms being in the ground state. We can obtain a suitable expression of $\hat{\varrho}_e(t)$ directly by solving $|\psi_{\mathrm{atomic}}(t)\rangle$. The evaluation of $\hat{\varrho}_g(t)$, however, is more complicated because we have to trace over all the possible states connected to a single photon in the radiation field. In order to do so, we make use of Eq. (4.2). We obtain

$$\begin{aligned} \hat{\varrho}_g(t) \;=\; & \frac{1}{\hbar^2} \sum_{\alpha_1,\alpha_2 \in \{1,2\}} \sum_{j_1,j_2 \in S_g} \sum_{i_1,i_2 \in S_e} \\ & \int_{t_0}^{t} \int_{t_0}^{t} dt_1 dt_2 \, \langle 0|_{\mathrm{rad}} \left(\mathbf{d}_{\alpha_2}^{j_2 i_2} \cdot \hat{\mathbf{E}}_{\perp}^{+}(\mathbf{R}_{\alpha_2}, t_2) \right) \left(\mathbf{d}_{\alpha_1}^{i_1 j_1} \cdot \hat{\mathbf{E}}_{\perp}^{-}(\mathbf{R}_{\alpha_1}, t_1) \right) |0\rangle \\ & |j_1\rangle_{\alpha_1} \langle i_1|_{\alpha_1} \, \langle 0|_{\mathrm{rad}} \, |\psi_{\mathrm{atomic}}(t_1)\rangle \langle \psi_{\mathrm{atomic}}(t_2)| \, |0\rangle_{\mathrm{rad}} \, |i_2\rangle_{\alpha_2} \langle j_2|_{\alpha_2} \end{aligned}$$

which can be evaluated by using the above expressions for the Green's function $\mathbf{G}_{\square}$ (see Eqs. (4.4) and (4.3)). In order to do this, we make use of the replacement

$$\begin{aligned} & \langle 0|_{\mathrm{rad}} \left(\mathbf{d}_{\alpha_2}^{j_2 i_2} \cdot \hat{\mathbf{E}}_{\perp}^{+}(\mathbf{R}_{\alpha_2}, t_2) \right) \left(\mathbf{d}_{\alpha_1}^{i_1 j_1} \cdot \hat{\mathbf{E}}_{\perp}^{-}(\mathbf{R}_{\alpha_1}, t_1) \right) |0\rangle_{\mathrm{rad}} \\ & \qquad \rightarrow \left[\mathbf{d}_{\alpha_2}^{j_2 i_2} \cdot \hat{\mathbf{E}}_{\perp}^{+}(\mathbf{R}_{\alpha_2}, t_2), \mathbf{d}_{\alpha_1}^{i_1 j_1} \cdot \hat{\mathbf{E}}_{\perp}^{-}(\mathbf{R}_{\alpha_1}, t_1) \right] , \end{aligned}$$

introduced in the previous chapter, and apply the relation in Eq. (3.15).

4.3 RESULTS

By applying the methods discussed in the preceding section, we can evaluate the time evolution during the time interval $t \in [0, 2\tau)$. It turns out that only four probability amplitudes of $|\psi_{\mathrm{atomic}}(t)\rangle$ are non vanishing:

$$\begin{aligned} & |6^2P_{1/2},\ F = 1\ m = 0\rangle_1 \otimes |6^2S_{1/2},\ F = 1\ m = 0\rangle_2 \otimes |0\rangle_{\mathrm{rad}} \\ & |6^2S_{1/2},\ F = 1\ m = -1\rangle_1 \otimes |6^2P_{1/2},\ F = 1\ m = 1\rangle_2 \otimes |0\rangle_{\mathrm{rad}} \\ & |6^2S_{1/2},\ F = 1\ m = 1\rangle_1 \otimes |6^2P_{1/2},\ F = 1\ m = -1\rangle_2 \otimes |0\rangle_{\mathrm{rad}} \\ & |6^2S_{1/2},\ F = 0\ m = 0\rangle_1 \otimes |6^2P_{1/2},\ F = 0\ m = 0\rangle_2 \otimes |0\rangle_{\mathrm{rad}} \end{aligned}$$

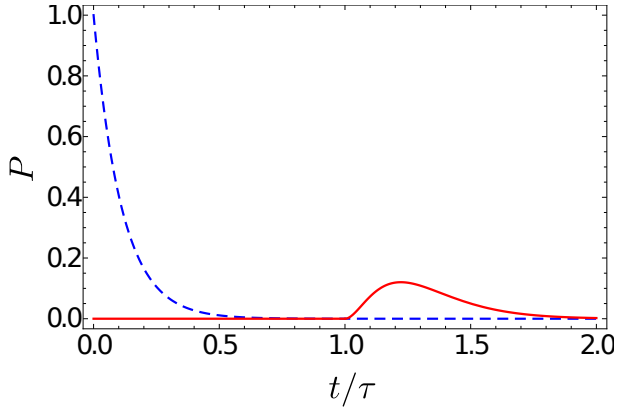

Figure 4.5.: Time evolution of the excitation probability P for ion 1 (dashed line) and for ion 2 (solid line): The interaction time t is plotted in units of the time τ which a photon needs to travel from the first ion to the second ion. We set the spontaneous decay rate $\Gamma\tau = 3$.

If the hyperfine splitting is large in comparison to the spontaneous decay rate Γ, as it is the case for $^{171}Yb^{+}$, we can neglect

$$|6^2S_{1/2},\ F=0\ m=0\rangle_1 \otimes |6^2P_{1/2},\ F=0\ m=0\rangle_2 \otimes |0\rangle_{\text{rad}}$$

safely in the time window of interest.

In Fig. 4.5, we plot the excitation probabilities of the two ions for vanishing Zeeman splitting. For the sake of simplicity, we have considered the limiting case that the parabolic mirrors cover the full solid angle around the ions. As discussed in Sec. 4.1, the process generates entangled matter qubits if one uses the states $|6^2P_{1/2},\ F=1\ m=1\rangle$ and $|6^2P_{1/2},\ F=1\ m=-1\rangle$ of the second ion as qubit states. However, these states are not stable, spontaneous decay transfers them to the ground states $|6^2S_{1/2},\ F=1\ m=1\rangle$ and $|6^2S_{1/2},\ F=1\ m=-1\rangle$ by emitting a single photon. By detecting whether or not both ions are in one of the states $|6^2S_{1/2},\ F=1\ m=\pm1\rangle$, we check if the entanglement generation was successful.

The post-selection is equivalent to a von Neumann measurement described by the projection operator

$$\hat{P} = |00\rangle\langle 00| + |01\rangle\langle 01| + |10\rangle\langle 10| + |11\rangle\langle 11|$$

where $|q_1q_2\rangle$ ($q_1, q_2 \in \{0,1\}$) correspond to the states of the logical qubit, i.e., $|6^2S_{1/2},\ F=1\ m=\pm1\rangle$. As we are interested in entanglement generation over large distances, we consider situations in which the life time of the excited states $\frac{1}{3\Gamma}$ ($\approx$ 8ns) is much shorter than the time τ the photon needs to travel from one atom to the other, i.e., $\Gamma\tau \gg 1$.

In the limiting case of parabolic mirrors covering the full solid angle around the ions and for $\Gamma(t-\tau) \to \infty$ with $\tau < t < 2\tau$, we obtain

$$\hat{P}\hat{\varrho}(t)\hat{P} = \frac{2}{27}(|01\rangle - |10\rangle)(\langle 01| - \langle 10|)$$

which corresponds to a maximally entangled state generated with a success probability $4/27 \approx 0.15$. Of course, in a real experiment, one has to take additional effects into account. As we see in the next section, it should be possible to achieve free-space communication over several kilometers.

4.4 EXPERIMENTAL FEASIBILITY

In this section, we investigate the experimental feasibility of our protocol. We consider a more realistic model of the parabolic mirrors, which takes their finite size (the mirrors do not cover the full solid angle) and their finite conductivity into account. We also discuss the implementation of our post-selection scheme and give estimates for the achievable repetition rate as well as the achievable rate for entanglement generation of our protocol.

4.4.1 *Realistic parabolic mirrors*

For obtaining a more realistic model of the mirrors, we focus on the mirrors described in [24]. The parabolic mirror described in [24] covers the solid angle

$$\Omega = \{(\varphi, \theta) \,:\, \varphi \in (0, 360^\circ), \theta \in (20^\circ, 135^\circ)\} \,,$$

around the ion whereby the angle 135° gives the front opening of the parabola and the angle 20° accounts for the hole on the backside for inserting the ion trap. This has to be taken into account in integrals over the solid angle as in Eqs. (4.3) and (4.4).

Furthermore, the mirrors are made out of aluminum which has a finite electrical conductivity. The properties of the material are well described by introducing a frequency dependent dielectric constant $\epsilon(\omega)$. In our case $\epsilon(\omega_{eg}) = -18.74 + i3.37$ [46]. Now, we have to split the field in a transverse electric (TE) and a transverse magnetic (TM) part and apply Fresnel equations to deal with the boundary conditions. However, these equations are different for the two basic polarizations and give angle-dependent phase shifts and reflectivities, which leads to a further reduction of the efficiency of entanglement generation. One might think that this effect could also reduce the fidelity of the entangled state but this is not the case. Such a reduction could occur if a $\sigma_+(\sigma_-)$ decay of the first ion could drive a $\sigma_-(\sigma_+)$ transition of the second ion but due to the symmetry of the setup this does not occur. This is evident from the following reasoning: After collimation by the parabolic mirror, the polarization vector of the electric field in the exit pupil of the parabolic mirror reads [47] $\boldsymbol{\sigma}_\pm \simeq (r^2-4)(\cos\phi \pm i\sin\phi)\cdot\mathbf{e}_r + (r^2+4)(\sin\phi \mp i\cos\phi)\cdot\mathbf{e}_\phi$ with r being the distance to the optical axis in units of the mirror's focal length, ϕ being the azimuthal angle, and $\mathbf{e}_r$ and $\mathbf{e}_\phi$ being the unit vectors in radial and azimuthal direction, respectively. Upon reflection on the parabolic surface, these vectors correspond to TM- and TE-components. The influence of the metallic mirror can be accounted for by additional complex pre-factors which depend on r only. It is straightforward to show that the overlap $\int \tilde{\boldsymbol{\sigma}}_\pm \cdot \boldsymbol{\sigma}^*_\mp$ of this modified field $\tilde{\boldsymbol{\sigma}}_\pm$ with the state of opposite helicity vanishes.

We can summarize all the above effects by introducing a factor η which has to be multiplied by the probability for a successful entanglement creation to take the more realistic model of the mirrors into account: $\eta = 1$ corresponds to perfectly conducting parabolic mirrors that cover the full solid angle. In the specific case treated here, we have $\eta \approx 0.47$.

Of course, we have to consider experimental imperfections, mainly connected with the free-space transmission of the one-photon wave packet. This gives rise to beam wandering and phase-front distortions due to atmospheric turbulences [25]. In both cases, the intensity at the focus is reduced [48–50] affecting the success probability. Once the distance between the two parabolic mirrors becomes large enough, beam

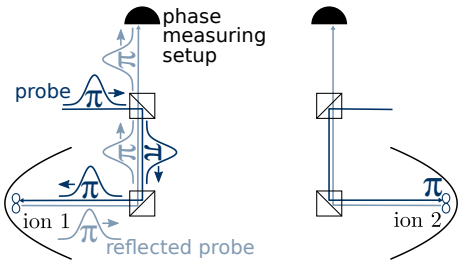

Figure 4.6.: Postselection: Successful entanglement generation is probed by the dispersive interaction of weak linearly polarized coherent states (π) with the ions. Only if an ion resides in one of the desired entangled states, a phase shift is imprinted onto the coherent state. Probe pulses are coupled into the parabolic mirrors by means of beam splitters. For simplicity, the coherent pulses used for dispersive state detection are indicated for only one of the two ions.

broadening plays a crucial role, which also results in a lower success probability. All these effects, however, diminish the success probability but seem to leave the fidelity rather untouched, which is of great importance for practical applications.

4.4.2 *Post-selection*

For implementing our scheme, the post-selection of the final state of the ions is a crucial ingredient. This post-selection can be realized by again using the high photon collection efficiency of the parabolic mirrors to our advantage by probing the qubit states directly by dispersive state detection. This can be implemented by coupling weak coherent-state pulses to the π transitions from $S_{1/2}, F = 1, m = \pm 1$ to $P_{1/2}, F = 1, m = \pm 1$ as depicted in Fig. 4.6. Population in the $S_{1/2}, m = \pm 1$ states is then detected by the phase shifts imprinted onto the coherent states. The detuning and pulse amplitudes can be chosen such that one is far from saturating the respective transitions. For example, choosing an on-resonance saturation parameter of $s_0 = 0.01$ and a detuning of two line widths, the excitation probability is about 10^{-5} while the phase of the coherent pulse is shifted by 25° according to the formalism of Ref. [51].

One has to balance the amplitude and the detuning of the incident coherent state carefully. Larger amplitudes and smaller detunings result in lower error probabilities for detecting the phase of the coherent state but also enforce a stronger excitation of the ion. The latter might lead to transferring the ion out of the $m = \pm 1$ state during state detection, hindering the phase shift of the coherent state and hence resulting in erroneous post-selection. Furthermore, the reflectivity of the beam splitters in front of the parabolic mirrors not only affects the success probability of our entangling scheme but also influences the error in measuring the phase of the coherent state.

We compute the corresponding error probabilities according to the Helstrom bound [52]. The a priori probabilities in this calculation are obtained from all relevant branching ratios, excitation probabilities, and reflectivities. The amplitude of the coherent state is chosen such that the probability to excite the ions with the probe pulse is 5×10^{-4}. We also choose this value as an upper bound for the acceptable error probability. This is motivated by the fact that post-selection schemes probing the $m = 0$ states are limited in fidelity to values ≤ 0.995 by the branching ratio of the $P_{1/2}$ state

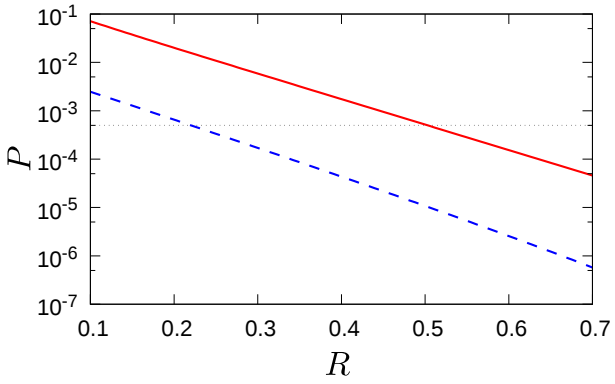

Figure 4.7.: Error probability P in determining the phase of a coherent pulse probing the π-transitions from $S_{1/2}$ to $P_{1/2}$ plotted over the beam splitter reflectivity R. Solid line: ion 1, dashed line: ion 2. In both cases, the relative detuning with respect to the resonance is two line widths corresponding to a phase shift of 0.14π. The length of the pulse is 10^4 upper-state lifetimes or 81μs, respectively. The amplitude of the coherent state incident onto the ion is chosen such that the probability to excite the respective upper state is 5×10^{-4}, as marked by the thin dotted line. The calculation for ion 2 accounts for the threshold reflectivity found for ion 1, which is marked by the crossing of the solid and the dotted line.

to the $D_{3/2}$ state of 0.5%. Keeping all errors in our post-selection scheme, an order of magnitude below this value is reasonable and desirable.

The minimum error probabilities as a function of the reflectivity of the beam splitters coupling the coherent states into the parabolic mirrors are plotted in Fig. 4.7. First, we determined the reflectivity for the beam splitter in front of ion 1 that ensures being below the error threshold for a set of suitable parameters yielding $R_1 = 0.5$. Next, this result was used in the calculations for ion 2 leading to $R_2 = 0.22$. From these reflectivity values, one would obtain a reduction of the success probability for entanglement generation by 61%.

In practice, the Helstrom bound will not be reached entirely with the obtainable error probability depending on the method employed for measuring the phase of the probe pulse. Nevertheless, the error threshold marked in Fig. 4.7 can be reached. This may be achieved at the cost of using beam splitters with larger reflectivities and thus accepting lower success probabilities.

To guarantee that the entangled state is not destroyed, we have to ensure that no information about the state of the qubit is extracted by our post-selection. The latter condition is satisfied if the magnetic field fixing the quantization axis is sufficiently small (i.e., the frequency shifts caused by the Zeeman effect are small compared to the spontaneous decay rate). In this case, the phase shift imprinted on an ion in the $m = -1$ Zeeman state is practically the same as for the other ion in the $m = +1$ state. Therefore, probing the qubit dispersively does not project the ions into one of these states and entanglement is preserved. The parameter set in Fig. 4.7 yields a fidelity of 0.998 when post selecting. Even higher fidelities can be reached by larger beam splitter reflectivities (accompanied by decreasing success probabilities), lower pulse amplitudes, or longer pulse lengths. A lower pulse amplitude has to be compensated

for by larger beam splitter reflectivities or longer pulse lengths. The latter in turn affects the repetition rate.

4.4.3 *Repetition rate*

We, finally, estimate the achievable repetition rate. Typically, an experimental cycle starts with Doppler cooling the ion, which takes about 200 μs for the ions treated here [53]. For the trap frequencies inherent to the parabolic mirror trap, 500 kHz in the radial direction and 1 MHz along the optical axis, the average number of motional quanta according to the Doppler limit is 20 and 10, respectively. This corresponds to widths of the ion wave function in position space of about 0.13 and 0.07 wavelengths. With these numbers, we estimate that the ions experience 78% of the focal intensity obtained by diffraction-limited focusing. Applying only Doppler cooling, the success probability of our scheme would be reduced accordingly. One could additionally apply resolved side-band cooling but the increase of the success rate is obviously accompanied by a lower repetition rate due to the elongated cooling procedure. Furthermore, as soon as there is a broadened focus due to incompletely compensated atmospheric aberrations etc., the above spread of the ion's wave function is negligible.

After cooling, both ions have to be prepared in the state $S_{1/2}, F = 0$ which takes less than 1 μs [54]. Additionally, ion 2 has to be flipped to the state $S_{1/2}, F = 1, m = 0$. This can be accomplished in 6 μs using microwaves [54] or in 100 ps applying Raman transitions [55]. Likewise, ion 1 is brought to the $P_{1/2}, F = 1, m = 0$ state by an optical π-pulse on a time scale smaller than a nanosecond. The post-selection requires around 80 μs, as it was outlined in Sec. 4.4.2. The photon traveling time from ion 1 to ion 2 is of the order of 10 μs for distances of a few kilometers. At least, the same time has to be spent in communicating the post-selection via a classical communication channel. Thus, the time spent for state preparation, attempting entanglement of the ions, and post-selection is on the order of 100 μs.

From the numbers given above, one would estimate a repetition rate of 3.3 kHz if Doppler cooling is applied after each entanglement attempt. One could increase the repetition rate if Doppler cooling is performed regularly after a certain number of entanglement trials. Since one entanglement trial takes about 100 μs, a repetition rate of more than 10 kHz is not feasible, unless one accepts a reduced fidelity and/or success probability. Assuming a realistic heating rate of 10 quanta per ms [56], the spread of the ion wave function would roughly double in the radial direction within 8 ms. Accepting the accompanying, continuously increasing loss of success probability, one could enhance the repetition rate towards 9.8 kHz, which is close to the inverse of the duration of one entanglement trial. Anyhow, in every experimental realization, the repetition rate is dictated by the specific requirements on fidelity, success probability, and inter-ion distance.

4.5 COMPARISON WITH OTHER SCHEMES

Our protocol has been designed to be compatible with a free-space communication channel. In this section, we compare our protocol to other multimode schemes which could be adapted to be compatible with a free-space communication channel. We focus in particular on the scheme implemented in [42] also using $^{171}Yb^{+}$ ions to encode the matter qubit. A similar scheme can also be applied using nitrogen-vacancy centers [43]

and has recently been used to demonstrate the first loophole-free Bell test [57]. In this scheme, the spontaneous decay process is used to generate two single photons each of them entangled with one of the matter qubits. The photons are directed to a 50/50 non-polarizing beam splitter and the output ports of the beam splitter are observed using single photon detectors. Heralded entanglement is generated by detecting the photons at different output ports, i.e., by not observing the Hong-Ou-Mandel effect. This, however, requires perfect mode matching of the incoming photons on the beam splitter. Deviations from the ideal scenario cause a loss of the fidelity of the entangled state. In [42], fibers were used as mode filters to enhance mode matching. The coupling of photons propagating in free-space to a fiber, however, is connected with severe photon losses.

In our scheme, the coupling of the photon wave packet to the second ion basically serves as a mode filter. Excitation of the second ion only takes place if the photon is in the correct modes. Thus, as discussed previously, experimental deviations cause a reduction of the success probability but leave the fidelity unaltered. This makes our scheme a well-suited candidate for free-space communication.

4.6 SUMMARY

In summary, a protocol for preparing maximally entangled states of two matter qubits with high fidelity has been proposed. This scheme has been designed to be compatible with a free-space communication channel, which is relevant, for example, for building a satellite-based quantum communication network. For circumventing limitations connected to such a free-space approach, the scheme relies on the usage of parabolic mirrors for enhancing the photon collection efficiency and, as such, also the success probability of the scheme. The matter qubits are encoded in the level structure of two distant $^{171}Yb^{+}$ ions located at the foci of the parabolic mirrors.

Due to this free-space approach, the theoretical description of the setup involves an extreme multimode scenario to model the radiation field. Semiclassical methods as well as the photon-path representation introduced in chapter 3 have been used to deal with the boundary conditions at the two parabolic mirrors, which leads to an intuitive representation of the quantum dynamics of the two ions and the radiation field.

To obtain a more realistic description, we have focused on the experimental details in Ref. [58] and on more realistic boundary conditions. Our results confirm the feasibility of the scheme to achieve reasonable success probabilities, which, in combination with a relatively high repetition rate, leads to a reasonable rate for preparing entangled matter qubits. Indeed, we expect an entanglement rate of 54 per second under diffraction-limited focusing.

One of the main issues is the fidelity of these states. The scheme is robust against imperfections arising in the experimental implementation. All these effects reduce the success probability of entanglement generation but leave the fidelity untouched.

5

COHERENT CONTROL OF ABSORPTION AND SPONTANEOUS EMISSION PROCESSES

Efficient matter-field coupling in free-space is crucial for quantum technological applications and has been subject of recent experimental [30, 59, 60] and theoretical [61] investigations. In the previous section, we have discussed the use of parabolic mirrors to enhance matter-field coupling of a single atom to a single photon in free-space. Thereby, we have used the parabolic mirrors as mode converters to generate inward-moving dipole waves which couple optimally to a single atom in dipole approximation. By absorbing such a wave packet, it is possible to generate entangled states between distant matter qubits. However, for achieving efficient matter-field coupling on the single-photon level, it is crucial to control the temporal envelope of the single-photon wave packet precisely. Deviations from the ideal wave packet form cause a severe reduction in the coupling efficiency, which has a direct impact on the success probability of elementary communication protocols.

To enhance the coupling efficiency, an interesting probabilistic method for generating and shaping a single-photon wave packet has been developed recently [62, 63]. The inherent probabilistic nature of the procedure stems from the usage of a photon source based on spontaneous four-wave mixing [64] and the shaping of the wave packet by using electro-optical amplitude modulation. The probabilistic nature of these processes results in a heralded single-photon source. However, for applications concerning readout and retrieval processes of quantum information, procedures capable of performing such tasks on demand in a deterministic way are favorable.

For fiber- and cavity-based architectures, a proposal to overcome the obstacles of probabilistic photon generation and probabilistic wave packet shaping has been developed by Cirac. et al. [28] and has been implemented experimentally by Ritter et al. [29]. In this experiment, a laser pulse controls the interaction of a single trapped atom with the radiation field inside a high finesse cavity. Exploiting the extreme cavity-induced mode selection of the high finesse cavity and the resulting vacuum Rabi oscillations governing the coherent spontaneous photon emission and absorption processes, a matter qubit can be converted efficiently on demand to a single photonic qubit prepared in a time-reversal symmetric wave packet state. Due to this symmetry of the wave packet, the quantum information stored in this single photon can be retrieved with high fidelity after transmission through an optical fiber and stored in another matter qubit.

However, this efficient readout and retrieval procedure is not suitable for free-space quantum communication protocols which do not involve any strong mode selection mechanism because in free-space the spontaneous photon emission process is of a considerably different nature. In view of these differences, the natural question arises whether it is possible to design an efficient readout and retrieval procedure suitable

for free-space quantum communication protocols. It turns out that this can indeed be done.

In this chapter, we present techniques to obtain enhanced control over emission and absorption processes of single quantum emitters in free space. By applying these techniques, it is possible to enhance matter-field coupling and to assemble more efficient protocols for achieving free-space quantum communication. We also show a potential application of these new techniques by presenting a new protocol for achieving quantum state transfer between two distant matter qubits connected by a free-space link. However, the techniques developed in this chapter are not limited to free-space links. They can also be applied to many architectures which do not necessarily rely on the mode selection by an optical resonator but on the direct coupling of a quantum emitter to a one-dimensional waveguide, such as nanowires, nanofibers, or coplanar waveguides (circuit QED).

This chapter is organized as follows. We start with analyzing the impact of the temporal envelope of a single-photon wave packet on the attempt to efficiently excite a single atom in free-space in Sec. 5.1 . In Sec. 5.2, we develop methods for controlling spontaneous emission and absorption processes in free-space based on stimulated Raman adiabatic passage (STIRAP). We apply these methods in Sec. 5.3 to achieve efficient transfer of an excitation from one atom to a second remote atom mediated by the radiation field. In Sec. 5.4, we present an alternative version of the STIRAP assisted schemes based on precisely controlled Rabi oscillations. Finally, in Sec. 5.5, we apply these schemes for assembling a protocol for achieving efficient high-fidelity quantum state transfer between distant matter qubits.

5.1 EFFICIENT SINGLE-PHOTON ABSORPTION IN FREE-SPACE

In this section, we analyze the absorption of a single photon by a single atom. We focus on the impact of the temporal envelope of the single-photon wave packet on this process. In the following, we consider a single two-level atom tightly trapped at position $\mathbf{R}$ in free-space. We model the interaction between the atom and the radiation field by using the dipole approximation and the RWA with $\mathbf{d}$ being the corresponding dipole matrix element and ω_{eg} being the transition frequency between the excited and the ground state. As initial state, we consider the single atom to be in the ground state $|g\rangle$ and the radiation field to be in a single photon state $|\psi_{\text{photonics}}(t_0)\rangle_{\text{rad}}$. By using the photon-path-representation developed in chapter 3, we obtain the following expression for the probability amplitude for exciting the atom

$$P_e(t) = \left| \int_{t_0}^{t} e^{-\Gamma/2(t-t')} E^{\text{in}}(t') dt' \right|^2 \tag{5.1}$$

with

$$E^{\text{in}}(t) = \frac{1}{\hbar} e^{i\omega_{eg}(t-t_0)} \langle 0|\mathbf{d} \cdot \hat{\mathbf{E}}_{\perp}^{+}(\mathbf{R}, t)\, |\psi_{\text{photonic}}(t_0)\rangle_{\text{rad}}$$

describing the temporal profile of the incoming single-photon wave packet. Thereby, $\hat{\mathbf{E}}_{\perp}^{+}(\mathbf{R}, t)$ denotes again the field operator in the interaction picture.

We assume that the modes of most importance are the ones with frequencies around ω_{eg}. By focusing on this frequency domain and applying Eq. (3.7), we can derive the following inequality

$$\Gamma \geq \int_{\mathbb{R}} \left| E^{\text{in}}(t) \right|^2 dt \, . \tag{5.2}$$

Equality is achieved by an inward-moving dipole wave which can couple perfectly to the dipole matrix element $\mathbf{d}$. By using parabolic mirrors, it is possible to approach this idealized situation. In the following, we intend to excite the atom at time $t = t_\mathrm{a}$ and assume that the incoming wave packet is prepared in the infinite past, i.e., $t_0 \to -\infty$. By introducing the scalar product

$$\langle f_1, f_2 \rangle_{L^2((-\infty,t_\mathrm{a}])} = \int_{-\infty}^{t_\mathrm{a}} f_1^*(t') f_2(t') dt'$$

on the Hilbert space $L^2((-\infty, t_\mathrm{a}])$, the probability for exciting the atom can be written as follows

$$P_e\left(t_a\right) = \left| \langle f_\Gamma, E^\mathrm{in} \rangle_{L^2((-\infty,t_\mathrm{a}])} \right|^2$$

with

$$f_\Gamma(t) = e^{-\Gamma/2(t_\mathrm{a}-t)} .$$

By using the Cauchy–Schwarz inequality, we obtain

$$P_e\left(t_a\right) \leq ||f_\Gamma||^2_{L^2((-\infty,t_\mathrm{a}])} \left|\left|E^\mathrm{in}\right|\right|^2_{L^2((-\infty,t_\mathrm{a}])} = \frac{1}{\Gamma} \left|\left|E^\mathrm{in}\right|\right|^2_{L^2((-\infty,t_\mathrm{a}])}$$

with $||\cdot||_{L^2((-\infty,t_\mathrm{a}])}$ denoting the norm induced by the scalar product $\langle \cdot, \cdot \rangle_{L^2((-\infty,t_1])}$. The inequality (5.2) implies

$$\left|\left|E^\mathrm{in}\right|\right|^2_{L^2((-\infty,t_\mathrm{a}])} \leq \int_{\mathbb{R}} \left|E^\mathrm{in}(t)\right|^2 dt \leq \Gamma .$$

According to the above expressions, unit probability for exciting the atom can only be achieved for

$$\left|\left|E^\mathrm{in}\right|\right|^2_{L^2((-\infty,t_\mathrm{a}])} = \Gamma . \tag{5.3}$$

Hence, we require an inward-moving dipole wave. This, however, is just a necessary but not a sufficient condition to achieve a high probability for absorbing the photon and exciting the atom. In order to achieve unit excitation probability, the temporal envelope of the wave packet has to fulfill the additional property

$$\left| \langle f_\Gamma, E^\mathrm{in} \rangle_{L^2((-\infty,t_\mathrm{a}])} \right| = ||f_\Gamma||_{L^2((-\infty,t_\mathrm{a}])} \left|\left|E^\mathrm{in}\right|\right|_{L^2((-\infty,t_\mathrm{a}])} . \tag{5.4}$$

Due to the properties of the scalar product and the conditions given by Eqs. (5.3) and (5.4), the incoming wave packet which can achieve a perfect excitation of the atom at time t_a is up to a global phase factor uniquely defined and given by

$$E^\mathrm{in}(t) = \Gamma e^{-\Gamma/2(t_\mathrm{a}-t)} \theta(t_\mathrm{a} - t) . \tag{5.5}$$

The above expression corresponds to the time reversed version of the wave packet generated by a spontaneously decaying atom in free-space. In fact, it is possible to derive the above result by using the time reversal symmetry of the theory [61]. The initial state of the photonic radiation field which corresponds to such a wave packet is given by

$$\begin{aligned} |\psi_\mathrm{photonic}(t_0)\rangle_\mathrm{rad} &= -\frac{1}{\hbar} \int_{-\infty}^{t_\mathrm{a}} e^{-\Gamma/2(t_\mathrm{a}-t)} e^{-i\omega_{eg}(t-t_0)} \mathbf{d}^* \cdot \hat{\mathbf{E}}_\perp^-(\mathbf{R}, t) \, |0\rangle_\mathrm{rad} \, dt \\ &= \sum_i \hat{a}_i^\dagger |0\rangle_\mathrm{rad} \sqrt{\frac{\omega_i}{2\epsilon_0 \hbar}} e^{i(t_0-t_a)\left(\omega_{eg}-\omega_i\right)} \frac{\mathbf{d}^* \cdot \mathbf{g}_i(\mathbf{R})}{\omega_i - \omega_{eg} - i\Gamma/2} . \end{aligned} \tag{5.6}$$

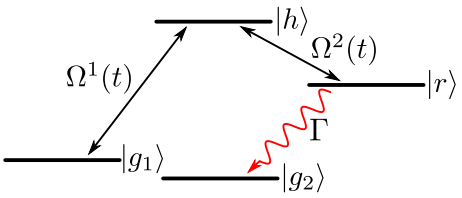

Figure 5.1.: Basic atomic level scheme: Levels $|g_1\rangle$ and $|g_2\rangle$ are radiatively stable energy eigenstates. The ancillary level $|h\rangle$ is required for efficient coherent population transfer between levels $|g_1\rangle$ and $|r\rangle$ by STIRAP. The dipole allowed optical transitions $|g_1\rangle \leftrightarrow |h\rangle$ and $|r\rangle \leftrightarrow |h\rangle$ are driven by the STIRAP lasers with Rabi frequencies $\Omega^1(t)$ and $\Omega^2(t)$.

Note that the perfect absorption of this wave packet requires an infinite amount of time (we set $t_0 = -\infty$) and for all finite time intervals the absorption probability is going to be below unity. However, as the interaction time $t_a - t_0$ increases, we approach unit absorption probability exponentially fast and we can achieve almost unit excitation probability as long as $\Gamma(t_a - t_0) \gg 1$.

5.2 STIRAP ASSISTED CONTROL OF SPONTANEOUS EMISSION AND ABSORPTION PROCESSES IN FREE-SPACE

In the previous section, we have seen that the perfect excitation of a single atom by a single photon in free-space can only be achieved by a wave packet with an exponentially rising temporal envelope. Unfortunately, it is a difficult task to generate such a single-photon wave packet.

To overcome this problem, we develop a method to coherently control the elementary emission and absorption processes of single atoms in free-space. Thereby, it is possible to tailor the shape of single-photon wave packets by controlling the spontaneous decay process of a single excited atom. In a similar way, it is also feasible to manipulate the absorption process of a single atom such that other wave packets than the ones with exponentially rising temporal envelope can be absorbed almost perfectly.

For controlling the emission and absorption processes, a slightly more complicated level structure is needed. A suitable atomic level structure is depicted in Fig. 5.1. The states $|g_1\rangle$ and $|g_2\rangle$ are radiatively stable or metastable ground states. The state $|h\rangle$ is an ancillary level which is employed during an adiabatic process. By applying two (classical) laser pulses characterized by the time-dependent Rabi frequencies $\Omega^1(t)$ and $\Omega^2(t)$, we can coherently transfer the population from state $|g_1\rangle$ to state $|r\rangle$ via STIRAP. Thereby, we obtain enhanced control over the spontaneous emission and absorption processes. During this STIRAP process, the population of state $|h\rangle$ is negligible. The overall system can be described by the Hamilton operator

$$\hat{H} = \hat{H}_{\text{atom}} + \hat{H}_{\text{field}} + \hat{H}_{\text{i}} \tag{5.7}$$

with the Hamiltonian of the free radiation field

$$\hat{H}_{\text{field}} = \hbar \sum_i \omega_i a_i^\dagger a_i$$

and the Hamiltonian of the free atom

$$\hat{H}_{\text{atom}} = \hbar\omega_{g_1}|g_1\rangle\langle g_1| + \hbar\omega_{g_2}|g_2\rangle\langle g_2| + \hbar\omega_h|h\rangle\langle h| + \hbar\omega_r|r\rangle\langle r| \; .$$

By describing the laser fields classically, the interaction between the atom and the radiation field is characterized by the Hamiltonian

$$\begin{aligned}\hat{H}_{\mathrm{i}} &= -\left(\hat{\mathbf{E}}_{\perp}^{-}(\mathbf{R})\cdot\mathbf{d}^{*}|g_2\rangle\langle r| + \mathrm{H.c.}\right)\\ &\quad -\frac{\hbar}{2}\left(e^{i(\omega_h-\omega_{g_1}+\Delta_1)(t-t_0)}\Omega^1(t)|g_1\rangle\langle h| + \mathrm{H.c.}\right)\\ &\quad -\frac{\hbar}{2}\left(e^{i(\omega_h-\omega_r+\Delta_2)(t-t_0)}\Omega^2(t)|r\rangle\langle h| + \mathrm{H.c.}\right). \end{aligned} \tag{5.8}$$

We have neglected the coupling of the quantized radiation field to the atomic transitions $|h\rangle \leftrightarrow |g_1\rangle$, $|h\rangle \leftrightarrow |r\rangle$, which would cause a spontaneous decay of the excited state $|h\rangle$, because we assume that the population of the state $|h\rangle$ is negligible. In the following, we again focus on initial states which just correspond to a single excitation in the system. So, either one photon is in the field and the atom is in state $|g_2\rangle$ or the field is in the vacuum state and the atom is in one of the states $|g_1\rangle$, $|h\rangle$, and $|r\rangle$. For these initial states, the time-dependent Schrödinger equation can be solved by the ansatz

$$|\psi(t)\rangle = |\psi_{\mathrm{part}}(t)\rangle\,|0\rangle_{\mathrm{rad}} + |g_2\rangle\,|\psi_{\mathrm{photonic}}(t)\rangle_{\mathrm{rad}} \tag{5.9}$$

with $|\psi_{\mathrm{part}}(t)\rangle$ constituting a linear superposition of the atomic states $|g_1\rangle$, $|h\rangle$, and $|r\rangle$ and

$$|\psi_{\mathrm{photonic}}(t)\rangle_{\mathrm{rad}} = \sum_i f_i(t)\hat{a}_i^{\dagger}\,|0\rangle_{\mathrm{rad}}$$

being the wave function describing the single-photon wave packet. Similar to the procedure used in chapter 3, the one-photon probability amplitudes $f_i(t)$ can be eliminated from the Schrödinger equation. Thus, in the interaction picture, we obtain the following effective inhomogeneous Schrödinger equation for the atomic state. In case of free-space, we get

$$\begin{aligned} i\frac{d}{dt}\,|\widetilde{\psi}_{\mathrm{part}}(t)\rangle &= \frac{1}{\hbar}\hat{H}_{\mathrm{part}}\,|\widetilde{\psi}_{\mathrm{part}}(t)\rangle - |r\rangle E^{\mathrm{in}}(\mathbf{R},t),\\ \frac{1}{\hbar}\hat{H}_{\mathrm{part}} &= -i\frac{\Gamma}{2}|r\rangle\langle r|\\ &\quad -\left(e^{i\Delta_1(t-t_0)}\frac{\Omega^1(t)}{2}|g_1\rangle\langle h| + e^{i\Delta_2(t-t_0)}\frac{\Omega^2(t)}{2}|r\rangle\langle h| + \mathrm{H.c.}\right). \end{aligned} \tag{5.10}$$

The inhomogeneous term

$$E^{\mathrm{in}}(\mathbf{x},t) = e^{i\omega_{eg}(t-t_0)}\frac{1}{\hbar}\,\langle 0|\,\mathbf{d}\cdot\hat{\mathbf{E}}_{\perp}^{+}(\mathbf{x})e^{-\frac{i}{\hbar}\hat{H}_{\mathrm{field}}(t-t_0)}\,|\psi_{\mathrm{photonic}}(t_0)\rangle$$

describes the coherent driving of the atomic state $|r\rangle$ by a freely evolving incoming single-photon wave packet with $\omega_{eg} = \omega_r - \omega_{g_2}$ being the transition frequency of the optical transition $|g_2\rangle \leftrightarrow |r\rangle$. Similar to the method used in [37], the anti-hermitian part of the Hamiltonian $\hat{H}_{\mathrm{part}}$ takes the spontaneous decay of the atomic state $|r\rangle$ into account.

A convenient description of the dynamics is obtained by adiabatically eliminating the state $|h\rangle$ from the Schrödinger equation (5.10). For this purpose, let us assume that $\Delta_1 = \Delta_2$ and that the Rabi frequencies are of the form $\Omega^1(t) = \Omega\sin(\theta(t))$ and $\Omega^2(t) = \Omega\cos(\theta(t))$ with $\Omega > 0$. Furthermore, we assume that the laser fields are sufficiently intense and that the change of their amplitudes is sufficiently slow, i.e., $|\dot{\theta}(t)|, \Gamma \ll \Omega$. Under these conditions the adiabatic approximation applies [65] and the atomic state $|\psi_{\mathrm{part}}(t)\rangle$ follows the dark-state $|D(t)\rangle = \cos(\theta(t))\,|g_1\rangle - \sin(\theta(t))\,|r\rangle$, i.e.,

$$|\widetilde{\psi}_{\mathrm{part}}(t)\rangle = c(t)\,|D(t)\rangle\ .$$

By properly tuning the Rabi frequencies $\Omega_1(t)$ and $\Omega_2(t)$, we can transfer the population from $|g_1\rangle$ to $|r\rangle$ or reverse coherently, a technique known as STIRAP [66]. The adiabatic approximation leads to the following equation

$$\frac{d}{dt}c(t) = -\frac{1}{2}\Gamma(t)c(t) - i\sin(\theta(t))E^{\text{in}}(\mathbf{R},t) \tag{5.11}$$

describing the time evolution of the system with

$$\Gamma(t) = \Gamma\sin^2\left[\theta(t)\right]$$

being the time-dependent spontaneous decay rate of the dark-state $|D(t)\rangle$. The time dependence of the spontaneous decay rate of the dark-state is a direct consequence of the time dependence of the overlap of the dark-state with the excited level $|r\rangle$. According to chapter 3, the time evolution of the single-photon wave packet is given by

$$\begin{aligned}|\psi_{\text{photonic}}(t)\rangle &= e^{-\frac{i}{\hbar}\hat{H}_{\text{rad}}(t-t_0)}\,|\psi_{\text{photonic}}(t_0)\rangle \\ &\quad -\frac{i}{\hbar}\int_{t_0}^{t} e^{-\frac{i}{\hbar}\hat{H}_{\text{rad}}(t-t_1)}\mathbf{d}^*\cdot\hat{\mathbf{E}}_{\perp}^{-}(\mathbf{R})\,|0\rangle_{\text{rad}}\sin(\theta(t_1))c(t_1)e^{-i\omega_{eg}(t_1-t_0)}dt_1\,.\end{aligned} \tag{5.12}$$

By controlling the STIRAP pulses, we are able to control the time dependence of the spontaneous emission process and the time dependence of the absorption process, as described by Eq. (5.11).

5.2.1 *Tailoring single-photon wave packets*

This additional control over the spontaneous emission process allows us to tailor the temporal envelope of the single-photon wave packets generated by the spontaneous decay process of the atom. For tailoring such a wave packet, we consider an atom initially prepared in state $|g_1\rangle$ and the radiation field being in the vacuum state. In order to fulfill the requirements of the adiabatic approximation, we assume that initially $\Omega^1(t_0) \ll \Omega^2(t_0)$.

In this case, the last term in Eq. (5.11) does not contribute. Thus, the solution of Eq. (5.11) with the initial condition $c(t_0) = 1$ is given by

$$c(t) = e^{-\frac{\Gamma}{2}\int_{t_0}^{t}\sin^2(\theta(t'))dt'}\,. \tag{5.13}$$

According to Eq. (5.12), the temporal envelope of the emerging single-photon wave packet is determined by the atomic amplitude $\langle r|\widetilde{\psi}_{\text{part}}(t)\rangle = -c(t)\sin(\theta(t))$. Thus, by controlling $\langle r|\widetilde{\psi}_{\text{part}}(t)\rangle$, we can tailor the temporal envelope of the generated wave packet.

By exploiting the relation in Eq. (5.13), we obtain

$$\sin(\theta(t)) = -\frac{\langle r|\widetilde{\psi}_{\text{part}}(t)\rangle}{\sqrt{1-\Gamma\int\limits_{t_0}^{t}\left|\langle r|\widetilde{\psi}_{\text{part}}(t')\rangle\right|^2 dt'}}\,. \tag{5.14}$$

Thereby, $\langle r|\widetilde{\psi}_{\text{part}}(t)\rangle$ has to be chosen in such a way that $|\sin(\theta(t))| \leq 1$. By using Eq. (5.14), we can determine the STIRAP pulses $\Omega^2(t) = \Omega\sin(\theta(t))$ and $\Omega^2(t) = \Omega\cos(\theta(t))$ needed to tailor the wave packet. By doing so, we are able to control the

shape of the wave packet to a large extend. The only limitation is connected to the fact that the excitation of the atom cannot be depopulate faster than with the spontaneous decay rate Γ (due to the absence of additional photons which could cause stimulated emission).

5.2.2 *Almost perfect absorption of single-photon wave packets*

Let us focus on the dynamics of an atom initially prepared in the state $|g_2\rangle$ and trapped at the point $\mathbf{R}$ interacting with a single photon in the radiation field. Hence, the initial state of the system is given by

$$|\psi(t_0)\rangle = |g_2\rangle \, |\psi_{\text{photonic}}(t_0)\rangle_{\text{rad}} \ .$$

Again, we apply the adiabatic approximation and assume that the second atom follows the dark-state $|D(t)\rangle$, which leads to the following expression for the time evolution of the wave function

$$|\psi(t)\rangle = |g_2\rangle \, |\psi_{\text{photonic}}(t)\rangle_{\text{rad}} + c(t) \, |D(t)\rangle \, |0\rangle_{\text{rad}} \ .$$

By integrating Eq. (5.11) for the initial condition $c(t_0) = 0$, we obtain

$$c(t) = -i \int_{t_0}^{t} e^{-\frac{1}{2}\int_{t_1}^{t} \Gamma(t_2) dt_2} \sin(\theta(t_1)) E^{\text{in}}(\mathbf{R}, t_1) dt_1 \ .$$

The above expression resembles Eq. (5.1) derived in Sec. 5.1 describing the absorption process in free-space in the absence of additional laser fields but now with a time-dependent spontaneous decay rate $\Gamma(t)$. Following the discussion in Sec. 5.1, we can analyze again the absorption process in more detail.

In the following, we intend to excite the atom at time $t = t_{\text{a}}$ and assume that the incoming wave packet is prepared in the infinite past, i.e., $t_0 \to \infty$. Excitation, thereby, means that we transfer the population of the atom from state $|g_2\rangle$ to the dark-state $|D(t)\rangle$. By using the scalar product on the Hilbert space $L^2((t_0, t_{\text{a}}])$, we can write the corresponding excitation probability as

$$P_e\,(t_a) = \left| \langle f_1, E^{\text{in}} \rangle_{L^2((t_0, t_{\text{a}}])} \right|^2$$

with

$$f_1(t) = e^{-\frac{1}{2}\int_{t}^{t_{\text{a}}} \Gamma(t_2) dt_2} \sin(\theta(t))$$

whereby

$$||f_1||^2_{L^2((t_0, t_{\text{a}}])} = \frac{1}{\Gamma} \left[1 - e^{-\int_{t_0}^{t_a} \Gamma(t_2) dt_2} \right] \leq \frac{1}{\Gamma} \ . \tag{5.15}$$

Due to the fact that $\left|\left|E^{\text{in}}\right|\right|^2_{L^2((-\infty, t_{\text{a}}])} \leq \Gamma$, we can only approach unit excitation probability for

$$E^{\text{in}}(t) = \Gamma f_1(t) \tag{5.16}$$

and

$$\int_{t_0}^{t_a} \Gamma(t_2) dt_2 \to \infty \tag{5.17}$$

which implies

$$\left|\left|E^{\text{in}}\right|\right|^2_{L^2((-\infty, t_{\text{a}}])} \to \Gamma \ . \tag{5.18}$$

Hence, we again require an almost perfect coupling of the incoming single-photon wave packet to the second atom and an infinite interaction time $t_a - t_0$ to achieve perfect single-photon absorption. However, we approach unit excitation probability exponentially fast. Hence, it is possible to achieve almost unit excitation probability for finite values of $\int_{t_0}^{t_a} \Gamma(t_2) dt_2$. This time, however, we can use the additional control to adapt the absorption process to the shape of the incoming wave packet. Thereby, we can achieve almost unit excitation probability not only for single-photon wave packets with an exponentially rising temporal envelope.

5.3 EFFICIENT EXCITATION TRANSFER FROM ONE ATOM TO ANOTHER

The schemes for tailoring single-photon wave packets by controlling the spontaneous decay process and for controlling the absorption process of single atoms in free-space introduced in the previous section can be combined to achieve almost perfect excitation transfer from one atom to another remote atom.

For achieving such an almost perfect excitation transfer, we again make use of the setup consisting out of two parabolic mirrors an two atoms trapped close to their focal points introduced in chapter 4 and depicted in Fig. 4.1. In the following, we assume that the first atom at focal point $\mathbf{R}_1$ is used to generate a suitable wave packet that is absorbed by the second atom at focal point $\mathbf{R}_2$ later on almost perfectly. Furthermore, we assume that the first atom is initially prepared in state $|g_1\rangle_1$, that the second atom is prepared in state $|g_2\rangle_2$, and that the field is initially prepared in the vacuum state $|0\rangle_{\text{rad}}$. Thus, the initial state of the overall system is given by

$$|\psi(t_0)\rangle = |g_1\rangle_1 |g_2\rangle_2 |0\rangle_{\text{rad}} \ .$$

As discussed above, we control the dynamics of the atoms by applying two additional laser fields per atom with their induced Rabi frequencies

$$\begin{aligned} \Omega_i^1(t) &= \Omega \sin(\theta_i(t)) \\ \Omega_i^2(t) &= \Omega \cos(\theta_i(t)) \end{aligned}$$

and induced mixing angles θ_i for atom $i \in \{1,2\}$. According to Eq. (5.12), the single photon wave packet generated by the first atom is described by

$$|\psi_{\text{photonic}}(t)\rangle_{\text{rad}} = \frac{i}{\hbar} \int_{t_0}^{t} e^{-\frac{i}{\hbar}\hat{H}_{\text{rad}}(t-t_1)} \mathbf{d}_1^* \cdot \hat{\mathbf{E}}_\perp^-(\mathbf{R}_1) \, |0\rangle^P \, \langle r|\widetilde{\psi}_{\text{part}}(t_1)\rangle_1 e^{-i\omega_{eg}(t_1-t_0)} dt_1$$

with $\mathbf{d}_i$ denoting the dipole matrix element of atom i. This results in the following expression describing the incoming radiation field coupling to the second atom

$$\begin{gathered} E^{\text{in}}(\mathbf{R}_2, t) = \\ \tfrac{1}{\hbar} \langle 0| \, \mathbf{d}_2 \cdot \hat{\mathbf{E}}_\perp^+(\mathbf{R}_2) e^{-\frac{i}{\hbar}\hat{H}_{\text{field}}(t-t_0)} \, |\psi_{\text{photonic}}(t_0)\rangle \, e^{i\omega_{eg}(t-t_0)} \\ = -\tfrac{i}{\hbar^2} \int_{t_0}^{t} \langle 0|_{\text{rad}} \left(\mathbf{d}_2 \cdot \hat{\mathbf{E}}_\perp^+(\mathbf{R}_2)\right) e^{-i\left[\frac{1}{\hbar}\hat{H}_{\text{rad}} - \omega_{eg}\right](t-t_1)} \left(\mathbf{d}_1^* \cdot \hat{\mathbf{E}}_\perp^-(\mathbf{R}_1)\right) |0\rangle_{\text{rad}} \, \langle r|\widetilde{\psi}_{\text{part}}(t_1)\rangle_1 dt_1 \end{gathered}$$

The above expression can be simplified by using the dyadic Green's function of the d'Alamber operator (see chapter 3). We obtain

$$E^{\text{in}}(\mathbf{R}_2, t) = -\frac{1}{\epsilon_0 \hbar} \int_{t_0}^{t} \mathbf{d}_2 \cdot \nabla \times \nabla \times \mathbf{G}_\Box(\mathbf{R}_2, \mathbf{R}_1, t - t_1) \cdot \mathbf{d}_1^* \langle r|\widetilde{\psi}_{\text{part}}(t_1)\rangle_1 e^{i\omega_{eg}(t-t_1)} dt_1 \ .$$

By using the semiclassical expressions for $\nabla \times \nabla \times \mathbf{G}_{\Box}(\mathbf{R}_2, \mathbf{R}_1, t - t_1)$ derived in the previous chapter (see Eq. (4.3)), we obtain

$$\frac{1}{\epsilon_0 \hbar} \mathbf{d}_2 \cdot \nabla \times \nabla \times \mathbf{G}_{\Box}(\mathbf{R}_2, \mathbf{R}_1, t) \cdot \mathbf{d}_1^* = \alpha \Gamma \delta(t - \tau)$$

for $t < 2\tau$ with α being a suitable constant. It is possible to achieve

$$|\alpha| \to 1$$

which corresponds to a perfect coupling of the second atom to the photon wave packet generated by the first atom. In practice, however, as already discussed in chapter 3, the value $|\alpha|$ is limited by the reflectivity of the mirrors, the attenuation of the photon during transmission from mirror 1 and mirror 2, and the fact that the parabolic mirrors do not cover the full solid angle around the atoms. By applying the semiclassical expression above, we obtain

$$E^{\text{in}}(\mathbf{R}_2, t) = -\alpha \Gamma \langle r | \widetilde{\psi}_{\text{part}}(t - \tau) \rangle_1 e^{i\omega_{eg}\tau} \, .$$

According to our previous analysis in Subsec. 5.2.2, optimal absorption at time t_a is achieved only if

$$\alpha \langle r | \widetilde{\psi}_{\text{part}}(t - \tau) \rangle_1 = f_1(t) \text{ up to a global phase factor}$$

with

$$f_1(t) = e^{-\frac{1}{2}\Gamma \int_t^{t_a} \sin^2(\theta_2(t'))dt'} \sin(\theta_2(t)) \, .$$

This requirement is satisfied by many possible choices for the STIRAP pulses. A particular simple solution is to tailor a time symmetric single-photon wave packet by applying suitable STIRAP pulses to the first atom and to apply a time reversed and by τ delayed pulse configuration to the second atom, i.e.,

$$\theta_1(t - \tau) = \theta_2(-t) \, .$$

Thereby, an almost perfect transfer of the excitation from atom one to atom two is performed. This is possible due to time reversal symmetry of the system.

In the following, we analyze the transfer of the excitation in more detail by going beyond the adiabatic approximation. We focus on the generation of time symmetric single-photon wave packets with a Gaussian temporal envelope (other choices are also possible).

For generating such a single-photon wave packet, the probability amplitude of finding the first atom in an excited state also has to be of a Gaussian form

$$\langle r | \widetilde{\psi}_{\text{part}}(t) \rangle \quad = \quad \left(\frac{2}{\pi \Gamma^2 \sigma^2} \right)^{1/4} e^{-(t_{\max} - t)^2 / \sigma^2} \tag{5.19}$$

with $\sigma\Gamma$ and $(t_{\max} - t_0)/\sigma$ being sufficiently large. The corresponding shapes of the STIRAP pulses $\Omega_1^1(t) = \Omega \sin(\theta_1(t))$ and $\Omega_1^2(t) = \Omega \cos(\theta_1(t))$ generating a time-symmetric single-photon wave packet are determined by Eq. (5.14). These pulses for the wave packet generation (applied to the first atom) and the wave packet absorption (applied to the second atom) are depicted in Fig. 5.2 (a) and (b) for the parameters $\sigma\Gamma = 10$ and $\Gamma(t_{\max} - t_0) = 25$.

To validate the results obtained by applying the adiabatic approximation, we have solved Eq. (5.10) numerically. For this purpose, we consider the idealized situation of a

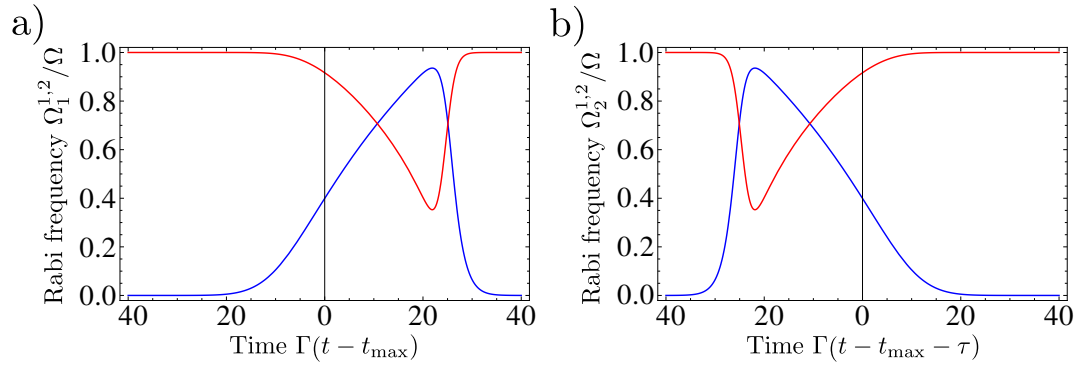

Figure 5.2.: STIRAP pulses for generating the wave packet by the first atom (a) and its subsequent absorption by the second atom (b). The corresponding Rabi frequencies Ω_i^1 (blue) and Ω_i^2 (red) are plotted over time. The parameters are $\sigma\Gamma = 10$, $\Gamma(t_{\max} - t_0) = 25$.

perfect coupling of the second atom to the photon wave packet, i.e., $|\alpha|^2 = 1$. However, the factor $|\alpha|^2$ enters just as a scaling factor. The corresponding probability of finding the first atom in state $|r\rangle$ during the generation of a time-symmetric single-photon wave packet is depicted in Fig. 5.3. These numerical results demonstrate that the proposed STIRAP-assisted photon emission and absorption scheme enables the engineering of a time-symmetric single-photon wave packet, provided the Rabi frequencies involved in the STIRAP process are sufficiently high.

The success probability of absorbing a time-symmetric single-photon wave packet and of transferring the population from the initial state $|g_2\rangle$ to state $|g_1\rangle$ is depicted in Fig. 5.4. With an increasing Rabi frequency Ω, this probability quickly approaches unity. This demonstrates that the proposed STIRAP-assisted scheme leads to almost perfect absorption of a time-symmetric single-photon wave packet if the Rabi frequencies Ω involved in the STIRAP process are large in comparison with the spontaneous decay rate Γ. Furthermore, numerical calculations confirm that the maximal probability of finding the atoms in state $|h\rangle$ scales with Ω^{-2}. For $\Omega = 10\Gamma$ and the parameters chosen in Fig. 5.3 and Fig. 5.4, for example, its values are smaller than 10^{-3}. This is valid for STIRAP-assisted photon emission as well as absorption. Thus, the assumption of a negligible population of the ancillary atomic level $|h\rangle$ can be satisfied easily for sufficiently high Rabi frequencies and it is possible to enhance matter-field coupling and to overcome limitations connected to the temporal profile of the single-photon wave packets.

5.4 AN ALTERNATIVE CONTROL SCHEME

In the previous sections, we discussed the use of STIRAP for obtaining enhanced control over spontaneous emission and absorption processes. In fact, this is not the only possible way to achieve that. We could also obtain enhanced control by applying just one additional laser in a simple tripod structure like the one depicted in Fig. 5.5.

In the following, we assume that the excited level $|r\rangle$ decays dominantly to the ground state $|g_2\rangle$. Thus, Rabi oscillations characterized by the time-dependent Rabi frequency $\Omega(t)$ are either driven using a dipole forbidden transition or a Raman transition.

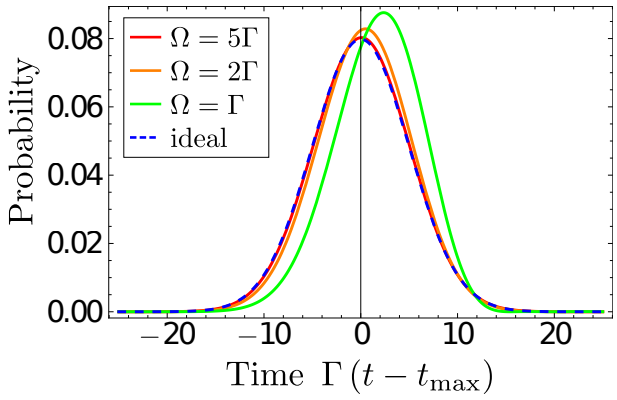

Figure 5.3.: Time dependence of the probability of detecting an atom in state $|r\rangle$ during the generation of a time-symmetric single-photon wave packet for several Rabi frequencies Ω: The time t is plotted in units of the mean spontaneous decay time $1/\Gamma$. The parameters are $\sigma\Gamma = 10$, $\Gamma(t_{\max} - t_0) = 25$, $\Delta_1 = \Delta_2 = 0$ and $|\alpha|^2 = 1$. The result of the adiabatic approximation is denoted by 'ideal'.

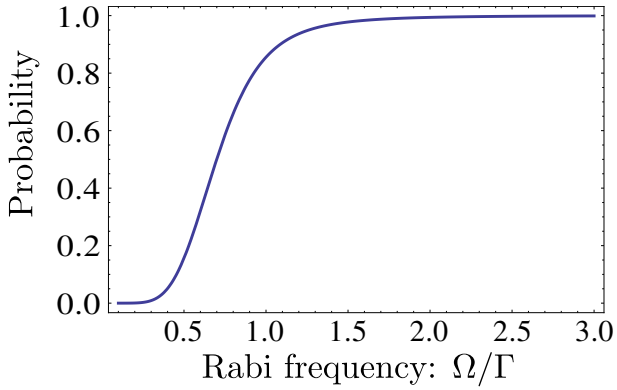

Figure 5.4.: Success probability of absorbing a time-symmetric single-photon wave packet and its dependence on the Rabi frequency Ω (in units of Γ): The parameters are $\sigma\Gamma = 10$, $\Gamma(t_{\max} - t_0) = 25$, $\Delta_1 = \Delta_2 = 0$ and $|\alpha|^2 = 1$.

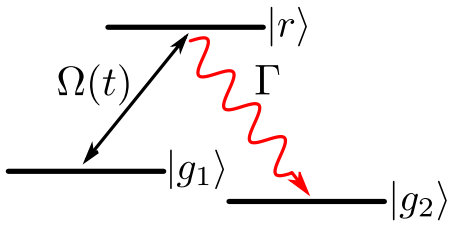

Figure 5.5.: Basic atomic level scheme: Levels $|g_1\rangle$ and $|g_2\rangle$ are radiatively stable energy eigenstates. The optical transition $|g_1\rangle \leftrightarrow |r\rangle$ is driven by a laser with Rabi frequencies $\Omega(t)$. The excited level $|r\rangle$ dominantly decays to the ground state $|g_2\rangle$.

By focusing again on initial states with a single excitation in the system, we can solve the time-dependent Schrödinger equation by the same ansatz (see Eq. (5.9)) used in the previous section but this time $|\psi_{\text{part}}(t)\rangle$ constituting a linear superposition only of the atomic states $|g_1\rangle$ and $|r\rangle$. By eliminating the degrees of freedom connected to $|\psi_{\text{photonic}}(t)\rangle_{\text{rad}}$, we can derive the following equation describing the time evolution of $|\psi_{\text{part}}(t)\rangle$ in the interaction picture

$$i\frac{d}{dt}\,|\widetilde{\psi}_{\text{part}}(t)\rangle = \frac{1}{\hbar}\hat{H}_{\text{part}}\,|\widetilde{\psi}_{\text{part}}(t)\rangle - |r\rangle E^{\text{in}}(\mathbf{R},t)$$

with

$$\frac{1}{\hbar}\hat{H}_{\text{part}} = -i\frac{\Gamma}{2}|r\rangle\langle r| + i\left(\frac{\Omega(t)}{2}|r\rangle\langle g_1| - \text{H.c.}\right)$$

and $E^{\text{in}}(\mathbf{R},t)$ describing the incoming single-photon wave packet. Due to the simple structure of the above equations, they can be solved analytically. For tailoring a single photon wave packet, we again assume that the atom is initially prepared in the state $|g_1\rangle$ and that the field is in the vacuum state, i.e.,

$$\begin{aligned} |\widetilde{\psi}_{\text{part}}(t_0)\rangle &= |g_1\rangle \\ |\psi_{\text{photonic}}(t_0)\rangle_{\text{rad}} &= 0\,. \end{aligned}$$

As in the previous sections, we control the shape of the wave packet by controlling the overlap $\langle r|\widetilde{\psi}_{\text{part}}(t)\rangle$. The corresponding probability amplitude fulfills the following differential equation

$$\frac{d}{dt}\langle r|\widetilde{\psi}_{\text{part}}(t)\rangle = -\frac{\Gamma}{2}\langle r|\widetilde{\psi}_{\text{part}}(t)\rangle + \frac{\Omega(t)}{2}\langle g_1|\widetilde{\psi}_{\text{part}}(t)\rangle\,.$$

For the sake of simplicity, we assume that the probability amplitude $\langle r|\widetilde{\psi}_{\text{part}}(t)\rangle$ is real valued. In this case, we can restrict to purely real valued Rabi frequencies $\Omega(t)$. If we drive at most half a Rabi cycle, we obtain

$$\langle g_1|\widetilde{\psi}_{\text{part}}(t)\rangle = \sqrt{1 - \left|\langle r|\widetilde{\psi}_{\text{part}}(t)\rangle\right|^2 - \Gamma\int_{t_0}^{t}\left|\langle r|\widetilde{\psi}_{\text{part}}(t')\rangle\right|^2 dt'}$$

and thus

$$\Omega(t) = 2\frac{\frac{d}{dt}\langle r|\widetilde{\psi}_{\text{part}}(t)\rangle + \frac{\Gamma}{2}\langle r|\widetilde{\psi}_{\text{part}}(t)\rangle}{\sqrt{1 - \left|\langle r|\widetilde{\psi}_{\text{part}}(t)\rangle\right|^2 - \Gamma\int_{t_0}^{t}\left|\langle r|\widetilde{\psi}_{\text{part}}(t')\rangle\right|^2 dt'}}\,. \tag{5.20}$$

By using Eq. (5.20), we can determine the optimal shape of our laser pulse. For generating a single-photon wave packet with a Gaussian envelope (see Eq. 5.19) with the parameters $\sigma\Gamma = 10$, $\Gamma(t_{\text{max}} - t_0) = 25$, we need a pulse of the form depicted in Fig.5.6.

Due to time reversal symmetry, similar considerations also hold true for the photon absorption process and ideal photon absorption can be achieved. Thus, we have two schemes at our disposal for controlling the absorption and emission processes of single quantum emitters in free-space.

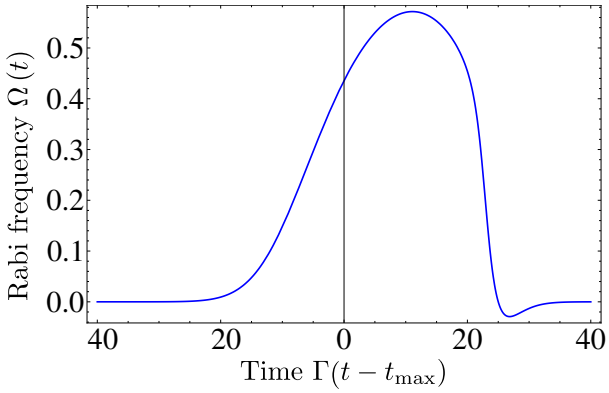

Figure 5.6.: Laser pulse for the generation of a wave packet with a Gaussian envelope. The corresponding Rabi frequency $\Omega(t)$ is plotted over time. The parameters are $\sigma\Gamma = 10$, $\Gamma(t_{\max} - t_0) = 25$.

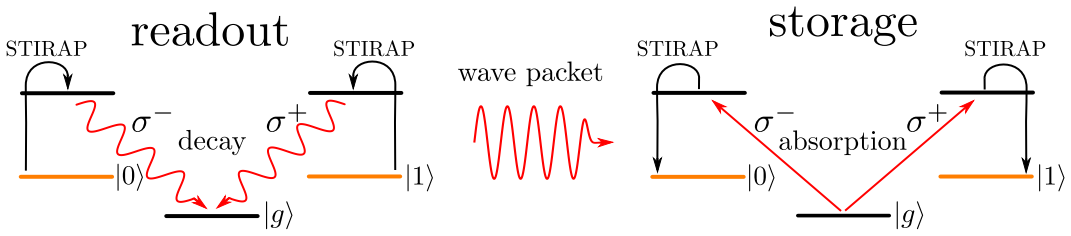

Figure 5.7.: Advanced protocol for quantum state transfer in free-space: The qubit states are formed by Zeeman sublevels of two degenerate metastable states denoted by $|0\rangle$ and $|1\rangle$ (colored in orange). The non degenerate ground state of the atom is denoted by $|g\rangle$. The red arrows indicate the relevant spontaneous decay and photon absorption processes. The black arrows indicate the relevant STIRAP processes.

5.5 A PROTOCOL FOR EFFICIENT HIGH-FIDELITY QUANTUM STATE TRANSFER BETWEEN REMOTE MATTER QUBITS

One of the main motivations for achieving efficient matter-field coupling on the single-photon level is to implement protocols for quantum communication to generate remote entangled states or to realize quantum state transfer between remote matter qubits. We can use the schemes developed in the previous sections as basic building blocks for such protocols.

In the following, we focus on single-photon-mediated high-fidelity quantum state transfer of arbitrary qubit states encoded in matter qubits via a free-space channel. In the simplest protocol, one of the previously discussed level structures (see Fig. 5.1 and Fig. 5.5) is used for encoding a qubit in a linear superposition of the atomic levels $|g_1\rangle$ and $|g_2\rangle$ of an atom trapped at the focus of a parabolic cavity. The readout of this qubit is performed by one of the previously proposed schemes (either via a STIRAP assisted process or by driving a suitable Rabi oscillation). If this atom is prepared initially in state $|g_1\rangle$, it is transferred to state $|g_2\rangle$ by emitting a single photon. Alternatively, if it is prepared initially in state $|g_2\rangle$, it remains in this state and no photon is emitted. Correspondingly, if the atom is prepared in a linear superposition of both states, this qubit state is coherently mapped onto a coherent superposition of the presence and absence of a single photon. After photon propagation through free-space, the retrieval of this photonic qubit is accomplished by the time-reversed process acting on a second atom initially prepared in state $|g_2\rangle$. This way, it is possible to store the original qubit again in a second distant matter qubit positioned at the focal point of another parabolic cavity. However, this simple procedure has the drawback that photon loss cannot be detected by the receiver (photon loss is described by $|\alpha| < 1$). Thus, photon loss leads to a significant reduction of the fidelity of the original qubit state.

This problem can be circumvented by an advanced free-space quantum communication protocol whose atomic excitation scheme is depicted in Fig. 5.7. For this protocol, also, both schemes discussed in Sec. 5.2 and Sec. 5.4 are applicable. A controlled spontaneous decay process is used to encode an initially prepared qubit state of a trapped atom in the polarization state of the generated single-photon wave packet. Thereby, the states of the matter qubit may be formed by Zeeman sublevels of a degenerate metastable atomic state. After photon propagation, the retrieval of this photonic qubit and storage in another matter qubit is achieved with the corresponding time-reversed absorption process. In this protocol, photon loss only affects the success probability of the retrieval process and not the fidelity of the retrieved qubit state. Provided the transmission of the generated single-photon wave packet is successful, the quantum state of the first atom is transferred with high fidelity to the distant second atom. Atomic level structures suitable for implementing such a scheme are available in alkaline earth and alkaline-earth-like atoms, for example. These atoms offer ground states with vanishing electronic spin and are therefore of interest for quantum information processing [67, 68] and for realizations of optical frequency standards [69]. For this scheme, isotopes with vanishing nuclear spin are of particular interest due to their non-degenerate ground states. The matter qubit may be encoded in long-lived metastable states and the single-photon wave packet may be generated by dipole allowed optical transitions from suitable excited states to the non-degenerate ground state of the atom. The presence of such a non-degenerate ground state is necessary to ensure that the excited states decay to only one state of the level structure. Successful cooling and trapping of such atoms, like ^{88}Sr and ^{174}Yb, has already been reported

[70, 71]. A possible level scheme in ^{88}Sr for the STIRAP assisted version of the protocol is given by

$$\begin{aligned} |g\rangle &\equiv 5s^2\ {}^1S_0 \\ |0\rangle, |1\rangle &\equiv 5s4d\ {}^1D_2\ (m = \pm 1) \\ |r_0\rangle, |r_1\rangle &\equiv 5s5p\ {}^1P_1\ (m = \pm 1) \\ |h_0\rangle, |h_1\rangle &\equiv 5s4f\ {}^1F_3\ (m = \pm 1)\,. \end{aligned}$$

The laser-induced transfer between levels $|h_0\rangle$, $|h_1\rangle$ and $|r_0\rangle$, $|r_1\rangle$ could be realized by a two-photon process (e.g., via the intermediate levels $5s5d\ {}^1D_2$).

5.6 SUMMARY

In this chapter, we have studied the absorption and spontaneous emission process of single quantum emitters coupled to a multimode radiation field. We focused on the coupling of single quantum emitters to single photons propagating in free-space. However, the results developed in this chapter are not restricted to free-space but can be applied to many architectures which do not necessarily rely on the mode selection by an optical resonator but on the direct coupling of a quantum emitter to a one-dimensional waveguide, such as nanowires, nanofibers, or coplanar waveguides (circuit QED).

In the first part of this chapter, we focused on the requirements for achieving efficient single-photon absorption by a single quantum emitter. These absorption processes, in general, require a precise control of the shape of the incoming single-photon wave packet. Any deviations from the ideal shape of the incoming wave packet result in a severe loss of success probability.

Motivated by the importance of these processes for quantum communication protocols, we developed methods for obtaining coherent control of elementary emission and absorption processes of single quantum emitters in free space. By using these methods, it is possible to control the spontaneous decay process to tailor the shape of the emitted photons. It is also possible to control the time-reversed process of single photon absorption and to achieve almost unit excitation probability for a large class of single-photon wave packets. By combining these methods, we have shown that efficient excitation transfer between remote atoms in an extreme multimode environment can be achieved.

Based on these schemes, we developed a protocol for high-fidelity quantum state transfer between distant matter qubits by photon propagation in free-space. In contrast to already known quantum state transfer schemes, our protocol does not require high finesse cavities and optical fibers so that it offers interesting perspectives for applications in free-space quantum communication or a variety of architectures based on the direct coupling of single quantum emitters coupled to the multimode environment in a one-dimensional waveguide.

6

DISSIPATION ENABLED EFFICIENT EXCITATION TRANSFER FROM A SINGLE PHOTON TO A SINGLE QUANTUM EMITTER

In the previous chapter, we have shown that by applying additional laser pulses it is possible to control the spontaneous emission and absorption process of the single quantum emitters. By using this enhanced control, a single quantum emitter can efficiently absorb a single photon of quite arbitrary temporal shape provided the shape of the photon and its arrival time is known in advance. Similar schemes are also known for fiber- and cavity-based architectures.

Unfortunately, in practice, the precise temporal shape of the incoming photon might change due to processes in the optical medium, such as dispersion, and is not always known. Furthermore, scaling up a quantum network based on the schemes discussed above might be challenging as they require a synchronization of the nodes involved due to the requirement that the arrival time of the incoming photon has to be known.

One can circumvent these complications by using protocols based on electromagnetically induced transparency [72, 73] which can be used to store a single-photon wave packet of quite arbitrary pulse shape in a collective excitation of a macroscopically large number of atoms [73] or in a solid [74]. However, the controlled manipulation of the resulting macroscopic excitation for purposes of quantum information processing is highly challenging. Thus, it would be of advantage to be able to perform an efficient excitation transfer from a single photon of a quite arbitrary shape to a single quantum emitter without the need of tailoring conditional laser pulses.

A coherent scheme overcoming the complications of such a conditional pulse shaping has been proposed by Duan and Kimble [75]. It takes advantage of a trapped atom's state dependent frequency shift of the cavity mode which results in a phase flip of an incoming single photon reflected by the cavity. This scheme has been used to build a nondestructive photon detector [76], a quantum gate between a matter and a photonic qubit [77], and a quantum memory for the heralded storage of a single photonic qubit [78]. However, for the heralded storage of a single photonic qubit, the outgoing photon has to be measured and quantum feedback has to be applied. Hence, the efficiency of this scheme is limited by the efficiency of the single-photon detectors used for measuring the reflected photon.

In view of these recent developments, the natural question arises whether it is possible to achieve highly efficient excitation transfer from a single photon with a rather arbitrary pulse shape to a single quantum emitter also in a way that the challenging complications arising from conditional tailoring of laser pulses and from imperfections affecting postselective photon detection processes can be circumvented. Here, we present such a scheme which can be used to accomplish basic tasks of quantum information processing, such as implementing a deterministic single-atom quantum memory or a deterministic frequency converter for a photonic qubit. Contrary to previous proposals based on coherent quantum processes, our scheme is enabled by an

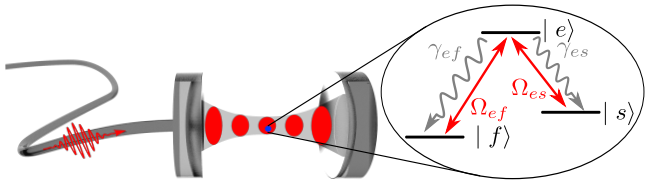

Figure 6.1.: Schematic representation of a fiber-based scenario with strong mode selection by an optical resonator: A single three-level atom is trapped inside the cavity.

appropriate balancing of dissipative processes, such as spontaneous photon emission and cavity decay. It is demonstrated that this way a single-photon wave packet of a rather arbitrary shape can trigger a highly efficient excitation transfer to a material quantum emitter. For photon wave packets with sufficiently small bandwidths, the high efficiency of this excitation transfer is independent of the photon wave packet's shape. This single-photon induced optical pumping [79] does not require mode selection by an optical resonator and is applicable to accomplish various tasks including highly efficient coupling of a single atom to a single photon propagating in a one-dimensional waveguide or even in free-space.

This chapter is organized as follows. We start with a discussion of our scheme in case of a cavity and fiber-based architecture. We introduce the corresponding theoretical model in Sec. 6.1. In Sec. 6.2, we evaluate the dynamics and derive the necessary conditions for a highly efficient excitation transfer, balancing the dissipative processes involved, which can be seen as an impedance matching condition. We show in Sec. 6.3 that our scheme can also be applied in case of no mode selection by a high finesse cavity is taking place. Finally, we demonstrate the usefulness of our scheme for building a deterministic quantum memory and a deterministic frequency converter between photonic qubits of different wavelengths in Sec. 6.4.

6.1 SCENARIO AND MODEL

We start with a discussion of the scheme for a fiber- and cavity-based architecture. We consider a single three-level atom (with a lambda configuration) trapped in a high finesse cavity, which is connected to a fiber. The corresponding setup is schematically depicted in Fig. 6.1. A photon propagating through the fiber can enter this cavity by transmission through a mirror of the single-sided cavity. In the following, we show that by properly balancing the dissipative processes in the system the single photon can induce an efficient state transfer from the state $|s\rangle$ to the state $|f\rangle$. As shown later on, this process can be used as basic building block for several protocols of quantum communication and quantum information processing.

We assume that each of the transitions $|e\rangle \leftrightarrow |s\rangle$, $|e\rangle \leftrightarrow |f\rangle$ is resonantly coupled exclusively to one cavity mode. The two cavity modes can be distinguished either due to different polarizations or different frequencies. We also model the spontaneous decay of the excited state $|e\rangle$ by taking the coupling of the atom to the continua of electromagnetic field modes orthogonal to the modes of the resonant cavity and of the fiber into account. In our subsequent discussion, we assume that the dipole and rotating

wave approximations are applicable. In the interaction picture, the Hamiltonian is given by

$$\begin{aligned}
\hat{H}_{\mathrm{int}}(t)/\hbar &= \left[i\Omega_{es}\hat{a}_{es}^{\mathrm{C}\dagger}|s\rangle\langle e| + i\Omega_{ef}\hat{a}_{ef}^{\mathrm{C}\dagger}|f\rangle\langle e| + \mathrm{H.c.}\right] && (6.1)\\
&+ \left[\sqrt{2\kappa_{es}}\hat{a}^{\mathrm{F}_{es}}(t)\hat{a}_{es}^{\mathrm{C}\dagger} + \sqrt{2\kappa_{ef}}\hat{a}^{\mathrm{F}_{ef}}(t)\hat{a}_{ef}^{\mathrm{C}\dagger} + \mathrm{H.c.}\right] && (6.2)\\
&- \frac{1}{\hbar}\left[e^{-i\omega_{es}(t-t_0)}\mathbf{d}_{es}\cdot\hat{\mathbf{E}}^{-}_{\mathrm{B}_{es}}(t)|s\rangle\langle e| + \mathrm{H.c.}\right] && (6.3)\\
&- \frac{1}{\hbar}\left[e^{-i\omega_{ef}(t-t_0)}\mathbf{d}_{ef}\cdot\hat{\mathbf{E}}^{-}_{\mathrm{B}_{ef}}(t)|f\rangle\langle e| + \mathrm{H.c.}\right], && (6.4)
\end{aligned}$$

$\hat{a}_{es}^{\mathrm{C}}$ and $\hat{a}_{ef}^{\mathrm{C}}$ being the annihilation operators of the cavity modes. These modes couple resonantly to the atomic transitions $|e\rangle \leftrightarrow |s\rangle$ and $|e\rangle \leftrightarrow |f\rangle$ with the atomic transition frequencies ω_{es} and ω_{ef} and the corresponding vacuum Rabi-frequencies Ω_{es} and Ω_{ef}. The coupling of the cavity modes to the fiber modes can be described by collective annihilation operators of the fiber [80], i.e.,

$$\sqrt{2\kappa_k}\hat{a}^{\mathrm{F}_k}(t) = \sum_{j\in\mathrm{F}_k} c_j\hat{a}_j e^{-i\left(\omega_j-\omega_k\right)(t-t_0)} \text{ for } k\in\{es,ef\}$$

with $\hat{a}_j$ ($j \in \mathrm{F}_{es}(\mathrm{F}_{ef})$) describing the orthogonal fiber modes with frequencies ω_j coupling to the atomic transitions $|e\rangle \leftrightarrow |s\rangle$ ($|e\rangle \leftrightarrow |f\rangle$) and with $2\kappa_{es}$ ($2\kappa_{ef}$) denoting the associated cavity loss rates due to photon exchange between the cavity and the fiber modes F_{es} (F_{ef}) through one of the mirrors. In the dipole and rotating wave approximation, the coupling of the atomic transition $|e\rangle \leftrightarrow |s\rangle$ ($|e\rangle \leftrightarrow |f\rangle$) to the reservoir of orthogonal electromagnetic background modes B_{es} (B_{ef}) is characterized by the electric field operator whose negative frequency part is denoted $\hat{\mathbf{E}}^{-}_{\mathrm{B}_{es}}(t)$ ($\hat{\mathbf{E}}^{-}_{\mathrm{B}_{ef}}(t)$) and the dipole matrix element $\mathbf{d}_{es}$ ($\mathbf{d}_{ef}$). We consider an initial state $|\psi(t_0)\rangle$ in which a single photon with frequencies centered around ω_{es} is propagating through the fiber towards the left mirror. The remaining parts of the radiation field are assumed to be in the vacuum state and the atom is initially prepared in state $|s\rangle$, i.e.,

$$|\psi(t_0)\rangle = |s\rangle|\psi_{\mathrm{in}}\rangle^{\mathrm{F}_{es}}|0\rangle^{\mathrm{F}_{ef}}|0\rangle_{es}^{\mathrm{C}}|0\rangle_{ef}^{\mathrm{C}}|0\rangle^{\mathrm{B}_{es}}|0\rangle^{\mathrm{B}_{ef}}.$$

The initial state of the single photon propagating through the fiber is denoted $|\psi_{\mathrm{in}}\rangle^{\mathrm{F}_{es}}$ and $|0\rangle_{es}^{\mathrm{C}}$, $|0\rangle_{ef}^{\mathrm{C}}$, $|0\rangle^{\mathrm{F}_{ef}}$ $|0\rangle^{\mathrm{B}_{es}}$ $|0\rangle^{\mathrm{B}_{ef}}$ are the vacuum states of the cavity modes, of the initially unoccupied fiber modes, and of the modes of the electromagnetic background.

6.2 DYNAMICS OF THE EFFICIENT EXCITATION TRANSFER AND THE IMPEDANCE MATCHING CONDITION

For evaluating the dynamics of the system, we focus on the subspace of the Hilbert space which describes a single excitation in the combined atom-cavity system. The corresponding subspace is spanned by the three quantum states

$$\begin{aligned}
|E\rangle &\equiv |e\rangle|0\rangle^{\mathrm{F}_{es}}|0\rangle^{\mathrm{F}_{ef}}|0\rangle_{es}^{\mathrm{C}}|0\rangle_{ef}^{\mathrm{C}}|0\rangle^{\mathrm{B}_{es}}|0\rangle^{\mathrm{B}_{ef}},\\
|S\rangle &\equiv |s\rangle|0\rangle^{\mathrm{F}_{es}}|0\rangle^{\mathrm{F}_{ef}}|1\rangle_{es}^{\mathrm{C}}|0\rangle_{ef}^{\mathrm{C}}|0\rangle^{\mathrm{B}_{es}}|0\rangle^{\mathrm{B}_{ef}},\\
|F\rangle &\equiv |f\rangle|0\rangle^{\mathrm{F}_{es}}|0\rangle^{\mathrm{F}_{ef}}|0\rangle_{es}^{\mathrm{C}}|1\rangle_{ef}^{\mathrm{C}}|0\rangle^{\mathrm{B}_{es}}|0\rangle^{\mathrm{B}_{ef}}.
\end{aligned}$$

The three states listed above are coupled among each other due to the vacuum Rabi oscillations and are coupled to four continua corresponding to the fiber and background

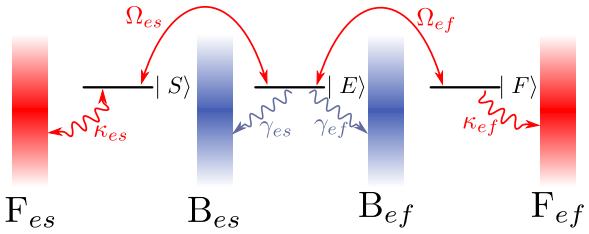

Figure 6.2.: Sketch illustrating the couplings of the states $|E\rangle$, $|S\rangle$ and $|F\rangle$ among each other as well as to the reservoirs F_{es} and F_{ef} representing the fiber modes and to the reservoirs B_{es} and B_{ef} representing the radiative background. The couplings among the states $|E\rangle$, $|S\rangle$ and $|F\rangle$ are characterized by the vacuum Rabi frequencies. The couplings of the state $|E\rangle$ to the reservoirs B_{es} and B_{ef} is characterized by the spontaneous decay rates γ_{es} and γ_{ef} and the couplings of the states $|S\rangle$ and $|F\rangle$ to the reservoirs F_{es} and F_{ef} is characterized by the cavity loss rates κ_{es} and κ_{es}.

modes. These couplings are illustrated in Fig. 6.2. The couplings to the reservoirs induce effects such as cavity leakage and spontaneous decay.

By applying the techniques developed by [37], which have already been used in chapter 3 to derive the single-photon-path-representation, we can describe the dynamics in the subspace spanned by the states $|E\rangle$, $|S\rangle$ and $|F\rangle$ by the following differential equation

$$\frac{d}{dt}|\psi_{\mathrm{P}}(t)\rangle = \hat{G}|\psi_{\mathrm{P}}(t)\rangle + |S\rangle\sqrt{2\kappa_{es}}f_{\mathrm{in}}(t)\ . \tag{6.5}$$

Thereby, the generator

$$\begin{aligned}\hat{G} \;=\; & \left[\Omega_{es}|S\rangle\langle E| + \Omega_{ef}|F\rangle\langle E| - \mathrm{H.c.}\right] \\ & -\kappa_{es}|S\rangle\langle S| - \kappa_{ef}|F\rangle\langle F| - \frac{\gamma_{ef}+\gamma_{es}}{2}|E\rangle\langle E|\end{aligned} \tag{6.6}$$

describes the vacuum Rabi oscillations coupling the states $|E\rangle$, $|S\rangle$ and $|F\rangle$ among each other as well as the coupling of these states to the remaining part of the Hilbert space which is connected to cavity loss and spontaneous decay of the atom. The corresponding spontaneous decay rates of the dipole transitions $|e\rangle \leftrightarrow |s\rangle$ and $|e\rangle \leftrightarrow |f\rangle$ are denoted γ_{es} and γ_{ef}. The inhomogeneity of Eq. (6.5) with amplitude

$$f_{\mathrm{in}}(t) = -i\ {}^{\mathrm{F}_{es}}\langle 0|\hat{a}^{\mathrm{F}_{es}}(t)|\psi_{\mathrm{in}}\rangle^{\mathrm{F}_{es}} \tag{6.7}$$

characterizes the incoming single photon. The general solution of Eq. (6.5) is given by

$$|\psi_{\mathrm{P}}(t)\rangle = \sqrt{2\kappa_{es}}\int_{t_0}^{t} e^{\hat{G}(t-t')}|S\rangle f_{\mathrm{in}}(t')dt'\ . \tag{6.8}$$

In the following, we concentrate on the adiabatic dynamical regime in which the bandwidth of the incoming single-photon wave packet, i.e.,

$$\Delta\omega = \sqrt{\int_{\mathbb{R}}\left|\tfrac{d}{dt}f_{\mathrm{in}}(t)\right|^2 dt \,/\, \int_{\mathbb{R}}|f_{\mathrm{in}}(t)|^2\,dt} \tag{6.9}$$

is much smaller than the eigenfrequencies of the generator $\hat{G}$, i.e.,

$$\Delta\omega \ll \kappa_{es}, \left| \frac{\kappa_{es} + (\gamma_{es} + \gamma_{ef})/2}{2} \pm \left[\left(\frac{\kappa_{es} - (\gamma_{es} + \gamma_{ef})/2}{2} \right)^2 - |\Omega_{es}|^2 - |\Omega_{ef}|^2 \right]^{1/2} \right|. \tag{6.10}$$

In this dynamical regime [81], we arrive at the approximate result

$$|\psi_{\mathrm{P}}(t)\rangle = \sqrt{2\kappa_{es}} f_{\mathrm{in}}(t) \int_0^\infty e^{\hat{G}t'} |S\rangle dt' = -\sqrt{2\kappa_{es}} f_{\mathrm{in}}(t) \hat{G}^{-1} |S\rangle$$

if the initial state has been prepared long before the wave packet arrives at the cavity, i.e., $t_0 \to -\infty$. Long after the photon has left the cavity again, i.e., for $t \to \infty$, the atomic transition probability $P_{|s\rangle \to |f\rangle}$ between initial and final states $|s\rangle$ and $|f\rangle$ is given by

$$\begin{aligned} P_{|s\rangle \to |f\rangle} &= \int_{\mathbb{R}} \Big[2\kappa_{ef} \left| \langle F|\psi_{\mathrm{P}}(t')\rangle \right|^2 \\ &\quad + \gamma_{ef} \left| \langle E|\psi_{\mathrm{P}}(t')\rangle \right|^2 \Big] dt' = \eta \int_{\mathbb{R}} |f_{\mathrm{in}}(t)|^2 \, dt \end{aligned} \tag{6.11}$$

with the efficiency

$$\eta = \frac{4\chi_{es}\chi_{ef}}{(\chi_{es} + \chi_{ef})^2} \frac{1}{1 + \gamma_{es} / \left[2 |\Omega_{es}|^2 / \kappa_{es} \right]} \tag{6.12}$$

and with the transition rates

$$\chi_{es} = \gamma_{es} + 2 |\Omega_{es}|^2 / \kappa_{es} \,, \tag{6.13}$$

$$\chi_{ef} = \gamma_{ef} + 2 \left| \Omega_{ef} \right|^2 / \kappa_{ef} \,. \tag{6.14}$$

The rates χ_{es} and χ_{ef} can be seen as effective spontaneous decay rates whereby the contributions $|\Omega_{es}|^2 / \kappa_{es}$ and $\left|\Omega_{ef}\right|^2 / \kappa_{ef}$ represent a cavity induced decay. Thereby, $\int_{t_0}^{t} |f_{\mathrm{in}}(t')|^2 dt'$ is the probability that in the time interval $[t_0, t]$ the single photon has arrived at the left mirror (not necessarily entering the cavity). Provided the photon has arrived at the left mirror (during the time interval $[t_0, \infty)$), the probability of the resulting excitation transfer to state $|f\rangle$ equals the efficiency η. For an efficiency close to unity, it is required that

$$\chi_{es} = \chi_{ef}, \tag{6.15}$$

$$\gamma_{es} \ll 2 |\Omega_{es}|^2 / \kappa_{es}. \tag{6.16}$$

The equality of the transition rates may be viewed as an optical impedance matching condition. The second condition in Eq. (6.16) implies that for unit efficiency the atom should not decay from state $|e\rangle$ back to state $|s\rangle$ by photon emission into the electromagnetic background. Interestingly, the optimal efficiency achievable is limited by the spontaneous decay $|e\rangle \to |s\rangle$ only and not by photon emission into the background modes coupling to the transition $|e\rangle \leftrightarrow |f\rangle$. In fact, if the spontaneous decay rate γ_{ef} is sufficiently large, we do not even require any coupling of the transition $|e\rangle \leftrightarrow |f\rangle$ to one of the cavity modes for achieving unit efficiency.

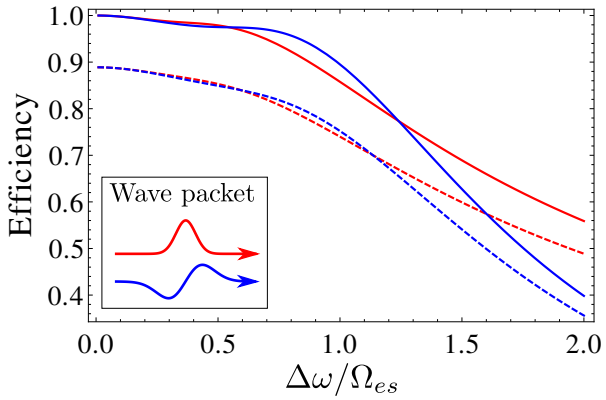

Figure 6.3.: Dependence of the state transfer efficiency $|s\rangle \rightarrow |f\rangle$ on the bandwidth $\Delta\omega$ of the photonic wave packet (in units of Ω_{es}): The red lines are results of the Gaussian envelope $f_{\text{in}}^{1}(t)$ and the blue lines of the antisymmetric envelope $f_{\text{in}}^{2}(t)$. The parameters are: $\Omega_{es} = \Omega_{ef} = \kappa_{es} = \kappa_{ef}$ and $\gamma_{es} = \gamma_{ef} = 0$ (solid lines; i.e., conditions (6.15) and (6.16) are satisfies), $\Omega_{es} = \Omega_{ef} = \kappa_{es} = \kappa_{ef} = 4\gamma_{es} = 4\gamma_{ef}$ (dashed lines; violation of the condition (6.16)).

In order to demonstrate the independence of this transition probability from the shape of the incoming wave packet, we have evaluated the time evolution for two different temporal envelopes, namely a symmetric Gaussian envelope

$$f_{\text{in}}^{(1)}(t) = \sqrt[4]{2\Delta\omega^2/\pi}e^{-\Delta\omega^2 t^2} \tag{6.17}$$

and an antisymmetric envelope of the form

$$f_{\text{in}}^{(2)}(t) = 2\sqrt[4]{2/\pi}\Delta\omega^{3/2}te^{-\frac{1}{3}\Delta\omega^2 t^2}/3^{3/4} \,. \tag{6.18}$$

They are normalized so that $\int_{\mathbb{R}} |f_{\text{in}}^{(1,2)}(t)|^2 dt = 1$, i.e., the photon certainly arrives at the left mirror of the cavity. The resulting probability $P_{|s\rangle\rightarrow|f\rangle}$ is the efficiency for performing the photon induced atomic state transfer $|s\rangle \rightarrow |f\rangle$. The solid lines in Fig. 6.3 correspond to perfect impedance matching as described by Eq. (6.15) with $\gamma_{es} = 0$. As long as the bandwidth of the incoming photon wave packet is sufficiently small (see Eq. (6.10)) the efficiency of the excitation transfer is close to unity and independent of the shape of the photon wave packet. The dashed lines in Fig. 6.3 describe cases with $\gamma_{es} \neq 0$ so that spontaneous decay of the atomic excitation $|e\rangle \rightarrow |s\rangle$ limits the efficiency of the excitation transfer. The spontaneous decay process $|e\rangle \rightarrow |f\rangle$ does not limit the overall efficiency and in the extreme case of $\Omega_{ef} = 0$, for example, a non-zero decay rate γ_{ef} is even essential for a highly efficient excitation transfer.

6.3 EXCITATION TRANSFER IN THE ABSENCE OF A CAVITY

In the previous section, it has been shown that by balancing dissipative processes, such as spontaneous decay processes and cavity leakage, an efficient state transfer of a single quantum emitter trapped inside a high finesse cavity can be triggered by a single photon of a quite arbitrary shape propagating along a fiber coupled to the high finesse cavity. It is noteworthy that none of the necessary conditions for achieving a high efficiency of this state transfer stated in Eqs. (6.15) and (6.16) demands that the

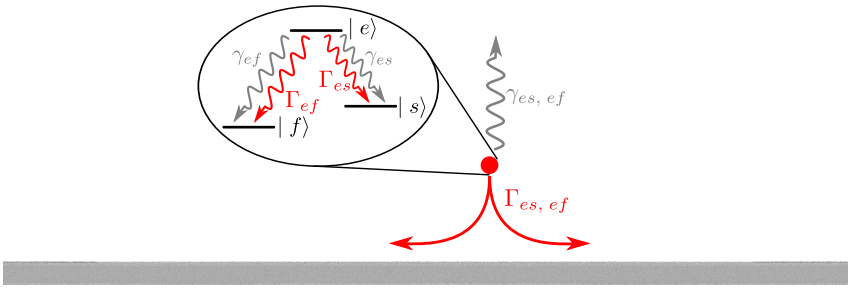

Figure 6.4.: Schematic representation of a setup in which a three-level atom is coupled to a one-dimensional waveguide without mode selection by an optical resonator. The rates Γ_{es} and Γ_{ef} describe the spontaneous decay of the atom caused by the coupling of the atom to the modes propagating along the one-dimensional waveguide. The decay rates γ_{es} and γ_{ef} describe the spontaneous decay of the excited state $|e\rangle$ caused by the coupling of the atom to the modes of the radiative background (i.e., modes not confined by the waveguide).

coherent cavity induced vacuum Rabi oscillations are dominating over the incoherent process, such as spontaneous decay or cavity loss. This can be seen as a hint that our scheme does not require the mode selection by an optical resonator. In this section, we demonstrate that our scheme can also be applied to enhance resonant matter field coupling between a single quantum emitter and a single photon propagating through a one-dimensional waveguide or even to resonant atom-photon interaction in free-space. We start with a model describing the interaction of a single photon propagating along a one-dimensional waveguide with a single three-level atom in the vicinity of that waveguide. A sketch of such a setup is depicted in Fig. 6.4 . We again assume that the RWA and the dipole approximation are applicable. In the interaction picture, we can describe the dynamics of the system by the Hamiltonian

$$\begin{aligned}\hat{H}_{\mathrm{int}}(t) = \; & -\left[e^{-i\omega_{es}(t-t_0)}\mathbf{d}_{es}\cdot\hat{\mathbf{E}}^{-}_{es}(\mathbf{x}_A,t)|s\rangle\langle e| + \mathrm{H.c.}\right] \\ & -\left[e^{-i\omega_{ef}(t-t_0)}\mathbf{d}_{ef}\cdot\hat{\mathbf{E}}^{-}_{ef}(\mathbf{x}_A,t)|f\rangle\langle e| + \mathrm{H.c.}\right]\end{aligned} \tag{6.19}$$

with $\mathbf{x}_A$ being the position of the atom. Thereby, we assume that the atomic transitions $|e\rangle \leftrightarrow |s\rangle$ and $|e\rangle \leftrightarrow |f\rangle$ are coupling two disjunct sets of modes, either due to different frequencies of the transitions or due to different dipole matrix elements. The negative frequency parts of the electric field operators connected to these two different sets of mode functions are denoted $\hat{\mathbf{E}}^{-}_{es}(\mathbf{x}_A,t)$ and $\hat{\mathbf{E}}^{-}_{ef}(\mathbf{x}_A,t)$. We can further subdivide the set of mode functions by distinguishing between the modes propagating along the one-dimensional waveguide and the modes connected to the radiative background (not confined by the waveguide). Thus, we can again introduce the reservoirs F_{es} and F_{ef} connected to the modes propagating along the waveguide and the reservoirs B_{es} and B_{ef} connected to the modes of the radiative background. In the following, we assume that initially a single photon, which can couple to the atomic transition $|e\rangle \leftrightarrow |s\rangle$, is propagating along the waveguide, that the radiative background as well as the modes

connected to the reservoir F_{ef} are in the vacuum state, and that the atom is prepared in the state $|s\rangle$. The corresponding initial state is give by

$$|\psi(t_0)\rangle = |s\rangle|\psi_{\mathrm{in}}\rangle^{\mathrm{F}_{es}}|0\rangle^{\mathrm{F}_{ef}}|0\rangle^{\mathrm{B}_{es}}|0\rangle^{\mathrm{B}_{ef}} \tag{6.20}$$

with $|\psi_{\mathrm{in}}\rangle^{\mathrm{F}_{es}}$ being the initial state of the single photon propagating through the fiber.

In close analogy to the previous section, we can derive the following equation describing the probability amplitude for exciting the atom by using the methods presented in chapter 3

$$\frac{d}{dt}\langle e|\psi(t)\rangle = -\tfrac{1}{2}\left(\Gamma_{es}+\gamma_{es}+\Gamma_{ef}+\gamma_{ef}\right)\langle e|\psi(t)\rangle + i\sqrt{\Gamma_{es}}f_{\mathrm{in}}(t) \tag{6.21}$$

with Γ_{es} and Γ_{ef} being the spontaneous decay rates connected to the reservoirs F_{es} and F_{ef} and γ_{es} and γ_{ef} again denoting the spontaneous decay rates induced by the electromagnetic background (i.e., the reservoirs B_{es}, B_{ef}). The function $f_{\mathrm{in}}(t)$ is defined by the equation

$$\sqrt{\Gamma_{es}}f_{\mathrm{in}}(t) = \tfrac{1}{\hbar}e^{i\omega_{es}(t-t_0)}\langle 0|\mathbf{d}_{es}^{*}\cdot\left(\hat{\mathbf{E}}_{es}^{-}(\mathbf{x}_A,t)\right)^{\dagger}|\psi_{\mathrm{in}}\rangle^{\mathrm{F}_{es}} \tag{6.22}$$

and describes the incoming single photon propagating through the waveguide. The solution of Eq. (6.21) is given by the following integral expression

$$\langle e|\psi(t)\rangle = i\sqrt{\Gamma_{es}}\int_{t_0}^{t} e^{-\left(\Gamma_{es}+\gamma_{es}+\Gamma_{ef}+\gamma_{ef}\right)(t-t')/2}f_{\mathrm{in}}(t')\,. \tag{6.23}$$

In the following, we again concentrate on the adiabatic dynamical regime in which the bandwidth of the incoming single-photon wave packet $\Delta\omega$ (see previous section) is much smaller than the total spontaneous decay rate of the excited state, i.e.,

$$\Delta\omega \ll \left(\Gamma_{es}+\gamma_{es}+\Gamma_{ef}+\gamma_{ef}\right)/2\,. \tag{6.24}$$

In the adiabatic regime, the probability amplitude of finding the atom in the excited state follows the temporal profile of the incoming single-photon wave packet and we obtain

$$\langle e|\psi(t)\rangle = i\frac{2\sqrt{\Gamma_{es}}}{\Gamma_{es}+\gamma_{es}+\Gamma_{ef}+\gamma_{ef}}f_{\mathrm{in}}(t) \tag{6.25}$$

if the initial state has been prepared long before the wave packet arrives at the atom, i.e., $t_0 \to -\infty$. We can use the above result to evaluate the probability for triggering an efficient excitation transfer from state $|s\rangle$ to the state $|f\rangle$. Long after the photon has left the atom, i.e., for $t \to \infty$ the corresponding atomic transition probability is given by

$$P_{|s\rangle\to|f\rangle} = \left(\Gamma_{ef}+\gamma_{ef}\right)\int_{\mathbb{R}}\left|\langle e|\psi(t')\rangle\right|^2 \tag{6.26}$$

$$= \eta\int_{\mathbb{R}}\left|f_{\mathrm{in}}(t')\right|^2 dt'\,. \tag{6.27}$$

It is possible to achieve

$$\int_{\mathbb{R}}\left|f_{\mathrm{in}}(t')\right|^2 dt' = 1\,. \tag{6.28}$$

This can be done in case of a photon which is approaching the atom simultaneously from the left and from the right (in a symmetric way) or in a chiral waveguide [82–84].

Another possible implementation is a waveguide in which the photon is reflected at the end of the waveguide, close to the atom, such that the photon constructively interferes with itself at the position of the atom. The corresponding efficiency for triggering the state transfer is given by

$$\eta = \frac{4\chi_{es}\chi_{ef}}{\left(\chi_{es}+\chi_{ef}\right)^2}\frac{1}{1+\gamma_{es}/\Gamma_{es}} \tag{6.29}$$

with

$$\chi_{es} = \gamma_{es}+\Gamma_{es}\,, \tag{6.30}$$
$$\chi_{ef} = \gamma_{ef}+\Gamma_{ef} \tag{6.31}$$

being the analogs of the transition rates introduced in the previous section. Note that we can obtain the above expressions by just applying the replacements

$$2\left|\Omega_{es}\right|^2/\kappa_{es} \rightarrow \Gamma_{es}, \tag{6.32}$$
$$2\left|\Omega_{ef}\right|^2/\kappa_{ef} \rightarrow \Gamma_{ef} \tag{6.33}$$

to the results for cavity and fiber-based systems derived in the previous section. Hence, the conditions for an efficient state transfer have a similar structure. The necessary conditions for a state transfer efficiency close to unity are given by

$$\chi_{es} = \chi_{ef}, \tag{6.34}$$
$$\gamma_{es} \ll \Gamma_{es}. \tag{6.35}$$

Within this framework a free-space scenario without any waveguide can be described by interpreting the modes F_{ef} as the only modes which couple to the atomic transition $|e\rangle \leftrightarrow |f\rangle$ so that $\gamma_{ef}=0$. In such a case, the continuum F_{es} may be interpreted as the modes by which the three-level system is excited by the incoming single photon with the rate Γ_{es}. Consequently, the background modes B_{es} are the additional orthogonal background modes to which the atomic transition $|e\rangle \leftrightarrow |s\rangle$ can decay with rate γ_{es}. In particular, in a free-space scenario almost perfect excitation of the transition $|s\rangle \rightarrow |e\rangle$ [61] requires that the impedance matching condition $\Gamma_{es}=\Gamma_{ef}$ is satisfied and that $\gamma_{es} \ll \Gamma_{es}$. The second condition $\gamma_{es} \ll \Gamma_{es}$ demands that the incoming single photon forms almost a perfect inward-moving dipole wave. This second condition has already been discussed in chapter 5. If these conditions are fulfilled, an incoming photon wave packet of almost arbitrary temporal shape can trigger an efficient state transfer of the atom.

6.4 DETERMINISTIC PROTOCOLS FOR QUANTUM INFORMATION PROCESSING

In the previous sections, we showed that by balancing dissipative processes a single incoming photon could trigger an highly efficient state transfer of a single quantum emitter. In this section, we demonstrate that this scheme can serve as a basic building block for various tasks relevant for quantum information processing.

6.4.1 *A quantum memory for photonic qubits*

One possible application of our scheme is to build a quantum memory based on a single atom. A qubit encoded in one degree of freedom of a propagating photon such

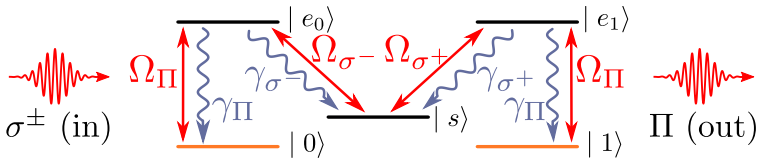

Figure 6.5.: An atomic level structure for converting a polarization-encoded photonic qubit encoded into a matter qubit. The atom is initially prepared in the state $|s\rangle$ and the ground or metastable states $|0\rangle$ and $|1\rangle$ are used to store the matter qubit.

as the polarization can be converted to a matter qubit deterministically and can be stored in the atomic level structure of the atom. This can be achieved by using an atom with a level structure depicted in Fig. 6.5, for example, with the atom initially prepared in state $|s\rangle$ and with the qubits states $|0\rangle$ and $|1\rangle$ constituting long-lived stable states. Storage efficiencies close to unity can be achieved if the conditions (6.15) and (6.16) for a fiber- and cavity-based architecture respectively the conditions (6.34) and (6.34) for the direct coupling of the atom to the waveguide are satisfied. In the case of a cavity, they imply $\gamma_{\sigma^\pm} \ll 2\left|\Omega_{\sigma^\pm}\right|^2/\kappa_{\sigma^\pm}$. In the absence of a cavity, $\gamma_{\sigma^\pm} \ll \Gamma_{\sigma^\pm}$ is required whereby we defined the rates $\Gamma_{\sigma^\pm}$ by using the replacements (6.32) and (6.33). If the properties of the photon emitted during this storage process are independent of the state of the initial photonic qubit, no information about this photonic input state is transferred to the background or to the fiber modes involved. Thus, the photonic excitation transfer to the material degrees of freedom does not suffer from decoherence and can be performed with a fidelity close to unity. In the case of a cavity, this condition can be satisfied by choosing equal vacuum Rabi frequencies and cavity loss rates for the $\sigma^\pm$ transitions, i.e., $\Omega_{\sigma^-} = \Omega_{\sigma^+}$ and $\kappa_{\sigma^-} = \kappa_{\sigma^+}$. In the absence of a cavity, for this purpose, one has to choose equal photon emission rates into the waveguide, i.e., $\Gamma_{\sigma^-} = \Gamma_{\sigma^+}$. The required tuning of spontaneous decay rates may be achieved with the help of additional dressing lasers, for example [85].

6.4.2 *A frequency converter for photonic qubits*

The proposed scheme can also be used for a deterministic frequency converter of photonic qubits which can serve as an interface between several quantum information processing architectures. A possible atomic level structure for performing frequency conversion of a polarization-encoded photonic qubit is depicted in Fig. 6.6. Such a level structure can be found in an alkaline earth atom, such as ^{88}Sr. For converting the frequency of the photonic qubit, the atom has to be prepared either in state $|g_0\rangle$ or in state $|g_1\rangle$ depending on whether the frequencies of the photonic qubit should be decreased or increased. To ensure that the resulting converted photon is emitted into a waveguide, for example, the corresponding vacuum Rabi frequencies or emission rates into the waveguide have to be sufficiently large. Hence, in the case of a cavity, it is required that $\gamma^{>}_{\sigma^\pm} \ll 2\left|\Omega^{>}_{\sigma^\pm}\right|^2/\kappa^{>}_{\sigma^\pm}$ and $\gamma^{<}_{\sigma^\pm} \ll 2\left|\Omega^{<}_{\sigma^\pm}\right|^2/\kappa^{<}_{\sigma^\pm}$. In the absence of a cavity, the conditions read $\gamma^{>}_{\sigma^\pm} \ll \Gamma^{>}_{\sigma^\pm}$ and $\gamma^{<}_{\sigma^\pm} \ll \Gamma^{<}_{\sigma^\pm}$ again defining the rates $\Gamma_{\sigma^\pm}$ by using the replacements (6.32) and (6.33).

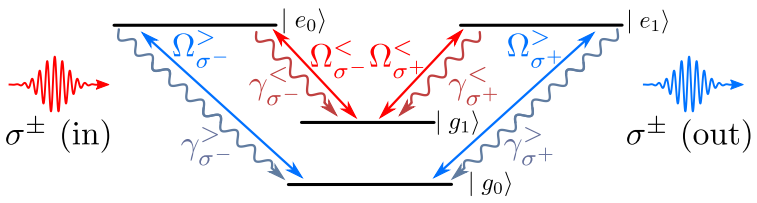

Figure 6.6.: An atomic level structure for converting the frequency of a polarization encoded photonic qubit. The atom is initially prepared either in the state $|g_0\rangle$ ($|g_1\rangle$) for down (up) converting the frequency.

6.5 SUMMARY

In this chapter, we have presented a dissipation dominated scheme for triggering a highly efficient excitation transfer from a single-photon wave packet of arbitrary temporal shape but small bandwidth to a single quantum emitter.

We have shown that by balancing the decay rates characterizing relevant dissipation processes, such as spontaneous photon emission into waveguides or the electromagnetic background, appropriately these processes can be turned into a valuable tool for purposes of quantum information processing. Our scheme for single-photon induced optical pumping offers the advantage that no additional control of the system by additional laser fields or by post-selection is required. This is useful for scaling up quantum communication networks, as no synchronization of the nodes of the network and no single-photon detectors for a post-selection of an outgoing photon are required. We have also demonstrated that our scheme can be applied to a variety of different scenarios including fiber- and cavity-based architectures as well as architectures without any optical resonators. It can serve as a basic building block for various protocols relevant for quantum information processing and quantum communication. As examples, we have discussed setups for a deterministic single-atom single-photon quantum memory and a deterministic frequency converter between photonic qubits of different wavelengths which could serve as an interface between several quantum information processing architectures.

7

THE IMPACT OF THE CENTER OF MASS MOTION ON EFFICIENT PHOTON ABSORPTION

7.1 INTRODUCTION

In the previous chapters, we studied matter-field interactions on the single-photon level and their possible quantum technological applications. Thereby, we assumed that the quantum emitters were tightly trapped at fixed positions, i.e., that the center of mass motion of the quantum emitters is negligible. In practice, however, the traps confining the quantum emitters are not infinitely steep. Thus, for reaching the goal of efficient matter-field coupling on the single-photon level in extreme multimode environments, the center of mass motion has to be taken into account.

As a basic example of efficient matter-field coupling, we revisit the problem of the efficient absorption of a single photon by a single atom in free-space discussed in the previous chapter, this time taking into account the center of mass degrees of freedom. However, taking into account the center of mass motion of a quantum system complicates the situation considerably because effects such as the recoil of the atom due to emission and absorption processes [86] can entangle the center of mass and the photonic degrees of freedom in an intricate way. It appears that achieving almost perfect single-photon absorption in free-space or with the help of a parabolic mirror requires the preparation of a highly entangled quantum state of the center of mass and the photonic degrees of freedom. Even by nowadays technological capabilities, the controlled preparation of such entangled quantum states constitutes a major technological obstacle and appears unrealistic.

In this chapter, we explore the influence of the center of mass motion of a trapped material two-level system on single-photon absorption in free-space or equivalently in a parabolic cavity with large focal length. One may be tempted to conclude that almost perfect excitation of a trapped two-level system by single-photon wave packet which is not entangled with the atom's center of mass motion is only achievable in sufficiently steep traps with high trap frequencies. However, our investigations demonstrate that almost perfect photon absorption is possible even in weakly confining traps and for initially prepared thermal states of the center of mass motion provided the trap frequency is modulated periodically in an appropriate way. Our analysis also exhibits the crucial role played by the characteristic dynamical parameters, namely the spontaneous photon emission rate of the electronic transition involved and the trap frequency.

This chapter is organized as follows. In Sec. 7.2, the quantum electrodynamical model describing single-photon absorption by a trapped moving two-level system is presented. Based on the dipole and rotating wave approximation, the dynamics of the single-photon induced excitation process and its relation to the relevant correlation function of the radiation field is discussed in section 7.3. In Sec. 7.4, characteristic

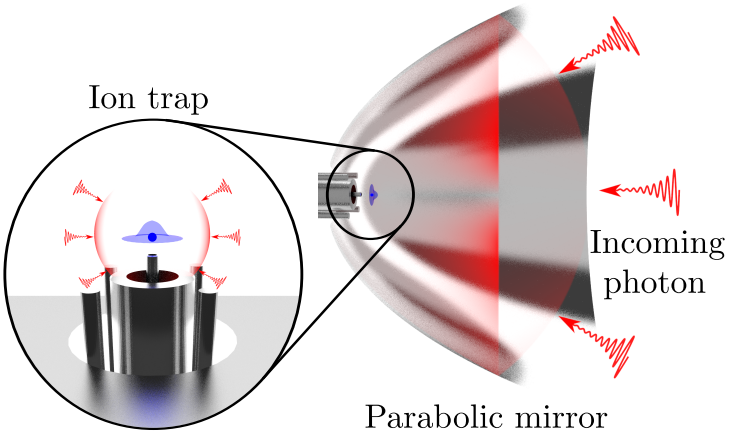

Figure 7.1.: Single-photon absorption process in a parabolic cavity: A two-level system trapped close to the focal point $\mathbf{x} = 0$ of a parabolic cavity is excited by an asymptotically incoming single-photon wave packet. This wave packet couples to the two-level system in the same way as a single-photon wave packet capable of exciting this two-level system almost perfectly in free-space. A suitable setup with a trapped ion at the focal point of the parabolic mirror has been described in [24, 30, 58] .

features of the excitation probability and its deviation from the ideal motionless case are investigated for tightly confining trapping potentials. In the subsequent section 7.5, these results are generalized to weakly confining trapping potentials with particular emphasis on the experimentally interesting dynamical regime of spontaneous photon emission rates large in comparison with relevant trapping frequencies. We finally explore possibilities to optimize the excitation probability by periodic modulation of the trap frequency of a harmonic trap in Sec. 7.6.

7.2 A QUANTUM ELECTRODYNAMICAL MODEL

In the following, we consider a single trapped atom or ion whose internal electronic dynamics is modeled by a two-level system resonantly coupled to an optical single-photon radiation field and explore its capability of absorbing this single photon almost perfectly. As discussed in the previous chapter, efficient photon absorption by an atom at a fixed position (infinitely steep trap) can only be achieved by an inward-moving dipole wave which couples perfectly to the dipole matrix element of the atomic transition. For achieving that, we again assume that the center of the trap is positioned in the focal point of a large parabolic mirror which is capable of focusing a well directed asymptotically incoming single-photon radiation field towards the two-level system trapped close to the focal point of the parabola. This excitation process is schematically depicted in Fig. 7.1 .

To describe the dynamics of this single-photon excitation process, we apply the dipole approximation and RWA for modeling the matter-field interaction. Also, the velocity of the two-level system's center of mass motion is assumed to be negligible in comparison with the speed of light in vacuum c so that the dynamics of the center of mass motion can be described in the non-relativistic approximation. Under these conditions, the

total Hamiltonian governing the dynamics of the quantum electrodynamical interaction between the moving two level system and the radiation field is given by

$$\hat{H} = \hat{H}_{\text{atom}} + \hat{H}_{\text{trap}} + \hat{H}_{\text{rad}} + \hat{H}_{\text{int}} \,, \tag{7.1}$$

with $\hat{H}_{\text{rad}}$ being the Hamiltonian of the free radiation field (see chapter 2). The Hamiltonians $\hat{H}_{\text{atom}} = E_g|g\rangle\langle g| + E_e|e\rangle\langle e|$ and $\hat{H}_{\text{trap}} = \hat{\mathbf{p}}^2/2m + V_{\text{T}}(\hat{\mathbf{x}})$ describe the dynamics of the electronic degrees of freedom and of the center of mass motion of the trapped two-level system. The transition frequency of the relevant electronic transition is denoted $\omega_{eg} = (E_e - E_g)/\hbar$ and $\hat{\mathbf{x}}$, $\hat{\mathbf{p}}$, and m are position operator, momentum operator, and mass of the two-level system's center of mass degrees of freedom. The Hamiltonian $\hat{H}_{\text{int}} = -\hat{\mathbf{E}}_{\perp}^{(+)}(\hat{\mathbf{x}}) \cdot \mathbf{d}|e\rangle\langle g| + \text{H.c.}$ describes the interaction between the two-level system and the transverse radiation field in the dipole and rotating wave approximations with the two-level system's dipole matrix element $\mathbf{d} = \langle e|\hat{\mathbf{d}}|g\rangle$ and its dipole operator $\hat{\mathbf{d}}$. In contrast to our previous investigations, the field operator $\hat{\mathbf{E}}_{\perp}^{(+)}$ which enters in $\hat{H}_{\text{int}}$ is evaluated at the center of mass of the atom which is now treated as a dynamical degree of freedom. Thereby, we take effects like the recoil of the atom due to an emitted or absorbed photon into account. In the regime where the velocity of the atom is negligible in comparison with the speed of light in vacuum c, the operator $\hat{H}_{\text{int}}$ leads to an excellent description of these processes.

In order to describe the dynamics of the absorption by a single photon, we have to solve the time-dependent Schrödinger equation induced by the Hamiltonian $\hat{H}$. For studying the impact of the center of mass motion on the absorption process, we assume that the initial state of the system at time $t = t_0$ resembles a separable pure state of the form

$$|\psi_0\rangle = |g\rangle\,|\psi_{\text{cm}}\rangle\,|\psi_{\text{photonic}}\rangle \;. \tag{7.2}$$

Thereby, $|\psi_{\text{cm}}\rangle$ describes the pure initial state of the center of mass degree of freedom and $|\psi_{\text{photonic}}\rangle$ denotes the initial one-photon state of the radiation field. In the following, we are particularly interested in the center of mass induced dynamics of this single-photon excitation process for a photon state which is capable of exciting a two-level system located at the fixed position $\mathbf{x} = 0$, such as the focal point of a parabolic mirror, almost perfectly. As discussed in the previous chapter, without additional control of the photon emission and absorption processes, the corresponding wave packet is uniquely defined. It is given by an inward-moving dipole wave which can couple to the dipole matrix element of the atom perfectly and has an exponentially rising temporal profile, i.e., the time reversed version of the wave packet generated by the spontaneous emission process. As derived in chapter 5, the corresponding initial quantum state of the radiation field is given by

$$|\psi_{\text{photonic}}(t_0)\rangle \;=\; \sum_i \hat{a}_i^\dagger|0\rangle_{\text{rad}} \sqrt{\frac{\omega_i}{2\epsilon_0\hbar}} \frac{\mathbf{d}^* \cdot \mathbf{g}_i(\mathbf{x}=0)}{\omega_i - \omega_{eg} - i\Gamma/2} e^{i\omega_i t_{\text{out}}} \,. \tag{7.3}$$

7.3 DYNAMICS OF SINGLE-PHOTON ABSORPTION

In this section, we explore the dynamics of optimal resonant single photon absorption (in free-space) by a moving trapped two-level system whose Hamiltonian is given by Eq. (7.1). In view of the rotating wave approximation, the Hamiltonian (7.1) conserves the numbers of excitations. Therefore, for an initial state of the form of Eq. (7.2), the general solution of the Schrödinger equation is given by a pure quantum state which

is a superposition of the photonic vacuum state correlated with the excited two-level system and of a single-photon multimode state correlated with the two-level system in its ground state and with its center of mass degrees of freedom generally entangled with the field modes. As the center of mass motion is assumed to be non-relativistic, the resulting modification of the spontaneous photon emission process from the excited two-level system is negligible so that it is still described by the spontaneous decay rate Γ in free-space, i.e.,

$$\Gamma = \frac{\omega_{eg}^3 \mid \mathbf{d} \mid^2}{3\pi\epsilon_0\hbar c^3} . \tag{7.4}$$

From the time-dependent Schrödinger equation, we find that the probability of detecting the two-level system in its excited state $|e\rangle$ at time t is given by

$$\begin{aligned} P_e(t) &= \int_{t_0}^{t} dt_1 e^{i(\omega_{eg}+i\Gamma/2)(t-t_1)} \int_{t_0}^{t} dt_2 e^{-i(\omega_{eg}-i\Gamma/2)(t-t_2)} \\ &\quad \frac{\mathbf{d}^*}{\hbar} \cdot \langle\psi_{\rm cm}|\mathbf{G}^{(1)}(\hat{\mathbf{x}}_I(t_1),t_1,\hat{\mathbf{x}}_I(t_2),t_2)|\psi_{\rm cm}\rangle \cdot \frac{\mathbf{d}}{\hbar} . \end{aligned} \tag{7.5}$$

This excitation probability is determined by the mean value of the normally ordered field correlation tensor of first order, i.e.,

$$\mathbf{G}^{(1)}(\hat{\mathbf{x}}_I(t_1),t_1,\hat{\mathbf{x}}_I(t_2),t_2) = \langle\psi_{\rm photonic}|\hat{\mathbf{E}}_\perp^-(\hat{\mathbf{x}}_I(t_1),t_1)\otimes\hat{\mathbf{E}}_\perp^+(\hat{\mathbf{x}}_I(t_2),t_2)|\psi_{\rm photonic}\rangle ,$$

averaged over the two-level system's initially prepared center of mass state $|\psi_{\rm cm}\rangle$. Thereby, the position operator

$$\hat{\mathbf{x}}_I(t) = \exp(i\hat{H}_{\rm trap}(t-t_0)/\hbar)\ \hat{\mathbf{x}}\ \exp(-i\hat{H}_{\rm trap}(t-t_0)/\hbar)$$

denotes the time evolution of the center of mass position of the two-level system in the interaction picture. For the pure one-photon state $|\psi_{\rm photonic}\rangle$, the first order correlation tensor factorizes, i.e.,

$$\mathbf{G}^{(1)}(\mathbf{x}_1,t_1,\mathbf{x}_2,t_2) = \mathbf{F}^*(\mathbf{x}_1,t_1)\otimes\mathbf{F}(\mathbf{x}_2,t_2) ,$$

with the effective one-photon amplitude $\mathbf{F}(\mathbf{x},t) =_{\rm rad} \langle 0|\hat{\mathbf{E}}_\perp^+(\mathbf{x},t)|\psi_{\rm photonic}\rangle$. We obtain

$$\begin{aligned} P_e(t) &= \frac{1}{\hbar^2}\int_{t_0}^{t} dt_1 e^{i(\omega_{eg}+i\Gamma/2)(t-t_1)} \int_{t_0}^{t} dt_2 e^{-i(\omega_{eg}-i\Gamma/2)(t-t_2)} \\ &\quad \langle\psi_{\rm cm}|\mathbf{d}^*\cdot\mathbf{F}^*(\hat{\mathbf{x}}_I(t_1),t_1)\,\mathbf{F}(\hat{\mathbf{x}}_I(t_2),t_2)\cdot\mathbf{d}|\psi_{\rm cm}\rangle . \end{aligned} \tag{7.6}$$

The equation above resembles the expressions derived in Sec. 5.1. We reobtain these expressions by replacing the operators $\hat{\mathbf{x}}_I(t)$ in Eq. 7.6 by the fixed position $\mathbf{R}$, which corresponds to an infinitely steep trapping potential which locates the atom at position $\mathbf{R}$.

It should also be noted that the time evolution of the operators $\hat{\mathbf{x}}_I(t)$ entering in Eq. (7.6) describing the center of mass position during the photon absorption is only determined by the trapping potential. There is no term directly linked to the recoil of the atom caused by the absorption of the photon or its subsequent emission. This is connected to the fact that after absorbing the photon the atom experience its first recoil and after that just interacts with the vacuum state of the field. Thus, for absorbing the photon, the recoil does not play a role. After absorbing the photon, the atom just experiences a spontaneous decay, which is independent of the velocity and therefore

independent of the recoil in case that the speed of the atom is much smaller than the speed of light. Therefore, the recoil itself does not influence the probability for exciting the atom. The simple structure of Eq. (7.6) is thus a direct consequence of the fact that in a parabolic mirror with large focal length or in free-space the photon emitted by an atom does not return to the atom at a later point in time. If the photon would go back to the atom, the corresponding expression for the probability of exciting the atom would be much more complicated because we would have to take into account the momentum kick of the center of mass motion caused by the first absorption of the photon and its subsequent emission.

If the two-level system were positioned in the center of a spherically symmetric cavity of radius R with ideally conducting walls, for example, the discrete orthonormal mode functions coupling to the two level system in the dipole approximation would be given by

$$\begin{aligned} \mathbf{g}_n(\mathbf{x}) &= \sqrt{\frac{1}{R}}\nabla \times \left(j_1(\omega_n r/c)\ \mathbf{x} \times \nabla Y_1^0(\theta,\varphi)\right) \\ &= -\sqrt{\frac{3}{4\pi R}}\frac{\omega_n}{c}\left(e^{i\omega_n r/c}\mathbf{g}_n^{(+)}(\mathbf{x}) + e^{-i\omega_n r/c}\mathbf{g}_n^{(-)}(\mathbf{x})\right) \end{aligned} \tag{7.7}$$

with

$$\begin{aligned} \mathbf{g}_n^{(+)}(\mathbf{x}) &= -\mathbf{e}_r \cos\theta \left(\frac{1}{(\omega_n r/c)^2} + \frac{i}{(\omega_n r/c)^3}\right) \\ &\quad -\mathbf{e}_\theta \frac{\sin\theta}{2}\left(\frac{1}{(\omega_n r/c)^2} - i\left(\frac{1}{(\omega_n r/c)} - \frac{1}{(\omega_n r/c)^3}\right)\right) \end{aligned} \tag{7.8}$$

and with the angular momentum eigenfunction $Y_1^0(\theta,\varphi)$ [87]. For real-valued frequencies ω_n, the relation $\mathbf{g}_n^{(-)}(\mathbf{x}) = \left(\mathbf{g}_n^{(+)}(\mathbf{x})\right)^*$ applies. Here, $j_1(u) = \sin u/u^2 - \cos u/u$ denotes the spherical Bessel function of fractional order [87] and $r = \mid \mathbf{x} \mid$. The angle between the direction of the dipole matrix element $\mathbf{d}$ and $\mathbf{x}$ is denoted θ. Furthermore, $\mathbf{e}_r$ and $\mathbf{e}_\theta$ are the spherical coordinate unit vectors in the r and θ directions with the z-direction oriented parallel to the dipole vector $\mathbf{d}$. In the continuum limit of large cavity sizes, i.e., $\omega_{eg}R/c \gg 1$, the mode frequencies are given approximately by $\omega_n = c\pi(n+1)/R$ with $n \geq 0$ being an integer.

In the continuum limit, i.e., $R \to \infty$, this one-photon amplitude can be determined in a straightforward way by contour integration. Thus, we obtain the result

$$\begin{aligned} \mathbf{F}(\mathbf{x},t) &= -\frac{\hbar\Gamma}{\mathbf{d}\cdot\mathbf{e}_z}\left(\frac{3}{2}\mathbf{g}_n^{(+)}(\mathbf{x})\Theta(-t_+)e^{-i\omega_n t_+} \right. \\ &\quad \left. +\frac{3}{2}\mathbf{g}_n^{(-)}(\mathbf{x})\Theta(-t_-)e^{-i\omega_n t_-}\right)\Big|_{\omega_n=\omega_{eg}+i\Gamma/2} \end{aligned} \tag{7.9}$$

with $t_\pm = t - t_{\text{out}} \mp r/c$. Close to the ideal position $\mathbf{x} = 0$ of the two-level system, i.e., for $\eta = \omega_{eg}r/c \ll 1$, this one-photon amplitude simplifies to

$$\begin{aligned} \mathbf{F}(\mathbf{x},t) &= -\frac{\hbar\Gamma}{\mathbf{d}\cdot\mathbf{e}_z}e^{i(\omega_{eg}+i\Gamma/2)(t_{\text{out}}-t)}\Theta(t_{\text{out}}-t) \\ &\quad \times\left(\mathbf{e}_z\left(1-\frac{\eta^2}{10}\right) + \mathbf{e}_\theta \sin\theta\frac{\eta^2}{10} + O(\eta^4)\right). \end{aligned} \tag{7.10}$$

For a two-level system trapped in an infinitely steep potential at position $\mathbf{x} = 0$ and for times $t \geq t_0$, this one-photon excitation probability reduces to

$$P_{id}(t) = e^{-\Gamma|t_{\text{out}}-t|}\left(1-e^{-\Gamma(\tau-t_0)}\right)^2 \tag{7.11}$$

with $\tau = t\Theta(t_{\text{out}} - t) + t_{\text{out}}\Theta(t - t_{\text{out}})$. In this idealized situation, almost unit excitation probability can be achieved for $\Gamma\,(t_{\text{out}} - t_0) \gg 1$.

As already discussed in the previous chapters and in accordance with current experimental activities [24, 30, 59], this excitation process can be realized with the help of a parabolic mirror with large focal length f and with the two-level system's trap centered at the parabola's focal point $\mathbf{x} = 0$. Inserting Eq. (7.9) into Eq. (7.5) yields the time dependence of the excitation probability $P_e(t)$.

In the following sections, we distinguish two interesting dynamical regimes. If the trap frequency ω_T of a harmonically trapped two-level system is much larger than the spontaneous decay rate Γ, the spontaneous decay process is so slow that details of the center of mass motion are averaged out in the time integrals of Eq. (7.5). Consequently, the excitation probability dominantly depends on the time averaged center of mass motion. In the opposite limit, i.e., $\omega_T \ll \Gamma$, the spontaneous photon emission process occurs almost instantaneously on the time scale of the center of mass motion. Consequently, the time evolution of the excitation probability depends on details of the two-level system's center of mass motion in the trap during the short time period in which the photon absorption takes place. Later on, we show that in this regime the success probability for absorbing the photon can be enhanced by preparing a suitable initial center of mass state. In addition to these two dynamical regimes, we can discriminate the physical situations by the ratio between Δx, the spatial extension of the center of mass state, and λ_{eg}, the typical wavelength of the incoming photon wave packet. For $\frac{\Delta x}{\lambda_{eg}} \ll 1$, the so-called Lamb-Dicke regime, the spatial variation of the incoming wave packet is small compared to the length scale induced by the center of mass state and we can approximate the photon amplitude $\mathbf{F}(\mathbf{x}, t)$, a truncated Taylor series. If $\frac{\Delta x}{\lambda_{eg}}$ approaches one or becomes large than one, this method will not work anymore and the evaluation of $P_e(t)$ becomes much more complicated.

7.4 SINGLE-PHOTON ABSORPTION AND STRONG CONFINEMENT OF THE CENTER OF MASS MOTION

In this section, we study the photon absorption in case of a strong confinement of the center of mass motion, i.e., $\frac{\Delta x}{\lambda_{eg}} \ll 1$. In this case, we capture the spatial variation of the incoming wave packet by expanding the photon amplitude $\mathbf{F}(\mathbf{x}, t)$ in a Taylor expansion up to second order in $\mathbf{x}$. By doing so, we obtain the result

$$P_e(t) = \Gamma^2 \int_{t_0}^{t} dt_1 \int_{t_0}^{t} dt_2\, \Theta(t_{\text{out}} - t_1)\Theta(t_{\text{out}} - t_2) e^{-\Gamma(t + t_{\text{out}} - t_1 - t_2)} \times \left(1 - 2\frac{\omega_{eg}^2}{10c^2}\langle\psi_{\text{cm}}| \left(\hat{z}_I^2(t_2) + 2\hat{x}_I^2(t_2) + 2\hat{y}_I^2(t_2)\right) |\psi_{\text{cm}}\rangle + O(\eta^4)\right) \tag{7.12}$$

with $\hat{x}_I(t), \hat{y}_I(t), \hat{z}_I(t)$ denoting the time-dependent Cartesian x, y, z components of the position operator of the center of mass degrees of freedom in the interaction picture. Thereby, the z-direction is oriented parallel to the dipole vector $\mathbf{d}$. In the following, we assume that the atom or ion is confined in a harmonic trap with a trapping potential

$$V_T(\mathbf{x}) \quad = \quad m\omega_j^2 z^2/2 + m\omega_x^2 x^2/2 + m\omega_y^2 y^2/2\,. \tag{7.13}$$

In the interaction picture, the resulting dynamics of the z component of the center of mass position is given by

$$\hat{z}_I(t) = \hat{z}\cos(\omega_z(t-t_0)) + \frac{\hat{p}_z}{m\omega_z}\sin(\omega_z(t-t_0)) \tag{7.14}$$

with analogous expressions for the other Cartesian components. Inserting these expressions in Eq. (7.12) yields the result

$$\frac{P_e(t)}{P_{id}(t)} = 1 - \frac{\omega_{eg}^2}{5c^2}\left(\frac{\hbar A_z(\tau)}{2m\omega_z} + 2\sum_{j=x,y}\frac{\hbar A_j(\tau)}{2m\omega_j}\right) \tag{7.15}$$

with $\tau = t\Theta(t_{\rm out}-t) + t_{\rm out}\Theta(t-t_{\rm out})$ and with

$$\begin{aligned} A_j(\tau) &= \langle\psi_{\rm cm}|\hat{b}_j^{\dagger 2}|\psi_{\rm cm}\rangle\frac{\Gamma e^{2i\omega_j(\tau-t_0)}}{\Gamma+2i\omega_j}\frac{1-e^{-(\Gamma+2i\omega_j)(\tau-t_0))}}{1-e^{-\Gamma(\tau-t_0)}} \\ &\quad +\langle\psi_{\rm cm}|(\hat{b}_j^{\dagger}\hat{b}_j+1/2)|\psi_{\rm cm}\rangle + c.c. \end{aligned} \tag{7.16}$$

for $j = x, y, z$.

According to Eq. (7.15) for small spontaneous photon emission rates, i.e., $\Gamma \ll \omega_j$, and large interaction times, i.e., $\Gamma(\tau - t_0) \gg 1$, the excitation probability $P_e(t)$ is determined by the time averaged center of mass motion. In this dynamical regime, we have $A_j(\tau) = 2\langle\psi_{\rm cm}|(\hat{b}_j^{\dagger}\hat{b}_j + 1/2)|\psi_{\rm cm}\rangle + O(\Gamma/\omega_j)$ so that the deviation of the excitation probability $P_e(t)$ from its ideal value $P_{id}(t)$ is proportional to the mean energy of the center of mass degrees of freedom in the harmonic trap, i.e.,

$$\begin{aligned} \frac{P_e(t)}{P_{id}(t)} &= 1 - \frac{\omega_{eg}^2}{5c^2}\left(\frac{\hbar\omega_z\langle\psi_{\rm cm}|(\hat{b}_z^{\dagger}\hat{b}_z+1/2)|\psi_{\rm cm}\rangle}{m\omega_z^2}\right. \\ &\quad \left. +2\sum_{j=x,y}\frac{\hbar\omega_j\langle\psi_{\rm cm}|(\hat{b}_j^{\dagger}\hat{b}_j+1/2)|\psi_{\rm cm}\rangle}{m\omega_j^2}\right). \end{aligned} \tag{7.17}$$

As the mean energy of a harmonic oscillator is lower bounded by its zero point energy in this dynamical regime, the excitation probability $P_e(t_{out})$ assumes its maximal value if the center of mass degrees of freedom are prepared in the ground state of the harmonic trap so that $\hat{b}_j|\psi_{\rm cm}\rangle = 0$ for $j = x, y, z$.

According to Eq. (7.15) in the opposite limit of long interaction times, i.e., $\Gamma(\tau - t_0) \gg 1$, but large spontaneous photon emission rates, i.e., $\Gamma \gg \omega_j$, the excitation probability $P_e(t)$ is determined by the center of mass motion at time $\tau = t\Theta(t_{\rm out}-t) + t_{\rm out}\Theta(t - t_{\rm out})$. In this dynamical regime, we obtain the approximate result

$$A_j(\tau) = \langle\psi_{\rm cm}|\left(\hat{b}_j^{\dagger}e^{i\omega_j(\tau-t_0)} + \hat{b}_j e^{-i\omega_j(\tau-t_0)}\right)^2|\psi_{\rm cm}\rangle \tag{7.18}$$

by neglecting terms of the order of $O(\omega_j/\Gamma)$. The resulting strong dependence of the excitation probability $P_e(t)$ on the center of mass motion at time τ can be exploited for minimizing the deviations of the excitation probability from its ideal values $P_{id}(t)$. This can be achieved by preparing appropriate initial states $|\psi_{\rm cm}\rangle$ which minimize the quantities $A_j(\tau)$. For this purpose, squeezed vacuum states [88] of the center of mass motion of the form

$$|\psi_{\rm cm}\rangle = \hat{S}(\xi_z)\hat{S}(\xi_x)\hat{S}(\xi_y)|0\rangle_{\rm cm} \tag{7.19}$$

offer interesting possibilities. In Eq. (7.19), $|0\rangle_{\rm cm}$ denotes the ground state of the harmonic trap, i.e., $\hat{b}_j|0\rangle_{\rm cm} = 0$ for $j = x, y, z$, and

$$\hat{S}(\xi_j) \;=\; e^{\xi_j^* \hat{b}_j^2/2 - \xi_j \hat{b}_j^{\dagger 2}/2} \tag{7.20}$$

are the squeezing operators for the Cartesian components j. For complex valued squeezing parameters of the form $\xi_j = r_j \exp(2i\varphi)$ with $r_j > 0$, for example, we obtain the result

$$\frac{P_e(t)}{P_{id}(t)} \;=\; 1 - \frac{\omega_{eg}^2}{5c^2}\left(\Delta z_0^2 e^{-2r_z} + 2\Delta x_0^2 e^{-2r_x} + 2\Delta y_0^2 e^{-2r_y}\right) \tag{7.21}$$

at all times t for which $\sin(\omega_j(\tau - t_0) - \varphi) = 0$. Thereby, the quantities $\Delta z_0 = \sqrt{\hbar/(2m\omega_z)}$ etc. denote the extensions of the ground state of the harmonic trap along the corresponding Cartesian directions. In contrast, at times for which $\cos(\omega_j(\tau - t_0) - \varphi) = 0$, these extensions are enhanced periodically by corresponding factors of e^{2r_z} etc. Thus, strong squeezing of the initial state of Eq. (7.19) in all directions, i.e., $r_j \gg 1$, implies a significant increase of the excitation probability at all interaction times t with $\sin(\omega_j(\tau - t_0)) = 0$. As we see later on, this can be used to overcome limitations of the excitation probability caused by the finite trap frequency of realistic traps.

7.5 SINGLE-PHOTON ABSORPTION AND WEAK CONFINEMENT OF THE CENTER OF MASS MOTION

In this section, we extend our investigation to the case of a weak confinement of the center of mass motion. For this purpose, we also have to deal with large Lamb-Dicke parameters, i.e., $\frac{\Delta x}{\lambda_{eg}} \gg 1$.

In these cases, the center of mass motion is not confined to a region around the ideal position $\mathbf{x} = 0$ small in comparison with the wavelength of the resonantly absorbed photon. Hence, a Taylor expansion of the mode functions $\mathbf{g}_n(\mathbf{x})$ around $\mathbf{x} = 0$ is no longer adequate. We start with the general form of the one-photon amplitude as given by Eq. (7.9). Inserting this one-photon amplitude into Eq. (7.5) yields the excitation probability.

In the following, we focus on scenarios with $\Gamma\Delta x/c \ll 1$, which is well satisfied for typical spontaneous decay times $1/\Gamma$ of dipole allowed optical transitions of the order of nanoseconds and extensions of center of mass wave packets Δx small in comparison with a few meters. For $\Gamma\Delta x/c \ll 1$, this one-photon amplitude can be further simplified to the expression

$$\begin{aligned}\mathbf{F}(\mathbf{x}, t) \;=\; & -\frac{3\hbar\Gamma}{2\mathbf{d}\cdot\mathbf{e}_z}\Theta(t_{\rm out} - t)e^{-i(\omega_{eg} + i\Gamma/2)(t - t_{\rm out})} \\ & \times \left(\mathbf{g}_n^{(+)}(\mathbf{x})e^{i\omega_n r/c} + \mathbf{g}_n^{(-)}(\mathbf{x})e^{-i\omega_n r/c}\right)|_{\omega_n = \omega_{eg}}\,.\end{aligned} \tag{7.22}$$

In many trapping experiments, typical spontaneous photon emission rates of electronic transitions Γ are large in comparison with typical trap frequencies, i.e., $\Gamma \gg \omega_T$. In this dynamical regime, the single-photon absorption process takes place almost instantaneously on the characteristic time scale induced by the trapping potential. To be precise, we demand that for the typical velocities

$$\Delta v(t) = \sqrt{\langle\psi_T|\left(\tfrac{d}{dt}\hat{\mathbf{x}}_I(t)\right)^2|\psi_T\rangle} \tag{7.23}$$

the condition

$$\Delta v(t)/\Gamma \ll \lambda_{eg} \tag{7.24}$$

is satisfied in a time interval a view lifetimes of the excited state $1/\Gamma$ around t_{out}. This can also be seen as condition for a negligible Doppler shift compared to the spontaneous decay rate of the atomic transition. In this dynamical regime, the integration over times t_1 and t_2 appearing in Eq. (7.5) can be performed with the help of partial integration [81] and the excitation probability at time t is determined dominantly by the position operators $\hat{\mathbf{x}}_I(t_1)$ and $\hat{\mathbf{x}}_I(t_2)$ at time $\tau = t\Theta(t_{\text{out}} - t) + t_{\text{out}}\Theta(t - t_{\text{out}})$ and at the initial time t_0. Consequently, for large interaction times, i.e., $\Gamma(\tau - t_0) \gg 1$, and by neglecting terms exponentially small in this parameter, Eq. (7.5) simplifies to

$$\begin{aligned}\frac{P_e(t)}{P_{id}(t)} &= \frac{9}{4}\langle\psi_{\text{cm}}| \Big(\mathbf{e}_z \cdot \mathbf{g}_n^{(+)}(\hat{\mathbf{x}}_I(\tau))e^{i\omega_n|\hat{\mathbf{x}}_I(\tau)|/c} \\ &\quad + \mathbf{e}_z \cdot \mathbf{g}_n^{(-)}(\hat{\mathbf{x}}_I(\tau))e^{-i\omega_n|\hat{\mathbf{x}}_I(\tau)|/c}\Big)^2 |_{\omega_n=\omega_{eg}}\, |\psi_{\text{cm}}\rangle. \end{aligned} \tag{7.25}$$

For a spherically symmetric trapping potential, a simple analytical relation can be obtained from Eq. (7.25) if at the observation time t the center of mass degrees of freedom can be described by an isotropic Gaussian state $\hat{\rho}_{\text{cm}}(\tau)$ centered around $\mathbf{x} = 0$ with spatial variance $\text{Tr}\left[\hat{\rho}_{\text{cm}}(\tau)\,\hat{\mathbf{x}}^2\right] \equiv \text{Tr}\left[\hat{\rho}_{\text{cm}}\,\hat{\mathbf{x}}_I^2(\tau)\right]$, i.e.,

$$\frac{P_e(t)}{P_{id}(t)} = \frac{3e^{-2\eta_0^2}}{10\eta_0^6}\left(-2\eta_0^4 - \eta_0^2 + \left(2\eta_0^4 - \eta_0^2 + 1\right)e^{2\eta_0^2} - 1\right) \tag{7.26}$$

with the effective (time-dependent) Lamb-Dicke parameter

$$\eta_0 = \tfrac{\omega_{eg}}{c_0}\sqrt{\text{Tr}\left[\hat{\rho}_{\text{cm}}\,\hat{\mathbf{x}}_I^2(\tau)\right]/3}\,. \tag{7.27}$$

This result can be applied to a large class of center of mass states including squeezed vacuum and thermal states (with respect to the isotropic trapping potential). The dependence of the excitation probability $P_e(t)/P_{id}(t)$ on the effective Lamb-Dicke parameter η_0 is depicted in Fig. 7.2 for $\Gamma \gg \omega_{\text{T}}$. The corresponding time dependence of the excitation probability $P_e(t)$ is illustrated in Fig. 7.3 for several values of η_0. It is apparent that for small effective Lamb-Dicke parameters η_0 almost perfect excitation is achievable at time t_{out}. For all effective Lamb-Dicke parameters, almost instantaneous excitation with a large spontaneous decay rate, i.e., $\Gamma \gg \omega_T$, is more effective than excitation with a small spontaneous decay rate, i.e., $\Gamma \ll \omega_T$.

7.6 OPTIMIZING SINGLE-PHOTON ABSORPTION BY COHERENT CONTROL OF THE CENTER OF MASS MOTION

As discussed in Sec. 7.5, the maximum probability for exciting the two-level system in the regime $\Gamma \gg \omega_{\text{trap}}$ is mainly limited by the spatial width of the center of mass state during the short time of the order $1/\Gamma$ in which the absorption process takes place. This limitation is of particular significance in cases in which no sub-Doppler cooling techniques are applied and in which the spatial width is not sufficiently small. A straightforward strategy to overcome this hurdle is to increase the depth of the trap and thus enhance the confinement of the center of mass degrees of freedom. This procedure, however, is typically limited by experimental constraints and therefore

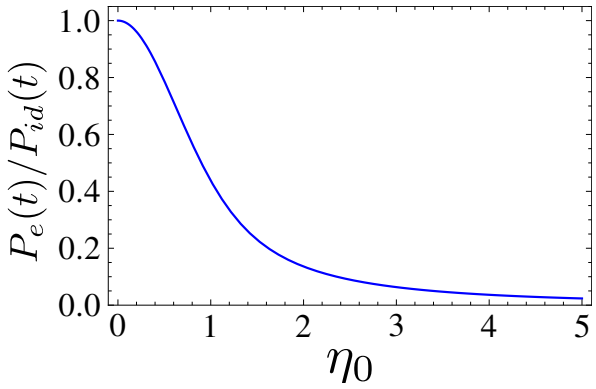

Figure 7.2.: Probability $P_e(t)$ of exciting a two-level system in a spherically symmetric trap and its dependence on the effective Lamb-Dicke parameter η_0 (see Eq. (7.27)): The center of mass state $\hat{\rho}_{\text{cm}}(\tau)$ is assumed to be an isotropic Gaussian state. The spontaneous decay rate is assumed to be large compared to the trap frequency, i.e., $\Gamma \gg \omega_{\text{trap}}$.

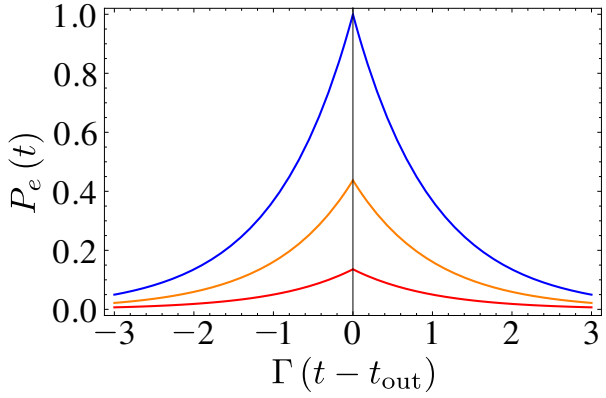

Figure 7.3.: Time dependence of the excitation probability $P_e(t)$ in a spherical symmetric trap for an isotropic Gaussian center of mass state $\hat{\rho}_{\text{cm}}(\tau)$: The parameter η_0 characterizing the center of mass state is chosen to be $\eta_0 \to 0$ (blue), $\eta_0 = 1$ (orange), and $\eta_0 = 2$ (red). The trapping frequency is small, i.e., $\Gamma \gg \omega_T$, so that the time dependence of η_0 can be neglected. The interaction time is large, i.e., $\Gamma(\tau - t_0) \gg 1$.

cannot constitute an ultimate solution. As discussed in Sec. 7.4, even if the relevant trapping frequency becomes larger than the spontaneous photon emission rate, the achievable spatial confinement of the center of mass state is limited ultimately by the zero point fluctuations in the trap. However, as discussed in Sec. 7.5, if the photon absorption process takes place almost instantaneously, it is possible to increase the excitation probability by preparing a center of mass state whose width is sufficiently small during the photon absorption process, such as a squeezed state, for example. The squeezing of the center of mass state in ion traps has already been demonstrated in experiment [89, 90]. One method for achieving significant squeezing is to modulate the trapping frequency with twice the average trapping frequency [91]. This way, almost perfect one-photon excitation can be achieved even in a weakly confining harmonic trapping potential.

For this purpose, let us consider the dynamics of the center of mass motion of a non-relativistic particle of mass m in a periodically modulated spherically symmetric harmonic trapping potential of the form

$$\begin{aligned} V_T(\mathbf{x},t) &= \frac{1}{2}m\omega^2(t)\mathbf{x}^2, \\ \omega^2(t) &= \omega_T^2 + \omega_T^2\delta\sin(\omega_M(t-t_0)) \,. \end{aligned} \tag{7.28}$$

The trapping potential above corresponds to the well-studied problem of a parametric oscillator. The time evolution of the classical as well as the quantum mechanical problem can be expressed by using solutions of the Mathieu differential equation [87]. It is well known that the solutions of the Mathieu equation become unstable in the region $\omega_M \approx 2\omega_T$ [87]. This phenomenon of parametric resonance can be used to achieve significant squeezing of the center of mass state.

If the modulation strength of the trapping potentials is small, i.e., $\mid \delta \mid \ll 1$, and $\omega_M = 2\omega_T$, the dynamics of the center of mass motion can be determined perturbatively. The unperturbed dynamics is defined by the modulation strength $\delta = 0$ and by the corresponding explicitly time independent Hamiltonian $\hat{H}_0 = \hat{\mathbf{p}}^2/(2m) + m\omega_T^2\mathbf{x}^2/2$. The resulting time evolution of an initially prepared pure state $|\psi_{\rm cm}\rangle$ is given by

$$|\psi_{\rm cm}(t)\rangle = \hat{S}(\xi_x(t))\hat{S}(\xi_y(t))\hat{S}(\xi_z(t))e^{-i\hat{H}_0(t-t_0)/\hbar}|\psi_{\rm cm}\rangle \tag{7.29}$$

with the time-dependent squeezing parameters $\xi_x(t) = \xi_y(t) = \xi_z(t) = r(t)e^{-2i\varphi(t)}$ being approximately determined by

$$r(t) = \omega_T\delta(t-t_0)/4, \varphi(t) = \omega_T(t-t_0) - \pi/2 \,. \tag{7.30}$$

The time evolution of the squeezing parameter $r(t)$ is depicted in the numerical results of Fig. 7.4 for several scenarios. The plot illustrates that for $\omega_M = 2\omega_T$ the numerical results are in excellent agreement with the approximate analytical expression of Eq. (7.30) even for moderately large modulation amplitudes. Even if the condition $\omega_M = 2\omega_T$ is violated, significant squeezing can be achieved. For larger deviations of ω_M from $2\omega_T$ (roughly $\mid \omega_M^2 - (2\omega_T)^2 \mid \gtrsim 2\delta\omega_T^2$), a transition from an unstable solution of the Mathieu equation to a stable solution takes place. Squeezing can also be achieved in the stable region, but in this case, the value of the squeezing parameter is bounded from above (see the solid blue line in Fig. 7.4).

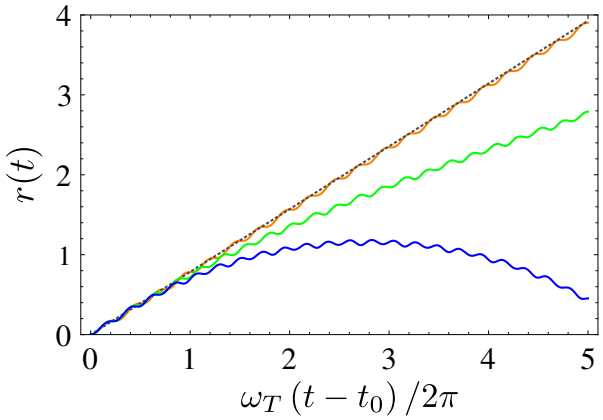

Figure 7.4.: Time evolution of the squeezing parameter $r(t)$ for $\delta = 0.5$: Numerically exact results for modulation frequencies $\omega_M = 2\omega_T$ (orange solid line), $\omega_M = 2.2\omega_T$ (green solid line), $\omega_M = 2.3\omega_T$ (blue solid line), and the associated approximation (dotted line) given by Eq. (7.30).

For an initially prepared energy eigenstate of the unperturbed trapping Hamiltonian $\hat{H}_0$, the corresponding mean values and variances of the position operator are given by

$$\langle \hat{\mathbf{x}}_I(t) \rangle = 0, \tag{7.31}$$

$$\langle \hat{\mathbf{x}}_I^2(t) \rangle = \frac{\langle \psi_{\rm cm} | \hat{H}_0 | \psi_{\rm cm} \rangle}{m\omega_T^2} \left(e^{-2r(t)} \cos^2 \varphi(t) + e^{2r(t)} \sin^2 \varphi(t) \right). \tag{7.32}$$

This implies that also for any incoherent mixture of energy eigenstates, such as a thermal state, for $\delta > 0$ at times t with $\sin(\varphi(t)) = 0$ the position uncertainties are squeezed significantly. For a thermal state, the mean energy of the unperturbed isotropic harmonic motion in the trap at temperature T is given by $\langle \hat{H}_0 \rangle = 3\hbar\omega_T \, (1/2 + 1/[\exp(\hbar\omega_T/(kT)) - 1])$. The squeezing $r(t)$ induced by the periodic modulation of the trapping frequency with twice the trapping frequency ω_T increases linearly with the interaction time $(t - t_0)$. Thus, it is capable of reducing the uncertainty around the mean position $\langle \hat{\mathbf{x}}_I(t) \rangle = 0$ significantly even for an initially prepared thermal state. Consequently, even if the center of mass motion is confined only weakly by a trapping potential, the excitation probability can achieve values very close to the ideal motionless case.

The influence of squeezing of initially prepared thermal center of mass states on the excitation probability $P_e(t)$ is illustrated in Fig. 7.5 for several scenarios. These results were derived under the assumption that the condition stated in Eq. (7.24) is satisfied. If the degree of squeezing becomes too large, this condition is violated and our results do not apply. However, for typical experimental parameters (see, for example, [24, 30, 59]) a significant increase of the excitation probability can be achieved before the condition (7.24) is violated. Although our discussion has concentrated on a spherically symmetric harmonic trapping potential, generalizations to anisotropic cases are straightforward. They lead to different degrees of squeezing in different directions.

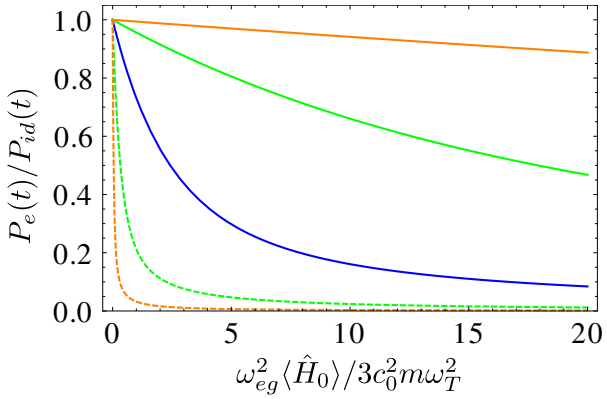

Figure 7.5.: Influence of squeezing of initially prepared thermal center of mass states on excitation probability $P_e(t)$: The parameters are $r = 0$ (blue), $r = 1$ (green), and $r = 2$ (orange). The solid lines correspond to $\sin^2(\varphi(t)) = 0$ and the dashed lines correspond to $\sin^2(\varphi(t)) = 1$ during the short time the absorption of the photon takes place.

7.7 SUMMARY

In this chapter, we have extended our investigation of matter-field coupling on the single-photon level by taking the center of mass motion into account. In particular, we have concentrated on the excitation of a single two-level atom by a single photon in free-space.

It has been demonstrated that the achievable excitation probability depends crucially on the ratio between the time scales of spontaneous photon emission and absorption on the one hand and of the center of mass motion in the trap on the other hand. If single-photon absorption and emission take place on a time scale long in comparison with the characteristic time scale of the center of mass motion in the trap, it is the time averaged center of mass motion which determines and limits the achievable single-photon excitation probability. In the opposite limit of fast spontaneous photon emission and absorption, it is the spatial width of the center of mass wave packet at the absorption time which limits the achievable single-photon excitation probability. Thus, due to the finite trap frequency of realistic setups, the excitation probability is thereby typically limited especially if the center of mass state is not cooled to the ground state of the trap. However, in the limit of fast spontaneous photon emission and absorption, the probability for exciting the atom can be increased significantly by squeezing the spatial width of the center of mass wave packet. By modulating a harmonic trapping potential with twice the trapping frequency and inducing parametric resonance, significant squeezing at particular times during the periodic center of mass motion can be achieved. This way, the single-photon wave packets can reach almost perfect excitation of a two-level system in free-space. This holds true even if the center of mass motion is only weakly confined and prepared in a thermal state initially.

8

PHOTON PATH REPRESENTATION FOR MULTI-PHOTON STATES

In this chapter, we extend our previous investigations of matter-field coupling by incorporating resonant multi-photon processes. So far, we have focused on situations were, at most, a single photon was present in the quantized radiation field. This allowed us to describe the corresponding dynamics of the system by using the single photon-path-representation developed in chapter 3. We extend the photon-path-representation to also include multi-photon processes in an extreme multimode environment.

The investigation of multi-photon processes in the presence of multimode environments is of interest due to the emergence of a new approach for harnessing the nonlinear optical processes induced by the coupling of the radiation field to single quantum emitters coupled to one-dimensional waveguides. However, this approach is inherently connected to multimode scenarios in which a large number of field modes participates in the coupling of the quantum emitters to the radiation field. This vast number of degrees of freedom complicates the theoretical investigation, especially, if highly non-classical multi-photon states, such as photon number states are involved in the systems dynamics. Such states have already been realized in experiment [92, 93] and are of great interest for applications such as quantum information processing and quantum communication. Hence, it is of importance to develop suitable theoretical methods to investigate the matter-field interaction involving highly non-classical multi-photon states and taking into account a multimode description of the radiation field.

In recent years, several methods addressing this issue have been developed. The Bethe-ansatz [94] as well as the input-output formalism [95] have been used to analyze the photon transport in a waveguide with an embedded qubit and one- and two-photon scattering matrix elements have been evaluated [96, 97]. Similar techniques have been applied to evaluate scattering matrix elements for even higher photon number states [98–101]. These methods can also be used to study effects which are of interest for many applications in quantum information processing, such as a cavity-free photon blockade [102] or a source of strongly correlated photons [103]. Recently, the input-output formalism has been generalized to treat many spatially distributed atoms coupled to a common waveguide [104]. Particular interesting phenomena arise when non-Markovian processes are investigated. Recently, a multi-photon scattering theory has been developed to treat [105] these kinds of situations. Starting from initial coherent states, similar to the technique developed by Mollow [37], displacement transformations are applied and generalized master equations for describing the dynamics have been derived. By exploiting suitable relations between coherent states and photon number states, the scattering matrix elements for several scenarios of interest have been evaluated.

We drive this line of research forward by developing a diagrammatic method for accessing the non-Markovian time evolution of highly non-classical multi-photon number states interacting with multiple quantum emitters. Similar to the photon-path-representation for single-photon states developed in chapter 3, the diagrammatic method presented here allows the interpretation of the systems dynamics in terms sequence of spontaneous emission and absorption processes interconnected by photons propagating from one quantum emitter to another or being reflected by a boundary of a waveguide or a mirror. Hence, we refer to our method as photon-path-representation for multi-photon states. This photon-path-representation allows us not only to evaluate transition amplitudes between initial and final states in the form of a scattering matrix but also enables us to study the full time evolution of the quantum state describing the combined system of emitters and radiation field. Our method directly addresses the time evolution of single quantum emitters interacting with photon number states without exploiting the properties of coherent states in an intermediate step of the calculation. This photon-path-representation is not only restricted to one-dimensional waveguides but can also be used to evaluate the time evolution of several quantum emitters interacting with the radiation field in large or half-open cavities or even in free-space. We, thereby, used a similar technique as the one developed by Mollow [37] for describing the spontaneous decay process but we adapted and extended this method to be able to evaluate the time evolution of initial photon number states and to take multiple atoms and the possible presence of a cavity into account. For the sake of simplicity, we restrict our considerations to two-level systems, but it is an easy task to generalize the multi-photon-path-representation to describe general multi-level systems.

The main advantage of this method is that for evaluating the time evolution for finite times and finitely many photons exactly only a finite number of diagrams has to be taken into account. This is achieved by exploiting the retardation effects caused by the multimode radiation field and the properties of the initial photon number states. The accuracy of this diagrammatic method is just limited by the dipole approximation and the assumption that the time scale induced by the atomic transition frequencies is by far the shortest relevant for the dynamics of the system. Thus, our method offers the possibility to study nonlinear and non-Markovian processes induced by resonant matter-field interactions involving highly non-classical multi-photon states and the full multimode description of the radiation field without further approximations in a descriptive diagrammatic fashion. This is not only interesting from a fundamental point of view but also from an applied perspective to accomplish tasks relevant for quantum information processing for example.

This chapter is organized as follows. In Sec. 8.1, we introduce our theoretical model and the approximations involved. The multi-photon-path-representation for describing the time evolution of relevant quantum mechanical transition amplitudes is presented in Sec. 8.2 and is applied to several physical scenarios in Sec. 8.3.

8.1 QUANTUM ELECTRODYNAMICAL MODEL

We revisit our description of N quantum emitters, e.g., atoms or ions situated at the positions $\mathbf{R}_A$ ($A \in \{1,2,...N\}$), interacting with the bosonic environment in a one-dimensional waveguide or the radiation field confined in large or half-open cavities or even in free-space. For the sake of simplicity, we assume that the quantum emitters can be described by identical two-level systems, in the following just referred to as atoms.

The atoms are assumed to be trapped in such a way that their center of mass motion is negligible. The dipole matrix element of atom A is given by $\mathbf{d}_A = \langle e|_A \hat{\mathbf{d}}_A |g\rangle_A$ and the corresponding transition frequency is denoted ω_{eg}. In the following, we assume that the dipole and the rotating-wave approximation (RWA) are applicable. For justifying the RWA, we assume that the time scale induced by the atomic transition frequency ω_{eg} is by far the shortest relevant for the systems dynamics. Thus, the interaction between the atoms and the quantized electromagnetic field can be described by the Hamiltonian

$$\hat{H} = \hat{H}_0 + \hat{H}_1 \tag{8.1}$$

with

$$\hat{H}_0 = \sum_i \hbar\omega_i \hat{a}_i^\dagger \hat{a}_i + \hbar\omega_{\mathrm{eg}} \sum_{A=1}^{N} |e\rangle_A \langle e|_A \ , \tag{8.2}$$

$$\hat{H}_1 = -\sum_{A=1}^{N} \hat{\mathbf{E}}_\perp^-(\mathbf{x}_A) \cdot \hat{\mathbf{d}}_A^- + \mathrm{H.c.} \tag{8.3}$$

and with the dipole transition operator

$$\hat{\mathbf{d}}_A^- = \left(\hat{\mathbf{d}}_A^+\right)^\dagger = \mathbf{d}_A^* |g\rangle_A \langle e|_A \tag{8.4}$$

of the atom A. The coupling to the radiation field is modeled by introducing suitable field operators $\hat{\mathbf{E}}_\perp^\pm(\mathbf{x}_A)$. The field operators can be expressed by introducing suitable orthonormal mode functions $\mathbf{g}_i(\mathbf{x})$

$$\hat{\mathbf{E}}_\perp^-(\mathbf{x}) = \left(\hat{\mathbf{E}}_\perp^+(\mathbf{x})\right)^\dagger = -i\sum_i \sqrt{\frac{\hbar\omega_i}{2\epsilon_0}} \mathbf{g}_i(\mathbf{x}) \hat{a}_i^\dagger \ . \tag{8.5}$$

The bosonic environment respectively the radiation field is modeled by choosing suitable mode functions with suitable eigenfrequencies ω_i.

8.2 MULTI-PHOTON-PATH-REPRESENTATION

8.2.1 *Analytical solution of the Schrödinger equation*

In this chapter, we investigate the time evolution of initial multi-photon number states with n_P photonic and n_A atomic excitations which are of the form

$$|\psi(t_0)\rangle = \prod_{i=1}^{n_P} \left(\sum_j f_j^{(i)}(t_0) a_j^\dagger \right) |0\rangle^P \prod_{i=1}^{n_A} |e\rangle_{A_i} \langle g|_{A_i} |G\rangle^A \tag{8.6}$$

with $|0\rangle^P$ representing the vacuum state of the field and $|G\rangle^A = |g\rangle_1 ... |g\rangle_N$ denoting the ground state of the whole atomic system. The $f_j^{(i)}(t_0)$ have to be chosen such that $\langle \psi(t_0), \psi(t_0)\rangle = 1$ and each of the sums $\sum_j f_j^{(i)}(t_0) a_j^\dagger$ represents an initial single-photon wave packet.

To develop the photon-path-representation, we reformulate the Schrödinger equation induced by the Hamilton operator $\hat{H}$ in form of a suitable integral equation. In a next step, this integral equation can be used to perform a fix-point iteration which generates the exact solution after reaching convergence.

At first, we switch to the interaction picture in which the Schrödinger equation is given by

$$i\hbar\frac{d}{dt}\left|\widetilde{\psi}(t)\right\rangle = \hat{\widetilde{H}}_1(t)\left|\widetilde{\psi}\right\rangle \tag{8.7}$$

with

$$\hat{\widetilde{H}}_1(t) = e^{i/\hbar\hat{H}_0(t-t_0)}\hat{H}_1 e^{-i/\hbar\hat{H}_0(t-t_0)} \tag{8.8}$$

and $|\widetilde{\psi}(t)\rangle$ denoting the wave function in the interaction picture. By integrating this equation, we obtain

$$\left|\widetilde{\psi}(t)\right\rangle = -\frac{i}{\hbar}\int_{t_0}^{t}\hat{\widetilde{H}}_1(t_1)\left|\widetilde{\psi}(t_1)\right\rangle dt_1 + \left|\psi(t_0)\right\rangle \ . \tag{8.9}$$

Eq. (8.9) could be used to define such an iteration procedure mentioned previously. The drawback of this procedure, however, would be that an infinite number of iterations is required in order to approach the exact solution even if we are only interested in a finite time interval. The reason for this complication are processes which can be understood as the absorption of a photon almost immediately after its emission (on the time scale $1/\omega_{eg}$). It is well known that such processes lead to the spontaneous decay of the excited atoms [37, 106]. For defining an iteration procedure which terminates after a finite number of steps, we have to modify the integral equation in order to take the spontaneous decay process directly into account. It turns out that all the other possible processes are connected to intrinsic time delays induced by the finite speed of light. These time delays cause the corresponding iteration procedure to terminate after a finite number of iterations if a finite time interval and a finite number of initial photons is considered.

In order to modify the integral equation (8.9), we split the integral in two parts and obtain

$$\begin{aligned}\left|\widetilde{\psi}(t)\right\rangle \ &= \ -\frac{i}{\hbar}\int_{t-\epsilon}^{t}\hat{\widetilde{H}}_1(t_1)\left|\widetilde{\psi}(t_1)\right\rangle dt_1 \\ &\quad -\frac{i}{\hbar}\int_{t_0}^{t-\epsilon}\hat{\widetilde{H}}_1(t_1)\left|\widetilde{\psi}(t_1)\right\rangle dt_1 + \left|\psi(t_0)\right\rangle\end{aligned} \tag{8.10}$$

with $\epsilon\omega_{eg} \gg 1$. In the next step, we combine Eqs. (8.7) and (8.10). We obtain

$$i\hbar\tfrac{d}{dt}\left|\widetilde{\psi}(t)\right\rangle = \hat{\widetilde{H}}_1(t)\left|\widetilde{\psi}(t-\epsilon)\right\rangle - \tfrac{i}{\hbar}\int_{t-\epsilon}^{t}\hat{\widetilde{H}}_1(t)\hat{\widetilde{H}}_1(t_1)\left|\widetilde{\psi}(t_1)\right\rangle dt_1 \ . \tag{8.11}$$

By applying the definition of $\hat{\widetilde{H}}_1(t_1)$, we get

$$\begin{aligned}\hat{\widetilde{H}}_1(t_2)\hat{\widetilde{H}}_1(t_1) \ &=: \ \hat{\widetilde{H}}_1(t_2)\hat{\widetilde{H}}_1(t_1) : \\ &\quad + \sum_{A_1,A_2}\left|e\right\rangle_{A_2}\left\langle g\right|_{A_2}\left|g\right\rangle_{A_1}\left\langle e\right|_{A_1} e^{i\omega_{eg}(t_2-t_1)} \\ &\quad \left[\hat{\mathbf{E}}_\perp^+(\mathbf{x}_{A_2},t_2)\cdot\mathbf{d}_{A_2}, \hat{\mathbf{E}}_\perp^-(\mathbf{x}_{A_1},t_1)\cdot\mathbf{d}_{A_1}^*\right]\end{aligned} \tag{8.12}$$

with $\hat{\mathbf{E}}_\perp^\pm(\mathbf{x}_a,t)$ denoting the field operators in the interaction picture and $: \ldots :$ denoting the normal ordering of the field operators.

The commutator which appears in the last line of eq. (8.12) describes the propagation of a photon emitted by atom A_1 to atom A_2. For a photon propagating in vacuum, these functions can be directly related to the dyadic Green's function of the d'Alembert operator. This connection is derived in Appendix A but the corresponding commutator can be evaluated in much more general situations. If the dispersion relation of the

radiation field is linear or can be well approximated by a linear dispersion relation in the relevant frequency regime around ω_{eg}, it is possible to derive the following property

$$e^{i\omega_{eg}(t_2-t_1)}\left[\hat{\mathbf{E}}_{\perp}^{+}(\mathbf{x}_{A_2},t_2)\cdot\mathbf{d}_{A_2},\hat{\mathbf{E}}_{\perp}^{-}(\mathbf{x}_{A_1},t_1)\cdot\mathbf{d}_{A_1}^{*}\right]=\delta_{A_1,A_2}\hbar^2\Gamma\delta(t_1-t_2) \tag{8.13}$$

for all $|t_1-t_2|<\tau_{A_1,A_2}$ with $\tau_{A_1,A_2}>0$ and Γ being the spontaneous decay rate of an atom. The constant τ_{A_1,A_2} is connected to the finite speed of light. It reflects the time a photon emitted by atom A_1 needs to reach atom A_2. In case that $A_1=A_2$, it is the time which a photon emitted by atom A_1 needs to return to the same atom after being reflected by the boundary of a waveguide or the surface of a cavity (In free space or an open waveguide this recurrence never occurs and $\tau_{A_1,A_1}=\infty$.). In Eq. (8.13), we neglected, similar to Ref. [37], that the corresponding processes take place on a time scale given by $1/\omega_{eg}$ and not instantaneously as implied by the use of the δ-function. This approximation can be justified by the initial assumption that the time scale induced by the atomic transition frequency is by far the shortest relevant for the systems dynamics which already entered in the RWA. Furthermore, we assumed that the Lamb-shift which would also enter in Eq. (8.13) has already been incorporated in the atomic transition frequency ω_{eg}. By using Eq. (8.13) and choosing $0<\epsilon<\tau_{A_1,A_2}$ for all A_1,A_2, Eq. (8.11) simplifies to

$$\begin{aligned}\frac{d}{dt}\left|\widetilde{\psi}(t)\right\rangle &= -\hat{\Gamma}/2\left|\widetilde{\psi}(t)\right\rangle-\frac{i}{\hbar}\hat{\tilde{H}}_1(t)\left|\widetilde{\psi}(t-\epsilon)\right\rangle\\ &\quad-\frac{1}{\hbar^2}\int_{t-\epsilon}^{t}:\hat{\tilde{H}}_1(t)\hat{\tilde{H}}_1(t_1):\left|\widetilde{\psi}(t_1)\right\rangle dt_1\end{aligned} \tag{8.14}$$

with $\hat{\Gamma}=\Gamma\sum_{A=1}^{N}\left|e\right\rangle_A\left\langle e\right|_A$. This is quite similar to the introduction of the non-hermitian Hamilton operator in Ref. [37]. Eq. (8.14) is equivalent to the integral equation

$$\begin{aligned}\left|\widetilde{\psi}(t)\right\rangle &= e^{-\hat{\Gamma}(t-t_0)/2}\left|\psi(t_0)\right\rangle\\ &\quad-\frac{i}{\hbar}\int_{t_0}^{t}e^{-\hat{\Gamma}(t-t_1)/2}\hat{\tilde{H}}_1(t_1)\left|\widetilde{\psi}(t_1-\epsilon)\right\rangle dt_1\\ &\quad-\frac{1}{\hbar^2}\int_{t_0}^{t}\int_{t_2-\epsilon}^{t_2}e^{-\hat{\Gamma}(t-t_2)/2}:\hat{\tilde{H}}_1(t_2)\hat{\tilde{H}}_1(t_1):\left|\widetilde{\psi}(t_1)\right\rangle dt_1dt_2\,.\end{aligned} \tag{8.15}$$

We can solve Eq. (8.15) by using a fix point iteration starting with $\left|\widetilde{\psi}(t)\right\rangle=0$. By doing so and by taking the limit $\epsilon\to0$, we can express the solution for $\left|\widetilde{\psi}(t)\right\rangle$ by

$$\begin{aligned}\left|\widetilde{\psi}(t)\right\rangle &= \sum_{m=0}^{\infty}\left(-\frac{i}{\hbar}\right)^m\lim_{\epsilon\to0}\int_{t_0}^{t}\int_{t_0}^{t_m-\epsilon}\ldots\int_{t_0}^{t_3-\epsilon}\int_{t_0}^{t_2-\epsilon}e^{-\hat{\Gamma}(t-t_m)/2}\\ &\quad\mathcal{T}\left[\prod_{l=1}^{m}\hat{\tilde{H}}_1(t_l)e^{-\hat{\Gamma}(t_l-t_{l-1}-\epsilon)/2}\right]\left|\psi(t_0)\right\rangle dt_1dt_2\ldots dt_{m-1}dt_m\end{aligned} \tag{8.16}$$

with $\mathcal{T}$ denoting the time ordering of the product. For this purpose, we used that the contributions generated by the last line of Eq. (8.15) vanish as $\epsilon\to0$.

For evaluating this solution, we express Eq. (8.16) by a sum of normally ordered terms. The corresponding expressions can be evaluated by introducing the functions

$$\begin{aligned}T_1^{A_1,A_2}(t_2-t_1) &= \frac{1}{\hbar^2}e^{i\omega_{eg}(t_2-t_1)}\left[\hat{\mathbf{E}}_{\perp}^{+}(\mathbf{x}_{A_2},t_2)\cdot\mathbf{d}_{A_2},\hat{\mathbf{E}}_{\perp}^{-}(\mathbf{x}_{A_1},t_1)\cdot\mathbf{d}_{A_1}^{*}\right]\\ &\quad-\delta_{A_2,A_1}\Gamma\delta(t_2-t_1)\end{aligned} \tag{8.17}$$

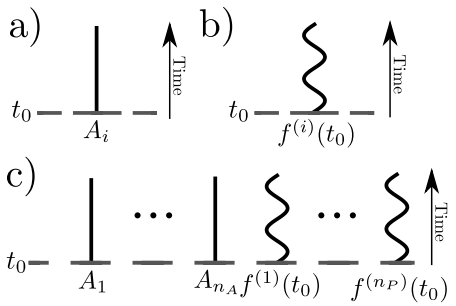

Figure 8.1.: Diagrammatic representation of the excitations contributing to the initial state: representation of (a) an initial atomic excitation, (b) an initial photonic excitation and (c) the whole initial state.

describing the propagation of the photons. The expression $\delta_{A_2,A_1}\Gamma\delta(t_2 - t_1)$ in Eq. (8.17) does not contribute due to the structure of the integrals in Eq. (8.15) and only the expressions $T_1^{A_1,A_2}(t)$, which are connected to time delays caused by the finite speed of light, have to be taken into account.

Thus, only finitely many terms of the sum $\sum_{m=0}^{\infty}$ contribute to the expression in Eq. (8.15) if a finite time interval is considered. This is a major advantage of our multi-photon-path-representation because it allows us to determine $|\widetilde{\psi}(t)\rangle$ without further approximations.

8.2.2 *Graphical interpretation of the multi-photon-path-representation*

To apply the previous results and for giving a suitable interpretation of the derived analytical expressions, we develop a diagrammatic method. By doing so, each expression generated by applying the commutation relation (8.17) to bring Eq. (8.16) in a normally ordered form is represented by a certain diagram. By generating all possible diagrams and summing up the corresponding expressions, it is possible to evaluate $|\widetilde{\psi}(t)\rangle$.

This diagrammatic method connects each term of Eq. (8.16) with a descriptive photon path which can be interpreted as a sequence of absorption and spontaneous emission processes.

At first, we list the basic elements of such a diagram. Later on, we give a list of rules to generate all possible diagrams. Finally, we establish a connection between the different diagrams and the corresponding analytical expressions.

We start with a graphical representation of the initial state $|\psi(t_0)\rangle$ defined in Eq. (8.6).

Each initial atomic excitation of an atom A_i is represented by a graphical element of the form depicted in Fig. 8.1 (a). Each initial photonic excitation is represented by an element of the form depicted in Fig. 8.1 (b) (corresponds to $\sum_j f_j^{(i)}(t_0)a_j^\dagger$). By putting all these elements together, it is possible to represent the initial state defined in Eq. (8.6) by the diagram depicted in Fig. 8.1 (c).

We can also represent the excitations contributing to the state $|\widetilde{\psi}(t)\rangle$ in a similar way. Thereby, each atomic excitation of the state $|\widetilde{\psi}(t)\rangle$ is represented by an graphical element of the form depicted in Fig. 8.2 (a) which we denote as outgoing atomic excitation. Each photonic excitation of the state $|\widetilde{\psi}(t)\rangle$ is represented by an element of

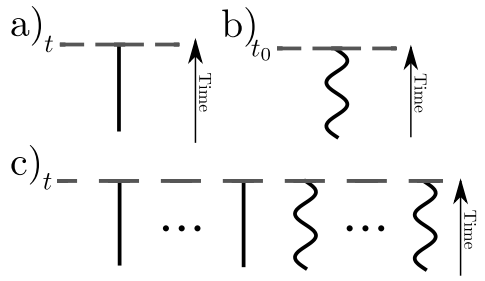

Figure 8.2.: Diagrammatic representation of the excitations contributing to the state $|\widetilde{\psi}(t)\rangle$: representation of (a) an outgoing atomic excitation, (b) an outgoing photonic excitation and (c) the excitations of the whole state $|\widetilde{\psi}(t)\rangle$.

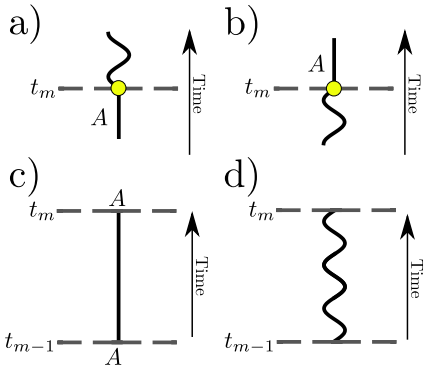

Figure 8.3.: Diagrammatic representation of basic processes: representation of (a) an emission of a photon by an excited atom, (b) an absorption of a photon by an atom in the ground state, (c) a propagation of an atomic excitation (atomic excitation line) and (d) a propagation of a photonic excitation (photon line).

the form depicted in Fig. 8.2 (b) which we refer to as outgoing photonic excitation. By putting all these elements together, it is possible to represent all excitations contributing to the final state $|\widetilde{\psi}(t)\rangle$ by the diagram depicted in Fig. 8.2 (c).

In order to represent photon emission and absorption processes involving an atom A at the intermediate time step t_m (with $t > t_m > t_0$), we introduce the diagrams 8.3 (a) respectively 8.3 (b). The propagation of the atomic or photonic excitations involved in these processes is represented by the elements depicted in Fig. 8.3 (c) respectively Fig. 8.3 (d). In the following, we refer to this elements as atomic excitation lines (Fig. 8.3 (c)) and photon lines (Fig. 8.3 (d)). These lines connect the emission processes, absorption processes, initial and outgoing excitations among each other. In a diagram, an atomic excitation line refers to one atom only (i.e., its beginning and end is connected to the same atom).

By using these graphical elements, it is possible to assemble a complete diagram according to a certain set of rules. For a process which involves m absorption respectively emission processes taking place at the intermediate time steps $t_1 ... t_m$ with $t_0 < t_1 < t_2 < ... < t_m < t$ the corresponding rules are as follows:

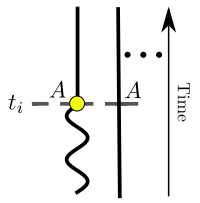

Figure 8.4.: Forbidden diagram: The diagram describes a process in which an already excited atom A absorbs a photon. By excluding diagrams like this, we take the saturation effects of the two-level atoms into account.

1. At each emission process starts exactly one photon line and ends exactly one atomic excitation line.
2. At each absorption process starts exactly one atomic excitation line and ends exactly one photon line.
3. Each atomic excitation line starts either at an initial atomic excitation or an absorption process and ends either at an outgoing atomic excitation or an emission process.
4. Each photon line starts either at an initial photonic excitation or an emission process and ends either at an outgoing photonic excitation or an absorption process.
5. Atomic excitation lines corresponding to the same atom cannot coexist in time.

The non-linear behavior of the two-level atoms is reflected by the last rule. Thus, diagrams containing parts like the one depicted in Fig. 8.4 are forbidden. Ignoring this rule would result in a time evolution in which the atoms behave like harmonic oscillators which do not show saturation effects.

Finally, we have to connect the diagrams with the analytical expressions contributing to the wave function $|\widetilde{\psi}(t)\rangle$. By doing so, each atomic excitation line and photon line is assigned to a certain expression and the whole diagram corresponds to an integral over a product of these expressions. The correspondence rules for photon lines are as follows: For a line connecting

1. an emission process of atom A_e at time t_e with an absorption process at time t_a ($t_a > t_e$) by atom A_a, we write
$$- T_1^{A_e,A_a}(t_a - t_e) \; . \tag{8.18}$$
2. an initial photonic excitation $f^{(i)}(t_0)$ with an absorption process at atom A_a and time t_a, we write
$$\tfrac{i}{\hbar} \left[\hat{\mathbf{E}}_\perp^+(\mathbf{x}_{A_a}, t_a) \cdot \mathbf{d}_{A_a}, \textstyle\sum_j f_j^{(i)}(t_0) a_j^\dagger \right] e^{i\omega_{eg}(t_a - t_0)} \; . \tag{8.19}$$
3. an initial photonic excitation $f^{(i)}(t_0)$ with an outgoing photonic excitation, we write
$$\sum_j f_j^{(i)}(t_0) a_j^\dagger \; . \tag{8.20}$$

4. an emission process of atom A_e at time t_e with an outgoing photonic excitation, we write
$$\frac{i}{\hbar}\hat{\mathbf{E}}_{\perp}^{-}(\mathbf{x}_{A_e}, t_e)\cdot\mathbf{d}_{A_e}^{*}e^{-i\omega_{eg}(t_e-t_0)}\ . \tag{8.21}$$

The correspondence rules for atomic excitation lines are as follows:

1. If the line does not end at an outgoing atomic excitation and starts at time t_b and ends at t_e, we write
$$e^{-\Gamma(t_e-t_b)/2}\ . \tag{8.22}$$

2. If the line is an outgoing atomic excitation and starts at time t_b, we write
$$e^{-\Gamma(t-t_b)/2}\left|e\right\rangle_A\left\langle g\right|_A\ . \tag{8.23}$$

The expression assigned to the complete diagram is now given by the product of all these terms acting on the state $\left|G\right\rangle^A\left|0\right\rangle^P$ integrated over all intermediate time steps $t_1, t_2 ... t_m$ with $t_0 < t_1 < t_2 < ... < t_m < t$, i.e.,
$$\int_{t_0}^{t}\int_{t_0}^{t_m}...\int_{t_0}^{t_3}\int_{t_0}^{t_2}...dt_1dt_2...dt_m\ . \tag{8.24}$$

We obtain $\left|\widetilde{\psi}(t)\right\rangle$ by summing over all possible diagrams. Thereby, we sum over each diagram only once and additional summations over equivalent diagrams have to be excluded. We consider two diagrams to be equivalent if the corresponding photon and atomic excitation lines connect emission and absorption processes involving the same atoms at the same time steps $t_1 ... t_n$ and the same initial and final excitations among each other.

In this section, we only dealt with the derivation of the multi-photon-path-representation in the case of identical two-level atoms. In fact, it is a straightforward task to generalize this path representation to multi-level atoms. By following the steps of the previous subsection 8.2.1, an expression quite similar to Eq. (8.16) can be derived and can be represented by a similar diagrammatic method.

8.3 EXAMPLES

8.3.1 *Processes involving only a single excitation*

To discuss the multi-photon-path-representation and the corresponding diagrammatic method in more detail, we provide some examples. We start with the description of processes involving only a single excitation. Thereby, we establish a connection between the multi-photon-path-representation and the single-photon-path-representation developed in chapter 3.

We start with a discussion of the spontaneous decay of a single initially excited atom (atom 1) coupled to the radiation field propagating in free-space or in an open waveguide.

This process is described by the diagrams depicted in Fig. 8.5 (a) and Fig. 8.5 (b). According to the rules derived in the previous section, the diagram depicted in Fig. 8.5 (a) is linked to the expression
$$e^{-\Gamma(t-t_0)/2}\left|e\right\rangle_1\left|0\right\rangle^P \tag{8.25}$$

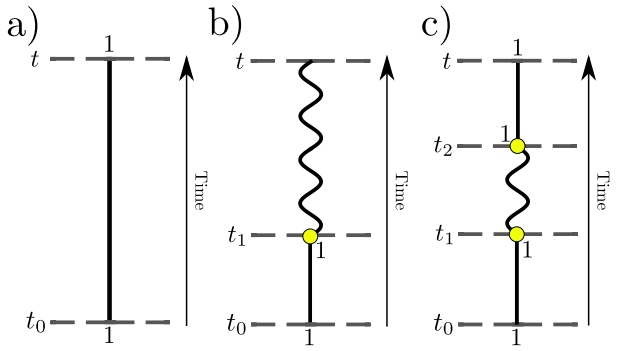

Figure 8.5.: Diagrammatic representation of the spontaneous emission process of a single atom in free-space or in an open waveguide.

and describes the depopulation of the excited state due to the spontaneous decay process. The emitted single-photon wave packet is described by the expression connected to the diagram depicted in Fig. 8.5 (b)

$$\frac{i}{\hbar}\left|g\right\rangle_1 \int_{t_0}^{t} \hat{\mathbf{E}}_{\perp}^{-}(\mathbf{x}_1, t_1)\cdot\mathbf{d}_1^{*}\left|0\right\rangle^P e^{-\left(\Gamma/2+i\omega_{eg}\right)(t_1-t_0)}dt_1\,. \tag{8.26}$$

The diagram of next higher order is depicted in Fig. 8.5 (c) and corresponds to

$$-\left|e\right\rangle_1\left|0\right\rangle^P \int_{t_0}^{t}\int_{t_0}^{t_2} e^{-\Gamma(t-t_2)/2}T_1^{1,1}(t_2-t_1)e^{-\Gamma(t_1-t_0)/2}dt_1dt_2\,. \tag{8.27}$$

Thereby, the expression $T_1^{1,1}(t_2-t_1)$ describes the return of the wave packet to atom 1 after being emitted by the same atom. In general, processes such as this give rise to non-Markovian dynamics. In free-space or in an open waveguide, such a recurrence never takes place. Thus, $T_1^{1,1}(t_2-t_1)=0$ and the entire expression in Eq. (8.27) vanishes. The same holds true for all further diagrams and only the diagrams depicted in Fig. 8.5 (a) and Fig. 8.5 (b) contribute to the complete wave function describing this process which is given by

$$\left|\widetilde{\psi}(t)\right\rangle \;=\; e^{-\frac{\Gamma}{2}(t-t_0)}\left|e\right\rangle_1\left|0\right\rangle^P + \frac{i}{\hbar}\left|g\right\rangle_1\int_{t_0}^{t}\hat{\mathbf{E}}_{\perp}^{-}(\mathbf{x}_1,t_1)\cdot\mathbf{d}_1^{*}\left|0\right\rangle^P e^{-\left(\Gamma/2+i\omega_{eg}\right)(t_1-t_0)}dt_1\,.$$

If a photon emitted by atom 1 returns to the same atom after being reflected by the cavity, for example due to the presence of a mirror, $T_1^{1,1}(t_2-t_1)$ deviates from zero and further diagrams have to be taken into account. In case that multiple atoms are present in the system, it might occur that the excitation of one atom is transfered to a second atom via the spontaneous emission of a single-photon wave packet and its subsequent absorption by the second atom. In general, such an excitation transfer from one atom to another gives rise to non-Markovian dynamics, especially, if the distance between the two atoms becomes large or comparable to c_0/Γ. A diagram which corresponds to such a process is depicted in Fig. 8.6. Thereby, the initial excitation of atom 1 is transfered to the atom 2 which is described by the following expression

$$-\left|e\right\rangle_2\left|0\right\rangle^P \int_{t_0}^{t}\int_{t_0}^{t_2} e^{-\Gamma(t-t_2)/2}T_1^{1,2}(t_2-t_1)e^{-\Gamma(t_1-t_0)/2}dt_1dt_2\,. \tag{8.28}$$

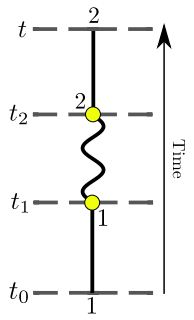

Figure 8.6.: Diagram describing a transfer of the excitation from the initially excited atom 1 to the atom 2 mediated by a single-photon wave packet.

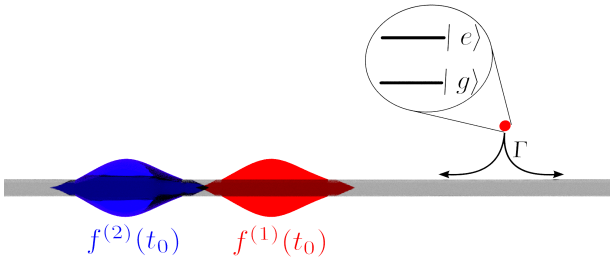

Figure 8.7.: Two photons, with the initial states $f^{(1)}(t_0)$ and $f^{(2)}(t_0)$, propagating in a one-dimensional waveguide and interacting with a two-level atom.

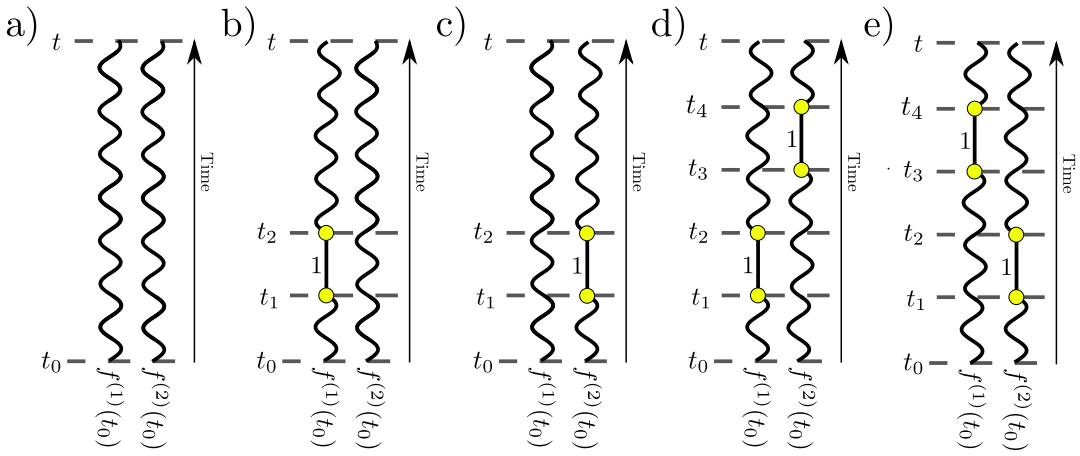

Figure 8.8.: Diagram describing the scattering of two photons by a single two-level atom.

8.3.2 *Scattering of two photons by a single atom*

Our method allows us to investigate nonlinear effects which come into play as soon as more than a single excitation is present in the system. In the following, we study the scattering of two photons propagating in free-space or in a waveguide by a single two-level atom at the fixed position $\mathbf{x}_1$. We assume that the atom is initially prepared in its ground state $|g\rangle_1$ and that two initial photonic excitations are present in the system, i.e.,

$$|\psi(t_0)\rangle = \left(\sum_j f_j^{(2)}(t_0)a_j^\dagger\right)\left(\sum_j f_j^{(1)}(t_0)a_j^\dagger\right)|0\rangle^P|g\rangle_1 \ .$$

A sketch of a possible experimental setup using a one-dimensional waveguide is depicted in Fig. 8.7. The corresponding diagrams connected to the probability amplitudes describing two outgoing photons are illustrated in Fig. 8.8. By adding up the expressions connected to these diagrams, we obtain the wave function describing the outgoing photons

$$|\widetilde{\psi}^{\text{out}}(t)\rangle = |\widetilde{\psi}^{(\text{a})}(t)\rangle + |\widetilde{\psi}^{(\text{b})}(t)\rangle + |\widetilde{\psi}^{(\text{c})}(t)\rangle + |\widetilde{\psi}^{(\text{d})}(t)\rangle + |\widetilde{\psi}^{(\text{e})}(t)\rangle \ .$$

The diagram shown in Fig. 8.8 (a) corresponds to the expression

$$\begin{aligned} |\widetilde{\psi}^{(\text{a})}(t)\rangle &= |\psi(t_0)\rangle \\ &= \left(\sum_j f_j^{(2)}(t_0)a_j^\dagger\right)\left(\sum_j f_j^{(1)}(t_0)a_j^\dagger\right)|0\rangle^P|g\rangle_1 \end{aligned}$$

and represents the free unperturbed time evolution of the incoming photons. The diagrams in Fig. 8.8 (b) and Fig. 8.8 (c) describe scattering processes in which one of the two photons gets absorbed by the atom which emits the photon later on due to spontaneous decay while the other photon is just passing by without interacting with the atom. These diagrams correspond to the expressions

$$\begin{aligned} |\widetilde{\psi}^{(\text{b})}(t)\rangle &= -\frac{1}{\hbar^2}\int_{t_0}^{t}\int_{t_0}^{t_2}\left(\hat{\mathbf{E}}_\perp^-(\mathbf{x}_1,t_2)\cdot\mathbf{d}_1^*\right)\left(\sum_j f_j^{(2)}(t_0)a_j^\dagger\right) \\ &\quad |0\rangle^P|g\rangle_1 e^{-\left(i\omega_{eg}+\Gamma/2\right)(t_2-t_1)} \\ &\quad \left[\hat{\mathbf{E}}_\perp^+(\mathbf{x}_1,t_1)\cdot\mathbf{d}_1,\sum_j f_j^{(1)}(t_0)a_j^\dagger\right]dt_1dt_2 \ , \end{aligned}$$

and

$$\begin{aligned} |\widetilde{\psi}^{(\text{c})}(t)\rangle &= -\frac{1}{\hbar^2}\int_{t_0}^{t}\int_{t_0}^{t_2}\left(\hat{\mathbf{E}}_\perp^-(\mathbf{x}_1,t_2)\cdot\mathbf{d}_1^*\right)\left(\sum_j f_j^{(1)}(t_0)a_j^\dagger\right) \\ &\quad |0\rangle^P|g\rangle_1 e^{-\left(i\omega_{eg}+\Gamma/2\right)(t_2-t_1)} \\ &\quad \left[\hat{\mathbf{E}}_\perp^+(\mathbf{x}_1,t_1)\cdot\mathbf{d}_1,\sum_j f_j^{(2)}(t_0)a_j^\dagger\right]dt_1dt_2 \ . \end{aligned}$$

The diagrams in Fig. 8.8 (d) and Fig. 8.8 (e) correspond to the expressions

$$
\begin{aligned}
|\widetilde{\psi}^{(\mathrm{d})}(t)\rangle \;=\; & \frac{1}{\hbar^4}\int_{t_0}^{t}\int_{t_0}^{t_4}\int_{t_0}^{t_3}\int_{t_0}^{t_2} e^{-\left(i\omega_{eg}+\Gamma/2\right)(t_2+t_4-t_1-t_3)} \\
& \left(\hat{\mathbf{E}}_{\perp}^{-}(\mathbf{x}_1,t_4)\cdot\mathbf{d}_1^{*}\right)\left(\hat{\mathbf{E}}_{\perp}^{-}(\mathbf{x}_1,t_2)\cdot\mathbf{d}_1^{*}\right)|0\rangle^{P}|g\rangle_1 \\
& \left[\hat{\mathbf{E}}_{\perp}^{+}(\mathbf{x}_1,t_1)\cdot\mathbf{d}_1,\sum_j f_j^{(1)}(t_0)a_j^{\dagger}\right] \\
& \left[\hat{\mathbf{E}}_{\perp}^{+}(\mathbf{x}_1,t_3)\cdot\mathbf{d}_1,\sum_j f_j^{(2)}(t_0)a_j^{\dagger}\right] dt_1dt_2dt_3dt_4
\end{aligned}
$$

and

$$
\begin{aligned}
|\widetilde{\psi}^{(\mathrm{e})}(t)\rangle \;=\; & \frac{1}{\hbar^4}\int_{t_0}^{t}\int_{t_0}^{t_4}\int_{t_0}^{t_3}\int_{t_0}^{t_2} e^{-\left(i\omega_{eg}+\Gamma/2\right)(t_2+t_4-t_1-t_3)} \\
& \left(\hat{\mathbf{E}}_{\perp}^{-}(\mathbf{x}_1,t_4)\cdot\mathbf{d}_1^{*}\right)\left(\hat{\mathbf{E}}_{\perp}^{-}(\mathbf{x}_1,t_2)\cdot\mathbf{d}_1^{*}\right)|0\rangle^{P}|g\rangle_1 \\
& \left[\hat{\mathbf{E}}_{\perp}^{+}(\mathbf{x}_1,t_1)\cdot\mathbf{d}_1,\sum_j f_j^{(2)}(t_0)a_j^{\dagger}\right] \\
& \left[\hat{\mathbf{E}}_{\perp}^{+}(\mathbf{x}_1,t_3)\cdot\mathbf{d}_1,\sum_j f_j^{(1)}(t_0)a_j^{\dagger}\right] dt_1dt_2dt_3dt_4\,,
\end{aligned}
$$

which represent scattering processes in which the atom absorbs and re-emits both of the photons, one after the other. The nonlinearity of these process is thereby represented by the rule that the atom can only absorb a second photon after the photon absorbed first has been re-emitted into the radiation field.

8.3.3 *Rabi oscillations induced by photon number states*

By using the multi-photon-path-representation, it is straight forward to describe processes involving even higher numbers of photons. A striking example for such nonlinear multi-photon processes are Rabi oscillations. To provide an interesting example, which goes beyond the typical investigation of Rabi oscillations, we assume that the initial field state is given by a highly non-classical photon number state. We choose the initial state of the system to be of the form

$$
|\psi(t_0)\rangle = \frac{1}{\sqrt{n_p!}}\left(\sum_j f_j(t_0)a_j^{\dagger}\right)^{n_P}|0\rangle^{P}|g\rangle_1 \tag{8.29}
$$

with

$$
\sum_j |f_j(t_0)|^2 = 1 \tag{8.30}
$$

which describes an incoming field state consisting out of n_P identical photons. Furthermore, we assume that the interaction takes place in free-space or in an open waveguide and thus

$$
T_1^{1,1}(t_2-t_1) = 0 \tag{8.31}
$$

as discussed previously. In order to evaluate all the expressions which appear in the photon-path-representation, we have to specify the form of the incoming multi-photon wave packet. This can be done by introducing the function

$$
f_{\mathrm{in}}^{p}(t) = \frac{i}{\hbar}\left[\hat{\mathbf{E}}_{\perp}^{+}(\mathbf{x}_1,t)\cdot\mathbf{d}_1,\sum_j f_j(t_0)a_j^{\dagger}\right]\,. \tag{8.32}
$$

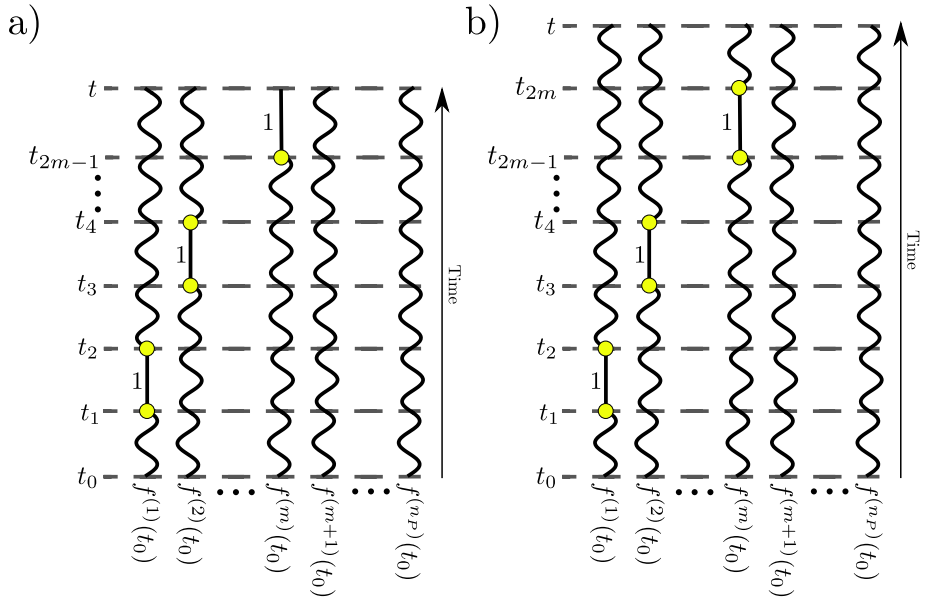

Figure 8.9.: Diagrams representing the time evolution of n_P photons interacting with a single atom in free-space or in an open waveguide. They contribute to the part of the wave function with the atom being in an excited state (a) and the atom being in a ground state (b).

We choose the exact form of $f_{\text{in}}^P(t)$ later on. All possible diagrams are now either of the form depicted in Fig. 8.9 (a) or of the form shown in Fig. 8.9 (b).

The diagrams illustrated in Fig. 8.9 (a) describe the part of the wave function $|\widetilde{\psi}(t)\rangle$ which is connected to an excited atom 1 and the diagrams depicted in Fig. 8.9 (b) represent the other part of the wave function connected to atom 1 being in the ground state.

The diagram in Fig. 8.9 (a) corresponds to the expression

$$\begin{aligned}&\tfrac{1}{\sqrt{n_P!}}\,|e\rangle_1\left(\textstyle\sum_j f_j(t_0)a_j^\dagger\right)^{n_P-m}(\tfrac{i}{\hbar})^{m-1}\int_{t_0}^{t}\dots\int_{t_0}^{t_2} f_{\text{in}}^P(t_{2m-1})\\ &\quad e^{-\Gamma(t-t_{2m-1})/2}e^{i\omega_{eg}(t_{2m-1}-t_0)}\prod_{i=1}^{m-1}\hat{\mathbf{E}}_\perp^-(\mathbf{x}_1,t_{2i})\cdot\mathbf{d}_1^*\\ &\quad f_{\text{in}}^P(t_{2i-1})e^{-\left(\Gamma/2+i\omega_{eg}\right)(t_{2i}-t_{2i-1})}dt_1\dots dt_{2m-1}\,|0\rangle^P\end{aligned}\tag{8.33}$$

and the diagram shown in Fig. 8.9 (b) corresponds to the expression

$$\begin{aligned}&\tfrac{1}{\sqrt{n_P!}}\,|g\rangle_1\left(\textstyle\sum_j f_j(t_0)a_j^\dagger\right)^{n_P-m}(\tfrac{i}{\hbar})^{m}\int_{t_0}^{t}\dots\int_{t_0}^{t_2}\\ &\quad\prod_{i=1}^{m}\hat{\mathbf{E}}_\perp^-(\mathbf{x}_1,t_{2i})\cdot\mathbf{d}_1^*e^{-\left(\Gamma/2+i\omega_{eg}\right)(t_{2i}-t_{2i-1})}\\ &\qquad f_{\text{in}}^P(t_{2i-1})dt_1\dots dt_{2m}\,|0\rangle^P\ .\end{aligned}\tag{8.34}$$

For determining the full solution, one has to sum up all the previous expressions respectively diagrams for $m = 0, 1, 2 \dots n_P$ weighted with the factor $n_P!/(n_P - m)!$. This factor is connected to the possible orderings in which the photons are involved in the absorption and emission processes. Due to the fact that the initial field state describes n_P identical photons, all possible orderings lead to the same expressions and can be taken into account by a weighting factor. All possible observables concerning the

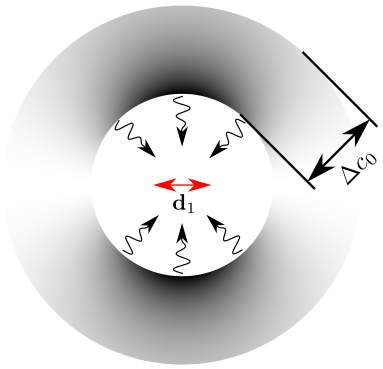

Figure 8.10.: Photon density of the multi-photon wave packet propagating in free-space described by Eqs. (8.29) and (8.35) incidenting on atom 1 with its dipole matrix element $\mathbf{d}_1$ (indicated by the red arrows). The photon density is increased in the dark areas and white indicates the absence of photons.

atomic degrees of freedom can now be calculated by making use of Eqs. (8.17), (8.31) and (8.30) for tracing out the field. By doing so, it is also possible to evaluate the probability of finding the atom in the excited state.

For evaluating these expressions, we have to choose the form of the incidenting wave packet described by $f_{\text{in}}^{P}(t)$. To ensure efficient coupling between the atom and the incoming photons, we assume that the average frequency of the photons matches the transition frequency of the atom. Furthermore, we assume that the incoming photons couple in an optimal way to the dipole matrix element of the atom. In free-space, this implies that the photons are forming an incoming dipole wave but a similar situation can also be realized in one-dimensional waveguides. For the sake of simplicity, we assume that the probability density of finding a photon at the position of the atom is equally distributed over the time interval $t_0 \leq t_{\text{in}} \leq t \leq t_{\text{in}} + \Delta$ and vanishes for $t > t_{\text{in}} + \Delta$. The photon density of this initial wave packet in the free-space scenario is depicted in Fig. 8.10. This is modeled by the function

$$f_{\text{in}}^{P}(t) = e^{-i\omega_{\text{eg}}(t-t_0)} \sqrt{\frac{\Gamma}{\Delta}} \begin{cases} 1 & \text{if } t_{\text{in}} \leq t \leq t_{\text{in}} + \Delta \\ 0 & \text{otherwise} \end{cases} . \tag{8.35}$$

The corresponding results are depicted in Fig. 8.11 (a) and Fig. 8.11 (b). In these figures, we compare the results obtained for an incidenting photon number state described by Eq. (8.29) with the well known results obtained by using an initial coherent state of the form

$$|\psi^{\text{coherent}}(t_0)\rangle = e^{-n_P/2} e^{\sqrt{n_P}\left(\sum_j f_j(t_0) a_j^\dagger\right)} |0\rangle^P |g\rangle_1 \tag{8.36}$$

with the same average photon number [37]. The Rabi oscillations induced by $|\psi^{\text{coherent}}(t_0)\rangle$ correspond to the Rabi frequency

$$\Omega = 2\sqrt{n_P \Gamma / \Delta} . \tag{8.37}$$

By comparing these results it is evident that the atomic dynamics induced by the initial photon number state $|\psi(t_0)\rangle$ and the initial coherent state $|\psi^{\text{coherent}}(t_0)\rangle$ indeed

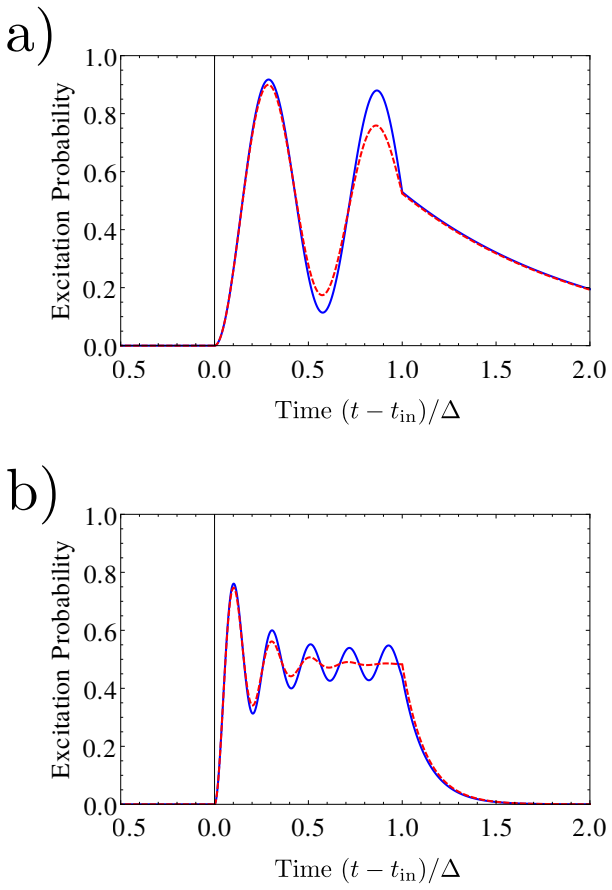

Figure 8.11.: Probability for exciting the atom plotted over time t. The solid line corresponds to an initial photon number state with 30 photons and the dashed line corresponds to a coherent state with the same average photon number. The parameters are $\Gamma\Delta = 1 (\Rightarrow \Omega\Delta/2\pi \approx 1.7, \Omega/\Gamma \approx 11.0)$ (a) and $\Gamma\Delta = 8$ $(\Rightarrow \Omega\Delta/2\pi \approx 4.9, \Omega/\Gamma \approx 3.9)$ (b).

differ considerably even for an relatively large average photon number of 30 as in our case. By considering the observables

$$|e\rangle_1 \langle g|_1 + |g\rangle_1 \langle e|_1 \ , \tag{8.38}$$

$$i\left(|e\rangle_1 \langle g|_1 - |g\rangle_1 \langle e|_1\right) \ , \tag{8.39}$$

the differences between the time evolution of the initial coherent state and the initial photon number state become even more significant. In the case of the initial photon number state, the observables in Eqs. (8.38) and (8.39) evaluate to zero for all times because the number of excitations in the system is conserved under the time evolution described by $\hat{H}$. However, the evaluation of these observables for the initial coherent state (according to Ref. [37]) reveals an oscillatory behavior quite similar to Fig. 8.11 (a) and Fig. 8.11 (b).

8.3.4 *Dynamics of two atoms*

By using our method, we cannot only study the interaction of a wave packet with a single atom in free-space or in an open waveguide, but we are also able to take

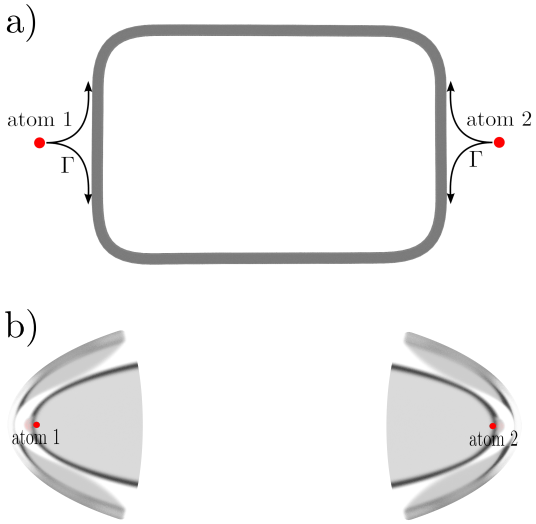

Figure 8.12.: Two atoms coupled to a multimode radiation field. Both setups depicted above lead to the same dynamics of the atoms. In (a) the photonic excitations can travel from one atom to another via a one-dimensional waveguide, while in (b) the photons are guided in free-space by two parabolic mirrors.

the presence of a cavity and multiple atoms into account, which results in highly non-Markovian dynamics. Thereby, a photon emitted by one atom can return to the same atom or might interact with an additional atom. In the following, we investigate an interesting example of such a situation. Suitable setups are illustrated in Fig. 8.12 (a) for waveguides respectively in Fig. 8.12 (b) for the free-space approach. Both scenarios shown in Fig. 8.12 (a) and (b) result in the same dynamics, just realized with different architectures.

The setup depicted in Fig. 8.12 (a) consists out of two atoms coupled to a waveguide forming a loop. A photon emitted by one of the atoms can travel to the other atom or can return to the original atom. In the following, we assume that the atoms exclusively couple to the radiation field guided by the one-dimensional waveguide. The corresponding free-space setup depicted in Fig. 8.12 (b) consists out of two parabolic mirrors facing each other and two atoms, each of them trapped close to the focal points $\mathbf{x}_1$ and $\mathbf{x}_2$ of these mirrors. We assume that the dipole matrix elements of these atoms are oriented along the symmetry axis of the setup. The ideally conducting parabolic mirrors enhance the matter-field interactions of the two atoms. The exclusive coupling to the radiation field guided by the one-dimensional waveguide in Fig. 8.12 (a) corresponds to the limit of the mirrors covering almost the full solid angle around the atoms. We investigate the time evolution of the initial state

$$|\psi(t_0)\rangle = |e\rangle_1 |e\rangle_2 |0\rangle^P \tag{8.40}$$

which corresponds to a radiation field in the vacuum state and the two atoms being in an excited state. The waveguide as well as the free-space scenario can be described by using the relations

$$\begin{aligned}\frac{1}{\hbar^2}e^{i\omega_{eg}(t_2-t_1)}\left[\hat{\mathbf{E}}_\perp^+(\mathbf{x}_1,t_2)\cdot\mathbf{d}_1,\hat{\mathbf{E}}_\perp^-(\mathbf{x}_1,t_1)\cdot\mathbf{d}_1^*\right] &= \frac{1}{\hbar^2}e^{i\omega_{eg}(t_2-t_1)}\left[\hat{\mathbf{E}}_\perp^+(\mathbf{x}_2,t_2)\cdot\mathbf{d}_2,\hat{\mathbf{E}}_\perp^-(\mathbf{x}_2,t_1)\cdot\mathbf{d}_2^*\right]\\ &= \Gamma\sum_{j\in\mathbb{Z}}\delta(t_2-t_1-2j\tau)e^{i\omega_{eg}2j\tau} \qquad (8.41)\end{aligned}$$

and

$$\begin{aligned}&\tfrac{1}{\hbar^2}e^{i\omega_{eg}(t_2-t_1)}\left[\hat{\mathbf{E}}_\perp^+(\mathbf{x}_1,t_2)\cdot\mathbf{d}_1,\hat{\mathbf{E}}_\perp^-(\mathbf{x}_2,t_1)\cdot\mathbf{d}_2^*\right]\\ &= \Gamma\sum_{j\in\mathbb{Z}}\delta(t_2-t_1-(2j+1)\,\tau)e^{i\omega_{eg}(2j+1)\tau}\,. \qquad (8.42)\end{aligned}$$

The constant τ denotes the typical time the photon needs to travel from atom 1 to atom 2 (for a detailed derivation see [107]). By using our path representation and the relations in Eqs. (8.41) and (8.42), we can evaluate the time evolution of the whole system. The main difficulty is caused by the fact that due to the presence of two excited atoms, we have to take the non-linear behavior of the two-level atoms into account. By using our diagrammatic method, we determined the probability of exciting both atoms for several physical parameters. The results are depicted in Fig. 8.13 (a) and Fig. 8.13 (b). We compared our results with results we obtained by neglecting the non-linear behavior of the atoms which we refer to as harmonic approximation (This harmonic approximation is directly related to the the Holstein-Primakoff transformation [108].). In this harmonic approximation, the atoms are replaced by harmonic oscillators, i.e.,

$$|g\rangle_i\langle e|_i\to b_i,\ |e\rangle_i\langle g|_i\to b_i^\dagger,\ |e\rangle_i\langle e|_i\to b_i^\dagger b_i\ i\in\{1,2\} \qquad (8.43)$$

with $b_i^\dagger$, b_i denoting the creation and annihilation operators of an harmonic oscillator. The evaluation of the time evolution by involving the harmonic approximation is much simpler because the Hamilton operator just describes a system of coupled harmonic oscillators. This harmonic approximation can be applied if saturation effects can be neglected.

By comparing the situations depicted in Fig. 8.13 (a) and Fig. 8.13 (b), we observe that the harmonic approximation is a good approximation in the case of Fig. 8.13 (a) but fails completely in case of Fig. 8.13 (b). This can be understood in a simple way. In the case of Fig. 8.13 (a), $\Gamma\tau\gg 1$. Thus, the probability that, for example, atom 2 is still excited before the photon emitted by atom 1 can reach it is very small and saturation effects are negligible. In the case of Fig. 8.13 (b), $\Gamma\tau$ is much smaller and thus saturation effects are indeed important.

8.4 SUMMARY

In this chapter, we have presented a diagrammatic method suitable for investigating the non-Markovian and nonlinear effects induced by highly non-classical multi-photon number states interacting with multiple quantum emitters involving a multimode description of the electromagnetic radiation field. This method can be seen as a generalization of the single-photon-path-representation introduced in chapter 3. Our method can be applied to study the dynamics of quantum emitters coupled to one-dimensional waveguides or the radiation field confined in large or half-open cavities, or even in free-space. Thereby, each expression can be represented by a descriptive photon

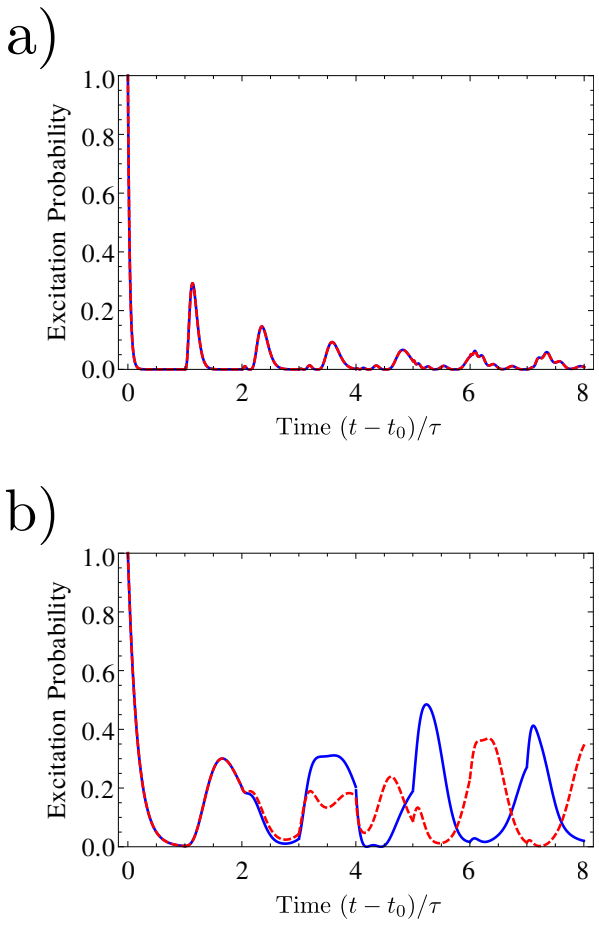

Figure 8.13.: Probability for exciting both atoms plotted over the time t. The solid line corresponds to the full solution obtained by applying our diagrammatic method and the dashed line corresponds to the harmonic approximation (replacing the two-level atoms by harmonic oscillators). The parameters are $1 = e^{i2\tau\omega_{eg}}$ with $\Gamma\tau = 15$ (a) and $\Gamma\tau = 3$ (b).

path consisting out of sequences of spontaneous emission and absorption processes involving multiple atoms and multiple photons simultaneously. The accuracy of this diagrammatic method is just limited by the dipole approximation and the assumption that the time scale induced by the atomic transition frequencies is by far the shortest relevant for the systems dynamics. Furthermore, it offers the unique feature that in order to obtain exact analytical expressions for a finite time interval only a finite number of diagrams has to be taken into account. By applying this diagrammatic method, we can study matter-field interactions of single quantum emitters with highly non-classical multi-photon field states in scenarios ranging from free-space over half-open cavities to one-dimensional waveguides. Thus, our method allows us to study nonlinear and non-Markovian effects induced by matter-field interactions on the single-photon level.

The investigation of nonlinear effects on the single-photon level is not only interesting from a fundamental point of view but also of interest for possible applications in quantum information processing and quantum communication. Thus, our method could be used to design suitable protocols for quantum information processing and quantum communication in a variety of architectures ranging from metallic nanowires coupled to quantum dots to possible applications in free-space.

Part II

QUANTUM SIMULATIONS

9

QUANTUM SIMULATION OF THE DYNAMICAL CASIMIR EFFECT WITH TRAPPED IONS

9.1 INTRODUCTION

In our previous discussions of cavity QED, we assumed that the positions of the macroscopic objects forming the optical resonators or mirrors are time independent. As it turns out, interesting effects can be observed by going beyond static mirrors and cavities. One effect of particular significance is the dynamical Casimir effect (DCE), first investigated by G.T. Moore and described in [32]. Similar to the Casimir effect, the DCE relies on fluctuations of the vacuum in a quantized theory of the electromagnetic radiation field. These vacuum fluctuations lie at the heart of quantum mechanics and quantum field theory and many interesting physical phenomena are directly connected to virtual photons of the vacuum, such as the Lamb shift [109] or the Casimir effect [110]. The dynamical Casimir effect [32] offers the possibility to turn these virtual photons into real measurable photons by moving the boundaries of a cavity with relativistic velocities and high accelerations [see Fig. 9.1(a)]. This requirement makes it difficult to observe the DCE in a cavity QED experiment. Several proposals have been made to overcome this problem [111], for example, by replacing the moving mirrors by a rapid modulation of the electrical properties of the medium inside the cavity. One proposal, based on superconducting circuits [112, 113], has been implemented recently [114–116]. However, in this architecture, it remains a challenge to analyze the generated microwave radiation on the single-photon level.

In this chapter, we investigate the possibility to implement a quantum simulation of the DCE by using an ion chain confined in a segmented surface trap [117], as depicted in Fig. 9.1 (b) (a segmented Paul trap is also suitable [118, 119]). Thereby, the photons are mapped on the phonons of the radial vibrational modes of the ion crystal. A spatial, respectively temporal, dependence of the radial trapping potential mimics the presence, respectively time modulation, of the cavity mirrors. The use of ion phonon modes in designed trap potentials has already been proposed for the quantum simulation of a large variety of physical phenomena, including Bose–Hubbard-like models [120–123] and microscopic models of friction [124, 125]. Experimentally, a controlled quench of the confining potential [126–129] permits the generation of topological defects and the study of the Kibble–Zurek scenario [130]. Moreover, the dynamics of phonons allows the investigation of the transport of heat in quantum systems [131, 132], as shown experimentally in [133].

In the following, we demonstrate that this precisely controlled architecture can also be exploited for the quantum simulation of the DCE. Using state-of-the-art setups and methods available for ion traps [90], the phonons respectively photons produced by the DCE can thus be measured on the single-phonon level with high accuracy.

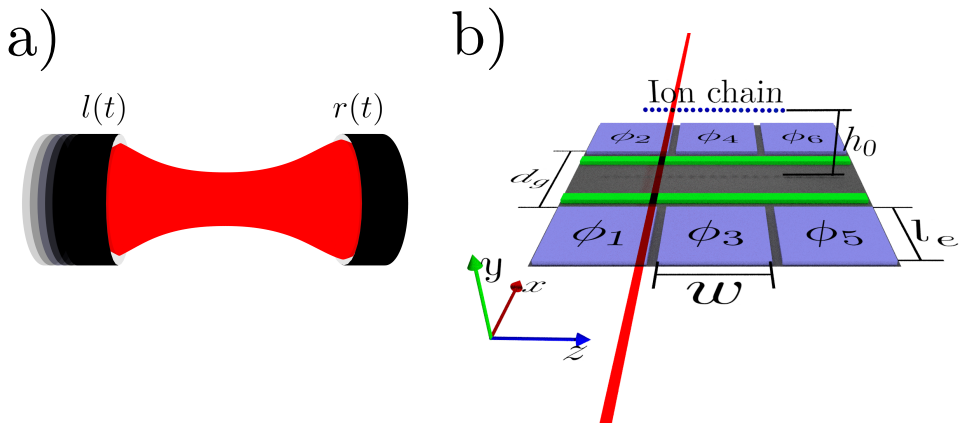

Figure 9.1.: Setup: (a) Dynamical Casimir effect. Modulating the positions of the left or the right mirror of a cavity [$l(t)$ and $r(t)$, respectively] results in the production of photons. (b) Proposed ion-trap-based quantum simulation. The dynamics of the radiation field inside the cavity is mapped to phonon modes of a chain of ions in a spatially-dependent trapping potential, which can be engineered in a segmented surface trap. The modulation of the mirror is simulated via a laser field creating a time-dependent optical trapping potential (red beam). The example shows 6 DC electrodes (blue) and two RF electrodes (green). The distance between the DC electrodes is denoted d_g, their length l_e (both along the x-axis), and their width along the z-axis w. The ion chain (blue dots) is trapped at the center of the trap at the height h_0 above the surface.

In the original work on the DCE [32], in the following referred to as Moore's model, the cavities were described by imposing suitable time-dependent boundary conditions. This has led to some problems with the Hamiltonian formulation of this theory. In our discussion, we avoid these problems by introducing an appropriate model for the propagation of the radiation field inside the mirrors. This description can be seen as a purely phenomenological model of the mirrors. In a certain limit, our model reduces to Moore's model. However, it can also be motivated by microscopic considerations. The used model for the mirrors has the additional benefit of a simple realization in the ion-trap quantum simulator, namely by a spatial variation of the radial trapping potential.

This chapter is divided into five parts. In Sec. 9.2, we introduce a Hamiltonian to model a one-dimensional version of cavity QED with moving boundaries and, in Sec. 9.3, we establish a connection between this Hamiltonian and Moore's model. In Sec. 9.4, we derive a discretized version of this Hamiltonian and show how it can be mapped onto an ion chain. In Sec. 9.5, we present the results of a numerical investigation in which the ion chain quantum simulation is compared to Moore's model using realistic experimental parameters. Finally, in Sec. 9.6, we address the robustness of the simulation against possible sources of errors and discuss the experimental techniques available for investigating the radiation generated by the DCE.

9.2 MODEL OF A VARIABLE LENGTH CAVITY

In this section, we present a one-dimensional version of cavity QED with moving boundaries.

In the following, we set the speed of light and all dielectric constants equals unity, i.e., $c = \epsilon_0 = \mu_0 = 1$. The Hamiltonian of our one-dimensional version of cavity QED with moving boundaries is given by

$$\hat{H} = \hat{H}_0 + \hat{H}_1(t) \tag{9.1}$$

whereby

$$\hat{H}_0 = \frac{1}{2} \int_{\mathbb{R}} \hat{\Pi}^2(z) + \left(\frac{\partial \hat{A}}{\partial z}(z) \right)^2 \mathrm{d}z \tag{9.2}$$

models the free radiation field with $\hat{A}(z)$ being the one-dimensional version of the vector potential and $\hat{\Pi}(z)$ being the corresponding canonical conjugated field operator, such that the following commutation relations hold true

$$[\hat{A}(z_1), \hat{A}(z_2)] = 0 \,, \tag{9.3a}$$
$$[\hat{\Pi}(z_1), \hat{\Pi}(z_2)] = 0 \,, \tag{9.3b}$$
$$[\hat{A}(z_1), \hat{\Pi}(z_2)] = i\hbar\delta(z_1 - z_2) \,. \tag{9.3c}$$

The operator $\hat{H}_1(t)$ describes the modification of the propagation of the electromagnetic radiation field due to the presence of the mirrors. As mentioned previously, the mirrors are not described by imposing fixed boundary conditions but by modeling the propagation of the field inside the mirrors. In the following, we choose

$$\hat{H}_1(t) = \frac{1}{2} \int_{\mathbb{R}} c_1(t,z) \hat{A}^2(z) \mathrm{d}z \tag{9.4}$$

with

$$c_1(t,z) = 0 \text{ for } z \in [l(t), r(t)] \tag{9.5}$$

and

$$c_1(t,z) > 0 \text{ for } z \notin [l(t), r(t)] \,. \tag{9.6}$$

As depicted in Fig. 9.1 (a), the position of the left mirror is given by $l(t)$ and the position of the right mirror is given by $r(t)$ with $l(t) < r(t)$.

The Heisenberg equations of motion induced by the Hamiltonian $\hat{H}_0$ coincide with the Klein–Gordon equation of a massless particle. To this, $\hat{H}_1$ introduces a time- and position-dependent effective mass $\hbar\sqrt{c_1(t,z)}$. This effective mass results in a band-gap similar to the band-gap in a photonic crystal. By choosing $c_1(t,z)$ sufficiently large for $z \notin [l(t), r(t)]$, the propagation of waves in that region is blocked, which models the presence of mirrors. In the limit $c_1(t,z) \to \infty$ for $z \notin [l(t), r(t)]$, we recover the dynamics of Moore's model exactly where the mirrors are modeled by imposing suitable boundary conditions at $l(t)$ and $r(t)$ (see Sec. 9.3). However, by taking the propagation of the radiation field inside the mirrors into account, we circumvent problems connected to Hamiltonian formulation of the theory that appear in case of Moore's model. A microscopic motivation of this Hamiltonian can be found in Appendix C.

It is convenient to express the field operators in the Schrödinger picture in terms of mode functions $A_\ell(z)$ and $\Pi_\ell(z)$ and associated annihilation and creation operators $\hat{a}_\ell$, $\hat{a}_\ell^\dagger$ with $\ell \in \mathbb{N}$,

$$\hat{A}(z) = \sqrt{\frac{\hbar}{2}} \sum_\ell (\hat{a}_\ell A_\ell(z) + \hat{a}_\ell^\dagger A_\ell^*(z)) \,, \tag{9.7a}$$

$$\hat{\Pi}(z) = -i\sqrt{\frac{\hbar}{2}} \sum_\ell (\hat{a}_\ell \Pi_\ell(z) - \hat{a}_\ell^\dagger \Pi_\ell^*(z)) \,. \tag{9.7b}$$

In order to fulfill the canonical commutation relations in equation Eq. (9.3), the mode functions, which are square integrable functions for all time instances t, have to satisfy the conditions

$$\sum_\ell A_\ell(z_1) A_\ell^*(z_2) - \text{c.c.} = 0 \,, \tag{9.8}$$

$$\sum_\ell \Pi_\ell(z_1) \Pi_\ell^*(z_2) - \text{c.c.} = 0 \,, \tag{9.9}$$

$$\sum_\ell A_\ell(z_1) \Pi_\ell^*(z_2) + \text{c.c.} = 2\delta(z_1 - z_2) \tag{9.10}$$

wherein c.c. stands for the complex conjugate. There is no unique choice for the mode functions and different choices lead to different non-equivalent definitions of photon numbers. In order to fix this problem, which has already been discussed in [32], we exploit that there is, in fact, a canonical choice for the mode functions whenever the function $c_1(t,z)$ modeling the boundaries of the cavity is time independent. In this case, we can choose the mode functions to be solutions of a generalized version of the Helmholtz equation

$$0 = \left(-\omega_\ell^2 - \frac{\partial^2}{\partial z^2} + c_1(t,z)\right) g_\ell(z) \,, \tag{9.11}$$

$$A_\ell(z) = \frac{1}{\sqrt{\omega_\ell}} g_\ell(z) \,, \tag{9.12}$$

$$\Pi_\ell(z) = \sqrt{\omega_\ell}\, g_\ell(z) \tag{9.13}$$

with $\omega_\ell > 0$. The solutions $g_\ell(z)$ are properly normalized and orthogonal functions,

$$\int_{\mathbb{R}} g_{\ell_1}(z) g_{\ell_2}^*(z) \mathrm{d}z = \delta_{\ell_1,\ell_2} \,, \tag{9.14}$$

which form a complete basis of the space of square integrable functions $L^2(\mathbb{R})$, i.e.,

$$\sum_\ell g_\ell(z_1) g_\ell^*(z_2) = \delta(z_1 - z_2) \,. \tag{9.15}$$

For the particular choice of mode functions according to Eqs. (9.11)-(9.13) , the time evolution of the field operators in the Heisenberg picture in case of fixed boundaries is just given by

$$\hat{A}(t,z) = \sqrt{\frac{\hbar}{2}} \sum_\ell \left\{ \exp\left[-i\omega_\ell (t - t_0)\right] \hat{a}_\ell A_\ell(z) + \text{H.c.} \right\} \,, \tag{9.16}$$

$$\hat{\Pi}(t,z) = -i\sqrt{\frac{\hbar}{2}} \sum_\ell \left\{ \exp\left[-i\omega_\ell (t - t_0)\right] \hat{a}_\ell \Pi_\ell(z) - \text{H.c.} \right\} \,. \tag{9.17}$$

By using this choice of mode functions, we obtain a canonical definition for the photon numbers.

In order to discuss the production of photons, we consider, like Ref. [32], an experiment that can be divided into three stages. In stage I, which corresponds to the time interval $[t_0, t_1)$, we consider a cavity with fixed boundaries, i.e., we assume that throughout this time interval the function $c_1(t,z)$ is constant in time. In stage II, which corresponds to the time interval $[t_1, t_2)$, we consider a cavity with time-dependent boundaries, i.e., a time-dependent function $c_1(t,z)$. In stage III, corresponding to the time interval $[t_2, \infty)$, we again consider a cavity with fixed boundaries, i.e., $c_1(t,z)$ is now again time independent. Thereby, $c_1(t,z)$ for $t > t_2$ and for $t < t_1$ not necessarily coincide.

Stage I is needed to be able to properly define our initial field configuration, which we choose to be the vacuum state of the radiation field. In stage II of the experiment, the actual photon production takes place. Finally, in stage III of the experiment, during which the mirrors are again at rest, a suitable measurement of the photon numbers and their distribution among the (now well defined) modes is performed.

9.3 CONNECTION TO MOORE'S MODEL

In his original work, Moore concluded that the quantum theory of the radiation field in a variable length cavity possesses no Hamiltonian and no Schrödinger picture (later an effective Hamiltonian which describes the essential features of the physical processes has been derived [134]). To quantize the radiation field, he instead exploited a certain symplectic structure on a function space S, the space of classical solutions of the wave equation. In this section, we establish a connection between our model and Moore's original formulation of the theory.

For doing so, we consider the Heisenberg equations of motion for our model induced by $\hat{H}$,

$$\frac{\partial}{\partial t}\hat{A}(t,z) = \hat{\Pi}(t,z)\,, \tag{9.18}$$

$$\frac{\partial}{\partial t}\hat{\Pi}(t,z) = \frac{\partial^2}{\partial z^2}\hat{A}(t,z) - c_1(t,z)\hat{A}(t,z)\,. \tag{9.19}$$

It is possible to solve these equations of motion by expanding the field operators $\hat{A}(t,z)$ and $\hat{\Pi}(t,z)$ using appropriate time-dependent mode functions $A_\ell(t,z)$ and $\Pi_\ell(t,z)$,

$$\hat{A}(t,z) = \sqrt{\frac{\hbar}{2}}\sum_\ell (\hat{a}_\ell A_\ell(t,z) + \hat{a}_\ell^\dagger A_\ell^*(t,z))\,, \tag{9.20}$$

$$\hat{\Pi}(t,z) = -i\sqrt{\frac{\hbar}{2}}\sum_\ell (\hat{a}_\ell \Pi_\ell(t,z) - \hat{a}_\ell^\dagger \Pi_\ell^*(t,z))\,. \tag{9.21}$$

The time-dependence of these mode functions is governed by the following equations

$$\left(\frac{\partial^2}{\partial t^2} - \frac{\partial^2}{\partial z^2} + c_1(t,z)\right) A_\ell(t,z) = 0\,, \tag{9.22}$$

$$\frac{\partial}{\partial t}A_\ell(t,z)\,|_{t=t_0} = -i\Pi_\ell(t_0,z)\,. \tag{9.23}$$

By using these equations to describe the time evolution of the mode functions during stage II, we are able to establish a connection to the annihilation and creation operators

$\hat{a}_\ell$ and $\hat{a}_\ell^\dagger$ associated to the mode functions in stage I and stage III. Since these are well defined by Eqs. (9.11)-(9.13), this connection allows us to describe the photon production caused by the moving mirrors.

We are now in the position to establish the connection to Moore's model as follows. The real and imaginary parts of the mode functions $A_\ell(t,z)$ correspond to functions in the vector space S defined by Moore [32], equipped with the time-invariant symplectic form

$$\{f_1 \mid f_2\} = \int_{\mathbb{R}} f_2(z,t)\frac{\partial f_1(z,t)}{\partial t} - \frac{\partial f_2(z,t)}{\partial t} f_1(z,t)\mathrm{d}z \,, \tag{9.24}$$

which is used in [32] to quantize the theory.

In order to connect our model with the boundary conditions used in [32], we consider the limit $c_1(t,z) \to \infty$ for z outside the interval $[l(t), r(t)]$, which corresponds to the limit of perfectly reflecting mirrors. In this limit, the canonical modes of stages I and III that satisfy $\omega_\ell^2 \ll c_1(t,z)$ for $z \notin [l(t), r(t)]$ have their main support in the region $[l(t), r(t)]$. Outside of this region, the corresponding mode functions experience an exponential damping. In the limit $c_1(t,z) \to \infty$ for $z \notin [l(t), r(t)]$, this exponential decrease becomes equivalent to the boundary conditions

$$0 = A_\ell(t, l(t)) = A_\ell(t, r(t)) \tag{9.25}$$

chosen in [32]. Similar considerations also hold true during stage II. Thus, the dynamics of the mode functions can be modeled by the boundary conditions in Eq. (9.25) if $c_1(t,z)$ is sufficiently large for $z \notin [l(t), r(t)]$. As a consequence, our model leads to the same results as Moore's model in all three stages in the limit $c_1(t,z) \to \infty$ for $z \notin [l(t), r(t)]$.

9.4 MAPPING TO ION CHAIN

In this section, we map the dynamics induced by the Hamiltonian $\hat{H}$ [see Eq. (9.1)] onto a system of trapped ions. To perform the mapping, we first introduce a model that allows us to represent the continuous one-dimensional space by the discrete ion positions. For the simulation of the DCE, a central region of the ion chain assumes the role of the space within the cavity while portions towards the ends stand in for the mirrors. Afterwards, we describe how the photons can be mapped onto collective radial phonon modes of the ion crystal.

9.4.1 *Discretized version of the radiation-field Hamiltonian*

To perform the mapping of the Hamiltonian $\hat{H}$ to an ion chain, we first need to express it in discretized variables. This can be achieved by dividing the real axis $\mathbb{R}$ in suitable intervals $[z_j, z_{j+1}]$ with $z_j < z_{j+1}$, $j \in \mathbb{Z}$. For simplicity, we focus on the case of equidistant ion spacings where the intervals are of equal length $d = z_{j+1} - z_j$. Generalizing the subsequent discussion to intervals of non-equal length is straightforward. This permits us to take a non-equidistant distribution of the ions and a resulting variation of nearest-neighbor coupling strengths into account.

To arrive at a discretized Hamiltonian, we introduce the coarse-grained operators

$$\hat{A}_j = \frac{1}{\sqrt{d}} \int_{z_j}^{z_{j+1}} \hat{A}(z)\mathrm{d}z \,, \tag{9.26a}$$

$$\hat{\Pi}_j = \frac{1}{\sqrt{d}} \int_{z_j}^{z_{j+1}} \hat{\Pi}(z)\mathrm{d}z \,, \tag{9.26b}$$

which satisfy the commutation relations

$$[\hat{A}_i, \hat{A}_j] = 0 \,, \tag{9.27a}$$

$$[\hat{\Pi}_i, \hat{\Pi}_j] = 0 \,, \tag{9.27b}$$

$$[\hat{A}_i, \hat{\Pi}_j] = i\hbar\delta_{i,j} \,. \tag{9.27c}$$

By using these operators, we obtain a discretized version of the Hamiltonian $\hat{H}$

$$\hat{H}^{\mathrm{d}} = \hat{H}_0^{\mathrm{d}} + \hat{H}_1^{\mathrm{d}}(t) \tag{9.28}$$

with

$$\hat{H}_0^{\mathrm{d}} = \frac{1}{2} \sum_{i\in\mathbb{Z}} \left[\hat{\Pi}_i^2 + d^{-2} \left(\hat{A}_{i+1} - \hat{A}_i \right)^2 \right] \tag{9.29}$$

and

$$\hat{H}_1^{\mathrm{d}}(t) = \frac{1}{2} \sum_{i\in\mathbb{Z}} c_1^i(t) \hat{A}_i^2 \tag{9.30}$$

where

$$c_1^i(t) = \frac{1}{d} \int_{z_i}^{z_{i+1}} c_1(t,z)\mathrm{d}z \,. \tag{9.31}$$

Above, we assumed that the modes of most importance are slowly varying on the length scale induced by the interval length d, which is well justified for the low-energetic modes. In the limit $d \to 0$, we recover the dynamics induced by the original Hamiltonian $\hat{H}$.

9.4.2 *Implementation using transverse phonons of an ion chain*

To implement the Hamiltonian $\hat{H}^{\mathrm{d}}$, we map it to the radial motion of a linear ion chain. Thereby, the position and momentum of each ion represent the fields $\hat{A}(z)$ and $\hat{\Pi}(z)$ averaged over one of the intervals $[z_i, z_{i+1}]$. We consider a linear chain of N ions confined in a suitable trapping potential V_{trap} and with equilibrium positions $\mathbf{R}_1, \mathbf{R}_2, \ldots, \mathbf{R}_N$. If we assume that the deviations from the equilibrium positions are small, we can apply a second-order tailor expansion around the equilibrium positions. In this harmonic approximation, the motional degrees of freedom along different symmetry directions are uncoupled. In the following, we focus on the radial motion along the x-direction, which is described by the Hamiltonian

$$\begin{aligned} \hat{H}^{\mathrm{ions}} &= \frac{1}{2m} \sum_{i=1}^{N} \hat{P}_i^2 - \frac{Z^2 e^2}{8\pi\epsilon_0} \sum_{i>j} \frac{(\hat{X}_i - \hat{X}_j)^2}{|| \mathbf{R}_i - \mathbf{R}_j ||^3} \\ &+ \frac{1}{2} \sum_{i=1}^{N} \frac{\partial^2 V_{\mathrm{trap}}(t, \mathbf{R}_i)}{\partial x^2} \hat{X}_i^2 \,. \end{aligned} \tag{9.32}$$

By applying the canonical transformation

$$\hat{X}_i \to (-1)^i \hat{X}_i \,, \tag{9.33a}$$

$$\hat{P}_i \to (-1)^i \hat{P}_i \,, \tag{9.33b}$$

Simulated Objects	Simulating Objects
Photons	Phonons
Field operators $\hat{A}(z)$ and $\hat{\Pi}(z)$	Position and Momentum operators of the radial motion $\hat{X}_i$ and $\hat{P}_i$
Variable-length cavity modeled by $c_1(t,z)$	Spatial- and time-dependent trapping potential V_{trap} respectively χ_i
Discretized Hamiltonian $\hat{H}^{\text{d}}$	Hamiltonian $\hat{H}^{\text{ions}}$ describing the radial motion of the ion chain

Table 9.1.: Summary of the connection between the simulated objects (radiation field in variable-length cavity) and the simulating objects (ion chain with time-dependent trapping potential).

we obtain

$$\begin{aligned}\hat{H}^{\text{ions}} &= \frac{1}{2m}\sum_{i=1}^{N}\hat{P}_i^2 - \frac{1}{2}\sum_{i>j}(-1)^{i-j}k_{i,j}(\hat{X}_i-\hat{X}_j)^2 \\ &+ \frac{1}{2}\sum_{i=1}^{N}\chi_i(t)\hat{X}_i^2 \end{aligned} \tag{9.34}$$

with

$$k_{i,j} = \frac{Z^2e^2}{4\pi\epsilon_0}\,||\,\mathbf{R}_i-\mathbf{R}_j\,||^{-3}\,, \tag{9.35}$$

$$\chi_i(t) = \frac{\partial^2 V_{\text{trap}}(t,R_i)}{\partial x^2} - \sum_{j\neq i}(1-(-1)^{i-j})k_{i,j}\,. \tag{9.36}$$

The mapping of the dynamics of the radiation field in a variable-length cavity to the dynamics of the ion chain is achieved by exploiting the formal similarity of Eq. (9.34) and Eq. (9.28). If we restrict the phonon Hamiltonian to nearest-neighbor interactions, $\hat{H}^{\text{ions}}$ indeed reproduces the Hamilton $\hat{H}^{\text{d}}$ if we establish the following relations

$$\hat{\Pi}_i = \hat{P}_i/\sqrt{m}\,, \tag{9.37}$$

$$\hat{A}_i = \hat{X}_i\sqrt{m}\,, \tag{9.38}$$

$$d^{-2} = k_{i+1,i}/m\,, \tag{9.39}$$

$$c_1^i(t) = \chi_i(t)/m\,. \tag{9.40}$$

The translation table from simulated objects to simulating objects is summarized in Tab. 9.1 .

The additional interaction terms beyond nearest neighbors can, to a large extent, be reabsorbed in a different choice for the approximations leading to $\hat{H}^{\text{d}}$. In fact, the discretization $\frac{1}{2}\sum_{j\in\mathbb{Z}} d^{-2}\left(\hat{A}_{j+1}-\hat{A}_j\right)^2$ of the term $\frac{1}{2}\int_{\mathbb{R}}\left(\frac{\partial\hat{A}}{\partial z}(z)\right)^2 \mathrm{d}z$ is not unique. The chosen discretization is motivated by the following approximation of the first derivative

$$\frac{\partial\hat{A}}{\partial z}(z) \approx \frac{1}{d}\left[\hat{A}(z+d)-\hat{A}(z)\right]\,. \tag{9.41}$$

There are, however, other possible approximations and as such other possible versions of $\hat{H}^{\mathrm{d}}$ (which give proper results if d is sufficiently small). This liberty can be exploited to account for interaction terms beyond nearest neighbors but we see below in Sec. 9.5 that this is not necessary to get good qualitative and even quantitative agreement using realistic parameters. The underlying reason is the fast decrease of dipolar interactions with distance. Since the integral over dipolar interactions in one dimension converges, any perturbative effect due to interactions beyond nearest neighbors saturates quickly when increasing the system size.

The remaining ingredient to simulate the DCE is the proper choice of the coefficients χ_i. By virtue of Eq. (9.40) and Eq. (9.31), these are directly connected to the function $c_1(t, z)$. Since the outermost ions represent the mirrors while the central part of the ion chain is to simulate the vacuum within the cavity, the coefficients χ_i need to vary across the chain. This can be achieved by exploiting the fact that the χ_i are not only determined by the confining potential V_{trap} along the x-direction, but also by the Coulomb repulsion between the neighboring ions, see Eq. (9.36). As we show in the next section, by properly balancing both contributions, we can design suitable coefficients χ_i, even with a small number of electrode segments.

To induce the dynamical Casimir effect, the coefficients χ_i, moreover, need to vary in time during stage II which can be realized by a time-dependent trapping potential V_{trap}. Since a small spatial motion of the mirrors corresponds to a change of the χ_i only over a small number of ions, this requires some local addressability. A suitable modulation can be achieved by combining a time-independent electric potential V_{E} (including the RF potential), generated via the segmented Paul trap, with an additional time-dependent optical potential V_{O} derived from a laser that addresses only one or a few of the ions [135]. Using the time-dependent optical potential, we can vary the boundary of the cavity during stage II of the experiment. This completes all required ingredients for the simulation of the DCE. In the next section, we demonstrate that good agreement to the ideal model can be obtained already for about 20 ions and in present-day architectures.

9.5 NUMERICAL COMPARISON BETWEEN MOORE'S MODEL AND ION CHAIN QUANTUM SIMULATION

In this section, we compare the ion chain quantum simulator for realistic experimental parameters to the idealized model introduced by Moore [32]. We first compute the trapping potential for realistic experimental parameters for a segmented trap where, for concreteness, we consider a surface trap as depicted in Fig. 9.1 (b) although a segmented Paul trap is equally well suited. It turns out that our requirements on the surface–ion distance or the width of the DC-electrodes are not very high and are met by many existing experimental setups, for example those of Refs. [118, 136–140]. Afterwards, we present numerical results for the photon production, as can be simulated in a chain of 20 ions with current technology.

9.5.1 *Trapping potential for realistic parameters*

The trap, we consider, consists of only 6 DC electrodes. This turns out to be sufficient to form a suitable electric potential V_{E}, which we compute by using the framework presented in [141] and by applying the gapless plane approximation. For the sake of

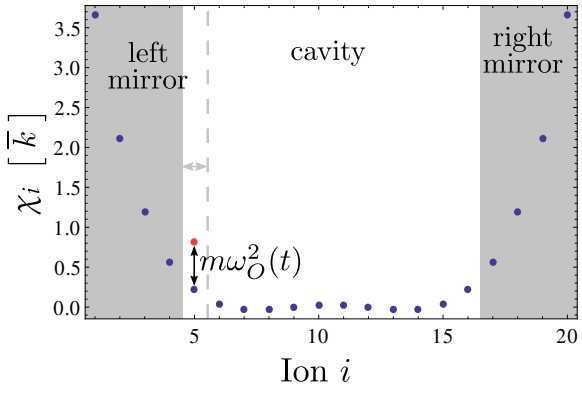

Figure 9.2.: The coefficients χ_i induced by the time independent potential V_E plotted over the ion number in units of $\bar{k}$. The ions in the gray/white areas represent the radiation field inside the mirrors/cavity. The time dependence of the cavity length is simulated by the time-dependent optical trapping potential characterized by $\omega_O^2(t)$.

simplicity, we assume that the extension of the RF-electrodes along the z-axis as well as the length of the DC-electrodes along the x-axis l_e are infinite. Inspired by [136], we assume a possible setup with $w = 80\,\mu$m, $h_0 = 80\,\mu$m, $d_g = 230\,\mu$m and we consider singly-charged ions. We set the voltages of the DC electrodes to the values

$$\begin{aligned} \phi_1 = \phi_2 = \phi_5 = \phi_6 = -5.61V\ , \\ \phi_3 = \phi_4 = 1.75V \end{aligned} \tag{9.42}$$

and use the RF electrodes to induce a confining potential that corresponds to a trapping frequency

$$\omega_{RF} = \sqrt{7.40\bar{k}/m}\ . \tag{9.43}$$

Here, $\bar{k} = \frac{e^2}{4\pi\epsilon_0 \overline{\Delta R}^3}$ is the average nearest-neighbor coupling strength, with

$$\overline{\Delta R} = || \mathbf{R}_{20} - \mathbf{R}_1 || /19 = 4.00\,\mu\text{m} \tag{9.44}$$

being the average nearest-neighbor distance. For calcium ions ($^{40}Ca^+$), for example, we obtain

$$\sqrt{\bar{k}/m} = 2\pi \cdot 1.17\ \text{MHz} \tag{9.45}$$

and $\omega_{RF} = 2\pi \cdot 3.18$ MHz. All these values lie in the range of existing experimental setups.

The calculation of the coefficients χ_i for these parameters yields the result depicted in Fig. 9.2. Here, we took the non-equidistant distribution of the ions for this trapping potential as well as all possible interactions (beyond nearest neighbors) into account.

The trapping potential is adjusted such that the χ_i deviate significantly from zero only in the outer regions of the chain. Since the electric field experiences an exponential damping within the mirrors, a rather small number of ions proves sufficient to model the space inside the mirrors, in this example, ions 1 to 4 and 17 to 20. The field inside the cavity is represented by the inner part of the ion chain, i.e., the ions 5 to 16.

We subject this ion chain to the three-stage protocol defined in Sec. 9.2. The time dependence in stage II, that we consider, corresponds to a periodically oscillating left mirror, i.e.,

$$r(t) = r_0 \,, \tag{9.46}$$

$$l(t) = l_0 + \delta \begin{cases} 0 & t \in [t_0, t_1) \\ \sin^2(\omega_D(t-t_1)/2) & t \in [t_1, t_2) \\ \sin^2(\omega_D(t_2-t_1)/2) & t \in [t_2, \infty) \end{cases} \tag{9.47}$$

where r_0 and l_0 denote the initial positions of the right and left mirrors, respectively. Further, $\delta/2$ is the amplitude of the variation and ω_D the driving frequency. This choice of the time dependence of the boundaries leads to an efficient photon production [134, 142, 143].

In order to simulate these mirror trajectories, we use a laser beam to change the radial confinement of ion 5 such that

$$\omega_O^2(t) = \alpha \frac{\bar{k}}{m} \begin{cases} 0 & t \in [t_0, t_1) \\ \sin^2(\omega_D(t-t_1)/2) & t \in [t_1, t_2) \\ \sin^2(\omega_D(t_2-t_1)/2) & t \in [t_2, \infty) \end{cases} \tag{9.48}$$

where we choose $\alpha = 0.6$. It is not a strict requirement to address precisely a single ion. Addressing several neighboring ions due to a larger beam waist just corresponds to a larger variation δ of the position of the left mirror. Similarly, a different depth of the optical potential $\alpha\bar{k}/m$ also just amounts to a different δ.

In the following section, we compare the dynamics for the ideally conducting mirrors modeled according to Moore [32] with our ion chain quantum simulation numerically. For evaluating the photon number, we choose the canonical set of mode functions for the experimental stage III, defined by Eqs. (9.11)-(9.13). We order the mode frequencies ω_ℓ as $\omega_1 < \omega_2 < ...$ and denote with $\hat{n}_1, \hat{n}_2...$ the corresponding photon number operators. For better comparison, we choose r_0, l_0, and δ such that the frequency of the lowest instantaneous eigenmode in the cavity matches the frequency of the lowest instantaneous vibrational mode of the ion chain at time instances corresponding to the maximal and minimal cavity length, i.e., $\omega_D(t-t_1) = 0$ and $\omega_D(t-t_1) = \pi$. This matching is obtained by

$$r_0 - l_0 = 15.22d \,, \tag{9.49}$$

$$\delta = 0.72d \,, \tag{9.50}$$

where $d = \left(\bar{k}/m\right)^{-1/2}$ denotes the length of the discretization intervals $[z_i, z_{i+1}]$ used in the previous section. The result for the 'cavity length', $r_0 - l_0$, can be understood by recalling that each ion represents the averaged field in one of the intervals $[z_i, z_{i+1}]$ and that the field inside the cavity is roughly represented by the 12 inner ions. The deviation between $15.22d$ and the length $12d$ expected from this simple consideration is caused by the non equidistant distribution of the ions and the discretization of the field.

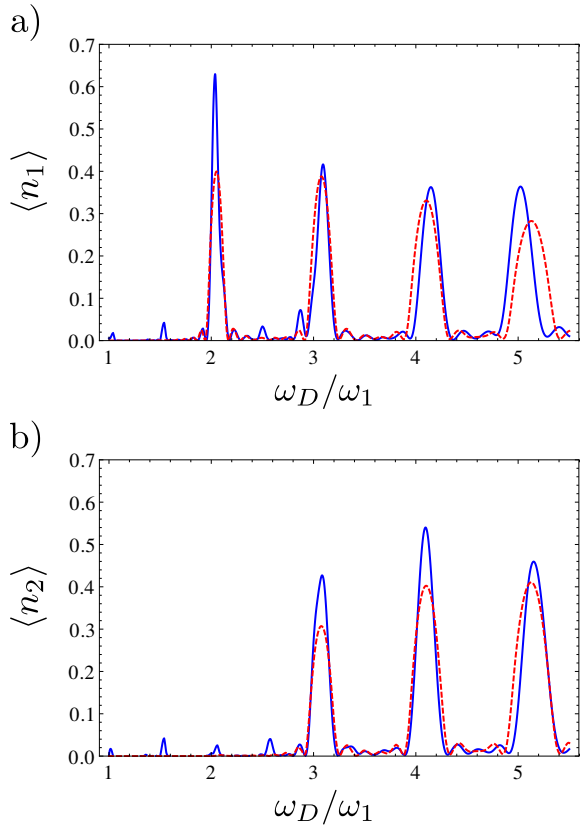

Figure 9.3.: Average photon number in (a) the lowest-frequency mode, $\ell = 1$, and (b) the second-lowest frequency mode, $\ell = 2$, as a function of the modulation frequency ω_D evaluated after 20 periods of mirror oscillation, $(t_2 - t_1)\,\omega_D = 20 \cdot 2\pi$. Strongly enhanced photon production is observed at the resonances $\omega_D = \langle \omega_{\ell_1} \rangle_T + \langle \omega_{\ell_2} \rangle_T$. Already for the considered small chain of only 20 ions, the expected results in the ion quantum simulator (blue solid line) show good qualitative agreement with the ideal results for Moore's model (red dashed line).

9.5.2 *Numerical simulation of the dynamical Casimir effect*

We have now all the necessary parameters to numerically simulate the DCE as can be studied in a realistic ion-trap experiment. We assume that during the experimental stage I the ion chain resides in its vibrational ground state. Since this initial state corresponds to the vacuum of the radiation field, all photons measured in stage III are those that have been produced in stage II. In Fig. 9.3, we show the final photon number in the modes 1 and 2 for 20 periods of mirror oscillations during the stage II. As a function of the driving frequency ω_D, one finds peaks of high photon production centered around integer multiples of the frequency ω_1. This finding is in agreement with well-known analytical results [134, 143]. The main contribution to these peaks stems from single-mode and two-mode squeezing, which is connected to the resonance condition $\omega_D = \langle \omega_{\ell_1} \rangle_T + \langle \omega_{\ell_2} \rangle_T$ with $\langle \omega_\ell \rangle_T$ denoting the time average of the instantaneous eigenfrequency $\omega_\ell(t)$ (averaged over one oscillation period of the mirror). The peaks depicted in Fig. 9.3 are slightly shifted from integer multiples of ω_1 because $\omega_\ell \neq \langle \omega_\ell \rangle_T$ and due to artifacts caused by the discretization of the model.

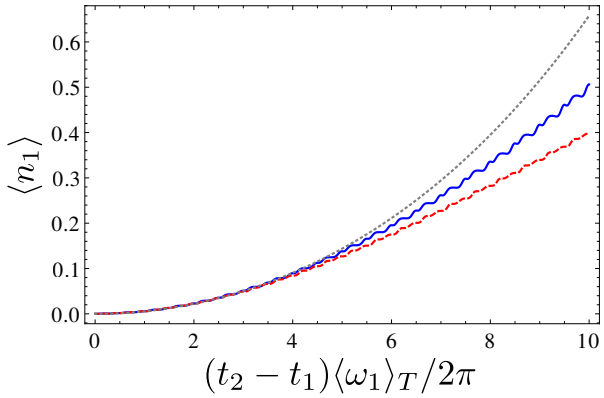

Figure 9.4.: Average photon/phonon number in mode 1 plotted over time for a driving frequency of $\omega_D = 2\langle\omega_1\rangle_T$. The ion-trap simulation (blue solid line) reaches good qualitative agreement as well with the ideal Moore's model (red dashed line) as with an approximate analytical result (grey dotted line). For short times, the agreement is even on a quantitative level.

Additionally, the trapped-ion quantum simulator allows one to monitor the photon production over time. Fig. 9.4 displays the corresponding results for the average photon number in mode 1 for a system driven with the frequency $\omega_D = 2\langle\omega_1\rangle_T$ (with $\langle\omega_1\rangle_T \approx 1.028\omega_1$). For this frequency, which lies at the first peak in Fig. 9.3 (a), the photon production is dominated by single-mode squeezing. When the resonance condition for single-mode squeezing, $\omega_D = 2\langle\omega_\ell\rangle_T$, is met, the average photon number is approximately given by [111]

$$\langle n_\ell \rangle = \sinh^2\left[\langle\omega_\ell\rangle_T \frac{\delta}{4\,(r_0 - l_0)}\,(t_2 - t_1)\right]\,, \tag{9.51}$$

valid if $\delta/\,(r_0 - l_0)$ is sufficiently small and the duration of the periodic driving is sufficiently short. At short times, this approximate expression indeed coincides with the results for the ion trap as well as for the ideal Moore's model. Some deviations occur at larger times but the qualitative agreement remains satisfactorily.

The additional small peaks of the blue curves in Fig. 9.3 (a) and (b) as well as the oscillations on the blue curve in Fig. 9.4 are artifacts connected to the fact that just a single ion was used to represent the motion of the left mirror. These artifacts can be reduced by smoothing the mirror motion, i.e., by increasing the number of ions that experience a periodic modulation during stage II.

9.6 EXPERIMENTAL CONSIDERATIONS

In this section, we support our previous analytical and numerical investigations by experimental considerations. We start with a discussion of the robustness of the simulation with respect to possible sources of errors, such as heating of the ion chain. Moreover, we review relevant techniques for measuring phononic excitations in ion chains, which allow for the probing of the radiation generated by the DCE.

9.6.1 *Possible error sources*

As the above results show, an ion chain with realistic parameters can indeed simulate the photon production in the DCE where we find a good agreement to Moore's model [32] already for 20 ions. Small deviations appear due to the limited number of ions. This is no fundamental limitation, however, and by increasing the number of ions or by using additional electrodes, it is possible to reduce these artifacts and further improve the simulation of the DCE. As mentioned previously, the protocol is also rather resilient towards a change in the (time-dependent) trapping potential. Insufficient control of the spatial dependence simply models a slightly modified cavity.

Additionally, in a realistic experiment, one has to make sure that the observed phonons are not generated by a heating of the ion chain. In the experimental setup of [136], which has similar parameters to the ones discussed above, a spectral density of electric field noise of $S_E(\omega) \leq 3.8 \cdot 10^{-13} \frac{\mathrm{V}^2}{\mathrm{m}^2}\mathrm{Hz}$ has been reported for $\omega = 2\pi \cdot 1.38\,\mathrm{MHz}$. Under the assumption that heating is dominated by electric field noise and that $S_E(\omega)\omega$ is approximately frequency independent, we obtain a heating rate of the lowest-lying mode [with $\omega_1 \approx 0.21(\bar{k}/m)^{1/2} = 2\pi \cdot 0.241\mathrm{MHz}$] of 1.31 quanta/ms. We can neglect the cross coupling between the RF and noise fields because of the relatively small frequency ω_1. For the higher modes ω_2, ω_3, ..., the effect of the electric field noise is even smaller since it causes a heating rate (ignoring cross coupling between RF and noise fields) that scales as $1/\omega^2$. Another source of heating are scattered photons from the laser beam. The corresponding heating rates can be suppressed by using sufficiently intense and sufficiently detuned standing-wave laser fields such that rates of 0.1 quanta/ms seem reasonable [135].

These heating rates have to be compared to the relevant experimental time scales. The data at the first peak in Fig. 9.3 (a) corresponds to a duration of the experimental stage II of about $(t_2 - t_1) = 0.041\mathrm{ms}$. Thus, heating is expected to increase the average phonon number of the 1st mode by roughly 0.054 phonons, which is one order of magnitude smaller than the number of phonons generated by the simulated DCE. Even more, one could further reduce the effect of ion heating due to electric field noise by decreasing the average nearest-neighbor distance between the ions. This would increase the frequencies of the modes and hence decrease the time needed to run the experiment. Therefore, according to these numbers, it is possible to cleanly observe the first as well as higher peaks in an experiment.

9.6.2 *Probing the radiation field on the single-photon level*

As discussed above, the main idea of our ion chain quantum simulation of the DCE is to map the photons of the radiation field on the phonons of the radial ion motion. Thus, for probing the radiation generated by the DCE, we have to measure the generated phononic excitations. This can be done with high accuracy on the single-phonon level by using the methods available for ion chains [90], which is one of the main advantages of our ion chain quantum simulation compared to other schemes [114–116].

One possibility for evaluating the number of phonons populating mode ℓ is to drive the corresponding red or blue detuned sideband for a short time period Δt by addressing a single ion with a laser beam. For this purpose, one should choose an ion that takes part in the collective motion described by the mode ℓ. By repeating

this experiment for several runs, the probability for exciting the ion $P_e(\Delta t)$ can be determined. For driving the blue detuned sideband, one obtains

$$P_e(\Delta t) = \sum_n P_\ell(n) \sin^2(\sqrt{n+1}\,\Omega_{0,1}\Delta t) \tag{9.52}$$

where $P_\ell(n)$ is the probability of finding n phonons in mode ℓ and $\Omega_{0,1}$ is a characteristic Rabi frequency determined by the intensity of the applied laser beam and the corresponding Lamb–Dicke parameter. For short time periods Δt, the above expression simplifies to $P_e(\Delta t) \approx \Omega_{0,1}^2 \Delta t^2 \langle 1 + \hat{n}_\ell \rangle + O(\Delta t^4)$, which allows us to evaluate the average phonon number [144, 145]. By measuring $P_e(\Delta t)$ for several Δt over a longer time period, it is possible to determine the phonon number distribution $P_\ell(n)$ by calculating the Fourier transform of $P_e(\Delta t)$ [89, 146]. In this way, we can probe not only the average photon number but even the detailed photon statistics of the radiation generated by the DCE.

In principle, it is also possible to apply other methods developed for probing the quantum state of motion and accessing other observables [90]. The choice of the most suitable method depends on the experimental parameters of the specific setup.

9.7 SUMMARY

In summary, we have presented a scheme to realize a quantum simulation of the DCE in a chain of trapped ions. Thereby, the photons inside the cavity with moving boundaries are mapped on the phononic excitations of the radial modes of the ion chain. To achieve the mapping, we derived a discrete model for the radiation field, which takes the propagation of radiation within the mirrors into account. We performed a numerical investigation in which we compared an ion chain quantum simulation of the DCE based on realistic experimental parameters with the idealized model introduced by Moore [32]. Already for 20 ions, we observe a good quantitative agreement between the ideal realization of the DCE and our ion trap quantum simulation. The scheme is robust against the most common sources of errors and its requirements are met by many existing experimental ion-trap setups.

The radiation generated by the DCE, including its full statistics, can be investigated on the single-photon respectively phonon level by using the methods available for ion traps [90]. This possibility of probing the radiation field on the single-photon level is one of the main advantages of our ion chain quantum simulation compared to other schemes [114–116]. In this chapter, we focused mainly on the DCE in a 1D cavity with a single oscillating mirror. It is interesting to adapt our scheme to explore further aspects of the DCE, such as the photon production in a cavity that oscillates as a whole [147] or the photon production in a semi-infinite system. The latter might be realized by simulating a single moving mirror at one end of the ion chain and by adding a dissipative process [144] removing the phononic excitations from the other end of the chain [148, 149].

10

CONCLUSION AND OUTLOOK

Efficient matter-field coupling on the single-photon level is a key ingredient for future quantum technologies. Many architectures for quantum communication and quantum information processing rely on efficient interfaces between single photons, which serve as flying qubits, and single material quantum systems, which serve as stationary qubits. These interfaces cannot only be used for performing quantum communication over larger distances but can also serve as building blocks for scalable quantum computation. Motivated by the current demand for efficient interfaces, we have developed suitable protocols for implementing efficient matter-field coupling on the single-photon level, which have been presented in the first part of this thesis. In the past decades, much progress has been made in the development of protocols for efficient matter-field coupling based on optical resonators. Following recent experimental developments, the first part of this thesis mainly focuses on schemes which can be applied to systems in which no mode selection by an optical resonator takes place. As this is a relatively new research area, there are a lot of open questions on how efficient interfaces between single material quantum systems and single photons propagating in a multimode radiation field can be realized. We present answers to some of these questions. On the theoretical level, a major challenge lies in the vast number of degrees of freedom, which have to be taken into account for describing the radiation field if no mode selection by an optical cavity takes place. As we are interested in enhancing the coupling between single photons and single quantum emitters, our main focus lies on the investigation of resonant multimode effects, for which we have to go beyond usual perturbative approaches.

In the course of our research, we have developed a protocol for generating entangled states between two remote material qubits, which is compatible with optical free-space communication. Furthermore, we have developed techniques to obtain enhanced control over emission and absorption processes of single quantum emitters coupled to multimode environments, such as free-space, or one-dimensional waveguides. By applying these techniques, it is possible to enhance matter-field coupling and to assemble more efficient protocols for achieving free-space as well as fiber-based quantum communication. As dissipative processes are unavoidable if single quantum systems are coupled to extreme multimode environments, such as a multimode radiation field, the investigation and control of these dissipative processes is of major interest. We have shown that by an appropriate balancing of dissipative processes, such as spontaneous photon emission and cavity decay, we can turn these processes into valuable tools for quantum information processing and computation. We have developed a protocol which relaxes the highly challenging requirements on the synchronization of the nodes of a quantum network and single-photon wave packet shaping and paves the way to scalable quantum communication networks.

Another focus of our research is the investigation of the impact of the atomic or ionic center of mass dynamics on the efficiency of matter-field coupling. Thereby, we have

developed a technique to overcome limitations on the coupling efficiency induced by the center of mass motion. This technique relaxes experimental constraints on laser cooling and the confinement of atoms or ions in a trapping potential and allows highly efficient single-photon absorption even in cases of weak confinement by a trapping potential or if no sub-Doppler cooling is applied.

Finally, we have developed a framework to study the resonant interaction of highly non-classical multi-photon states with single material quantum systems by taking the full multimode aspects of the radiation field into account. This framework allows us to investigate optical nonlinearities connected to multi-photon processes systematically. As a next step, the theoretical description of multi-photon processes provided by our framework could be used for designing suitable protocols for quantum information processing.

The features of quantum mechanics enable us to tackle problems which are hard or even impossible to solve by classical means. Unfortunately, the features of quantum mechanics which allow us to tackle computationally hard problems by using quantum computation are limiting our ability to get deeper insights into the dynamics of complex quantum systems with the help of classical computers. The relatively young research field of quantum simulations offers a solution to this dilemma. This field of research is concerned with the simulation of complex quantum systems by other well-controlled quantum systems. In the second part of this thesis, we have considered possible applications of quantum simulators on the theoretical level. Quantum simulators may help us to understand phenomena in a variety of fields ranging from condensed matter physics over chemistry to quantum field theory.

We have focused on the simulation of the dynamical Casimir effect, an interesting effect predicted theoretically by cavity QED. The dynamical Casimir effect is directly linked to the vacuum fluctuations of the electromagnetic radiation field and turns the virtual photons connected to the fluctuations of the vacuum to real observable photons. As vacuum fluctuations lie at the heart of quantum mechanics, gaining deeper insights into an effect, such as the dynamical Casimir effect, is of fundamental importance. However, the observation of this effect in a cavity QED experiment would require the rapid variation of the length of a cavity with relativistic velocities, which is a daunting challenge. We have developed a method for performing a quantum simulation of the dynamical Casimir effect in a one-dimensional cavity using an ion chain confined in a segmented ion trap.

As next steps, the method outlined in this second part of the thesis could be generalized to investigate additional aspects of the dynamical Casimir effect, such as photon generation in half-open cavities or for other interesting choices of mirror trajectories.

A

EVALUATION OF THE COMMUTATOR OF THE FIELD OPERATOR

In this appendix, we derive the relation

$$\begin{gathered}\tfrac{1}{\hbar^2}\left[\mathbf{d}_{\alpha_2}\hat{\mathbf{E}}_\perp(\mathbf{R}_{\alpha_2},t_2),\hat{\mathbf{E}}_\perp(\mathbf{R}_{\alpha_1},t_1)\mathbf{d}^*_{\alpha_1}\right]= \\ -\tfrac{i}{\epsilon_0\hbar}\mathbf{d}_{\alpha_2}\cdot\left[\nabla\times\nabla\times\mathbf{G}_\Box(\mathbf{R}_{\alpha_2},\mathbf{R}_{\alpha_1},t_2-t_1)-\nabla\times\nabla\times\mathbf{G}_\Box(\mathbf{R}_{\alpha_2},\mathbf{R}_{\alpha_1},t_1-t_2)\right]\cdot\mathbf{d}^*_{\alpha_1}\,,\end{gathered} \tag{1.1}$$

which connects the commutator of the electric field operators in the interaction picture with the dyadic Green's function of the d'Alembert operator. In order to do this, we consider the transverse part of this Green's function $\mathbf{G}^\perp_\Box(\mathbf{x},\mathbf{x}',t)$ defined by

$$\begin{aligned}\Box_{\mathbf{x}}\mathbf{G}^\perp_\Box(\mathbf{x},\mathbf{x}',t)&=\delta_\perp(\mathbf{x}-\mathbf{x}')\delta(t)\\ \mathbf{G}^\perp_\Box(\mathbf{x},\mathbf{x}',t)&=0\;\forall t<0\,,\end{aligned} \tag{1.2}$$

which fulfills suitable boundary conditions modeling the presence of a cavity or a mirror. It is straightforward to proof that $\mathbf{G}^\perp_\Box(\mathbf{x},\mathbf{x}',t)$ can be expressed by using the mode functions $\mathbf{g}_i(\mathbf{x})$ defined in Sec. 2.1,

$$\mathbf{G}^\perp_\Box(\mathbf{x},\mathbf{x}',t)=c^2\sum_i\Theta(t)\frac{\sin(\omega_i t)}{\omega_i}\mathbf{g}_i(\mathbf{x})\otimes\mathbf{g}_i(\mathbf{x}')\,.$$

By using Eq. (2.13), we get

$$\begin{aligned}\nabla_{\mathbf{x}}\times\nabla_{\mathbf{x}}\times\mathbf{G}_\Box(\mathbf{x},\mathbf{x}',t)&=\nabla_{\mathbf{x}}\times\nabla_{\mathbf{x}}\times\mathbf{G}^\perp_\Box(\mathbf{x},\mathbf{x}',t)\\ &=\sum_i\Theta(t)\omega_i\sin(\omega_i t)\mathbf{g}_i(\mathbf{x})\otimes\mathbf{g}_i(\mathbf{x}')\,.\end{aligned} \tag{1.3}$$

We obtain

$$\begin{gathered}\tfrac{1}{\hbar^2}\left[\mathbf{d}_{\alpha_2}\cdot\hat{\mathbf{E}}_\perp(\mathbf{R}_{\alpha_2},t_2),\hat{\mathbf{E}}_\perp(\mathbf{R}_{\alpha_1},t_1)\cdot\mathbf{d}^*_{\alpha_1}\right]\\ =-\tfrac{i}{\epsilon_0\hbar}\textstyle\sum_i\omega_i\sin(\omega_i(t_2-t_1))\left(\mathbf{d}_{\alpha_2}\cdot\mathbf{g}_i(\mathbf{R}_{\alpha_2})\right)\left(\mathbf{d}^*_{\alpha_1}\cdot\mathbf{g}_i(\mathbf{R}_{\alpha_1})\right)\end{gathered} \tag{1.4}$$

by evaluating the commutator of the electric field operators. By direct comparison between Eq. (1.3) and Eq. (1.4), we obtain the desired relation in Eq. 1.1.

B

SEMICLASSICAL PROPAGATION OF GREEN'S FUNCTIONS

In this appendix, we derive suitable semiclassical expressions for the Green's functions $\mathbf{G}_{\square}(\mathbf{x}_2, \mathbf{x}_1, t)$. In order to do so, we consider the convolution of $\mathbf{G}_{\square}(\mathbf{x}_2, \mathbf{x}_1, t)$ with a rapid oscillating function $f(t)$ with a slowly varying envelope

$$f(t) = f_0(t)e^{i\omega t} \tag{2.1}$$

with ω being the oscillation frequency and $f_0(t)$ being the slowly varying envelope. By choosing $f(t)$ as a rapidly oscillating function with a slowly varying envelope, we match the criteria for application of the semiclassical methods discussed in chapter 3. We are interested in the following expression

$$\int_{-\infty}^{t} \nabla \times \nabla \times \mathbf{G}_{\square}(\mathbf{x}_2, \mathbf{x}_1, t - t_1)\mathbf{d}_1^* f(t_1)dt_1 \, . \tag{2.2}$$

This choice is motivated by Eq. (3.17) where also the convolution between $\mathbf{G}_{\square}(\mathbf{x}_2, \mathbf{x}_1, t)$ and a rapidly oscillating function enters.

As described in Sec. 3.4, we divide the volume in two parts V_1 and V_2 as depicted in Fig. 3.2. In volume V_1, we just use $\mathbf{G}_{\square}^{\text{free}}(\mathbf{x}_2, \mathbf{x}_1, t)$ in order to evaluate the time evolution of the field and, in volume V_2, we use semiclassical methods in order to take the boundary conditions into account (see Eq. (3.23)). Without loss of generality, we assume that the support of f is confined to $[t_s, t_f]$ with $\mid t_f - t_s \mid \ll r/c$ and r being the radius of the sphere forming V_1.

Inside V_1, we obtain by using the free-space Green's function

$$\begin{aligned}
&\int_{-\infty}^{t_f} \nabla \times \nabla \times \mathbf{G}_{\square}^{\text{free}}(\mathbf{x}, \mathbf{x}_1, t - t_1)\mathbf{d}_1 f(t_1)dt_1 = \\
&\frac{1}{4\pi}\int_{-\infty}^{t} \nabla \times \nabla \times \left[\frac{1}{|| \, \mathbf{x} - \mathbf{x}_1 \, ||}\delta\left(t - || \, \mathbf{x} - \mathbf{x}_1 \, || \, /c\right)\right] \mathbf{d}_1 f(t_1)dt_1 \\
\approx -\frac{1}{4\pi c^2 \, || \, \mathbf{x} - \mathbf{x}_1 \, ||}&\left[\mathbb{1} - \frac{(\mathbf{x} - \mathbf{x}_1) \otimes (\mathbf{x} - \mathbf{x}_1)}{|| \, \mathbf{x} - \mathbf{x}_1 \, ||^2}\right] \int_{-\infty}^{t} \delta''\left(t - || \, \mathbf{x} - \mathbf{x}_1 \, || \, /c\right) \mathbf{d}_1 f(t_1)dt_1 \\
= -\frac{1}{4\pi c^2 \, || \, \mathbf{x} - \mathbf{x}_1 \, ||}&\left[\mathbb{1} - \frac{(\mathbf{x} - \mathbf{x}_1) \otimes (\mathbf{x} - \mathbf{x}_1)}{|| \, \mathbf{x} - \mathbf{x}_1 \, ||^2}\right] \mathbf{d}_1 f''(t - || \, \mathbf{x} - \mathbf{x}_1 \, || \, /c) \, .
\end{aligned}$$

In the following, we use the expression to evaluate the field for $t = r/c + t_s$. At this point in time, the field is confined to a spherical shell with the radii r and $r/c - \left(t_f - t_s\right)$. By using the semiclassical methods discussed in chapter 3, we can propagate the field through volume V_2. For this purpose, we have to construct suitable trajectories $\mathbf{x}^j(t_0)$, i.e., the rays of geometrical optics, connecting V_1 to the point $\mathbf{x}_2$. As initial condition, we have to choose $\mathbf{x}^j(t_0) \in V_1$ and the corresponding velocity

$$\dot{\mathbf{x}}^j(t_0) = c\frac{\mathbf{x}^j(t_0) - \mathbf{x}_1}{||\mathbf{x}^j(t_0) - \mathbf{x}_1||}$$

always pointing in the radial direction. By applying Eq. (3.23), we obtain

$$\begin{aligned}&\int_{-\infty}^{t} \mathbf{d}_2 \nabla \times \nabla \times \mathbf{G}_{\square}(\mathbf{x}_2, \mathbf{x}_1, t-t_1)\mathbf{d}_1 f(t_1)dt_1 \\ &= -\tfrac{1}{4\pi c^2}\sum_j \sqrt{\left|\det\left(\tfrac{\partial \mathbf{x}^j(t_j)}{\partial \mathbf{x}^j(t_0)}\right)\right|}^{-1} f''\left(t-(t_j-t_0)-\mid\mid \mathbf{x}^j(t_0)-\mathbf{x}_1 \mid\mid /c\right) \tfrac{1}{||\mathbf{x}^j(t_0)-\mathbf{x}_1||} \\ &\quad \times \mathbf{d}_2 \cdot \mathbf{M}_j \left[\mathbb{1} - \tfrac{\left(\mathbf{x}^j(t_0)-\mathbf{x}_1\right)\otimes\left(\mathbf{x}^j(t_0)-\mathbf{x}_1\right)}{||\mathbf{x}^j(t_0)-\mathbf{x}_1||^2}\right]\mathbf{d}_1 \,, \end{aligned} \tag{2.3}$$

whereby the sum is running over all trajectories $\mathbf{x}^j(t)$ with $\mathbf{x}^j(t_j) = \mathbf{x}_2$ for $t_j - t_0 = t - t_s - r/c$ and $\mathbf{x}^j(0) \in V_1$. The matrices $\mathbf{M}_j$ are unitary matrices which take the vectorial nature of the field into account. They describe the orientation of the field after propagating through volume V_2. They basically take the change of the orientation of the vector field and phase flips caused by the boundary conditions into account. By using some relations concerning the rays of geometrical optics, we can also write this in the form

$$\begin{aligned}&\int_{-\infty}^{t} \mathbf{d}_2 \nabla \times \nabla \times \mathbf{G}_{\square}(\mathbf{x}_2, \mathbf{x}_1, t-t_1)\mathbf{d}_1 f(t_1)dt_1 \\ &= -\tfrac{1}{4\pi c^2}\sum_j \tfrac{1}{r}\sqrt{\left|\det\left(\tfrac{\partial \mathbf{x}^j(t_j)}{\partial \mathbf{x}^j(t_0)}\right)\right|}^{-1} f''\left(t-r/c-(t_j-t_0)\right) \\ &\quad \times \mathbf{d}_2 \cdot \mathbf{M}_j \left[\mathbb{1} - \tfrac{\left(\mathbf{x}^j(t_0)-\mathbf{x}_1\right)\otimes\left(\mathbf{x}^j(t_0)-\mathbf{x}_1\right)}{||\mathbf{x}^j(t_0)-\mathbf{x}_1||^2}\right]\mathbf{d}_1 \,, \end{aligned} \tag{2.4}$$

whereby the sum is running over all trajectories with $\mathbf{x}^j(t_j) = \mathbf{x}_2$ for $t_j \geq t_0$ and $\mathbf{x}^j(t_0) \in \partial V_1$. The previous relations also holds true for arbitrary functions of the form (2.1) without a confined support. This can be justified by using that more general functions can be composed out of functions $f_1 ... f_n$ which fulfill the property and semiclassical propagation can be applied separately (because we are dealing with a linear partial differential equation).

The expression above induces the following relation for the Green's function

$$\begin{aligned}&\nabla \times \nabla \times \mathbf{G}_{\square}(\mathbf{x}_2, \mathbf{x}_1, t-t_1) = -\tfrac{1}{4\pi c^2}\sum_j \\ &\sqrt{\left|\det\left(\tfrac{\partial \mathbf{x}^j(t_j)}{\partial \mathbf{x}^j(t_0)}\right)\right|}^{-1} \delta''\left(t-r/c-(t_j-t_0)\right) \tfrac{1}{||\mathbf{x}^j(t_0)-\mathbf{x}_1||}\mathbf{d}_2 \cdot \mathbf{M}_j \left[\mathbb{1} - \tfrac{\left(\mathbf{x}^j(t_0)-\mathbf{x}_1\right)\otimes\left(\mathbf{x}^j(t_0)-\mathbf{x}_1\right)}{||\mathbf{x}^j(t_0)-\mathbf{x}_1||^2}\right]\mathbf{d}_1 \,. \end{aligned}$$

C

MICROSCOPIC MODEL OF THE MIRRORS

In this appendix, we motivate the Hamiltonian $\hat{H}_1(t)$, which models the mirrors. The basic idea is to describe the mirrors according to the Drude–Lorentz model [150] by a distribution of charges that can oscillate around fixed positions. These charges could be the bound electrons of an atom or the electrons in a metal, which oscillate with the plasma frequency.

The matter–field coupling can be modeled by the interaction term [33]

$$\hat{H}_{\mathrm{i}} = -\int_{\mathbb{R}^3} \hat{\mathbf{j}}(\mathbf{x}) \cdot \hat{\mathbf{A}}(\mathbf{x}) d^3\mathbf{x} \tag{3.1}$$

with being $\hat{\mathbf{j}}(\mathbf{x})$ the charge current. Its Fourier transform

$$\hat{\mathbf{j}}_\omega(\mathbf{x}) = \tfrac{1}{\sqrt{2\pi}} \int_{\mathbb{R}} \exp(i\omega t)\, \hat{\mathbf{j}}(t, \mathbf{x}) \mathrm{d}t \tag{3.2}$$

can be connected to the Fourier transform of the electric field

$$\hat{\mathbf{E}}_\omega(\mathbf{x}) = \tfrac{1}{\sqrt{2\pi}} \int_{\mathbb{R}} \exp(i\omega t)\, \hat{\mathbf{E}}(t, \mathbf{x}) \mathrm{d}t \tag{3.3}$$

by the relation

$$\hat{\mathbf{j}}_\omega(\mathbf{x}) = n(\mathbf{x}) \frac{e^2}{m} \sum_{m=1}^{N} G_m \frac{-i\omega}{\omega_m^2 - \omega^2 - i\gamma_m \omega} \hat{\mathbf{E}}_\omega(\mathbf{x}) \tag{3.4}$$

with the oscillator sum rule $\sum_{m=1}^{N} G_m = 1$ and $n(\mathbf{x})$ being the charge density. In this relation, the frequencies ω_m and decay rates γ_m are chosen heuristically to match the experimental findings. In the following, we assume that the main contributions in Eq. (3.4) for the relevant frequencies ω of the radiation field stem from terms with $\omega_m, \gamma_m \ll \omega$. In this case, we obtain

$$\hat{\mathbf{j}}_\omega(\mathbf{x}) = n(\mathbf{x}) \tfrac{ie^2}{m\omega} \hat{\mathbf{E}}_\omega(\mathbf{x}) \tag{3.5}$$

$$\Rightarrow \hat{\mathbf{j}}(t, \mathbf{x}) = -n(\mathbf{x}) \tfrac{e^2}{m} \hat{\mathbf{A}}(t, \mathbf{x})\,. \tag{3.6}$$

We have used that $\hat{\mathbf{E}}(t, \mathbf{x}) = -\frac{\partial}{\partial t} \hat{\mathbf{A}}(t, \mathbf{x})$. The back action of the charge distribution onto the radiation field can be taken into account by the effective Hamiltonian

$$\hat{H}_{\mathrm{eff}} = \frac{e^2}{2m} \int_{\mathbb{R}^3} n(\mathbf{x}) \hat{\mathbf{A}}^2(\mathbf{x}) d^3\mathbf{x}\,. \tag{3.7}$$

This effective Hamiltonian matches our model of the mirrors, Eq. (9.4).

BIBLIOGRAPHY

[1] A. Einstein, Ann. Phys. **322**, 891 (1905).

[2] W. Heisenberg, in *Original Scientific Papers Wissenschaftliche Originalarbeiten* (Springer, 1985), pp. 382–396.

[3] S. Weinberg, *The quantum theory of fields*, vol. 2 (Cambridge University Press, 1996).

[4] T. Maiman, Nature **187**, 493 (1960).

[5] S. Chu, L. Hollberg, J. E. Bjorkholm, A. Cable, and A. Ashkin, Phys. Rev. Lett. **55**, 48 (1985).

[6] W. Paul, Rev. Mod. Phys. **62**, 531 (1990).

[7] D. Wineland, R. Drullinger, and F. Walls, Phys. Rev. Lett. **40**, 1639 (1978).

[8] V. Giovannetti, S. Lloyd, and L. Maccone, Science **306**, 1330 (2004).

[9] M. A. Nielsen and I. L. Chuang, *Quantum computation and quantum information* (Cambridge university press, 2010).

[10] N. Gisin and R. Thew, Nat. Photon. **1**, 165 (2007).

[11] S. Lloyd, Science **273**, 1073 (1996).

[12] Y. Nakamura, Y. A. Pashkin, and J. Tsai, Nature **398**, 786 (1999).

[13] M. Arndt, O. Nairz, J. Vos-Andreae, C. Keller, G. Van der Zouw, and A. Zeilinger, Nature **401**, 680 (1999).

[14] C. Monroe, R. Raussendorf, A. Ruthven, K. Brown, P. Maunz, L.-M. Duan, and J. Kim, Phys. Rev. A **89**, 022317 (2014).

[15] D. Chang, A. S. Sørensen, P. Hemmer, and M. Lukin, Phys. Rev. Lett. **97**, 053002 (2006).

[16] A. Akimov, A. Mukherjee, C. Yu, D. Chang, A. Zibrov, P. Hemmer, H. Park, and M. Lukin, Nature **450**, 402 (2007).

[17] J. A. Schuller, E. S. Barnard, W. Cai, Y. C. Jun, J. S. White, and M. L. Brongersma, Nat. Mater. **9**, 193 (2010).

[18] T. M. Babinec, B. J. Hausmann, M. Khan, Y. Zhang, J. R. Maze, P. R. Hemmer, and M. Lončar, Nat. Nanotechnol. **5**, 195 (2010).

[19] J. Claudon, J. Bleuse, N. S. Malik, M. Bazin, P. Jaffrennou, N. Gregersen, C. Sauvan, P. Lalanne, and J.-M. Gérard, Nat. Photon. **4**, 174 (2010).

[20] E. Vetsch, D. Reitz, G. Sagué, R. Schmidt, S. T. Dawkins, and A. Rauschenbeutel, Phys. Rev. Lett. **104**, 203603 (2010).

[21] A. Goban, K. S. Choi, D. J. Alton, D. Ding, C. Lacroûte, M. Pototschnig, T. Thiele, N. P. Stern, and H. J. Kimble, Phys. Rev. Lett. **109**, 033603 (2012).

[22] J. You and F. Nori, Nature **474**, 589 (2011).

[23] M. Devoret and R. Schoelkopf, Science **339**, 1169 (2013).

[24] R. Maiwald, A. Golla, M. Fischer, M. Bader, S. Heugel, B. Chalopin, M. Sondermann, and G. Leuchs, Phys. Rev. A **86**, 043431 (2012).

[25] R. Ursin, F. Tiefenbacher, T. Schmitt-Manderbach, H. Weier, T. Scheidl, M. Lindenthal, B. Blauensteiner, T. Jennewein, J. Perdigues, P. Trojek, et al., Nat. Phys. **3**, 481 (2007).

[26] D. Stucki, N. Walenta, F. Vannel, R. T. Thew, N. Gisin, H. Zbinden, S. Gray, C. Towery, and S. Ten, New J. Phys. **11**, 075003 (2009).

[27] H.-J. Briegel, W. Dür, J. I. Cirac, and P. Zoller, Phys. Rev. Lett. **81**, 5932 (1998).

[28] J. Cirac, P. Zoller, H. Kimble, and H. Mabuchi, Phys. Rev. Lett. **78**, 3221 (1997).

[29] S. Ritter, C. Nölleke, C. Hahn, A. Reiserer, A. Neuzner, M. Uphoff, M. Mücke, E. Figueroa, J. Bochmann, and G. Rempe, Nature **484**, 195 (2012).

[30] M. Fischer, M. Bader, R. Maiwald, A. Golla, M. Sondermann, and G. Leuchs, Appl. Phys. B **117**, 797 (2014).

[31] A. Ralston and E. D. Reilly, eds., *Encyclopedia of computer science* (Chapman & Hall, London, 1993), 3rd ed.

[32] G. T. Moore, J. Math. Phys. **11**, 2679 (1970).

[33] C. Cohen-Tannoudji, J. Dupont-Roc, G. Grynberg, and M. O. Scully, *Photons & Atoms: Introduction to Quantum Electrodynamics* (Wiley, New York, 1989).

[34] W. P. Schleich, *Quantum optics in phase space* (John Wiley & Sons, 2011).

[35] R. J. Glauber and M. Lewenstein, Phys. Rev. A **43**, 467 (1991).

[36] V. Weisskopf and E. Wigner, Z. Phys. **65**, 18 (1930).

[37] B. Mollow, Phys. Rev. A **12**, 1919 (1975).

[38] V. P. Maslov and M. V. Fedoriuk, *Semi-Classical Approximation in Quantum Mechanics* (D. Reidel, Dordrecht, 1981).

[39] V. I. Arnold, *Mathematical methods of classical mechanics*, vol. 60 (Springer Science & Business Media, 1989).

[40] C. H. Bennett, G. Brassard, C. Crépeau, R. Jozsa, A. Peres, and W. K. Wootters, Phys. Rev. Lett. **70**, 1895 (1993).

[41] A. K. Ekert, Phys. Rev. Lett. **67**, 661 (1991).

[42] D. Moehring, P. Maunz, S. Olmschenk, K. Younge, D. Matsukevich, L.-M. Duan, and C. Monroe, Nature **449**, 68 (2007).

[43] H. Bernien, B. Hensen, W. Pfaff, G. Koolstra, M. Blok, L. Robledo, T. Taminiau, M. Markham, D. Twitchen, L. Childress, et al., Nature **497**, 86 (2013).

[44] T. Beth and G. Leuchs, eds., *Quantum Information Processing* (Wiley-VCH, Weinheim, 2005).

[45] M. Berry and K. Mount, Rep. Prog. Phys. **35**, 315 (1972).

[46] A. Rakić, A. Djurišić, J. Elazar, and M. Majewski, Appl. Opt. **37**, 5271 (1998).

[47] M. Sondermann, N. Lindlein, and G. Leuchs, arXiv:0811.2098 (2008).

[48] M. Lieb, Opt. Express **8**, 458 (2001).

[49] G. Leuchs, K. Mantel, A. Berger, H. Konermann, M. Sondermann, U. Peschel, N. Lindlein, and J. Schwider, Appl. Opt. **47**, 5570 (2008).

[50] A. April, B. Pierrick, and P. Michel, Opt. Express **19**, 9201 (2011).

[51] M. Sondermann and G. Leuchs, J. Europ. Opt. Soc. **8**, 13502 (2013).

[52] J. Bergou, J. Mod. Optics **57**, 160 (2010).

[53] S. Olmschenk, D. Hayes, D. N. Matsukevich, P. Maunz, D. L. Moehring, K. C. Younge, and C. Monroe, Phys. Rev. A **80**, 022502 (2009).

[54] S. Olmschenk, K. C. Younge, D. L. Moehring, D. N. Matsukevich, P. Maunz, and C. Monroe, Phys. Rev. A **76**, 052314 (2007).

[55] W. C. Campbell, J. Mizrahi, Q. Quraishi, C. Senko, D. Hayes, D. Hucul, D. N. Matsukevich, P. Maunz, and C. Monroe, Phys. Rev. Lett. **105**, 090502 (2010).

[56] J. J. McLoughlin, A. H. Nizamani, J. D. Siverns, R. C. Sterling, M. D. Hughes, B. Lekitsch, B. Stein, S. Weidt, and W. K. Hensinger, Phys. Rev. A **83**, 013406 (2011).

[57] B. Hensen, H. Bernien, A. Dréau, A. Reiserer, N. Kalb, M. Blok, J. Ruitenberg, R. Vermeulen, R. Schouten, C. Abellán, et al., Nature **526**, 682 (2015).

[58] R. Maiwald, D. Leibfried, J. Britton, J. C. Bergquist, G. Leuchs, and D. J. Wineland, Nat. Phys. **5**, 551 (2009).

[59] N. Lindlein, R. Maiwald, H. Konermann, M. Sondermann, U. Peschel, and G. Leuchs, Laser Physics **17**, 927 (2007).

[60] M. K. Tey, Z. Chen, S. A. Aljunid, B. Chng, F. Huber, G. Maslennikov, and C. Kurtsiefer, Nat. Phys. **4**, 924 (2008).

[61] M. Stobińska, G. Alber, and G. Leuchs, Europhys. Lett. **86**, 14007 (2009).

[62] P. Kolchin, C. Belthangady, S. Du, G. Yin, and S. Harris, Phys. Rev. Lett. **101**, 103601 (2008).

[63] C. Liu, Y. Sun, L. Zhao, S. Zhang, M. Loy, and S. Du, Phys. Rev. Lett. **113**, 133601 (2014).

[64] V. Balić, D. A. Braje, P. Kolchin, G. Yin, and S. E. Harris, Phys. Rev. Lett. **94**, 183601 (2005).

[65] M. Born and V. Fock, Z. Physik **51**, 165 (1928), ISSN 0044-3328.

[66] K. Bergmann, H. Theuer, and B. Shore, Rev. Mod. Phys. **70**, 1003 (1998).

[67] A. J. Daley, M. M. Boyd, J. Ye, and P. Zoller, Phys. Rev. Lett. **101**, 170504 (2008).

[68] A. V. Gorshkov, A. M. Rey, A. J. Daley, M. M. Boyd, J. Ye, P. Zoller, and M. D. Lukin, Phys. Rev. Lett. **102**, 110503 (2009).

[69] H. Katori, M. Takamoto, V. G. Pal'chikov, and V. D. Ovsiannikov, Phys. Rev. Lett. **91**, 173005 (2003).

[70] X. Xu, T. H. Loftus, J. L. Hall, A. Gallagher, and J. Ye, J. Opt. Soc. Am. B **20**, 968 (2003).

[71] Y. Takasu, K. Maki, K. Komori, T. Takano, K. Honda, M. Kumakura, T. Yabuzaki, and Y. Takahashi, Phys. Rev. Lett. **91**, 040404 (2003).

[72] M. Fleischhauer and M. D. Lukin, Phys. Rev. Lett. **84**, 5094 (2000).

[73] D. F. Phillips, A. Fleischhauer, A. Mair, R. L. Walsworth, and M. D. Lukin, Phys. Rev. Lett. **86**, 783 (2001).

[74] H. De Riedmatten, M. Afzelius, M. U. Staudt, C. Simon, and N. Gisin, Nature **456**, 773 (2008).

[75] L.-M. Duan and H. J. Kimble, Phys. Rev. Lett. **92**, 127902 (2004).

[76] A. Reiserer, S. Ritter, and G. Rempe, Science **342**, 1349 (2013).

[77] A. Reiserer, N. Kalb, G. Rempe, and S. Ritter, Nature **508**, 237 (2014).

[78] N. Kalb, A. Reiserer, S. Ritter, and G. Rempe, Phys. Rev. Lett. **114**, 220501 (2015).

[79] W. Happer, Rev. Mod. Phys. **44**, 169 (1972).

[80] C. Gardiner and P. Zoller, *Quantum noise*, vol. 56 (Springer Science & Business Media, 2004).

[81] M. Bender, Carl and A. Orszag, Steven, *Advanced Mathematical Methods for Scientist and Engineers I, Asymptotic Methods and Perturbation Theory* (Springer, New York, 1999).

[82] J. Petersen, J. Volz, and A. Rauschenbeutel, Science **346**, 67 (2014).

[83] J. Lin, J. B. Mueller, Q. Wang, G. Yuan, N. Antoniou, X.-C. Yuan, and F. Capasso, Science **340**, 331 (2013).

[84] R. Mitsch, C. Sayrin, B. Albrecht, P. Schneeweiss, and A. Rauschenbeutel, Nat. Commun. **5** (2014).

[85] P. Lambropoulos and P. Zoller, Phys. Rev. A **24**, 379 (1981).

[86] C. Kurtsiefer, O. Dross, D. Voigt, C. R. Ekstrom, T. Pfau, and J. Mlynek, Phys. Rev. A **55**, R2539 (1997).

[87] M. Abramowitz and I. Stegun, *Pocketbook of Mathematical Functions* (Harri Deutsch, Frankfurt/Main, 1984).

[88] W.-M. Zhang, D. H. Feng, and R. Gilmore, Rev. Mod. Phys. **62**, 867 (1990).

[89] D. Meekhof, C. Monroe, B. King, W. Itano, and D. Wineland, Phys. Rev. Lett. **76**, 1796 (1996).

[90] D. Leibfried, R. Blatt, C. Monroe, and D. Wineland, Rev. Mod. Phys. **75**, 281 (2003).

[91] D. Heinzen and D. Wineland, Phys. Rev. A **42**, 2977 (1990).

[92] B. T. Varcoe, S. Brattke, M. Weidinger, and H. Walther, Nature **403**, 743 (2000).

[93] E. Waks, E. Diamanti, and Y. Yamamoto, New J. Phys. **8**, 4 (2006).

[94] H. Bethe, Z. Phys. **71**, 205 (1931).

[95] C. W. Gardiner and M. J. Collett, Phys. Rev. A **31**, 3761 (1985).

[96] J.-T. Shen and S. Fan, Phys. Rev. Lett. **98**, 153003 (2007).

[97] S. Fan, Ş. E. Kocabaş, and J.-T. Shen, Phys. Rev. A **82**, 063821 (2010).

[98] T. Shi and C. P. Sun, Phys. Rev. B **79**, 205111 (2009).

[99] H. Zheng, D. J. Gauthier, and H. U. Baranger, Phys. Rev. A **82**, 063816 (2010).

[100] D. Roy, Phys. Rev. Lett. **106**, 053601 (2011).

[101] S. Xu and S. Fan, Phys. Rev. A **91**, 043845 (2015).

[102] H. Zheng, D. J. Gauthier, and H. U. Baranger, Phys. Rev. Lett. **107**, 223601 (2011).

[103] H. Zheng, D. J. Gauthier, and H. U. Baranger, Phys. Rev. A **85**, 043832 (2012).

[104] T. Caneva, M. T. Manzoni, T. Shi, J. S. Douglas, J. I. Cirac, and D. E. Chang, New J. Phys. **17**, 113001 (2015).

[105] T. Shi, D. E. Chang, and J. I. Cirac, Phys. Rev. A **92**, 053834 (2015).

[106] V. F. Weisskopf and E. P. Wigner, Z. Phys. **63**, 54 (1930).

[107] N. Trautmann, J. Bernád, M. Sondermann, G. Alber, L. L. Sánchez-Soto, and G. Leuchs, Phys. Rev. A **90**, 063814 (2014).

[108] T. Holstein and H. Primakoff, Phys. Rev. **58**, 1098 (1940).

[109] W. E. Lamb and R. C. Retherford, Phys. Rev. **72**, 241 (1947).

[110] H. B. Casimir, in *Proc. K. Ned. Akad. Wet* (1948), vol. 51, p. 150.

[111] V. Dodonov, Phys. Scripta **82**, 038105 (2010).

[112] J. Johansson, G. Johansson, C. Wilson, and F. Nori, Phys. Rev. A **82**, 052509 (2010).

[113] J. R. Johansson, G. Johansson, C. Wilson, and F. Nori, Phys. Rev. Lett. **103**, 147003 (2009).

[114] C. Wilson, G. Johansson, A. Pourkabirian, M. Simoen, J. Johansson, T. Duty, F. Nori, and P. Delsing, Nature **479**, 376 (2011).

[115] D. A. Dalvit, Nature **479**, 303 (2011).

[116] P. Lähteenmäki, G. Paraoanu, J. Hassel, and P. J. Hakonen, Proc. Natl. Acad. Sci. U.S.A. **110**, 4234 (2013).

[117] J. Chiaverini, R. B. Blakestad, J. Britton, J. D. Jost, C. Langer, D. Leibfried, R. Ozeri, and D. J. Wineland, Quantum Inf. Comput. **5**, 419 (2005).

[118] S. A. Schulz, U. Poschinger, F. Ziesel, and F. Schmidt-Kaler, New J. Phys. **10**, 045007 (2008).

[119] D. Kaufmann, T. Collath, M. T. Baig, P. Kaufmann, E. Asenwar, M. Johanning, and C. Wunderlich, Appl. Phys. B **107**, 935 (2012).

[120] D. Porras and J. I. Cirac, Phys. Rev. Lett. **93**, 263602 (2004).

[121] P. A. Ivanov, S. S. Ivanov, N. V. Vitanov, A. Mering, M. Fleischhauer, and K. Singer, Phys. Rev. A **80**, 060301(R) (2009).

[122] A. Bermudez, M. Martin-Delgado, and D. Porras, New J. Phys. **12**, 123016 (2010).

[123] A. Bermudez, T. Schaetz, and D. Porras, Phys. Rev. Lett. **107**, 150501 (2011).

[124] T. Pruttivarasin, M. Ramm, I. Talukdar, A. Kreuter, and H. Häffner, New J. Phys. **13**, 075012 (2011).

[125] A. Benassi, A. Vanossi, and E. Tosatti, Nat. Commun. **2**, 236 (2011).

[126] K. Pyka, J. Keller, H. L. Partner, R. Nigmatullin, T. Burgermeister, D. Meier, K. Kuhlmann, A. Retzker, M. B. Plenio, W. H. Zurek, et al., Nat. Commun. **4**, 2291 (2013).

[127] S. Ulm, J. Rossnagel, G. Jacob, C. Degünther, S. T. Dawkins, U. G. Poschinger, R. Nigmatullin, A. Retzker, M. B. Plenio, F. Schmidt-Kaler, et al., Nat. Commun. **4**, 2290 (2013).

[128] M. Mielenz, J. Brox, S. Kahra, G. Leschhorn, M. Albert, T. Schaetz, H. Landa, and B. Reznik, Phys. Rev. Lett. **110**, 133004 (2013).

[129] S. Ejtemaee and P. C. Haljan, Phys. Rev. A **87**, 051401(R) (2013).

[130] A. Del Campo, G. De Chiara, G. Morigi, M. Plenio, and A. Retzker, Phys. Rev. Lett. **105**, 075701 (2010).

[131] G.-D. Lin and L.-M. Duan, New J. Phys. **13**, 075015 (2011).

[132] A. Bermudez, M. Bruderer, and M. B. Plenio, Phys. Rev. Lett. **111**, 040601 (2013).

[133] M. Ramm, T. Pruttivarasin, and H. Häffner, New J. Phys. **16**, 063062 (2014).

[134] C. Law, Phys. Rev. A **49**, 433 (1994).

[135] C. Schneider, M. Enderlein, T. Huber, and T. Schätz, Nat. Photon. **4**, 772 (2010).

[136] G. Vittorini, K. Wright, K. R. Brown, A. W. Harter, and S. C. Doret, Rev. Sci. Instrum. **84**, 043112 (2013).

[137] C. Ospelkaus, U. Warring, Y. Colombe, K. Brown, J. Amini, D. Leibfried, and D. Wineland, Nature **476**, 181 (2011).

[138] D. Allcock, T. Harty, H. Janacek, N. Linke, C. Ballance, A. Steane, D. Lucas, R. Jarecki Jr, S. Habermehl, M. Blain, et al., Appl. Phys. B **107**, 913 (2012).

[139] K. Brown, C. Ospelkaus, Y. Colombe, A. Wilson, D. Leibfried, and D. Wineland, Nature **471**, 196 (2011).

[140] D. Stick, W. Hensinger, S. Olmschenk, M. Madsen, K. Schwab, and C. Monroe, Nat. Phys. **2**, 36 (2006).

[141] J. H. Wesenberg, Phys. Rev. A **78**, 063410 (2008).

[142] O. Méplan and C. Gignoux, Phys. Rev. Lett. **76**, 408 (1996).

[143] V. Dodonov, J. Phys. A **31**, 9835 (1998).

[144] F. Diedrich, J. Bergquist, W. M. Itano, and D. Wineland, Phys. Rev. Lett. **62**, 403 (1989).

[145] D. Wineland, W. M. Itano, J. Bergquist, and R. G. Hulet, Phys. Rev. A **36**, 2220 (1987).

[146] C. Roos, T. Zeiger, H. Rohde, H. Nägerl, J. Eschner, D. Leibfried, F. Schmidt-Kaler, and R. Blatt, Phys. Rev. Lett. **83**, 4713 (1999).

[147] A. Lambrecht, M.-T. Jaekel, and S. Reynaud, Phys. Rev. Lett. **77**, 615 (1996).

[148] D. Givoli, J. Comput. Phys. **94**, 1 (1991).

[149] M. Israeli and S. A. Orszag, J. Comput. Phys. **41**, 115 (1981).

[150] L. Rosenfeld, *Theory of electrons*, vol. 1 (North-Holland, 1951).

NOTATION

Symbol	Meaning
	Sets
$\mathbb{R}$	Set of real numbers
$\mathbb{C}$	Set of complex numbers
$\mathbb{N}$	Set of natural numbers without 0
$\mathbb{N}_0$	Set of natural numbers including 0
$\mathbb{Z}$	Set of integers
	Operations
$\otimes$	Tensor product or dyadic product
a^*	Complex conjugate of the complex number a
$\|a\|$	Absolute value of complex number a
$\hat{A}^\dagger$	Hermitian conjugate of the operator $\hat{A}$
$\mathbb{1}$	Identity operator acting on the corresponding vector space
$\mathbf{M}^T$	Transposition of the matrix $\mathbf{M}$
∇	Nabla operator
Δ	Laplace operator
$\Box$	D'Alembert operator
	Physical constants
c	Speed of light
ϵ_0	Vacuum permittivity
μ_0	Vacuum permeability
$\hbar$	Reduced Planck constant
	Vectors

Vectors are written in the form $\mathbf{a} = (a_1, a_2 ... a_n)^T$.

$\mathbf{a}_i$	The ith component of the vector $\mathbf{a}$
$\|\|\mathbf{a}\|\|$	Norm of the vector $\mathbf{a}$ (If not stated otherwise, the two-norm is used.)

CURRICULUM VITÆ

PERSONAL INFORMATION

Nils Trautmann geb. Griebe

E-Mail: nils.trautmann@physik.tu-darmstadt.de

Born: March 19th, 1989 in Erbach (Germany)

PHD STUDIES

2013–2017	Ph. D. Studies at Technische Universität Darmstadt, Institut für Angewandte Physik (supervised by Prof. Dr. Gernot Alber)

HIGHER EDUCATION

2011–2013	Master of Science in physics Technische Universität Darmstadt
2010–2013	Bachelor of Science in mathematics Technische Universität Darmstadt
2008–2011	Bachelor of Science in physics Technische Universität Darmstadt

EDUCATION

2005–2011	Higher Education Entrance Qualification Berufliches Gymnasium Michelstadt (Germany)
1999–2005	Secondary School Carl-Weyprecht-Schule (Germany)
1995–1999	Elementary School Grundschule Zell (Germany)

14th February 2017

LIST OF PUBLICATIONS

[1] N. Trautmann, G. Ferenczi, S. Croke, S. Barnett, submitted to J. Opt. (2016)
"Holographic quantum imaging: reconstructing spatial properties via two-particle interference"

[2] M. Sonnleitner, N. Trautmann, S. Barnett, Phys. Rev. Lett. **118**, 053601 (2017)
"Will a decaying atom feel a friction force?"

[3] N. Trautmann, G. Alber (2016)
"Elementary quantum electrodynamical processes in multimode scenarios - a photon path representation for multiphoton states"
to be published in "Lectures on Quantum Information"
(Wiley-VCH, edited by D. Bruss and G. Leuchs)

[4] N. Trautmann, G. Alber, G.Leuchs, Phys. Rev. A **94**, 033832 (2016)
"Efficient single-photon absorption by a trapped moving atom"
selected as "Editor's Suggestion"

[5] N. Trautmann, G. Alber, Phys. Rev. A **93**, 053807 (2016)
"Dissipation-enabled efficient excitation transfer from a single photon to a single quantum emitter"

[6] N. Trautmann, P. Hauke, New J. Phys. **18**, 043029 (2016)
"Quantum simulation of the dynamical Casimir effect with trapped ions"

[7] G. Alber, N. Trautmann, J. Phys. Conf. Ser. **672**, 012004 (2016)
"Cooperative quantum electrodynamical processes in an ellipsoidal cavity"

[8] N.Trautmann, G. Alber, G. S. Agarwal, G.Leuchs,
Phys. Rev. Lett. **114**, 173601 (2015)
"Time-Reversal-Symmetric Single-Photon Wave Packets for Free-Space Quantum Communication"

[9] N.Trautmann, J. Z. Bernád, M. Sondermann, G. Alber, L. L. Sánchez-Soto, G. Leuchs,
Phys. Rev. A **90**, 063814 (2014)
"Generation of entangled matter qubits in two opposing parabolic mirrors"

[10] G. Alber, N. Griebe, EPJ Web of Conferences **78**, 04001 (2014)
"Spontaneous Photon Emission in Cavities"